Design and Evaluation of Photodynamically Active Lipid-Based Nanoformulations for Combination Therapy against Skin Cancer

THESIS

Submitted in partial fulfillment of the requirements for the degree of

DOCTOR OF PHILOSOPHY

by

RUPESH SANJAYKUMAR JAIN

ID. No. 2018PHXF0038P

Under the Supervision of

Prof. GAUTAM SINGHVI

&

Co-supervision of

Dr. SUNIL KUMAR DUBEY

BIRLA INSTITUTE OF TECHNOLOGY AND SCIENCE PILANI (RAJASTHAN)
2023

BIRLA INSTITUTE OF TECHNOLOGY AND SCIENCE, PILANI

CERTIFICATE

This is to certify that the thesis entitled **Design and Evaluation of Photodynamically Active Lipid-Based Nanoformulations for Combination Therapy against Skin Cancer** submitted by **Rupesh Sanjaykumar Jain**, ID. No. **2018PHXF0038P** for the award of the Ph.D. degree of the institute embodies original work done by him under our supervision.

Signature (Supervisor):
Prof. Gautam Singhvi,
(Supervisor)
Associate Professor, Department of Pharmacy,
Birla Institute of Technology and Science,
 Pilani, Pilani Campus, Rajasthan 333031

Signature (Co-supervisor):
Dr. Sunil Kumar Dubey,
(Co-supervisor)
General Manager, Medical Research
R&D Healthcare Division Emami Ltd.,
13, BT Road, Belgharia, Kolkata 700056, India

Date:

Place:

Dedicated To

MY GRANDFATHER

LATE. SHANTILALJI JAIN

TABLE OF CONTENT

ACKNOWLEDGEMENT

LIST OF ABBREVIATIONS

% Cdr	Percentage cumulative drug release
%	Percentage
% rsd	Percentage relative standard deviation
% ee	Percent entrapment efficiency
% w/w	Percentage weight by weight
% v/v	Percentage volume by volume
% w/v	Percentage weight by volume
<	Less than
≤	Less than equal to
>	More than
≥	More than equal to
~	Approximately equal to
±	Plus or minus
=	Equal to
Λ_{max}	Wavelength of maximum absorbance
G	Gram
Mg	Milligram
°c	Degree centigrade
μm	Micrometer
μl	Microliter
Cm	Centimeter
Ml	Milliliter
Nm	Nanometer
Ng/ml	Nanogram per milliliter
μg/ml	Micrometer per milliliter
Mg/ml	Milligram per milliliter
G'	Storage modulus
G''	Loss modulus
Anova	Analysis of variance
Acn	Acetonitrile
Ftir	Fourier transform infrared spectrometer
Api	Active pharmaceutical ingredient
Dmso	Dimethyl sulfoxide
Cmax	Maximum concentration
Auc	Area under curve
Cpcsea	Committee for the purpose of control and supervision of experiments on animals
Conc.	Concentration
Ce6	Chlorin e6
Cur	Curcumin
Dsc	Differential scanning calorimetry
Fesem	Field emission scanning electron microscopy
Dls	Dynamic light scattering
Ao	Acridine orange

h	Hour
EDTA	Ethylene diamine tetra acetic acid
GC-HS	Gas chromatography - Headspace
RP-HPLC	Reverse phase - High performance liquid chromatography
IPA	Isopropyl alcohol
HETP	Height equivalent to theoretical plates
HQC	Higher quality control sample
ICH	International council for harmonization
IAEC	Institutional animal ethical committee
IL	Interleukin
IS	Internal standard
LOQ	Limit of quantification
LLOQ	Lower limit of quantification
LOD	Limit of detection
MeOH	Methanol
MDA	Malondialdehyde
LQC	Lower quality control
min	Minute
MQC	Medium quality control
NMR	Nuclear magnetic resonance
MWCO	Molecular weight cut off
p value	Significance level in statistical tests
n	Diffusional exponent indicating the drug release mechanism in Korsmeyer-peppas model
LPNs	Lipid-polymer hybrid nanoparticles
pH	Negative log to the base 10 of hydrogen ion concentration
PS	Photosensitizer
PLA	Poly (D,L-lactide)
PDI	Polydispersity index
R_t	Retention time
QC	Quality control
R_s	Resolution
R^2	Regression coefficient
SD	Standard deviation
rpm	Rotations per minute
SLNs	Solid-lipid nanoparticles
RT	Room temperature
sec	Second
PDC	Polymer drug conjugate
LPs	Liposomes
NLCs	Nanostructure lipid carriers
$t_{1/2}$	Half-life
USFDA	United States Food and Drug Administration

LIST OF TABLES

LIST OF FIGURES

Abstract

Skin cancer (SC) is the fourth most common type of cancer in the whole world. The main two subtypes that cover 95% of all cases are melanoma and non-melanoma skin cancer (NMSC). Non-melanoma skin cancer is a type of cutaneous malignancy and the most observed cancer in people. In NMSC involved Basal cell carcinoma (BCC), squamous cell carcinoma (SCC), extramammary Paget's disease (EMPD), Merkel cell carcinoma (MCC), and several carcinomas. In the NMSC, 70 to 80 % of skin cancer arises from BSC, and 20 to 25 % is responsible by SCC. According to the Italian Association for Cancer Research (AIRC), cutaneous melanoma makes up only 5% of skin tumors. Due to its rapid metastasis, melanoma remains one of the deadliest types of skin cancer. Several treatment options are available for skin cancer (malignant melanoma (MM) and NMSC), depending on the type, stage, and location of the cancer. Primary treatment modalities include surgery, radiation, topical, targeted, immunotherapy, and chemotherapy. Oral chemotherapy is non-invasive and does not require surgical procedures or radiation therapy. However, there are also limitations to oral chemotherapy for skin cancer. The effectiveness of oral chemotherapy can vary depending on the type and stage of skin cancer, and it may not be the most effective option for all cases. Furthermore, oral chemotherapy can have side effects, including nausea, vomiting, fatigue, and decreased blood cell counts, and lack of precision in oral chemotherapy can lead to the destruction of healthy cells.

Topical chemotherapy for skin cancer is commonly utilized as a cost-effective and convenient treatment approach and is non-invasive and localized in nature, as the medication is directly applied to the affected area. This targeted approach minimizes systemic side effects while effectively treating superficial skin cancers. The convenience and ease of use of topical chemotherapy allow patients to self-administer the treatment at home. Furthermore, it preserves healthy tissue and offers better cosmetic outcomes than surgical interventions or radiation therapy. However, topical monotherapy for skin cancer has certain drawbacks, including the potential risk of metastasis. While topical treatments are effective for superficial skin cancers, they may not adequately address deeper or more aggressive forms of skin cancer. These cancers have the potential to invade deeper layers of the skin and spread to other parts of the body, leading to metastasis. Topical medications primarily target the surface layers of the skin, and their limited penetration may not be sufficient to eliminate cancer cells that have already spread beyond the initial site. Therefore, relying solely on topical monotherapy for advanced or metastatic skin cancer may not be sufficient in controlling or eradicating skin cancer. In such cases, a combination of treatments, including Photodynamic Therapy (PDT) and topical

chemotherapy, may be necessary to address the risk of metastasis and achieve better treatment outcomes.

PDT offers the benefit of being a non-invasive treatment option that can be applied over a wide treatment area, yielding favorable clinical outcomes. Several clinical research studies have demonstrated the effectiveness of PDT in the treatment of pre-malignant and malignant non-melanoma skin cancer (NMSC). However, it presents certain drawbacks, including limited tumor penetration, insufficient light penetration, prolonged chemotherapy leading to drug resistance, metastasis appear, and sometimes becoming more aggressive and ultimately resulting in ineffective therapy. In this sense, enhancing PDT effectiveness by combining it with other therapeutic modalities has become an interesting field in melanoma and NMSC research.

In this aspect, topical administration of anticancer drugs along with photodynamically active molecules is a non-invasive approach, which stands to be a promising modality for treating aggressive cutaneous melanomas and basal cell carcinoma with the added advantage of synergistic effect and high patient compliance. Most of the drug molecules that have been discovered and are being used in pharmaceuticals are hydrophobic in nature, thereby posing challenges in their delivery. Its conventional preparations (gels, creams, ointments, etc.) exhibit lower efficacy and cause local toxicity due to rapid loco-regional drug release. To avoid these toxicities and problems associated with above mentioned and improve the efficacy of compounds, new carriers are required that should penetrate deeper into the viable epidermis or tumor tissues. In order to address these challenges, the focus has been switched to nanotherapeutics. Several reports state that lipidic nano-carriers are preferred for their promising delivery of therapeutic agents to localized skin surfaces due to their smaller size, greater permeation through biological barriers, better surface properties, high skin deposition, and sustained drug release properties; they were able to prove advantageous in treating skin cancer, including basal cell carcinoma and melanoma.

In this dissertation, the combination of dual-drug lipidic nanoparticles was explored for the topical delivery of Itraconazole (ITZ) as an anticancer agent and Chlorin e6 (Ce6) as a photoactivable molecule for treating skin cancer (Basal Cell Carcinoma and Melanoma cancer) using photodynamic therapy.

A simple and accurate HPLC analytical method was developed and validated to estimate the ITZ in the drug release, ex-vivo skin permeation study. A fluorescence spectrofluorometric method was developed to estimate chlorin e6 levels in samples obtained from drug release studies, ex-vivo experiments, etc. The initial optimization of the formulation was conducted

using the QbD approach with the ITZ, and the final optimized batch was formulated with chlorin e6 instead. The process of preparing a combined batch of dual drug lipidic nanoparticles (ITZ/Ce6@LNPs) involved hot emulsification, followed by size reduction using probe sonication. The optimized dual drug lipidic nanoparticle containing itraconazole and chlorin e6 exhibited a particle size of less than 100 nm, and entrapment efficiency for both molecules were found to be less than 81%. Our results depicted that topically applying this reactive oxygen species (ROS) generative dual drug-loaded lipidic nanoparticles incorporated in SEPINEO gel achieves better permeation (78 ± 7.34 %) across the skin and exhibited the higher skin retention. The therapeutic efficacy of the developed formulation was tested on B16F10 and A431 cell lines via cellular uptake, cytotoxicity evaluation, combination index Mitochondrial membrane potential, nuclear staining, DNA fragmentation, ROS generation, apoptosis, and cell cycle assays under NIR irradiation (665 nm at 0.5 W/cm^2). Co-delivering ITZ and Ce6 exhibited synergistic effects, higher cellular uptake, better cancer growth inhibition, and pronounced apoptotic events compared to the free drug-alone formulation. ITZ/Ce6@LNPs treatment showed the lowest IC$_{50}$ values compared to free Ce6 and free ITZ. The ~3.1 fold decrease in IC$_{50}$ values of ITZ/Ce6@LNPs than free Ce6 and free ITZ at 24 h in the presence of laser treatment. Therefore, it indicated that the longer retention of ITZ/Ce6@LNPs intracellularly reaches optimum concentration to exert cytotoxic action. Interestingly, a combination of ITZ and Ce6 lipidic nanoformulation showed higher apoptosis on the B16F10 and A431 cell lines than free drugs. Flow cytometry analysis demonstrated that ITZ/Ce6@LNPs exhibited more mitochondria membrane potential disruption in B16F10 and A431 cell lines. In the ex-vivo permeation study, it was observed that ITZ/Ce6@LNPs gel exhibited a permeation rate of up to 78% through the skin after 24 h, whereas the plain gel (ITZ+Ce6) showed a permeation rate of 30%. Further In-vivo topical biodistribution study was tested on the B16F10 cell-induced tumor-bearing mice model. The findings revealed that the fluorescence intensity of the ITZ/Ce6@LNPs gel increased at the tumor site for up to 12 h following topical application. In contrast, the group treated with free Ce6 exhibited a significantly lower signal, indicated that the ITZ/Ce6@LNPs gel has the potential to accumulate gradually at the tumor site. Further tumors were separated, and their major organs were collected for fluorescence imaging. However, some measurable ITZ/Ce6@LNPs fluorescence was present in the tumor, resulting in a significantly higher accumulation of ITZ/Ce6@LNPs observed in the tumor tissue. It suggests that ITZ/Ce6@LNPs selectively accumulated in the target tissue (superficial skin cancer), which is a desirable outcome for the designed formulation.

After observing the impressive combined chemo-photodynamic therapeutic effects of the ITZ/Ce6/LNPs gel in vitro studies, we proceeded to investigate its vivo anticancer potential. The developed ITZ/Ce6@LNPs gel exhibited the slowest tumor growth compared to the treatment group. The enhanced delivery of potent molecules to the tumor site led to a remarkable improvement in the in vivo anti-tumor efficacy against a C57 skin cancer mouse model. This improvement was characterized by increased generation of reactive oxygen species (ROS) and induction of apoptosis within the tumor. The average tumor volumes post eight days were 708 ± 31 mm^3 , 502 ± 10 mm^3 , 545 ± 17 mm^3 , 402 ± 10 mm^3 , 170 ± 18 mm^3 for control, free Ce6, ITZ, ITZ+Ce6 and ITZ/Ce6/LNPs gel, respectively

The ROS and TUNEL assay demonstrated a greater intensity of bright green fluorescence in tumor samples treated with the in-house developed gel, indicating an increased presence of apoptotic bodies and significant production of reactive oxygen species (ROS). Conversely, in the Ki-67 assay, the control group exhibited higher cell proliferation, as indicated by the strongest green fluorescence, while the in-house developed gel treatment group displayed lower green fluorescence, suggesting reduced cell proliferation.. This indicates that the in-house developed gel treatment resulted in reduced Ki-67 positive tumor cells and confirmed minimal tumor growth.

In another study, we have formulated dual drug lipidic nanoparticles using as a natural anticancer agent, including curcumin (CUR) and Chlorin e6 (Ce6) for the treatment of skin cancer (Melanoma and Basal cell carcinoma). Curcumin, an active anticancer agent, and chlorin e6, a photoactivable molecule, were developed into dual drug-based lipidic nanoparticles that produced (ROS) when activated at 665 nm by Near-infrared light (NIR). A simple and accurate simultaneous HPLC analytical method was developed and validated to estimate the CUR and Ce6 in the drug release, ex-vivo permeation study and biological samples. The simultaneously developed HPLC method was linear over the concentration range from 100 ng/ ml to 10000 ng/ml for both drugs. The coefficient of determination (R^2) was found to be more than 0.999 for both drugs. The initial optimization of the formulation was conducted using the QbD approach with the CUR, and the final optimized batch was formulated with Ce6 instead. The process of preparing a combined dual drug lipidic nanoparticles (DDLN) involved hot emulsification, followed by size reduction using probe sonication method. The optimized dual drug lipidic nanoparticle (DDLN) containing curcumin and chlorin e6 exhibited a particle size of less than 100 nm, and entrapment efficiency for both molecules were found to be less than 85%. The therapeutic efficacy of the developed formulation was tested on B16F10 and A431 cell lines via cytotoxicity evaluation, combination

index, cellular uptake, nuclear staining, DNA fragmentation, ROS generation, apoptosis, and cell cycle assays under NIR irradiation (665 nm). The DDLN treatment exhibited an IC_{50} value that was approximately 4.2 fold lower compared to free CUR, free Ce6, and the combination of free Ce6 and free CUR (FCE+FCC), under NIR irradiation (665 nm) in B16F10 and A431 cell lines at 24 h. It indicated that the longer retention of DDLN intracellularly reaches optimum concentration to exert cytotoxic action. The cellular uptake analysis showed that both cell lines exhibited clear, brighter fluorescence in the cytoplasm and nuclei were observed in DDLN-treated cells, suggesting quick internalization of DDLN. The geometric mean fluorescence of DDLN treated with laser light cells from 1672.2 ± 34.22 to 3445.54 ± 16.27 from 1 to 4 h for the B16F10 cell, whereas the geometric mean fluorescence of free Ce6-treated cells was increased from 850.4 ± 20.7 to 1620.7 ± 23.67. Similarly, the geometric mean fluorescence of DDLN (+ L) treated cells from 1752.32 ± 20.32 to 3945.54 ± 26.27 from 1 to 4 h for A431 cell lines. Co-delivering curcumin and chlorin e6 exhibited synergistic effects, higher cellular uptake, better cancer growth inhibition, and pronounced apoptotic events compared to the free drug-alone formulation. Our results depicted that topically applying this ROS generative dual drug-loaded lipidic nanoparticles incorporated in SEPINEO gel achieves better permeation (80 ± 2.45 %) across the skin and exhibited higher skin retention.

Dermatopharmacokinetic results of DDLN exhibited that the total concentration of CUR and Ce6 (DDLN gel) retained $AUC_{0–32}$ skin in the epidermis and dermis layers was significantly high compared to the FCE+FCC-gel. The total amount of concentration of CUR and Ce6 in the epidermis layer was increased with DDLN gel (CUR) (711.32 ± 39.02 $\mu g/cm^2 * h$) and for DDLN gel (Ce6) (833.89 ± 20.90 $\mu g/cm^2 * h$) in comparison to FCE+FCC-gel-CUR (294.91 ± 5.338 $\mu g/cm^2 * h$) and for FCE+FCC-gel-Ce6 (277.50 ± 4.202 $\mu g/cm^2 * h$). Dermatopharmacokinetic results stated that lipids-containing nanocarriers are efficient in intermingling with lipid bilayer membranes which results in lipid rearrangement that could exhibit higher permeation and higher residence time in the skin layers, which was confirmed with Confocal microscopy. This work puts forth photo-triggered ROS generative dual drug-based lipidic nanoparticles, which are simple and efficient to develop and exhibit synergistic therapeutic effects against cutaneous melanoma and basal cell carcinoma.

CHAPTER 1- INTRODUCTION

SKIN CANCER

DUAL-DRUG LIPIDIC NANOPARTICLES

CURRENT THERAPIES

PHOTODYNAMIC THERAPY

TOPICAL THERAPY
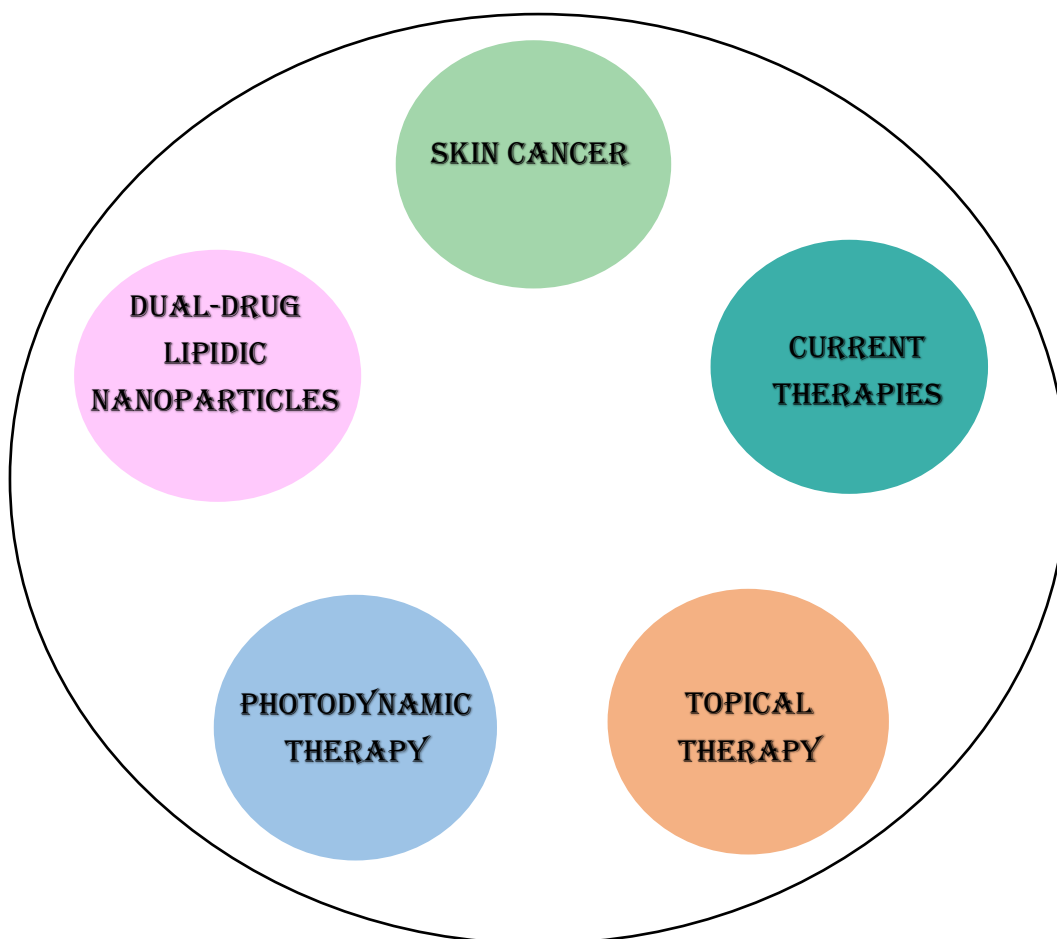
1.1. Introduction

The outermost organ of the human body is the skin, which has a surface area of approximately 1.5 to 2 square meters, providing a protective barrier against the external environment. The skin comprises of three distinct layers: the outer epidermis, which is 50-150 μm thick and serves as a biological barrier; the middle dermis layer, which is 250 μm thick and provides thermal insulation; and the inner subcutaneous fatty tissue, which acts as a cushion against mechanical forces. The stratum corneum of the epidermis is the barrier layer that acts as a defence system in the body by inhibiting the entry of pathogens and protecting from the external environment. The protective function of the stratum corneum limits the permeation of drugs through it. However, highly lipophilic drugs and low molecular weight drugs are passively delivered through the skin, and below the epidermis is a dermal layer that provides support and nourishment to the epidermis [1–3]. The human skin is prone to a disease/ disorder when it is exposed to extreme conditions or environmental or external factors. In skin disorders, various diseases are observed like malignant melanoma skin cancer, non-melanoma skin cancer actinic keratosis (AKs), and others. Skin cancer is a life-threatening disease, the most common sign of cancer in the skin is a change in the appearance of the skin, such as the formation of sores, a large brownish spot with darker speckles, painful lesions that itch or burn, etc. Skin cancer (SC) is the fourth most common type of cancer in the whole world. The main two subtypes that cover 95% of all cases are melanoma and non-melanoma skin cancer (NMSC). In skin cancer, the most dangerous are basal cell carcinoma (BCC), squamous cell carcinoma, and malignant melanoma [4]. BCC is the most common type of cancer in the United States. Every year 1 million new patients suffer from it, and 53000 new cases registered yearly in the United Kingdom. [5].

1.2. Types of Skin Cancer

Skin cancers can be roughly classified into (a) melanoma and (b) non-melanoma skin cancer (NMSC). Melanoma skin cancer is also one of the mainly aggressive and life-threatening skin cancers. Melanoma is a malignant tumor of melanocytes and mainly found in the skin. Melanoma is rapidly growing into the skin and metastasizes. Melanoma develops from the genetic mutation in the melanocytes, pigment-producing cells, which can be found in the skin. According to the data of surveillance of epidemiology, melanoma is the most common skin cancer in the United States, and is responsible for 4% of the all cancer death. This also predicted

that 1 in 5 Americans would develop skin cancer and annually 1 million new cases are found [6]. NMSC is more prevalent than melanoma skin cancer and it exhibits four times more occurrence than melanoma. In contrast, as melanoma shows a higher chance of metastasizing and resistance to therapies, it is associated with 70% of all SC-related deaths [7]. Melanoma is mainly divided into four classes concerning clinical and histopathological factors as superficial spreading melanoma, nodular melanoma, lentigo malignant melanoma, and Acral lentiginous melanoma, which are summarised in **Table 1.1** [6].

Table 1.1 - Different types of melanoma cancer based on the clinical manifestation

Description	Type of Melanoma Cancer			
	Superficial spreading melanoma	**Nodular melanoma**	**Lentigo maligna melanoma**	**Acral lentiginous melanoma**
Prevalence and locations	• Superficial spreading melanoma is the most common type of skin cancer, and responsible for about 70% of skin. It is generally found in a pre-existing mole. • The location of this cancer is the lower extremities in women and the backside in men	• Nodular melanoma is the second most common skin cancer and is responsible for about (15-20%) of cases. It found to have aggressive and rapid growth than superficial melanoma. The location of this cancer is trunk, head, and neck.	• Lentigo maligna melanoma is a lower risk of skin cancer than other melanoma. It is responsible for 10% of cases. The location of this cancer mainly found at face, neck, and arms.	• Acral lentiginous melanoma skin cancer is mainly responsible for 5 % of cases. The location of this cancer is beneath the nail beds, palms, and soles.
Pathophysiology and colour of skin cancer	• It is plaque-type and Irregular, asymmetric and border shape • The color of this cancer mainly black, red, buke and white • While growth ulceration and bleeding	• Irregular border • Ulceration, bleeding • The color of this cancer mainly found in Dark-black and blue.	• Irregular border • Raises with growth • Initially, the color of this cancer is tan brown and later changes to dark brown.	• Irregular border • Gradual thickening and ulceration with growth • The color of this cancer is dark brown.

The remaining are made up of some extremely rare and aggressive subtypes of SC [8–10]. In the last few decades due to various contributing factors, the incidence of skin cancers has been increasing steadily. Various factors are responsible for cutaneous skin carcinomas such as UV light exposure, skin etching, skin aging, some mechanical trauma, and ionizing radiation source. Sometimes genetic characteristics are also responsible for skin carcinoma [11]. Within NMSC, Basal Cell Carcinoma (BCC) and Squamous Cell Carcinoma (SCC) account for almost 99% of all cases. **(Figure 1.1)** [12] The lesser prevalent types of NMSC are Merkel cell carcinoma, cutaneous lymphomas, skin carcinosarcoma, Kaposi's sarcoma, and dermatofibrosarcoma. NMSCs are curable in most instances but in recent times the steeply increasing treatment cost, as well as high prevalence, have made these a matter of serious public health concern. The most prevalent type of skin cancer is BCC. Areas exposed to sunlight of mainly fair-skinned people are at risk of BCC the most. It occurs mostly on the face and the head [13–15]. Originating from basal cells of the epidermis, BCC lacks precursor lesions. Morphological observations have shown that many BCC cases occur directly from hair follicle keratinocytes. BCC is associated with invading tissues locally and spreading contiguously, but metastasis is extremely rare. Current treatment for BCC is not specific and due to its non-metastatic feature, surgical removal of the tumor is the most convenient way [16].
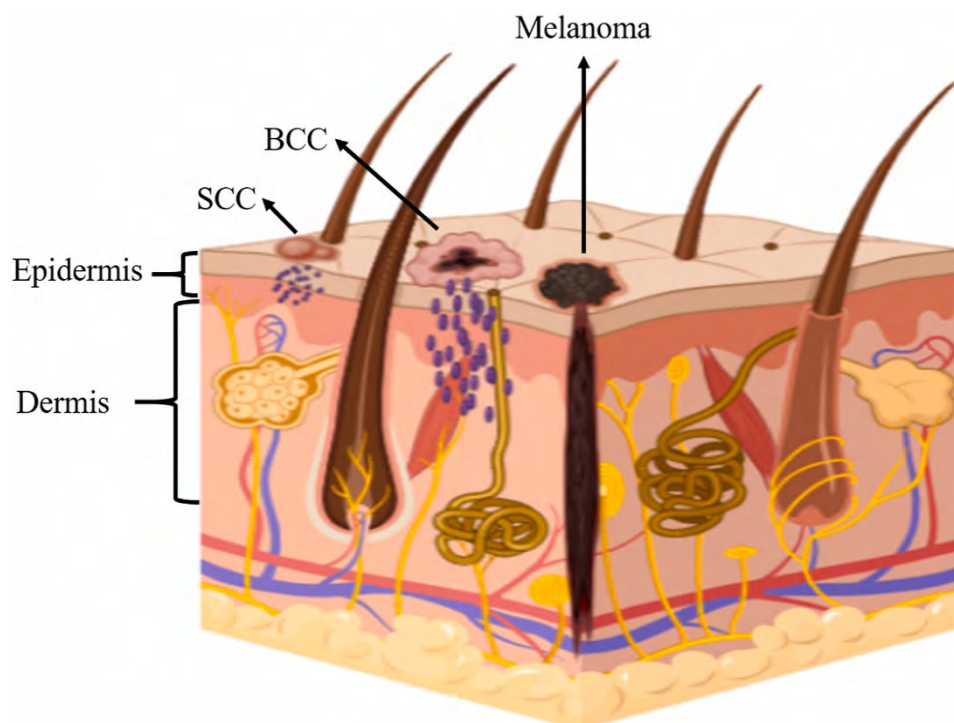
Figure 1.1 Types of Skin Cancer [12].

SCC is the second most common skin cancer [15]. Metastasis is more common in SCC than in BCC. After locally invading tissue and destroying it, SCC show a tendency to metastasize to the lymph nodes. In contrast to BCC, SCC has specific precursors like Bowen's disease and actinic keratosis. SCC is more prevalent in patients who are being treated with immunosuppressive therapy. If they have concomitant HPV (Human Papilloma Virus) infection, the chance of SCC occurrence rises significantly. However, there is no evidence of HPV increasing the risk of SCC in individuals with an intact immune system. Like BCC, there is no specific therapy for SCC, and the best approach is to surgically remove the tumor before it starts metastasizing [16–19].

Although malignant melanoma (MM) is less prevalent than BCC or SCC, this causes more death than all NMSCs combined. Light pigmentation, Ultraviolet (UV) exposure, and multiple numbers of nevi are the most common risk factors of MM. MM arising from previously present atypical nevus is common; however, it can also occur without one. As the prognosis for metastatic MM is still not promising, surgical removal of a tumor prior to metastasis is still the safest option available [16,20–22].

1.3. Several Signaling Keys Pathways in Skin Cancer

The mutations occurring at the basal layer are the main causes of MM. Based on the affected area, MM can be of two types, namely, cutaneous and non-cutaneous melanoma. This classification also provides a general idea of the depth of invasion associated with MM. Multiple studies have indicated the role of UV radiations in the appearance of BCC, SCC, and MM. The reactive oxygen species (ROS) formed due to UV-A radiations cause the destruction of DNA, lipids, and proteins on the skin via oxidation. A few common mutations involved in MM are BRAF, MEK, NRAS, and mitogen-activated protein kinase (MAPK). Sometimes these primary mutations steer different melanogenic pathways even when no mutation is present. Along with surgery and radiation therapy for MM, systemic therapy and antibody therapy are also being used widely [23–25].

Both BCC and SCC can be categorized under keratinocyte carcinoma due to their common origin from keratinocytes. Hedgehog pathway downregulation is identified to be associated with BCC while SCC is related to the upliftment of neoantigen as well as mutational events. Other than genetic interventions, neoplastic occurrences of NMSCs can also be triggered by various multifactorial elements like exposure to HPV, exposure to UV radiation, genodermatoses, synchronous diseases, tobacco use, immunosuppression, inflammatory

conditions, etc. Medicaments like alpha inhibitors (tumor necrosis factor) can also trigger NMSCs [23,26].

There are several pathways of skin cancer development. The MAPK pathway is composed of designated kinases upstream to downstream. A-Raf, B-Raf, and C-Raf/ Raf-1 come under the class MAPKKK (MAPK Kinase-Kinase). MEK-1 and MEK-2 come one step under MAPKK (MAPK Kinase). Lastly, ERK-1 and ERK-2 end the pathway as MAPKs. The phosphorylation of ERK activates multiple substrates that in turn stimulate cell proliferation [27]. Mutations at RAS or B-Raf are very common triggers for skin cancer pathogenesis. Mutation at RAS can also initiate another cancer pathway namely, the PI3K-Akt signaling pathway. It is possible to have skin cancer development in a single cell following both of these pathways [28]. PI3K pathway has also been observed to be activated genetically or due to a missing component (e.g., PTEN) [29]. PI3K can be activated by receptors with protein tyrosine kinase activity (Receptor Tyrosine Kinase, RTK). P13K converts PIP2 to PIP3, which is a potent second messenger in survival signaling [30]. PIP3 actively phosphorylates Akt that in turn initiates phosphorylation of various effector proteins involved in important cellular functions like proliferation, angiogenesis, survival, etc. The presence of phosphate and tensin homolog or PTEN generally stops this oncogenic pathway by converting PIP3 back into PIP2 but the absence of PTEN leads to tumor growth [31]. Apart from this, the Hedgehog (Hh) pathway is an important pathway for developing NMSCs, especially BCCs. Mutations at PTCH1 initiate oncogenesis. The mutation can occur due to UV signature, pyrimidine substitution in PTCH1, or loss of chromosome 9q22 heterozygosity. PTCH1 inhibits the activity of SMO, a G-protein-coupled receptor (GPCR). The binding of Sonic Hedgehog (SHh) to PTCH activates the SMO which in turn activates the GLI1 (Glioma-associated oncogene) proteins. Activation of GLI1 causes uncontrolled cell proliferation leading to cancer [32]. **Figure 1.2** represents the major pathways of skin cancer development.
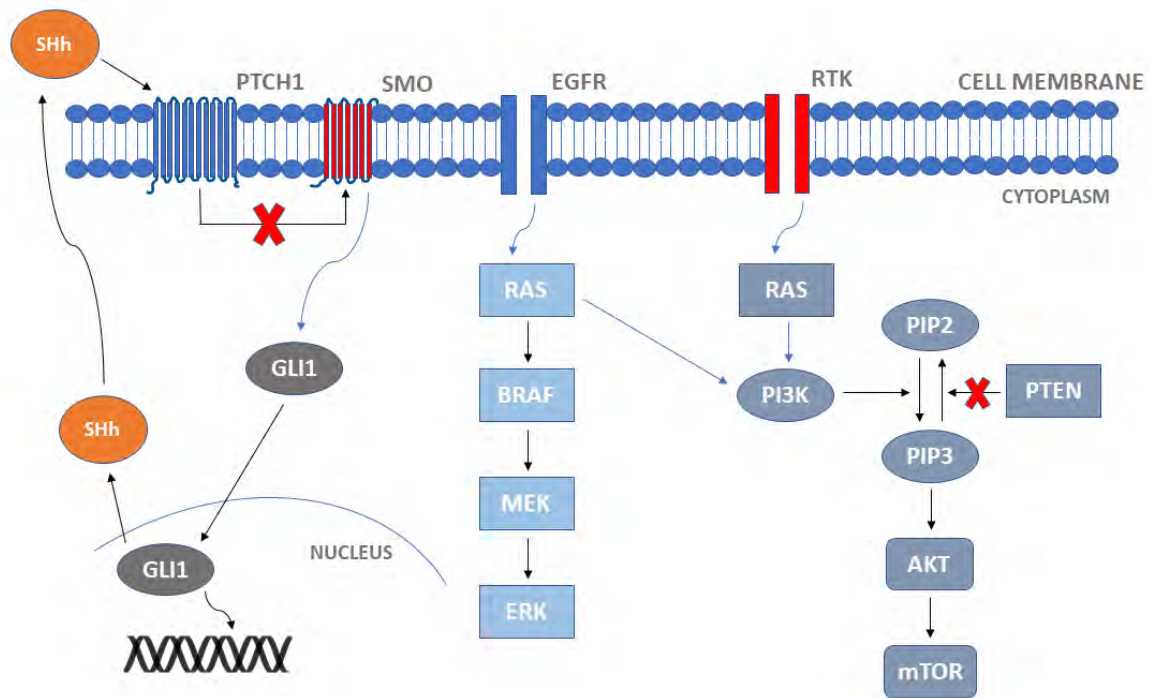
Figure 1.2 Major pathways of skin cancer development. MAPK Pathway: Mutations at RAS or B-Raf through EGFR signalling are common triggers for the activation of MEK (1 and 2). This further causes the phosphorylation of ERK, which is responsible for activating multiple substrates which stimulate uncontrolled cell proliferation. P13K Pathway: P13K pathway gets activated by RTK. P13K converts PIP2 to PIP3, which is a potent second messenger in survival signalling. PTEN does the opposite by converting PIP3 to PIP2. But lack of PTEN due to genetic reasons aids in the activation of AKT and mTOR further down the line. Sonic Hedgehog Pathway: The binding of SHh to PTCH activates SMO, which in turn activates GLI1 proteins. Activation of GLI1 is responsible for uncontrolled cell proliferation.

1.4. Currently Available Therapies for Skin Cancer

The choice of therapeutic approach or therapy approach is based on the progression stage, location of the tumor, and histological type of tumours (low-risk, intermediate-risk, and high-risk of skin cancer) along with patient-dependent factors such as age, skin type, gender, and previous history of treatment. In current medical practices, cancer therapy differs for melanoma and NMSC. The three most common approaches are radiation therapy, chemotherapy, and surgery **Figure 1.3** Although novel treatment strategies for skin cancer are emerging at a promising rate, surgery remains the most reliable method of eliminating cancer. Surgical excision, Mohr's macrophagic surgery, and curettage & electrodesiccation are the three types of surgeries performed to eradicate any type of skin cancer [33,34].
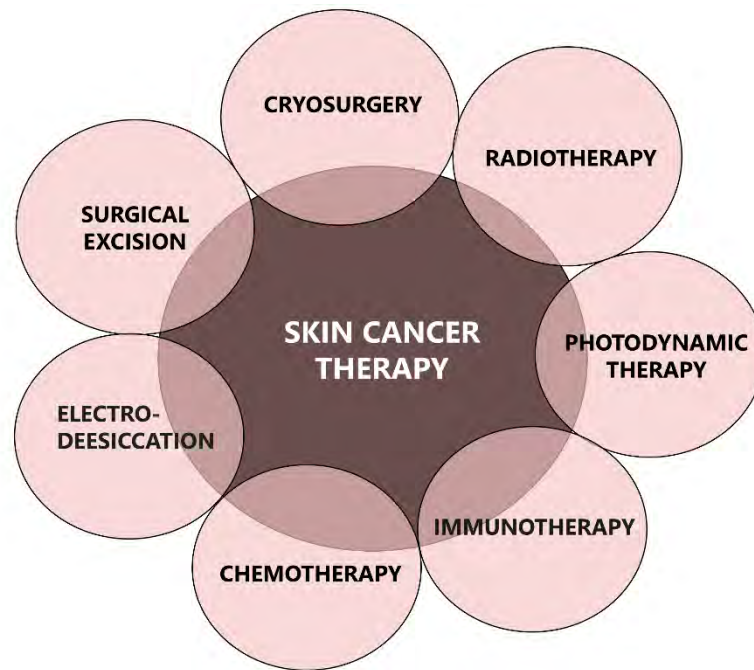
Figure 1.3 Therapeutic Strategies for skin cancer

1.4.1. Surgery Excision

It is the most utilized traditional technique to remove the cancerous lesions and is the also primary choice of therapy available for the skin cancer. Surgical procedures in dermatology are usually performed under local anaesthetic. During the procedure of surgery excision the cancerous tissues or lesions are cut without affecting its healthy tissue margin. The excised tumour and its surrounding bottom edges should be tagged with various dyes and sutures. However, the drawback associated with the surgical excision is that the recurrence rate of incomplete excised lesions increases with added adversity such as infection to the surrounding layers of lesions, removal of organs, affecting the quality of life of patients along with being contraindicated for physically impaired patients [35].

1.4.2. Curettage and Electrodesiccation Method

Curettage and Electrodesiccation is another therapeutic approach for treating carcinogenic lesions. Curettage has been typically merged with the electrodesiccation method. Curettage comprises of a sharp tool which is a curette for the scrapping of tumour lesion up to normal dermis layer, followed by applying an electric current to the affected area of tumor for denaturation, removal of remaining cancerous elements and controlling bleeding from the

wound. This procedure is appropriate for primary and low-risk tumours, and up to three cycles can be conducted in a single session. This procedure does not require histologic margin evaluation after the treatment, and also it is a quick and economical method to treat skin cancer. However, drawbacks associated with this method are the high recurrent rate of high-risk tumors complications such as low wound healing, which is generally avoided when treating areas like beard, scalp and pubic region, etc [36].

1.4.3. Mohs Surgery

In this procedure, the tumor is completely removed with the help of a scalpel or curette. At first, the layout of the tumor is drawn for the operating procedure, followed by marking the borders of the tumor. During this surgical procedure, the surgeon cuts the lesions layer by layer, evaluating each layer for histologic margins under a microscope until no cancerous cells remain. The advantages associated with this method are a higher cure rate of high-risk skin cancer without damaging healthy skin tissues. However, various disadvantages of Mohs surgery are the requirement of special laboratory, microscopy, time-consuming procedure, special training, etc [37].

1.4.4. Cryosurgery

Cryosurgery is a traditional therapy for the removal of cancerous cells by utilizing cryogenic agents. Various cryogenic agents have been fabricated, including liquid nitrogen, liquid oxygen, cold saline solution liquid, and air carbon dioxide. The basic principle involved in this procedure is the removal of cancer lesions by inducing necrosis with the help of a potent cryogenic agent. In cryosurgery, at least two freeze and thaw cycles are required, resulting in destruction or changes in the texture of cancerous lesions. The optimum temperature needed for this technique is -50 to $-60\ ^{o}$ C. In the procedure of cryosurgery, local anesthetic agents have been used such as 1% lidocaine (lignocaine) and epinephrine. Advantages associated with this technique are high cure rate, cost effectiveness, time-saving and ease to perform. Apart from these advantages, there are a few disadvantages also associated with this therapy, such as lack of histopathology report, wound healing complication, edema, hypertrophic scarring and pain [38].

1.4.5. Radiotherapy

Radiation therapy, also known as ionizing radiation, is another conventional anticancer therapy for treating skin cancer. The basic principle of radiotherapy is treating the tumours or aggressive lesions with the help of a radiation source which comprises ions (electrically charged particles or electrons). When electron-containing energy passes through the site (cancerous cells or lesions), it results in the destruction of the tumor cells by apoptosis, necrosis, and autophagy leading to cell death. The tumor penetrating dose selection of radiation is based on changing the energy dose concentration. The advantages associated are that this therapy is a non-invasive technique, is painlessness, and is suitable for physically impaired patients. The disadvantages of this therapy are low cure rate, risk of radiation-induced dermatitis, and high cost [39].

1.4.6. Chemotherapy

Chemotherapy can be used to treat certain types of skin cancer, although it is often used in combination with other treatments such as surgery, radiation therapy, or immunotherapy. Chemotherapy drugs work by targeting and killing rapidly dividing cancer cells. This makes it an effective treatment option for some types of skin cancer, particularly those that have spread to other parts of the body (metastasized) [40].

In skin cancer, chemotherapy is usually used for the treatment of advanced or metastatic disease, where cancer has spread to other parts of the body. Chemotherapy drugs can be delivered by oral, intravenous, or topical routes, depending on the type and stage of the skin cancer. Various therapies and drugs used for skin cancer treatment are mentioned in **Table 1.2.**

Table 1.2 – Drugs used in melanoma and non-melanoma cancer

Disease	Drugs
Melanoma cancer	Aldesleukin, Binimetinib, Encorafenib, Cobimetinib, Dabrafenib, Dacarbazine, Encorafenib, Temozolomide, Trametinib Dimethyl Sulfoxide, Talimogene Laherparepvec, Carboplatin, Cisplatin, paclitaxel, Interferon (IFN) Alfa-2b, Peginterferon Alfa-2b (Peg-IFN), Interleukin-2 (IL-2), Binimetinib, Ipilimumab, Trametinib, Vemurafenib, Pembrolizumab, Cobimetinib, Encorafenib, Novolumab etc.

Basal cell carcinoma	Imiquimod, 5-fluorouracil, Sonidegib, vismodegib, cemiplimab etc.
Cutaneous Squamous Cell carcinoma	Cemiplimab-rwlc, Keytruda (Pembrolizumab), Libtayo (Cemiplimab-rwlc) Pembrolizumab etc.

Apart from this, there are a few compounds that have good efficacy against skin cancer, such as vitamin D, salicylic acid, resveratrol, itraconazole, curcumin, etc [41,42].

1.4.6.1. Repurposing the Antifungal agent Itraconazole as a hedgehog inhibitor

Several inhibitors of the hedgehog (Hh) pathway have been explored for the treatment of BCC and MM. One specific mutation in the Hh pathway is responsible for 85% of BCC cases. Itraconazole (ITZ), a potent antifungal agent, was recently shown to be a potential and efficient for the treatment of BCC in a clinical trial. It effectively inhibited the Hh pathway and growth of BCC by directly binding with SMO **(Figure 1.4)**. It is also known as a cilial translocation inhibitor, directly preventing the localization of SMO to cilia. Recently, ITZ was granted orphan drug designation by the European Medical Agency (EMA) for the treatment of nevoid BCC. It acts via different pathways or mechanisms to prevent tumor growth, such as prevention of angiogenesis, cell cycle arrest, and autophagocytosis and decreases malignant apoptosis and cell proliferation. Kim et al. suggested that ITZ can suppress the growth of tumors that have proven resistant to other Hh inhibitors, such as vismodegib and sonidegib. The authors also suggested that ITZ treatment is highly effective in inhibiting BCC when combined with arsenic trioxide [43]. The study conducted by Liang et al. found that Itraconazole can effectively inhibit melanoma by suppressing multiple signaling pathways such as Hedgehog, Wnt, and PI3K/mTOR. The researchers observed that Itraconazole had a significant impact on the expression of various genes and proteins involved in these pathways. Specifically, the study found that Itraconazole was able to down-regulate the expression of Gli-1, Gli-2, Wnt3A, β-catenin, and cyclin D1, which are key players in the Hedgehog and Wnt pathways. In addition, Itraconazole was able to up-regulate the expression of Gli-3 and Axin-1, indicating its inhibitory effects on these pathways. These findings suggest that Itraconazole can potentially be used as a therapeutic agent for basal cell carcinoma and melanoma that involve dysregulation of these signaling pathways [44,45]

1.4.6.2. Curcumin:

Curcumin, a natural compound found in the spice turmeric, has been shown to have anti-cancer properties, particularly in skin cancer. Curcumin kills cancer cells by inhibiting the growth and spread of cancer cells through a number of molecular pathways:

- Inhibition of the PI3K/Akt/mTOR pathway: Curcumin can inhibit the activity of key proteins in this pathway, which is often overexpressed in cancer cells and plays a role in cell growth and survival.

- Inhibition of the NF-κB pathway: Curcumin can inhibit the activity of the transcription factor NF-κB, which is involved in inflammation and the growth and spread of cancer cells.

- Inhibition of the STAT3 pathway: Curcumin can inhibit the activity of the transcription factor STAT3, which is involved in cell growth, survival, and angiogenesis in cancer cells.

- Inhibition of the Wnt/β-catenin pathway: Curcumin can inhibit the activity of Wnt signaling pathway, which is involved in cell proliferation, survival, and migration in cancer cells.

- Inhibition of the MAPK pathway: Curcumin can inhibit the activity of proteins in the MAPK pathway, which is involved in cell growth, survival, and angiogenesis in cancer cells [46,47].

Curcumin also has been found to have antiproliferative and pro-apoptotic effects on skin cancer cells, meaning it can reduce the growth and survival of these cells and induce cell death. Additionally, Curcumin can increase the expression of p53 and induce apoptosis in BCC cells. This is achieved by increasing the phosphorylation of p53, which results in its stabilization and activation. Activated p53 then upregulates the expression of pro-apoptotic proteins, such as Bax and Bak, which can induce programmed cell death. In addition, curcumin can also decrease the expression of Bcl2, which is known to inhibit programmed cell death. By reducing Bcl2 expression, curcumin can further promote apoptosis in BCC cells. Overall, the ability of curcumin to modulate the expression of p53 and Bcl2 may contribute to its anti-cancer properties in inhibiting basal cell carcinoma [48] [48]
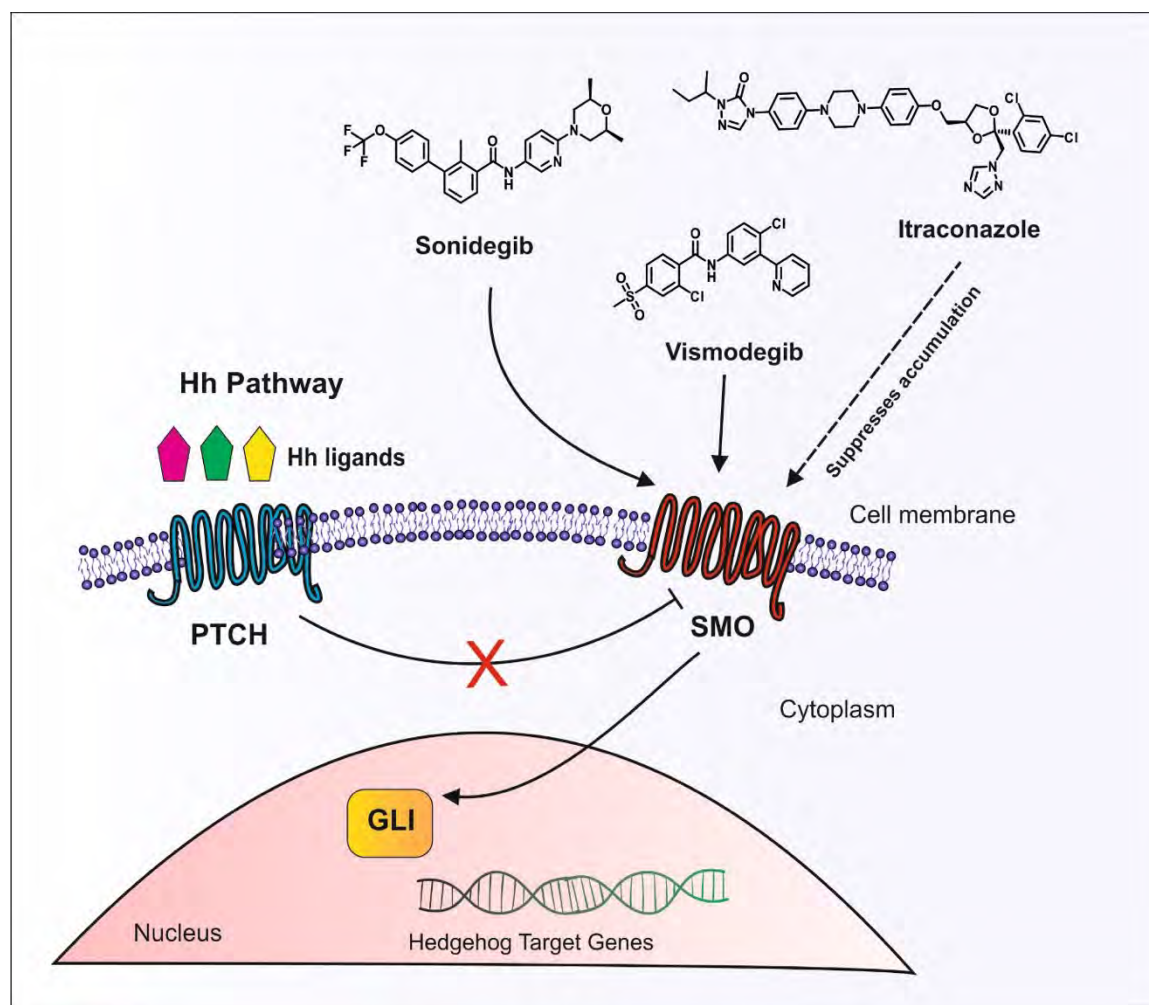
Figure 1.4 Hedgehog (Hh) signaling pathway in basal cell carcinoma (BCC). The smoothened (SMO) components are inhibited by vismodegib, sonidegib, and itraconazole. Hh signaling causes downstream activation of cancer-related genes [32]

1.4.7. Photodynamic therapy

Photodynamic therapy (PDT) is a clinically approved treatment that holds promise as a non-invasive approach for various types of cancer. PDT involves the use of a photosensitizer or photosensitizing agent, which is activated by a specific wavelength of light to generate reactive oxygen species (ROS) that can selectively destroy cancer cells [49,50]. The photosensitizer is typically applied topically to the skin and preferentially accumulates in cancer cells due to their unique characteristics, such as leaky vasculature. Upon irradiation with light of a specific wavelength, the photosensitizer is activated, leading to the production of oxygen species that induce cell death in the targeted cancer cells [51–53]. The photoactivation mechanisms of

photosensitizing drugs (PDT drugs) can be categorized into two types: Type I and Type II. In Type I photoactivation, upon absorption of photons, the PDT drug is excited to a triplet state. Subsequently, this excited state can result in the generation of reactive oxygen species (ROS) or transfer energy to ground-state molecular oxygen, leading to the formation of highly reactive singlet oxygen. This light-induced process is responsible for the therapeutic action of PDT drugs. A general application of PDT on skin disorders is schematically represented in (**Figure 1.5**) [54].

PDT can destroy tumors through three potential mechanisms. Firstly, during light irradiation, reactive oxygen species (ROS) are generated, leading to cancer cell death through apoptosis, autophagy, or necrosis. Secondly, PDT can target the tumor vasculature and disrupt the tumor microenvironment, contributing to tumor destruction. Lastly, PDT can stimulate or activate an immune response, which aids in tumor eradication. Factors such as inflammatory mediators and T-helper cells play a role in activating the immune response [55–58].
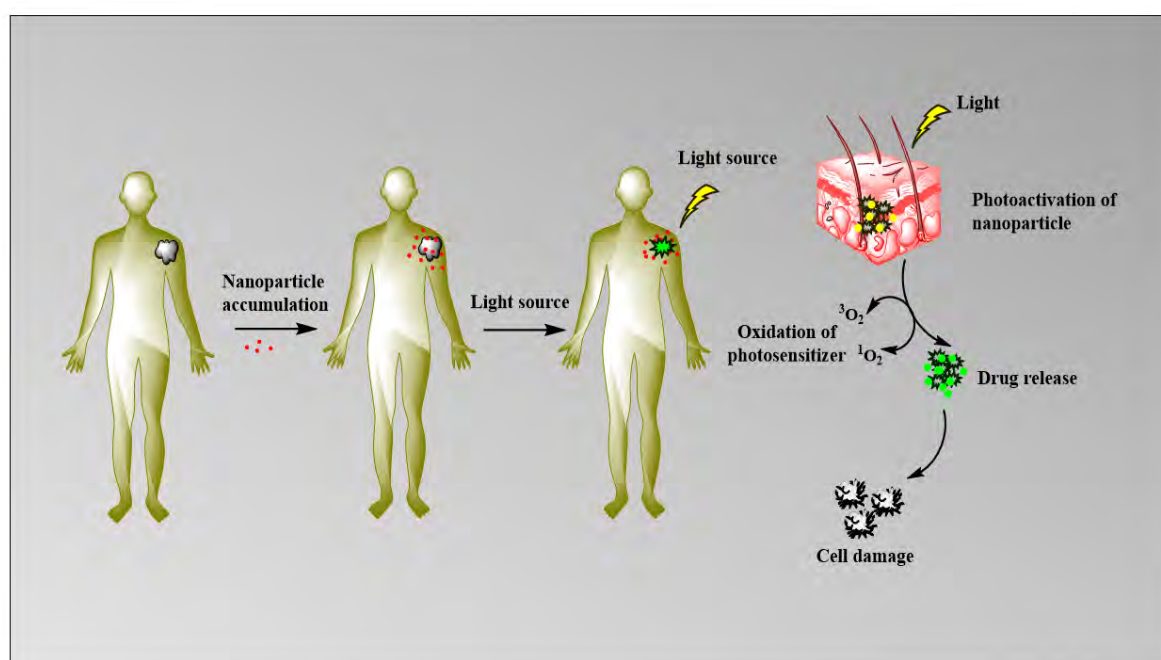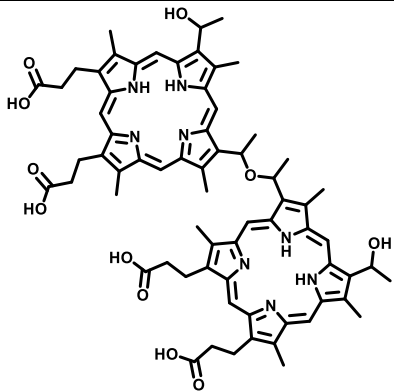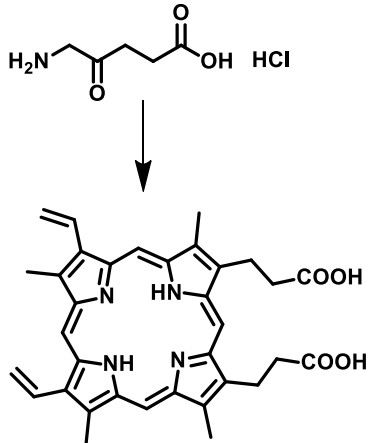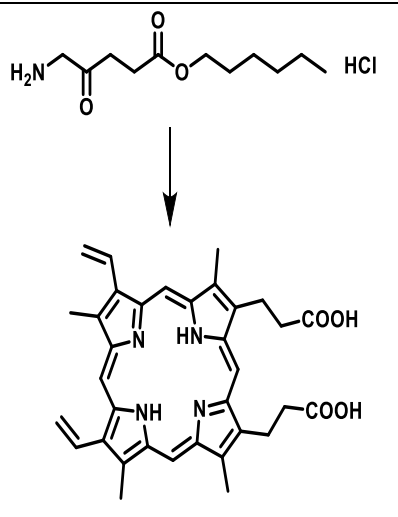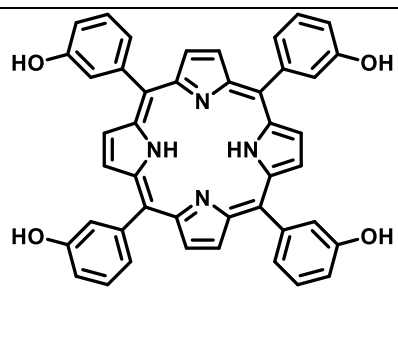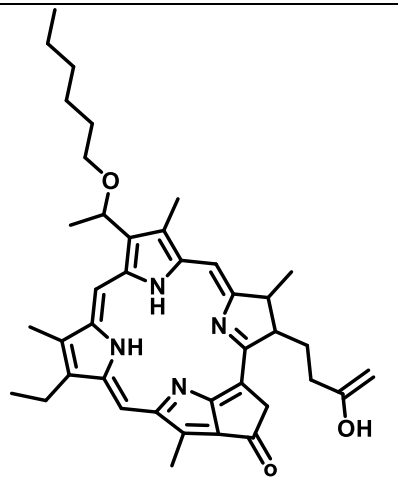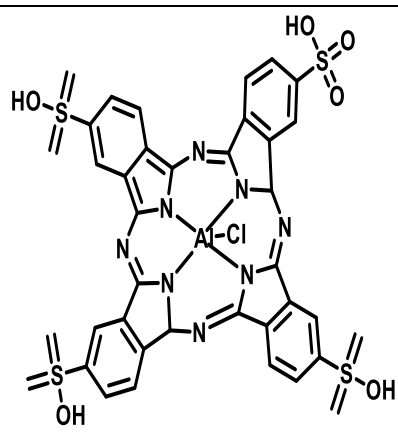
Figure 1.5 Schematic representation of PDT in skin cancer
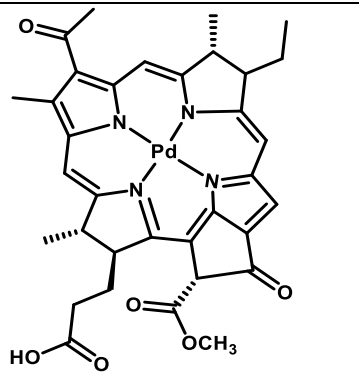
In comparison to conventional therapy, PDT has a lower occurrence of side effects, and it also increases the target specificity. Although PDT has many advantages over standard cancer therapies, it still has yet to be wildly utilized in clinical health care. PS molecules possess several intrinsic properties such as poor targeting, low solubility, and high hydrophobicity because of which they easily form aggregates in physiological conditions [59–61].

Even though several PS molecules have been modified to increase water solubility, their selectivity of the target site is still inadequate, leading to their unsuccessful clinical uses. **Table 1.3** Represents the clinical trials and approval status of various photosensitizers [62–76]

Table No. 1.3 Clinical trials and approval status of various photosensitizers [62–76]

Sr. No	Photosensitizer with Generic name	Chemical structure	Activation wavelength	Clinical outcomes	References
1	Porfimer Sodium (Photofrin)		630 nm	Approved for Bladder cancer, Endobronchial cancer, Esophageal cancer, Lung cancer, and cervical cancer In clinical trial- Brain cancer diagnosis	[62–64]
2	5-Aminolevulinic acid (Levulan and Ameluz)		635 nm	Approved for Non-melanoma skin cancers In clinical trial- Brain cancer diagnosis	[65–67]

3	Hexaminolevuli nate hydrochloride (Hexvix®)		635 nm	Bladder cancer diagnosis	[68,69]
4	5,10,15,20-Tetrakis(3-hydroxyphenyl) chlorin/ Temoporfin (Foscan)		652 nm	Approved for Head and neck cancer, prostate, and pancreatic cancer	[70,71]
5	2-(1-Hexyloxyethyl)-2-devinyl pyropheophorbi de-a (HPPH) (PhotoChlor)		665 nm	In clinical trial- Basal cell carcinoma, Esophagus, Mouth, and Throat cancers, Cervical intraepithelial neoplasia	[72,73]
6	Aluminum phthalocyanine tetrasulfonate chloride (Photosens)		676 nm	Approved in Russia In clinical trials- Stomach, Skin, Oral, and Breast cancers.	[74,75]

7	Palladium-Bacteriopheoph orbde (WST09)/ Padoporfin (Tookad)		763 nm	Approved for Prostate cancer in Mexico, Israel and 31 countries of European union	[76]

1.4.7.1. Chlorin e6: Chlorin e6 (Ce6) is a naturally occurring porphyrin compound that is found in certain species of algae. Ce6 has been studied for its potential use in photodynamic therapy (PDT). PDT with Ce6 has been studied in preclinical and clinical trials for a variety of cancer types, including head and neck cancer, lung cancer, oesophageal cancer, and skin cancer. Ce6 has been shown to be effective in killing cancer cells and has been demonstrated to have minimal toxicity to normal cells. Additionally, chlorin e6 has several advantages. It can be irradiate at deeper lesions or tissues, has a high clearance rate, and has high singlet oxygen and quantum yield [77].

The ROS produced by Ce6 during PDT can damage the cancer cells in several ways:

- By damaging the cell membrane: The ROS can cause damage to the cell membrane, leading to the leakage of cellular contents and eventual cell death.
- By disrupting cellular metabolism: The ROS can disrupt the normal metabolism of the cancer cells, leading to the inhibition of cell growth and proliferation.
- By triggering apoptosis: The ROS can trigger the process of apoptosis, a type of programmed cell death, in the cancer cells [78,79].

It is also known that Ce6-PDT modulates the immune system by activating dendritic cells, creating a pro-inflammatory environment and promoting the activation of T lymphocytes, which helps in the elimination of cancer cells. The specific molecular pathway by which Ce6 kills skin cancer cells during PDT is not fully understood. However, studies have shown that Ce6-PDT can activate a number of signalling pathways in cancer cells that lead to cell death. Mitochondrial pathway: Ce6-PDT has been shown to cause damage to the mitochondria, the powerhouses of the cell, leading to the release of cytochrome c and the activation of caspase-3, which triggers apoptosis. It's important to note that the efficacy of Ce6-PDT depends on several factors such as the type and stage of cancer, the amount of light used and the duration

of exposure. Also, the success of treatment can also be influenced by the patient's overall health, medications, and other factors. Despite these properties, chlorin e6 possesses major drawbacks such as hydrophobicity, limited penetration through the stratum corneum, and self-aggregation upon contact with water, resulting in lower quantum yield and singlet oxygen generation ($^1O_2$), consequently limiting its clinical efficacy [80].

1.5. Drug Properties :

Name: **Chlorin e6**

Chemical Name: (17*S*,18*S*)-18-(2-carboxyethyl)-20-(carboxymethyl)-12-ethenyl-7-ethyl-3,8,13,17-tetramethyl-17,18,22,23-tetrahydroporphyrin-2-carboxylic acid

Structural formula:
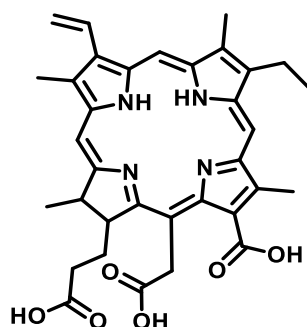
Molecular formula: $C_{34}H_{36}N_4O_6$

Molecular weight: 596.7

Log p: 4.7

Solubility: Chlorin e6 is a hydrophobic molecule and is not soluble in water. However, it is soluble in organic solvents such as dimethyl sulfoxide (DMSO), acetonitrile and ethanol.

Colour: Chlorin e6 is a dark green powder or crystalline substance.

Melting point: The melting point of chlorin e6 is around 195-200°C.

Absorption spectra: Chlorin e6 has strong absorption peaks in the red to near-infrared range (around 650-700 nm), which makes it suitable for use in photodynamic therapy.

Lipophilicity: Chlorin e6 is a lipophilic molecule, which means it has an affinity for lipid-based structures such as cell membranes. This property can contribute to its selective accumulation in cancer cells and other abnormal tissues.

Stability: Chlorin e6 is a stable compound and can retain its properties for a long time if stored properly [81].

Name: **Itraconazole**

Structural formula:
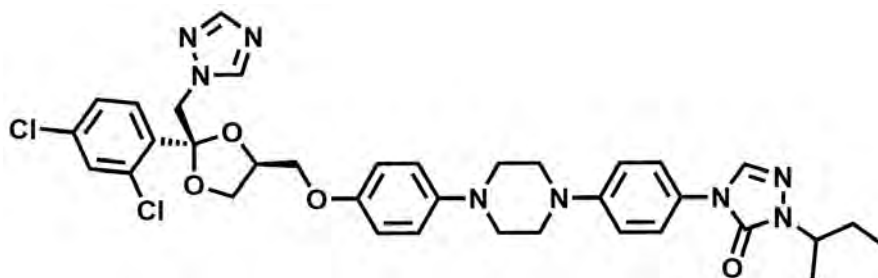
Molecular formula: $C_{35}H_{38}Cl_2N_8O_4$

Molecular weight: 706.64 g/mol

Melting point: 166-170 °C

Solubility: Itraconazole is practically insoluble in water but soluble in organic solvents such as ethanol, methanol, and dimethyl sulfoxide (DMSO).

pKa value: Itraconazole has a pKa of 3.7, indicating that it is a weak acid.

LogP value: The partition coefficient (logP) of itraconazole is 5.9, indicating that it is highly lipophilic.

BCS: II

Appearance: Itraconazole is a white to slightly yellow powder or crystalline solid.

Stability: Itraconazole is stable under normal conditions but is sensitive to light, heat, and moisture [82]

Name: **Curcumin**

Structural formula:
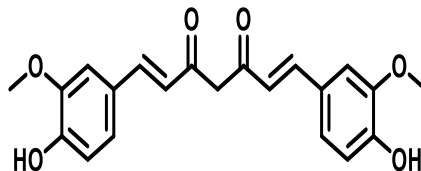
Molecular formula: $C_{21}H_{20}O_6$

Molecular weight: 368.38 g/mol

Appearance: Bright yellow crystalline powder

Melting point: 183-186°C

pKa: 8.5 (phenolic OH) and 13.3 (α,β-unsaturated carbonyl)

LogP; 2.93

Solubility: Curcumin is practically insoluble in water, but it is soluble in ethanol, DMSO, and other organic solvents. Curcumin is practically insoluble in water, with a solubility of less than 0.1 mg/L at room temperature. However, it is more soluble in organic solvents such as ethanol, DMSO, and acetone, with solubilities of about 10-20 mg/mL.

Stability: Curcumin is relatively stable under normal conditions of use and storage, but it can undergo degradation in the presence of light, oxygen, heat, and alkaline conditions [83].

1.6. Topical Therapy for Skin Cancer

Topical drug delivery has high potential in the treatment because it exhibits larger surface area, accessible to administration, and it more acceptable by the patient. Topical treatment of skin cancers appears favourable because of the lower risk of systemic side effects, and bypasses the first-pass metabolisms leading to enhanced bioavailability [84]. Topical therapy-based

approaches are comparatively safer where drugs are directly delivered to the skin tissue (target site involved in the origination of disease), thus avoiding exposure of the drug to rest body organs. Topical therapies are commonly employed in cases where multiple lesions are present or when the treatment area is extensive. They are also utilized for lesions that require time to heal. Typically, Topical therapies are an alternative option for patients who are not suitable candidates for surgery and can help prevent the formation of post-surgical scars. Various topical preparations are available for managing skin cancer, including corticosteroids, 5-fluorouracil, imiquimod, diclofenac, mechlorethamine, bexarotene, tazarotene, and photosensitizers. However, these treatments have associated side effects such as skin irritation, thinning of the skin, and dilated blood vessels. Moreover, they may not be suitable for long-term use [39]. When Imiquimod is applied over larger areas of the body, it can cause systemic symptoms such as headaches, fatigue, muscle pain, and flu-like symptoms [52]. Topical therapies currently face limitations due to various side effects, including pain, scarring, irritation, inflammation, and other complications such as contact dermatitis, itching, redness of the skin, swelling, and ulceration. Moreover, existing conventional topical formulations such as gels, creams, and ointments have limited penetration capabilities and often necessitate frequent and prolonged application. This leads to inconsistent patient adherence and increases the risk of developing severe inflammation. Besides, conventional preparations exhibit lower efficacy and cause local toxicity (e.g., skin atrophy, skin infections, stretch marks, and redness) due to rapid loco-regional drug release, low bioavailability at the site action, and low efficacy that leads to metastasis [85]. Furthermore, the problem associated with the delivery of PS molecules via the topical route includes limited light penetration ability and permeation through cancerous tissue or stratum corneum, rendering it ineffective. Additionally, the excessive thickness of the tumor, more collagen content inside the tumor, ulceration, infiltrative growth tissue, and the presence of melanin can cause resistance to PDT [33,61].

Hence, there is a need for novel carriers that can overcome these toxicities and treatment resistance while enhancing drug efficacy. These carriers should have the ability to penetrate deeper into the viable epidermis without systemic absorption and deliver the drug locally at the desired site in a controlled manner over an extended duration.

1.7. Challenges in Conventional Topical Delivery of Skin Cancer Therapeutics

Several treatment options are available for skin cancer (malignant melanoma (MM) and NMSC), depending on the type, stage, and location of the cancer. Primary treatment modalities include surgery, radiation, topical, targeted, immunotherapy, and chemotherapy. The main treatment option for skin cancer is surgery, although there are less invasive treatments available, including 5-FU, imiquimod, PDT, and other drugs, such as diclofenac sodium and ingenol mebutate. However, the recurrence rate is higher after surgical therapy, requiring the development of more effective treatments.

Monotherapy, or using a single treatment approach, in topical skin cancer treatment can be associated with several problems. One major challenge is the limited efficacy of monotherapy, as different types of skin cancer and individuals may respond differently to various treatments. Using a single treatment may not sufficiently address the disease's complexity or the patient's specific needs. Additionally, monotherapy can lead to the development of resistance, where skin cancer cells become less responsive to the treatment over time.

Topical monotherapy for skin cancer has certain drawbacks, including the potential risk of metastasis. While topical treatments are effective for superficial skin cancers, they may not adequately address deeper or more aggressive forms of skin cancer. These cancers have the potential to invade deeper layers of the skin and spread to other parts of the body, leading to metastasis. Topical medications primarily target the surface layers of the skin, and their limited penetration may not be sufficient to eliminate cancer cells that have already spread beyond the initial site. Therefore, relying solely on topical monotherapy for advanced or metastatic skin cancer may not be sufficient in controlling or eradicating skin cancer. Conventional preparations exhibit lower efficacy and cause local toxicity due to rapid loco-regional drug release. This resistance can diminish the effectiveness of the therapy and require alternative treatment options. In such cases, a combination of treatments, including Photodynamic Therapy (PDT) and topical chemotherapy, may be necessary to address the risk of metastasis and achieve better treatment outcomes. PDT is a novel and efficient strategy for tumor treatment; however, the photosensitizers' low solubility and low stability often limit their application in biological systems [86]. PS are mostly hydrophobic molecules with low solubility in the aqueous phase leads to less permeation through tumour. This property of PS negatively affects its biodistribution and cellular uptake. The low effectiveness of PS also significantly causes low tumor specificity and demands high energy input during prolonged illumination periods. Hence, incomplete lesion clearance is possible, where certain cancerous

lesions may not be completely eradicated. This may result in recurrence or incomplete removal of cancer cells, necessitating further treatment. The lack of targeting specific cancer cells while sparing healthy tissue is another limitation of monotherapy, potentially leading to damage to surrounding healthy skin cells [87–89].

To overcome these limitations of conventional therapy for skin cancer, advanced drug delivery systems (nanocarriers and combination-based treatment) are explored to deliver the therapeutics. Combining multiple treatment modalities is a safe and effective strategy in cancer management. Combination treatment is the co-delivery of two therapeutic agents or a combination of various therapies, such as chemotherapy with immunotherapy, photothermal therapy (PTT) combined with PDT, radiotherapy, or other therapies. A combinational therapy approach has various benefits, including enhanced therapeutic effects, reduced toxic effects, improved therapeutic outcomes, suppression of drug resistance, and release of the drug in a controlled and sustained manner. Combinational therapy approaches can also have multiple molecular targets in the tumor. In skin cancer, combined therapy helps to avoid adverse effects, such as burning sensations, and also decreases the tumor recurrence rate. PDT is mainly used in association with other therapies for improved efficacy and lesser incidence of drug resistance. For example, a combination of PDT with Imiquimod has been used in the treatment of BCC [90,91]. Moreover, PDT is preferred over other available anti-cancer treatment strategies due to various reasons, the most important being the specificity that PDT offers. With a precise light source and a proper photosensitizer molecule, accurate tumor site targeting can be achieved.

1.8. Nano-carrier-Based Topical Drug Delivery

Nanotechnology-based drug delivery systems has an enormous potential to improve the problems associated with the existing available topical drug delivery system. Nanocarrier-based drug delivery system improve selectivity and hence are helpful in targeting the affected site. It can also improve the solubility of poorly water soluble drugs, increasing permeation through the skin, modify the pharmacokinetics, and improve bioavailability. In addition to it can reduce the dose leading to a decrease in side effects [92]. Apart from this, nanocarriers can be used in topical delivery to treat skin cancer in several ways. These tiny particles can help to increase the penetration of the active ingredient through the skin's barrier and also protect it from degradation. For example, they can be used to deliver anti-cancer agents directly

to the tumor site, which can help to increase the effectiveness of the treatment and reduce side effects. Additionally, nanocarriers can be engineered to target specific cells or structures within the skin, such as tumor blood vessels, to improve the selectivity of the treatment [93]. Topical delivery of drugs using nanocarriers has been shown to be effective in preclinical studies for the treatment of skin cancer. For instance, lipidic nanoparticles can be used to encapsulate drugs such as doxorubicin, which has been shown to increase the penetration of the drug into the skin and reduce toxicity [94]. Also, nanoparticles such as polymeric nanoparticles (PNPs) have been shown to be effective in delivering drugs such as Paclitaxel to skin cancer tumors. Overall, the use of nanocarriers in topical delivery for the treatment of skin cancer can enhance the effectiveness of the treatment, increase the bioavailability of anti-cancer agents, and improve patient outcomes [95].

1.9. Different Nanocarriers-Based Topical Drug Delivery for Skin Cancer

Novel nanotechnological strategies developed for the treatment of skin cancer include liposomes, transfersomes, ethosomes, lipid nanoparticles, carbon nanotubes, dendrimers, polymeric nanospheres, nanosuspension, nanocapsules, nanoemulsion [96,97] [98–101].

1.9.1. Lipidic nano-system

Liposomes have proved to be an effective delivery system for the treatment of skin cancers. Liposomes are fatty bodies consisting of a bilayer of lipids formed due to hydrophobic interactions with the hydrophilic part facing the aqueous core. Hydrophobic, as well as hydrophilic drugs, can be delivered with the help of liposomes [96,97,102]. These were developed to enhance penetration across the stratum corneum and deliver the drugs in deeper tissues. The mechanism of drug release is based on the structural similarity between liposomes and stratum corneum [103]. Liposomes undergo fusion with the outermost layer of stratum corneum, disrupting its structure and increasing fluidity of bilayer. The interaction leads to the formation of intercellular lipid lamella, which enhances the mobility of lipophilic molecules in SC. This enhances drug penetration in the subsequent skin layers [104,105]. Mohan et al. successfully developed PEGylated nanoliposomes of resveratrol and 5-fluorouracil to improve chemotherapeutic efficacy for the treatment of head and neck squamous cell carcinoma. It reduced the threshold concentration necessary to achieve a synergistic effect. Bax (protein

coding gene which regulates apoptosis) and caspase 3 were upregulated, whereas bcl-2, cyclin D1, and akt (protein kinase B) were downregulated, resulting in apoptosis [106].

The use of transferosomes as delivery vehicles for skin cancer treatment is evolving because of their instinctive capability to bypass the skin [107]. They exhibit enhanced penetration across stratum corneum due to their deformable nature [108,109]. They are modifications of liposomes in which the bilayer is composed of edge activator, i.e., a surfactant such as tween 80, Span 80, sodium cholate, and phospholipids [110,111]. The edge activator destabilizes the bilayer by decreasing interfacial tension and leads to the formation of a metastable membrane, thereby enhancing the deformability [111]. A pyrimidine analog, 5-fluorouracil, is a well-known anti-cancer agent that acts by inhibiting thymidylate synthase. This prevents DNA replication as the synthesis of the nucleotide thymidine is dependent on thymidylate synthase [112]. However, topical delivery of 5-fluorouracil in conventional formulations exhibits poor percutaneous permeation. Formulation of 5-fluorouracil into a transfersomal gel increased its penetration, cytotoxic effect and showed a two-fold increase in drug release [107,113,114]. Transfersomes bypass the stratum corneum without getting ruptured and reach the epidermis. The osmotic gradient that is the difference in water content across the stratum corneum layers is sufficient to force these vesicles intact across the stratum corneum [107].

Cubosomes are self-assembled liquid crystalline particles that are made up of specific amphiphilic lipids in a certain ratio to water [115,116]. These nanostructured particles consist of three-dimensionally arranged curved lipid bilayers, organized as honeycombs. The unique structure comprises two internal aqueous channels that are exploited for carrying payloads like drugs, photosensitizers, etc. [117].

1.9.2. Lipid Nanoparticles: NLC and SLN

In recent years, the development of lipid nanoparticles for the treatment of skin malignancies has evolved to some extent. They came into the picture as liposomes posed stability problems, enhanced cutaneous absorption, and drug targeting [118,119]. SLN consists of solid lipids and surfactants providing stability, whereas, in NLC, solid lipids are replaced by liquid lipids. SLN exhibited less loading capacity and drug expulsion compared to NLC. [120]. On topical application of these formulations, they form a thin film on the surface of the skin resulting in occlusion due to the hydrophobic nature of the film [120,121]. This prevents evaporation of water from the skin surface, thereby increasing hydration of stratum corneum

from 10-20% to 50% [120,122–124]. This leads to swelling of corneocytes and an increase in the water content in intercellular lipids. The gaps between the corneocytes are increased, allowing the drug molecules to penetrate deeper. Occlusion also prevents the evaporation of volatile compounds and exerts reservoir effect on the drug. Initially, the drug penetrates at a faster rate under occlusion. Removal of the occlusive film leads to dehydration of stratum corneum, reducing the movement of the drug. This results in stratum corneum acting as a reservoir of the drug [120,125,126]. Nanoparticles increased surface area resulted in 15 times more occlusiveness as compared to microparticles due to enhanced contact with stratum corneum. SLN matrix has solid lipids that undergo beta modification on storage forming perfect crystals, thereby resulting in drug expulsion. NLC matrix containing a mixture of the solid and liquid matrix that do not create perfect crystals, thus preventing expulsion of the drug. In both of them increased penetration of non-polar compounds and had very less effect on polar compounds [123,127]. Bharadwaj et al. formulated paclitaxel loaded SNL for the treatment of skin cancer by using ultrasonication and high-speed homogenization method. SLNs were dispersed in topical gel and were found to exhibit sustained release. This gel exhibited quite a high efficiency as compared to conventional paclitaxel topical gel [128]. Khallaf et al. reported enhanced diffusion and release rate of 5-FU SLN formulated in sodium CMC gel, proving it to be promising drug delivery [129]. A study showed by Geetha et al. reported that anti-cancer agent sesamol's formulation in SLN increased its bioavailability by enhancing its retention on the skin and exerted the desired anti-cancer effect [130]. Doxorubicin permeability was found to be enhanced by formulating them in SLN, as reported by Tupal et al. [131] . Paruvathanahalli et. al. formulated 5-FU NLC hydrogel by high- pressure homogenization technique in which LBS was used as liquid lipid, Precirol ATO as solid lipid and polyoxyl-15-hydroxy stearate as a surfactant. He reported 2.78 and 2.09 folds increased retention and 3.9 fold increased in permeation whereas skin irritation was reduced significantly ($p < 0.05$) [132]. 5-ALA NLC was developed by Qidwai, which showed increased concentration in target skin layers, enhanced cytotoxicity, and penetration. This enhanced the efficiency of PDT as it directly affected the accumulation of Porphyrin IX photosensitizer [133]. As reported by khan et al. 5-fluorouracil formulation in carbopol based transfersomal gel increased skin permeation and deposition. They also compared the effect of tween-80 and span 80 as edge activators and found tween 80 superior to span 80 with vesicle size and entrapment efficiency [113]. Kyung oh et. al. studied the topical delivery of 5-ALA by using cationic transfersomes as vehicles for photodynamic therapy. The results indicated good storage stability and physicochemical properties in terms of entrapment efficiency and particle size. They also reported 7.5 to 8 folds

increased permeation of 5-ALA across the skin, 2.4 folds enhanced accumulation thereby enhancing induction of PpIX photosensitizer inside the body [134]. A major disadvantage of these vehicles is the delivery of hydrophobic drugs [104,107].

1.10. Gaps in the Current Research

Topical monotherapy for skin cancer has certain drawbacks, including the potential risk of metastasis. While topical treatments are effective for superficial skin cancers, they may not adequately address deeper or more aggressive forms of skin cancer. These cancers have the potential to invade deeper layers of the skin and spread to other parts of the body, leading to metastasis. Topical medications primarily target the surface layers of the skin, and their limited penetration may not be sufficient to eliminate cancer cells that have already spread beyond the initial site. Conventional topical products are associated with various drawbacks such low bioavailability at the site action and the requirement of high doses, causing skin irritation that significantly hinders the drug permeation through the stratum corneum or tumor tissues. Resistance to chemotherapy or other therapies can also occur when cancer cells develop mechanisms to pump out chemotherapy drugs before they can have an effect. This can happen when cancer cells have an increased amount of drug efflux pumps, which pump out anticancer molecules before they can reach their intended target. In such cases, a combination of treatments, including Photodynamic Therapy (PDT) and topical chemotherapy, may be necessary to address the risk of metastasis and achieve better treatment outcomes.

Chlorin e6 is a highly hydrophilic molecule, and it does not easily permeate from the stratum corneum make this treatment ineffective in the management of disseminated tumor. Another class of anticancer drug, Cyclopamine, a representative drug that targets the hedgehog pathway, has shown promise as an anticancer agent in the treatment of basal cell carcinoma (BCC). Preclinical studies have highlighted its potential for skin cancer therapy. However, the clinical efficacy of cyclopamine in treating skin cancer has been limited due to challenges such as low solubility and development of resistance.

Topical administration of anticancer drugs along with photodynamically active compounds is a non-invasive approach which stands to be a promising modality for treating aggressive cutaneous melanomas along with having the added advantage of high patient compliance.

To overcome the above problems, lipid nanocarriers have been explored as an alternative approach for topical drug delivery. It has many advantages, including directly delivered to the skin tissue (target site involved in the origination of disease), better permeation due to the

interaction of carrier lipids molecules with stratum corneum, and high drug loading, improved cellular uptake, and biocompatibility. Encapsulation of two molecules simultaneously in the lipidic nanocarriers is a very challenging task; here, we have developed and modified lipidic nanocarriers with the natural anticancer agent and photodynamically active compounds. Combining chemotherapy drugs with PDT has been shown to increase the efficacy of treatment and reduce the risk of drug resistance. This is because the combination of the two treatments can target multiple aspects of the cancer cells, making it more difficult for the cells to develop resistance. The new generation of photosensitizers such as chlorine e6, Pheophorbide A, and other PDT drugs can irradiate at deeper lesions or tissues because of the new generation of photosensitizers would be activated at the near-infrared (NIR) reason, and it has high singlet oxygen quantum yield.

Our hypothesis for this research work is to develop a topical formulation for skin delivery of the combination of Chlorin e6 and Itraconazole (ITZ) in skin cancer treatment, targeting the Hedgehog (Hh) pathway responsible for BCC and MM. We hypothesize that the co-delivery of chlorin e6 a photosensitizing agent and ITZ will lead to improved anti-tumor efficacy and reduced cancer resistance. ITZ acts via several mechanisms, including inhibition of the Hh pathway, prevention of angiogenesis, and induction of autophagy, making it a potential candidate for BCC and MM treatment. By combining it with Chlorin e6, we can target the tumors that have shown resistance to other hedgehog inhibitors like vismodegib and sonidegib, leading to more effective skin cancer treatment.

Additionally, there is a need to develop lipidic nanocarriers for the delivery of photodynamic therapy drugs, specifically chlorin e6 (Ce6) and curcumin, which could have a synergistic effect for the treatment of skin cancer. We aim to explore the potential of this combination therapy and investigate if the concurrent use of Ce6-PDT and curcumin could enhance the anti-cancer effect in BBC and MM by increasing the production of reactive oxygen species (ROS) and inducing apoptosis in cancer cells. Moreover, we anticipate that curcumin may sensitize the cancer cells to the light-mediated cytotoxicity of Ce6, leading to a more effective treatment option for skin cancer.

1.11. Objective and Specific Aims of the Current Work

Considering the gaps in the existing research, it was proposed to develop the nanotechnological-based dual drug-loaded anticancer molecules for topical delivery by using photodynamic therapy with improved uptake, penetration, and retention at cutaneous skin cancer.

The specific aims laid to achieve the major objectives include

To achieve the aim of the thesis, the following objectives have been designed that were divided into different chapters focusing on each objective.

1. Design and characterization of itraconazole and chlorin e6 dual-drug loaded lipidic nanocarriers for skin cancer treatment

    i.   Analytical method development and validation for the analysis of itraconazole (ITZ) and chlorin e6 (Ce6) by RP-HPLC and Spectrofluorometric techniques

    ii.   Preparation and characterization of dual drug-loaded lipidic nanoparticles of itraconazole and Chlorin e6 (ITZ/Ce6@LNPs) by quality-by-design approach

    iii.   Stability study of ITZ/Ce6@LNPs and ITZ/Ce6@LNPs Gel

    iv.   In-vitro Cell Culture Studies

    v.   Ex-vivo skin permeation studies

    vi.   Ex vivo bioimaging in tumor skin of the C57BL/6 mice

    vii.   Topical biodistribution study in C57BL/6 mice skin cancer model

    viii.   In vivo antitumor efficacy study in C57BL/6 mice skin cancer model

2. Design and characterization of curcumin and chlorin e6 dual-drug loaded lipidic nanocarriers for skin cancer treatment

    i.   Simultaneous analytical method development and validation for the analysis of curcumin (CUR) and chlorin e6 (Ce6) by RP-HPLC technique

    ii.   Preparation and characterization of dual drug-loaded lipidic nanoparticles (DDLN) of curcumin and chlorin e6 (ITZ/Ce6@LNPs) by quality-by-design approach

    iii.   Stability Study of DDLN and DDLN Gel

    iv.   In-vitro Cell Culture Studies

    v.   Ex-vivo skin permeation studies

    vi.   Ex-vivo skin permeation studies by confocal microscopy

    vii.   Dermatopharmacokinetic study of DDLN gel formulation

References:

[1]   M.B. Brown, G.P. Martin, S.A. Jones, F.K. Akomeah, Dermal and Transdermal Drug Delivery Systems : Current and Future Prospects, (2006) 175–187. https://doi.org/10.1080/10717540500455975.

[2]   D. Singh Malik, N. Mital, G. Kaur, Topical drug delivery systems: A patent review, Expert Opin Ther Pat. 26 (2016) 213–228. https://doi.org/10.1517/13543776.2016.1131267.

[3]   M. Gupta, U. Agrawal, S.P. Vyas, Nanocarrier-based topical drug delivery for the treatment of skin diseases, Expert Opin Drug Deliv. 9 (2012) 783–804. https://doi.org/10.1517/17425247.2012.686490.

[4]   P. Das, N. Deshmukh, N. Badore, C. Ghulaxe, P. Patel, A Review Article on Melanoma, 8 (2016) 112–117.

[5]   V. Smith, S. Walton, Treatment of Facial Basal Cell Carcinoma : A Review, 2011 (2011). https://doi.org/10.1155/2011/380371.

[6]   M. Rastrelli, S. Tropea, C.R. Rossi, M. Alaibac, Melanoma : Epidemiology , Risk Factors , Pathogenesis , Diagnosis and Classification, 1012 (2014) 1005–1011.

[7]   J.B. Loureiro, M. Abrantes, P.A. Oliveira, L. Saraiva, P53 in skin cancer: From a master player to a privileged target for prevention and therapy, Biochim Biophys Acta Rev Cancer. 1874 (2020) 188438. https://doi.org/10.1016/j.bbcan.2020.188438.

[8]   J.B. Loureiro, M. Abrantes, P.A. Oliveira, L. Saraiva, P53 in skin cancer: From a master player to a privileged target for prevention and therapy, Biochim Biophys Acta Rev Cancer. 1874 (2020) 188438. https://doi.org/10.1016/j.bbcan.2020.188438.

[9]   G. Sánchez, J. Nova, A.E. Rodriguez-Hernandez, R.D. Medina, C. Solorzano-Restrepo, J. Gonzalez, M. Olmos, K. Godfrey, I. Arevalo-Rodriguez, Sun protection for preventing basal cell and squamous cell skin cancers, Cochrane Database of Systematic Reviews. 2016 (2016). https://doi.org/10.1002/14651858.CD011161.PUB2.

[10]   V. Krishnan, S. Mitragotri, Nanoparticles for topical drug delivery: Potential for skin cancer treatment, Adv Drug Deliv Rev. 153 (2020) 87–108. https://doi.org/10.1016/j.addr.2020.05.011.

[11]   C. Matei, M. Tampa, T. Poteca, G. Sr, I. Rm, P. Sm, C. Giurcaneanu, Photodynamic therapy in the treatment of basal cell carcinoma, 6 (2013) 50–54.

[12]   B.S. Padya, A. Pandey, M. Pisay, K.B. Koteshwara, R. Chandrashekhar Hariharapura, K.U. Bhat, S. Biswas, S. Mutalik, Stimuli-responsive and cellular targeted nanoplatforms for multimodal therapy of skin cancer, Eur J Pharmacol. 890 (2021) 173633. https://doi.org/10.1016/j.ejphar.2020.173633.

[13]   C.L. Green, P.A. Khavari, Targets for molecular therapy of skin cancer, Semin Cancer Biol. 14 (2004) 63–69. https://doi.org/10.1016/j.semcancer.2003.11.007.

[14]   H.D. Graham, H.A. Mentz, R.B. Butcher, Basal cell carcinoma of the head and neck., J La State Med Soc. 141 (1989) 11–15. https://doi.org/10.1155/2011/496910.

[15]   V. Krishnan, S. Mitragotri, Nanoparticles for topical drug delivery: Potential for skin cancer treatment, Adv Drug Deliv Rev. 153 (2020) 87–108. https://doi.org/10.1016/j.addr.2020.05.011.

[16]   C.L. Green, P.A. Khavari, Targets for molecular therapy of skin cancer, Semin Cancer Biol. 14 (2004) 63–69. https://doi.org/10.1016/j.semcancer.2003.11.007.

[17]   F.C. Ames, R.C. Hickey, Metastasis from squamous cell skin cancer of the extremities., South Med J. 75 (1982) 920–3, 932. https://doi.org/10.1097/00007611-198208000-00005.

[18]   C.S.M. Wong, R.C. Strange, J.T. Lear, Basal cell carcinoma, BMJ. 327 (2003) 794–798. https://doi.org/10.1136/BMJ.327.7418.794.

[19] J.L. Webb, R.E. Burns, H.M. Brown, B.E. LeRoy, C.E. Kosarek, Squamous cell carcinoma., Compend Contin Educ Vet. 31 (2009) E9–E9.

[20] D.S. Rigel, J.A. Carucci, Malignant melanoma: Prevention, early detection, and treatment in the 21st century, CA Cancer J Clin. 50 (2000) 215–236. https://doi.org/10.3322/CANJCLIN.50.4.215.

[21] S.N. Pavri, J. Clune, S. Ariyan, D. Narayan, Malignant melanoma: Beyond the basics, Plast Reconstr Surg. 138 (2016) 330e–340e. https://doi.org/10.1097/PRS.0000000000002367.

[22] D.L. Cummins, J.M. Cummins, H. Pantle, M.A. Silverman, A.L. Leonard, A. Chanmugam, Cutaneous Malignant Melanoma, Mayo Clin Proc. 81 (2006) 500–507. https://doi.org/10.4065/81.4.500.

[23] H. Kaur, P. Kesharwani, Advanced nanomedicine approaches applied for treatment of skin carcinoma, Journal of Controlled Release. 337 (2021) 589–611. https://doi.org/10.1016/j.jconrel.2021.08.003.

[24] F. Tas, S. Keskin, A. Karadeniz, N. Dağoğlu, F. Sen, L. Kilic, I. Yildiz, Noncutaneous Melanoma Have Distinct Features from Each Other and Cutaneous Melanoma, Oncology. 81 (2011) 353–358. https://doi.org/10.1159/000334863.

[25] R.M. MacKie, A. Hauschild, A.M.M. Eggermont, Epidemiology of invasive cutaneous melanoma, Annals of Oncology. 20 (2009). https://doi.org/10.1093/ANNONC/MDP252.

[26] M.R. Albert, M.A. Weinstock, Keratinocyte Carcinoma, CA Cancer J Clin. 53 (2003) 292–302. https://doi.org/10.3322/CANJCLIN.53.5.292.

[27] M. Burotto, V.L. Chiou, J. Lee, The MAPK Pathway Across Different Malignancies : A New Perspective, (2014). https://doi.org/10.1002/cncr.28864.

[28] E. Oikonomou, E. Koustas, M. Goulielmaki, A. Pintzas, BRAF vs RAS oncogenes: are mutations of the same pathway equal? differential signalling and therapeutic implications, Oncotarget. 5 (2014) 11752. https://doi.org/10.18632/ONCOTARGET.2555.

[29] L. Lugović-Mihić, D. Ćesić, P. Vuković, G.N. Bilić, M. Šitum, S. Špoljar, Melanoma development: Current knowledge on melanoma pathogenesis, Acta Dermatovenerologica Croatica. 27 (2019) 163–168.

[30] M. Osaki, M. Oshimura, H. Ito, PI3K-Akt pathway : Its functions and alterations in human cancer, (2004) 667–676.

[31] L. Lugović-Mihić, D. Ćesić, P. Vuković, G.N. Bilić, M. Šitum, S. Špoljar, Melanoma development: Current knowledge on melanoma pathogenesis, Acta Dermatovenerologica Croatica. 27 (2019) 163–168.

[32] R. Jain, S.K. Dubey, G. Singhvi, The Hedgehog pathway and its inhibitors: Emerging therapeutic approaches for basal cell carcinoma, Drug Discov Today. (2021). https://doi.org/10.1016/J.DRUDIS.2021.12.005.

[33] M. Lalan, P. Shah, K. Barve, K. Parekh, T. Mehta, P. Patel, Skin cancer therapeutics: nano-drug delivery vectors—present and beyond, Futur J Pharm Sci. 7 (2021). https://doi.org/10.1186/s43094-021-00326-z.

[34] B. Zhao, Y.Y. He, Recent advances in the prevention and treatment of skin cancer using photodynamic therapy, Expert Rev Anticancer Ther. 10 (2010) 1797–1809. https://doi.org/10.1586/era.10.154.

[35] D. Kosutic, W. Haw, V. Ghura, Current Concepts in the Surgical Management of Non-melanoma Skin Cancers, Clin Oncol. 31 (2019) 738–748. https://doi.org/10.1016/J.CLON.2019.08.009.

[36] V. Gour, P. Agrawal, V. Pandey, I.L. Kanwar, T. Haider, R. Tiwari, V. Soni, Nanoparticles and skin cancer, Nano Drug Delivery Strategies for the Treatment of Cancers. (2021) 245–273. https://doi.org/10.1016/B978-0-12-819793-6.00011-4.

[37] E. Dika, G. Veronesi, A. Patrizi, S. De Salvo, C. Misciali, C. Baraldi, M. Mussi, E. Fabbri, F. Tartari, M. Lambertini, It's time for Mohs: Micrographic surgery for the treatment of high-risk basal cell carcinomas of the head and neck regions, Dermatol Ther. 33 (2020) e13474. https://doi.org/10.1111/DTH.13474.

[38] D. Buckley, C. Marczuk, T. Kennedy, Cryosurgery for basal cell carcinoma treated in primary care, Irish Journal of Medical Science (1971 -) 2020 189:4. 189 (2020) 1183–1187. https://doi.org/10.1007/S11845-020-02188-5.

[39] M. Veness, S. Richards, Role of modern radiotherapy in treating skin cancer, Australasian Journal of Dermatology. 44 (2003) 159–168. https://doi.org/10.1046/J.1440-0960.2003.06711.X.

[40] L. DeRidder, D.A. Rubinson, R. Langer, G. Traverso, The past, present, and future of chemotherapy with a focus on individualization of drug dosing, Journal of Controlled Release. 352 (2022) 840–860. https://doi.org/10.1016/J.JCONREL.2022.10.043.

[41] E.K. Sutedja, T.R. Arianto, R. Lesmana, O. Suwarsa, B. Setiabudiawan, The Chemoprotective Role of Vitamin D in Skin Cancer: A Systematic Review, Cancer Manag Res. 14 (2022) 3551–3565. https://doi.org/10.2147/CMAR.S389591.

[42] P. Ausina, J.R. Branco, T.M. Demaria, A.M. Esteves, J.G.B. Leandro, A.C. Ochioni, A.P.M. Mendonça, F.L. Palhano, M.F. Oliveira, W. Abou-Kheir, M. Sola-Penna, P. Zancan, Acetylsalicylic acid and salicylic acid present anticancer properties against melanoma by promoting nitric oxide-dependent endoplasmic reticulum stress and apoptosis, Scientific Reports 2020 10:1. 10 (2020) 1–15. https://doi.org/10.1038/s41598-020-76824-6.

[43] J. Kim, J.J. Lee, J. Kim, D. Gardner, P.A. Beachy, Arsenic antagonizes the Hedgehog pathway by preventing ciliary accumulation and reducing stability of the Gli2 transcriptional effector, Proc Natl Acad Sci U S A. 107 (2010) 13432–13437. https://doi.org/10.1073/pnas.1006822107.

[44] G. Liang, M. Liu, Q. Wang, Y. Shen, H. Mei, D. Li, W. Liu, Itraconazole exerts its anti-melanoma effect by suppressing Hedgehog, Wnt, and PI3K/mTOR signaling pathways, 2017. www.impactjournals.com/oncotarget.

[45] K.E. O'Reilly, E.V.S. de Miera, M.F. Segura, E. Friedman, L. Poliseno, S.W. Han, J. Zhong, J. Zavadil, A. Pavlick, E. Hernando, I. Osman, Hedgehog pathway blockade inhibits melanoma cell growth in vitro and in vivo, Pharmaceuticals. 6 (2013) 1429–1450. https://doi.org/10.3390/ph6111429.

[46] J.A. Bush, K.J.J. Cheung, G. Li, Curcumin Induces Apoptosis in Human Melanoma Cells through a Fas Receptor/Caspase-8 Pathway Independent of p53, Exp Cell Res. 271 (2001) 305–314. https://doi.org/10.1006/EXCR.2001.5381.

[47] S.H. Jee, S.C. Shen, C.R. Tseng, H.C. Chiu, M.L. Kuo, Curcumin Induces a p53-Dependent Apoptosis in Human Basal Cell Carcinoma Cells, Journal of Investigative Dermatology. 111 (1998) 656–661. https://doi.org/10.1046/J.1523-1747.1998.00352.X.

[48] S.-H. Jee, S.-C. Shen, C.-R. Tseng, H.-C. Chiu, M.-L. Kuo, Curcumin Induces a p53-Dependent Apoptosis in Human Basal Cell Carcinoma Cells, 1998.

[49] P. Agostinis, K. Berg, K.A. Cengel, T.H. Foster, A.W. Girotti, S.O. Gollnick, S.M. Hahn, M.R. Hamblin, A. Juzeniene, NIH Public Access, 61 (2012) 250–281. https://doi.org/10.3322/caac.20114.PHOTODYNAMIC.

[50] K.V. Krishna, N. Saha, A. Puri, Pre-clinical compartmental pharmacokinetic modeling of 2-[1-hexyloxyethyl]-2-devinyl pyropheophorbide-a (HPPH) as a photosensitizer in rat plasma by validated HPLC method, (2019). https://doi.org/10.1039/c8pp00339d.

[51]   L.S. Capella, A Light in Multidrug Resistance : Photodynamic Treatment of Multidrug-Resistant Tumors, (2003) 361–366. https://doi.org/10.1159/000071155.

[52]   H.R. Nava, S.S. Allamaneni, T.J. Dougherty, M.T. Cooper, Photodynamic Therapy (PDT) Using HPPH for the Treatment of Precancerous Lesions Associated With Barrett ' s Esophagus, 712 (2011) 705–712. https://doi.org/10.1002/lsm.21112.

[53]   D. Singh, N. Mital, G. Kaur, Topical Drug Delivery Systems : A Patent Review, 3776 (2016). https://doi.org/10.1517/13543776.2016.1131267.

[54]   J. Zhao, L. Duan, A. Wang, J. Fei, J. Li, Insight into the efficiency of oxygen introduced photodynamic therapy (PDT) and deep PDT against cancers with various assembled nanocarriers, Wiley Interdiscip Rev Nanomed Nanobiotechnol. 12 (2020) 1–20. https://doi.org/10.1002/wnan.1583.

[55]   A.P. Castano, P. Mroz, M.R. Hamblin, Photodynamic therapy and anti-tumour immunity, Nature Reviews Cancer 2006 6:7. 6 (2006) 535–545. https://doi.org/10.1038/nrc1894.

[56]   A.P. Castano, T.N. Demidova, M.R. Hamblin, Mechanisms in photodynamic therapy: part one—photosensitizers, photochemistry and cellular localization, Photodiagnosis Photodyn Ther. 1 (2004) 279–293. https://doi.org/10.1016/S1572-1000(05)00007-4.

[57]   A.P. Castano, T.N. Demidova, M.R. Hamblin, Mechanisms in photodynamic therapy: Part three—Photosensitizer pharmacokinetics, biodistribution, tumor localization and modes of tumor destruction, Photodiagnosis Photodyn Ther. 2 (2005) 91–106. https://doi.org/10.1016/S1572-1000(05)00060-8.

[58]   A.P. Castano, T.N. Demidova, M.R. Hamblin, Mechanisms in photodynamic therapy: part two—cellular signaling, cell metabolism and modes of cell death, Photodiagnosis Photodyn Ther. 2 (2005) 1–23. https://doi.org/10.1016/S1572-1000(05)00030-X.

[59]   D. Bechet, P. Couleaud, C. Frochot, M.L. Viriot, F. Guillemin, M. Barberi-Heyob, Nanoparticles as vehicles for delivery of photodynamic therapy agents, Trends Biotechnol. 26 (2008) 612–621. https://doi.org/10.1016/J.TIBTECH.2008.07.007.

[60]   J.P. Keene, D. Kessel, E.J. Land, R.W. Redmond, T.G. Truscott, DIRECT DETECTION OF SINGLET OXYGEN SENSITIZED BY HAEMATOPORPHYRIN AND RELATED COMPOUNDS, Photochem Photobiol. 43 (1986) 117–120. https://doi.org/10.1111/J.1751-1097.1986.TB09501.X.

[61]   R. Jain, R. Pradhan, S. Hejmady, G. Singhvi, S.K. Dubey, Fluorescence-based method for sensitive and rapid estimation of chlorin e6 in stealth liposomes for photodynamic therapy against cancer, Spectrochim Acta A Mol Biomol Spectrosc. 244 (2021) 118823. https://doi.org/10.1016/J.SAA.2020.118823.

[62]   Fda, Cder, HIGHLIGHTS OF PRESCRIBING INFORMATION, (n.d.).

[63]   Photodynamic Therapy With Porfimer Sodium in Treating Patients With Precancerous Lesions, Cancer, or Other Disease of the Aerodigestive Tract - Full Text View - ClinicalTrials.gov, (n.d.). https://clinicaltrials.gov/ct2/show/NCT00453336 (accessed August 22, 2022).

[64]   J. Akimoto, Photodynamic Therapy for Malignant Brain Tumors, Neurol Med Chir (Tokyo). 56 (2016) 151. https://doi.org/10.2176/NMC.RA.2015-0296.

[65]   Aminolevulinic acid hydrochloride, known as ALA HCl (Gleolan, NX Development Corp.) as an optical imaging agent indicated in patients with gliomas | FDA, (n.d.). https://www.fda.gov/drugs/resources-information-approved-drugs/aminolevulinic-acid-hydrochloride-known-ala-hcl-gleolan-nx-development-corp-optical-imaging-agent (accessed August 22, 2022).

[66]   Aminolevulinic acid, Meyler's Side Effects of Drugs. (2016) 237–238. https://doi.org/10.1016/B978-0-444-53717-1.00012-3.

[67] M. Schwake, S. Schipmann, M. Müther, M. Köchling, A. Brentrup, W. Stummer, 5-ALA fluorescence–guided surgery in pediatric brain tumors—a systematic review, Acta Neurochir (Wien). 161 (2019) 1099–1108. https://doi.org/10.1007/S00701-019-03898-1.

[68] G.G. Hermann, K. Mogensen, S. Carlsson, N. Marcussen, S. Duun, Fluorescence-guided transurethral resection of bladder tumours reduces bladder tumour recurrence due to less residual tumour tissue in T a/T1 patients: A randomized two-centre study, BJU Int. 108 (2011). https://doi.org/10.1111/J.1464-410X.2011.10090.X.

[69] A Randomized, Comparative Study of Hexvix Fluorescence Cystoscopy and Standard Cystoscopy in Patients With Non-invasive Bladder Cancer - Full Text View - ClinicalTrials.gov, (n.d.). https://clinicaltrials.gov/ct2/show/NCT00412971 (accessed August 22, 2022).

[70] W.M. Sharman, C.M. Allen, J.E. Van Lier, Photodynamic therapeutics: Basic principles and clinical applications, Drug Discov Today. 4 (1999) 507–517. https://doi.org/10.1016/S1359-6446(99)01412-9.

[71] Temoporfin | C44H32N4O4 - PubChem, (n.d.). https://pubchem.ncbi.nlm.nih.gov/compound/60751 (accessed August 23, 2022).

[72] Hpph | C39H48N4O4 - PubChem, (n.d.). https://pubchem.ncbi.nlm.nih.gov/compound/Hpph#section=Names-and-Identifiers (accessed August 23, 2022).

[73] D. Wu, Z. Liu, Y. Fu, Y. Zhang, N. Tang, Q. Wang, L. Tao, Efficacy of 2-(1-hexyloxyethyl)-2-devinyl pyropheophorbide-a in photodynamic therapy of human esophageal squamous cancer cells, Oncol Lett. 6 (2013) 1111–1119. https://doi.org/10.3892/OL.2013.1493/HTML.

[74] AL(III) Phthalocyanine chloride tetrasulfonic acid | C32H16AlClN8O12S4 - PubChem, (n.d.). https://pubchem.ncbi.nlm.nih.gov/compound/AL_III_-Phthalocyanine-chloride-tetrasulfonic-acid (accessed August 23, 2022).

[75] Aluminum phthalocyanine | C32H16AlN8+ - PubChem, (n.d.). https://pubchem.ncbi.nlm.nih.gov/compound/Aluminum-phthalocyanine (accessed August 23, 2022).

[76] M. Osuchowski, D. Bartusik-Aebisher, F. Osuchowski, D. Aebisher, Photodynamic therapy for prostate cancer – A narrative review, Photodiagnosis Photodyn Ther. 33 (2021) 102158. https://doi.org/10.1016/J.PDPDT.2020.102158.

[77] A. P, B. K, C. KA, F. TH, G. AW, G. SO, H. SM, H. MR, J. A, K. D, K. M, M. J, M. P, N. D, P. J, W. BC, G. J, Photodynamic therapy of cancer: an update, CA Cancer J Clin. 61 (2011) 250–281. https://doi.org/10.3322/CAAC.20114.

[78] B. Perillo, M. Di Donato, A. Pezone, E. Di Zazzo, P. Giovannelli, G. Galasso, G. Castoria, A. Migliaccio, ROS in cancer therapy: the bright side of the moon, Experimental & Molecular Medicine 2020 52:2. 52 (2020) 192–203. https://doi.org/10.1038/s12276-020-0384-2.

[79] H.J. Forman, F. Ursini, M. Maiorino, An overview of mechanisms of redox signaling, J. Mol. Cell. Cardiol. 73 (2014) 2–9. https://doi.org/10.1016/j.yjmcc.2014.01.018.

[80] A.I. Gavrina, M. V. Shirmanova, N.A. Aksenova, D. V. Yuzhakova, L.B. Snopova, A.B. Solovieva, P.S. Timashev, V. V. Dudenkova, E. V. Zagaynova, Photodynamic therapy of mouse tumor model using chlorin e6- polyvinyl alcohol complex, J Photochem Photobiol B. 178 (2018) 614–622. https://doi.org/10.1016/J.JPHOTOBIOL.2017.12.016.

[81] Chlorin e6 | C34H36N4O6 | CID 5479494 - PubChem, (n.d.). https://pubchem.ncbi.nlm.nih.gov/compound/Chlorin_e6 (accessed June 26, 2023).

[82] T3DB: Itraconazole, (n.d.). http://www.t3db.ca/toxins/T3D3516 (accessed June 26, 2023).

[83] L. Shen, H.F. Ji, Theoretical study on physicochemical properties of curcumin, Spectrochim Acta A Mol Biomol Spectrosc. 67 (2007) 619–623. https://doi.org/10.1016/J.SAA.2006.08.018.

[84] A.D. Vances, I.N. Translational, Nanoemulsions and nanoparticles for non-melanoma skin cancer : effects of lipid materials, (2013) 417–424. https://doi.org/10.1007/s12094-012-0982-0.

[85] V. Krishnan, K. Peng, A. Sarode, S. Prakash, Z. Zhao, S.K. Filippov, K. Todorova, B.R. Sell, O. Lujano, S. Bakre, A. Pusuluri, D. Vogus, K.Y. Tsai, A. Mandinova, S. Mitragotri, Hyaluronic acid conjugates for topical treatment of skin cancer lesions, Sci Adv. 7 (2021) 6627–6638. https://doi.org/10.1126/SCIADV.ABE6627.

[86] S. Hejmady, R. Pradhan, A. Alexander, M. Agrawal, G. Singhvi, B. Gorain, S. Tiwari, P. Kesharwani, S.K. Dubey, Recent advances in targeted nanomedicine as promising antitumor therapeutics, Drug Discov Today. 25 (2020) 2227–2244. https://doi.org/10.1016/j.drudis.2020.09.031.

[87] How Does Combination Therapy for Metastatic Melanoma Work?, (n.d.). https://www.webmd.com/cancer/melanoma-combination-therapy# (accessed June 27, 2023).

[88] R.B. Mokhtari, T.S. Homayouni, N. Baluch, E. Morgatskaya, S. Kumar, B. Das, H. Yeger, Combination therapy in combating cancer, Oncotarget. 8 (2017) 38022. https://doi.org/10.18632/ONCOTARGET.16723.

[89] N.M. Ayoub, Editorial: Novel Combination Therapies for the Treatment of Solid Cancers, Front Oncol. 11 (2021) 708943. https://doi.org/10.3389/FONC.2021.708943/BIBTEX.

[90] R. Jain, S.K. Dubey, G. Singhvi, The Hedgehog pathway and its inhibitors: Emerging therapeutic approaches for basal cell carcinoma, Drug Discov Today. (2021). https://doi.org/10.1016/J.DRUDIS.2021.12.005.

[91] L. Held, T.K. Eigentler, U. Leiter, C. Garbe, M.J. Berneburg, Effective Combination of Photodynamic Therapy and Imiquimod 5% Cream in the Treatment of Actinic Keratoses: Three Cases, Biomed Res Int. 2013 (2013). https://doi.org/10.1155/2013/102698.

[92] C. Dianzani, G.P. Zara, G. Maina, P. Pettazzoni, S. Pizzimenti, F. Rossi, C.L. Gigliotti, E.S. Ciamporcero, M. Daga, G. Barrera, Drug Delivery Nanoparticles in Skin Cancers, 2014 (2014).

[93] F.U. Din, W. Aman, I. Ullah, O.S. Qureshi, O. Mustapha, S. Shafique, A. Zeb, Effective use of nanocarriers as drug delivery systems for the treatment of selected tumors, Int J Nanomedicine. 12 (2017) 7291. https://doi.org/10.2147/IJN.S146315.

[94] M. Ibrahim, W.H. Abuwatfa, N.S. Awad, R. Sabouni, G.A. Husseini, Encapsulation, Release, and Cytotoxicity of Doxorubicin Loaded in Liposomes, Micelles, and Metal-Organic Frameworks: A Review, Pharmaceutics. 14 (2022) 254. https://doi.org/10.3390/PHARMACEUTICS14020254.

[95] D. Patel, B. Patel, H. Thakkar, Lipid Based Nanocarriers: Promising Drug Delivery System for Topical Application, European Journal of Lipid Science and Technology. 123 (2021) 1–12. https://doi.org/10.1002/ejlt.202000264.

[96] K. Orthaber, M. Pristovnik, K. Skok, B. Perić, U. Maver, Skin Cancer and Its Treatment: Novel Treatment Approaches with Emphasis on Nanotechnology, J Nanomater. 2017 (2017). https://doi.org/10.1155/2017/2606271.

[97] C. Dianzani, G.P. Zara, G. Maina, P. Pettazzoni, S. Pizzimenti, F. Rossi, C.L. Gigliotti, E.S. Ciamporcero, M. Daga, G. Barrera, Drug delivery nanoparticles in skin cancers, Biomed Res Int. 2014 (2014). https://doi.org/10.1155/2014/895986.

[98] M.H. Akhter, M. Rizwanullah, J. Ahmad, M.J. Ahsan, M.A. Mujtaba, S. Amin, Nanocarriers in advanced drug targeting: setting novel paradigm in cancer therapeutics, Artif Cells Nanomed Biotechnol. 46 (2018) 873–884. https://doi.org/10.1080/21691401.2017.1366333.

[99] L.B. Naves, C. Dhand, J.R. Venugopal, L. Rajamani, S. Ramakrishna, L. Almeida, Nanotechnology for the treatment of melanoma skin cancer, Prog Biomater. 6 (2017) 13–26. https://doi.org/10.1007/s40204-017-0064-z.

[100] D. Bei, J. Meng, B.B.C. Youan, Engineering nanomedicines for improved melanoma therapy: Progress and promises, Nanomedicine. 5 (2010) 1385–1399. https://doi.org/10.2217/nnm.10.117.

[101] M.C.F. Simões, J.J.S. Sousa, A.A.C.C. Pais, Skin cancer and new treatment perspectives: A review, Cancer Lett. 357 (2015) 8–42. https://doi.org/10.1016/j.canlet.2014.11.001.

[102] M.A. Tran, R.J. Watts, G.P. Robertson, Use of liposomes as drug delivery vehicles for treatment of melanoma, Pigment Cell Melanoma Res. 22 (2009) 388–399. https://doi.org/10.1111/j.1755-148X.2009.00581.x.

[103] J. De Leeuw, H.C. De Vijlder, P. Bjerring, H.A.M. Neumann, Liposomes in dermatology today, Journal of the European Academy of Dermatology and Venereology. 23 (2009) 505–516. https://doi.org/10.1111/j.1468-3083.2009.03100.x.

[104] G.M. El Maghraby, B.W. Barry, A.C. Williams, Liposomes and skin: From drug delivery to model membranes, European Journal of Pharmaceutical Sciences. 34 (2008) 203–222. https://doi.org/10.1016/j.ejps.2008.05.002.

[105] M. Slingerland, H.J. Guchelaar, H. Gelderblom, Liposomal drug formulations in cancer therapy: 15 years along the road, Drug Discov Today. 17 (2012) 160–166. https://doi.org/10.1016/j.drudis.2011.09.015.

[106] A. Mohan, S. Narayanan, S. Sethuraman, U.M. Krishnan, Novel resveratrol and 5-fluorouracil coencapsulated in PEGylated nanoliposomes improve chemotherapeutic efficacy of combination against head and neck squamous cell carcinoma, Biomed Res Int. 2014 (2014). https://doi.org/10.1155/2014/424239.

[107] S. Rai, V. Pandey, G. Rai, Transfersomes as versatile and flexible nano-vesicular carriers in skin cancer therapy: the state of the art, Nano Rev Exp. 8 (2017) 1325708. https://doi.org/10.1080/20022727.2017.1325708.

[108] B. H.A.E., Transfersomes for transdermal drug delivery, Expert Opin Drug Deliv. 3 (2006) 727–737.

[109] T. Jiang, T. Wang, T. Li, Y. Ma, S. Shen, B. He, R. Mo, Enhanced Transdermal Drug Delivery by Transfersome-Embedded Oligopeptide Hydrogel for Topical Chemotherapy of Melanoma, ACS Nano. (2018). https://doi.org/10.1021/acsnano.8b03800.

[110] B. H.A.E., Transfersomes for transdermal drug delivery, Expert Opin Drug Deliv. 3 (2006) 727–737.

[111] G.M. El Zaafarany, G.A.S. Awad, S.M. Holayel, N.D. Mortada, Role of edge activators and surface charge in developing ultradeformable vesicles with enhanced skin delivery, Int J Pharm. 397 (2010) 164–172. https://doi.org/10.1016/j.ijpharm.2010.06.034.

[112] N. Zhang, Y. Yin, S.J. Xu, W.S. Chen, 5-Fluorouracil: Mechanisms of resistance and reversal strategies, Molecules. 13 (2008) 1551–1569. https://doi.org/10.3390/molecules13081551.

[113] M.A. Khan, J. Pandit, Y. Sultana, S. Sultana, A. Ali, M. Aqil, M. Chauhan, Novel carbopol-based transfersomal gel of 5-fluorouracil for skin cancer treatment: In vitro characterization and in vivo study, Drug Deliv. 22 (2015) 795–802. https://doi.org/10.3109/10717544.2014.902146.

[114] I.A. Alvi, J. Madan, D. Kaushik, S. Sardana, R.S. Pandey, A. Ali, Comparative study of transfersomes, liposomes, and niosomes for topical delivery of 5-fluorouracil to skin cancer cells: Preparation, characterization, in-vitro release, and cytotoxicity analysis, Anticancer Drugs. 22 (2011) 774–782. https://doi.org/10.1097/CAD.0b013e328346c7d6.

[115] G. Garg, S. Saraf, S. Saraf, Cubosomes: An overview, Biol Pharm Bull. 30 (2007) 350–353. https://doi.org/10.1248/bpb.30.350.

[116] Z. Karami, M. Hamidi, Cubosomes: Remarkable drug delivery potential, Drug Discov Today. 21 (2016) 789–801. https://doi.org/10.1016/j.drudis.2016.01.004.

[117] Z. Karami, M. Hamidi, Cubosomes: Remarkable drug delivery potential, Drug Discov Today. 21 (2016) 789–801. https://doi.org/10.1016/j.drudis.2016.01.004.

[118] S. Küchler, W. Herrmann, G. Panek-Minkin, T. Blaschke, C. Zoschke, K.D. Kramer, R. Bittl, M. Schäfer-Korting, SLN for topical application in skin diseases-Characterization of drug-carrier and carrier-target interactions, Int J Pharm. 390 (2010) 225–233. https://doi.org/10.1016/j.ijpharm.2010.02.004.

[119] M. Agrawal, S. Saraf, S. Saraf, S.K. Dubey, A. Puri, R.J. Patel, Ajazuddin, V. Ravichandiran, U.S. Murty, A. Alexander, Recent strategies and advances in the fabrication of nano lipid carriers and their application towards brain targeting, Journal of Controlled Release. 321 (2020) 372–415. https://doi.org/10.1016/j.jconrel.2020.02.020.

[120] P. Desai, R.R. Patolla, M. Singh, Interaction of nanoparticles and cell-penetrating peptides with skin for transdermal drug delivery, Mol Membr Biol. 27 (2010) 247–259. https://doi.org/10.3109/09687688.2010.522203.

[121] C.M. Keck, P. Anantaworasakul, M. Patel, S. Okonogi, K.K. Singh, D. Roessner, R. Scherrers, K. Schwabe, C. Rimpler, R.H. Müller, A new concept for the treatment of atopic dermatitis: Silver-nanolipid complex (sNLC), Int J Pharm. 462 (2014) 44–51. https://doi.org/10.1016/j.ijpharm.2013.12.044.

[122] H. Zhai, H.I. Maibach, Effects of skin occlusion on percutaneous absorption: An overview, Skin Pharmacol Appl Skin Physiol. 14 (2001) 1–10. https://doi.org/10.1159/000056328.

[123] M.A. Iqbal, S. Md, J.K. Sahni, S. Baboota, S. Dang, J. Ali, Nanostructured lipid carriers system: Recent advances in drug delivery, J Drug Target. 20 (2012) 813–830. https://doi.org/10.3109/1061186X.2012.716845.

[124] A. Zeb, S.T. Arif, M. Malik, F.A. Shah, F.U. Din, O.S. Qureshi, E.S. Lee, G.Y. Lee, J.K. Kim, Potential of nanoparticulate carriers for improved drug delivery via skin, Springer Singapore, 2019. https://doi.org/10.1007/s40005-018-00418-8.

[125] M. Schneider, F. Stracke, S. Hansen, U.F. Schaefer, Nanoparticles and their interactions with the dermal barrier, Dermatoendocrinol. 1 (2009) 197–206. https://doi.org/10.4161/derm.1.4.9501.

[126] C.H. Loo, M. Basri, R. Ismail, H.L.N. Lau, B.A. Tejo, M.S. Kanthimathi, H.A. Hassan, Y.M. Choo, Effect of compositions in nanostructured lipid carriers (NLC) on skin hydration and occlusion, Int J Nanomedicine. 8 (2013) 13–22. https://doi.org/10.2147/IJN.S35648.

[127] M. A., D. N., Nanostructure lipid carriers: A promising tool for the drug delivery in the treatment of skin cancer, Asian Journal of Pharmaceutical and Clinical Research. 12 (2019) 15–26. https://doi.org/http://dx.doi.org/10.22159/ajpcr.2019.v12i5.31239.

[128] R. Bharadwaj, P.J. Das, P. Pal, B. Mazumder, Topical delivery of paclitaxel for treatment of skin cancer, Drug Dev Ind Pharm. 42 (2016) 1482–1494. https://doi.org/10.3109/03639045.2016.1151028.

[129] R.A. Khallaf, H.F. Salem, A. Abdelbary, 5-Fluorouracil shell-enriched solid lipid nanoparticles (SLN) for effective skin carcinoma treatment, Drug Deliv. 23 (2016) 3452–3460. https://doi.org/10.1080/10717544.2016.1194498.

[130] T. Geetha, M. Kapila, O. Prakash, P.K. Deol, V. Kakkar, I.P. Kaur, Sesamol-loaded solid lipid nanoparticles for treatment of skin cancer, J Drug Target. 23 (2015) 159–169. https://doi.org/10.3109/1061186X.2014.965717.

[131] A. Tupal, M. Sabzichi, F. Ramezani, M. Kouhsoltani, H. Hamishehkar, Dermal delivery of doxorubicin-loaded solid lipid nanoparticles for the treatment of skin cancer, J Microencapsul. 33 (2016) 372–380. https://doi.org/10.1080/02652048.2016.1200150.

[132] P.S. Rajinikanth, J. Chellian, Development and evaluation of nanostructured lipid carrier-based hydrogel for topical delivery of 5-fluorouracil, Int J Nanomedicine. 11 (2016) 5067–5077. https://doi.org/10.2147/IJN.S117511.

[133] A. Qidwai, S. Khan, S. Md, M. Fazil, S. Baboota, J.K. Narang, J. Ali, Nanostructured lipid carrier in photodynamic therapy for the treatment of basal-cell carcinoma, Drug Deliv. 23 (2016) 1476–1485. https://doi.org/10.3109/10717544.2016.1165310.

[134] E.K. Oh, S.E. Jin, J.K. Kim, J.S. Park, Y. Park, C.K. Kim, Retained topical delivery of 5-aminolevulinic acid using cationic ultradeformable liposomes for photodynamic therapy, European Journal of Pharmaceutical Sciences. 44 (2011) 149–157. https://doi.org/10.1016/j.ejps.2011.07.003.

CHAPTER 2

ANALYTICAL METHOD DEVELOPMENT AND VALIDATION

Introduction

Method development and validation are essential components in pharmaceutical drug development, quality control, and manufacturing processes, as they hold significant importance. Two commonly employed techniques for these purposes are high-performance liquid chromatography (HPLC) and fluorescence spectroscopy. HPLC, known for its effectiveness, is an analytical technique capable of segregating intricate mixtures into distinct constituents, facilitating the precise measurement and characterization of each individual component. HPLC can be used for both qualitative and quantitative analysis of small molecules, peptides, and proteins. Spectroscopy, on the other hand, is a technique that measures the interaction of light with matter. It includes various techniques such as UV-visible, infrared, and fluorescence spectroscopy, which can provide information on the chemical structure, concentration, and purity of a sample [1].

The process of developing and validating an analytical method involves a thorough evaluation of key parameters, including specificity, accuracy, precision, linearity, and robustness. These parameters are essential for ensuring the reliability and reproducibility of the analytical method. This process receives considerable attention from both the International Council for Harmonisation of Technical Requirements for Pharmaceuticals for Human Use (ICH) and the US Food and Drug Administration (USFDA), underlining its importance. Validation guarantees that the analytical method is suitable for its intended objective and generates accurate and precise outcomes within acceptable boundaries [2].

Chapter 2 is divided into three sections i.e., 2.1, 2.2, and 2.3. In section 2.1, the estimation of chlorin e6 by fluorescence spectroscopy was provided. In 2.2, the analysis of itraconazole by High-Performance Liquid Chromatography was given, while in section 2.3, the simultaneous estimation of chlorin e6 and curcumin using High-Performance Liquid Chromatography (for determining the quantities of drug permeated in deeper skin layers) was given.

2.1. Development and validation of analytical method of chlorin e6 by fluorescence spectroscopy

The present work was aimed at the development and validation of a selective, accurate, and sensitive spectrofluorimetric method for determining chlorin e6 in its lipidic nanoformulation formulations. In this study, a comprehensive validation of spectrofluorimetric analysis was conducted and successfully accomplished. The validation encompassed various aspects, including specificity, range, linearity, accuracy, precision, the limit of detection (LOD), the limit of quantification (LOQ), and ruggedness. The analytical validation parameters were executed in accordance with the guidelines set forth by the International Conference on Harmonization (ICH) [3–5]. Additionally, an evaluation was conducted to assess the impact of varying pH levels on the fluorescence intensity of chlorin e6. Also, the estimation of the degradation of chlorin e6 solution by applying laser light source has been performed. The developed and validated method will possess the major advantages of appropriate sensitivity, simplicity, and selectivity, with high throughput. To the best of our knowledge, the quantification and degradation of chlorin e6 by fluorescence spectroscopy has been performed for the first time.

2.1.1. Materials and analytical conditions

Chlorin e6 was purchased from Cayman Chemical Company, USA. Sodium chloride, potassium chloride, di-Sodium hydrogen phosphate, potassium di-hydrogen phosphate, were purchased from Merck Pvt. Ltd, Mumbai, India. Triton X and Dimethyl sulphoxide (DMSO) were purchased from the Sigma Alrich (St. Louis, MO, USA). Acetonitrile was procured from Merck Pvt. Ltd, Mumbai. All the solvents and chemicals utilized for the study were of analytical grade. A Fluorolog HORIBA Scientific Ltd. was used for the estimation of fluorescence intensity. Xenon arc lamp was used and 1 nm slit width was employed for both excitation and emission with the size of the cuvette being 1 cm. Laser light was purchased from China, the optical wavelength of laser light was 650 nm ± 20 nm and voltage capacity was 30 mW. Eco pH meter (Thermo Scientific) was used for measuring pH. Cool safe (SCANVAC) was used for freeze-drying.

2.1.2. Standard and sample preparation

An accurately weighed sample (1 mg) of chlorin e6 was transferred into an eppendorf tube containing 100 µl of DMSO and 900 µl of acetonitrile. It was sonicated for 5 minutes to attain

a stock solution with a concentration of 1000 µg/ml. From the primary stock solution, 1 µg/ml secondary stock solutions were prepared in acetonitrile solution. The secondary stock solutions were diluted with the same solvent to obtain a working solution in the concentration range of 50 to 1000 ng/ml. The stock solution was stored in the light-resistant volumetric flask at a temperature of -20 °C.

2.1.3. Procedure for the calibration curve

The dilutions of the chlorin e6 stock solution were prepared with acetonitrile to obtain a standard working solution ranging from 50 to 1000 ng/ml. The emission of 665 nm was used for measuring the fluorescence intensity of the standard working solutions, which were excited at 400 nm. The same was measured along with the absence of chlorin e6 in blank solutions. The corrected fluorescence intensity of chlorin e6 solutions in acetonitrile was plotted against the different drug concentrations to obtain the calibration curve.

2.1.4. Analytical validation

In the validation of the spectrofluorimetric method of chlorin e6, the following parameters were included as per the ICH guidelines: linearity, accuracy, precision, specificity, robustness, the LOD, and the LOQ. A Fluorolog HORIBA spectrofluorimetric instrument was used for the development of the analytical method.

2.1.4.1. Linearity and range

In the linearity of the fluorescence-based analytical method, standard working solutions of chlorin e6 were evaluated within a concentration range from 50-1000 ng/ml in acetonitrile. The above method was performed for six different concentrations (three replicates for each concentration). The fluorescence intensity of chlorin e6 solvent was plotted against drug concentration, and linearity was calculated by utilizing the linear regression equation. A coefficient of determination (R^2) value equal to or greater than 0.999 was considered as the desired threshold for the calibration curves in the aforementioned method. [6].

2.1.4.2. Limit of detection (LOD) and limit of quantification (LOQ)

The limit of detection (LOD) refers to the minimum concentration of an analyte that can be distinguished from the background noise level. The limit of quantification (LOQ) is the minimum concentration of an analyte that can be reliably and precisely measured with

acceptable accuracy. The LOD and LOQ of the proposed method of chlorin e6 were estimated by utilizing the following equations [7].

$$LOD = \frac{3.3\sigma}{S}$$

$$LOQ = \frac{10\sigma}{S}$$

In this context, the symbol σ denotes the standard deviation of the fluorescence intensity of the sample, while the symbol S represents the slope of the calibration curve.

2.1.4.3. Accuracy and precision

For the developed analytical method of chlorin e6 in acetonitrile, the accuracy and precision were assessed for both intra-day and inter-day variations. This was achieved through several analyses of different concentrations of quality control (QC) samples on three successive days. The inter-day validation was evaluated with three sets of three QC samples of different concentrations (75, 500, and 900 ng/ml) [8].

2.1.5. **Result and Discussion**

Chlorin e6, the second generation of photosensitizer, is derived from naturally occurring chlorophyll. It has been used for treating several types of cancers like melanoma, non-melanoma, head, and neck, etc. It is a need to develop a highly sensitive method for its determination. The presence of excitation and emission wavelength in fluorescence spectroscopy ensures its high accuracy, precision, specificity, and selectivity as compared to other methods. Chlorin e6 was found to exhibit emission in acetonitrile at 665 nm after excitation at 400 nm. A typical fluorescence contour plot, along with excitation and emission spectra of chlorin e6 (500 ng/ml) in acetonitrile are illustrated in **Figure 2.1** and **Figure 2.2** respectively. Thus, we aimed to utilize the excitation and emission spectra of chlorin e6 to develop a novel accurate, precise, and specific analytical method to analyse chlorin e6 in the lipidic formulation.
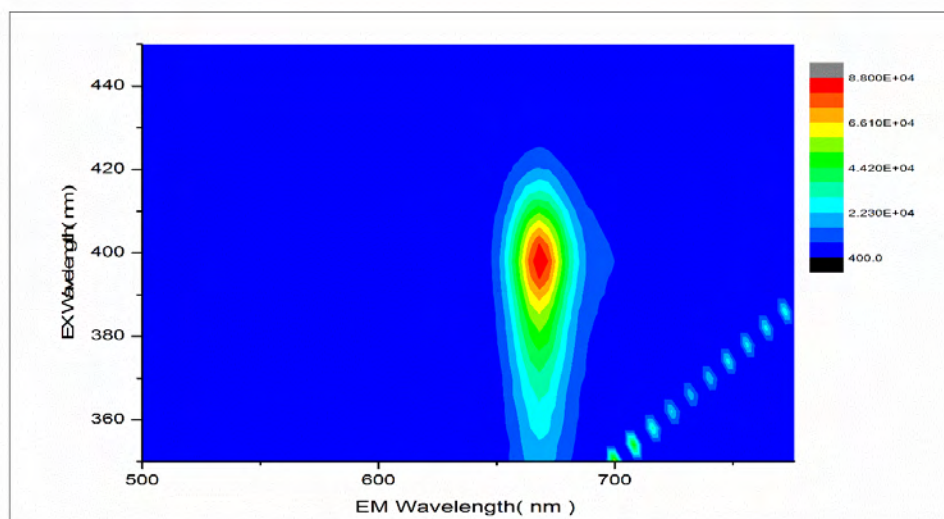
Figure 2.1. Contour plot of excitation and emission wavelengths of chlorin e6 (500 ng/ml)
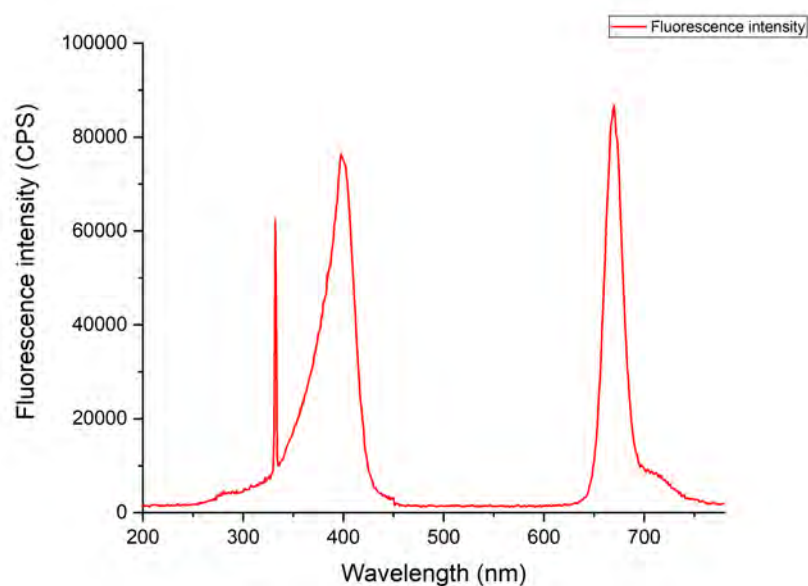
Figure 2.2. Excitation and emission spectra of chlorin e6 (500 ng/ml)

2.1.5.1. Method development and validation

The method validation was carried out in accordance with the guidelines, utilizing multiple parameters such as accuracy, precision, specificity, system suitability, and stability. A

Fluorolog HORIBA spectrofluorimetric instrument was used for the development of the analytical method.

2.1.5.2. Linearity and range

The analytical graph was constructed by plotting the fluorescence intensity versus concentration (ng/ml) to measure chlorin e6 by the above-proposed method. The calibration graph of chlorin e6 in ACN was represented in **Figure 2.3**. The graph was found to be linear over the concentration of chlorin e6. The analytical performance data for the spectrofluorimetric determination of chlorin e6 is illustrated in **Table 2.1.**
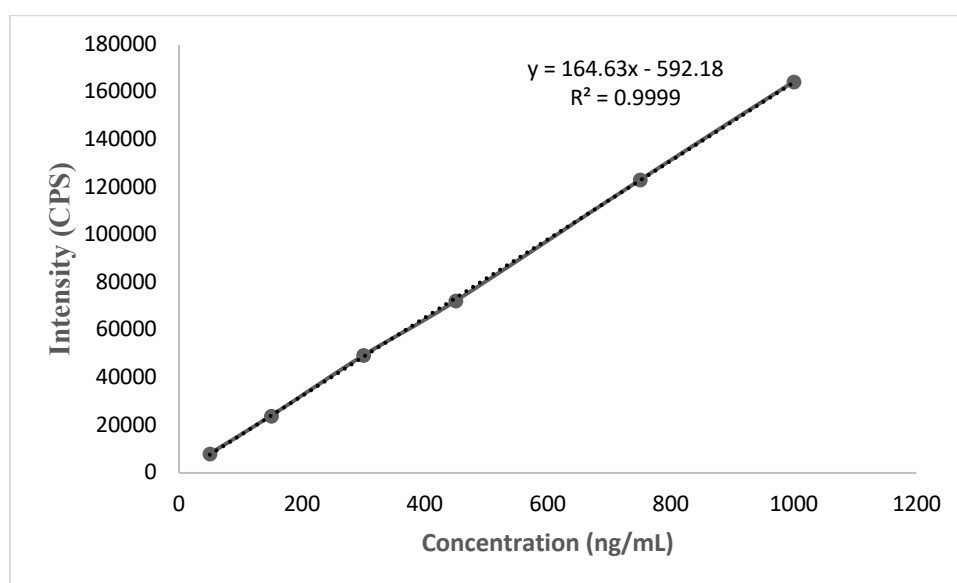
Figure 2.3. Linearity plot of chlorin e6

2.1.5.3. Limit of the detection (LOD) and limit of quantification (LOQ)

The determination of LOQ and LOD followed the equations recommended by the ICH guidelines, resulting in values of 29.53 ng/ml and 8.85 ng/ml, respectively. Also, the results have been represented in **Table 2.1**.

Table 2.1. Analytical performance data for spectrofluorimetric determination of chlorin e6

Analytical performance data for spectrofluorimetric determination of chlorin e6	
Parameters	**Results**
Wavelength (nm) (λex /λem)	400/665
Linearity range (ng/ml)	50-1000
Intercept (a)	592.18
Slope (b)	164.63
Correlation coefficient (R^2)	0.999
LOD (ng/ml)	8.85
LOQ (ng/ml)	29.53
Slit width (nm)	1

2.1.5.4. Precision and accuracy

To assess the precision of the proposed method, a series of measurements were conducted, and the intra-day precision was evaluated by measuring QC samples of chlorin e6 on the same day, but on three separate occasions. The inter-day precision was determined by measuring the QC samples of chlorin e6 on three consecutive days. The intra-day precision, expressed as the % RSD, for the three QC samples of chlorin e6 (LQC - 75 ng/ml, MQC - 500 ng/ml, HQC - 900 ng/ml), ranged from 0.1632 to 1.866. Similarly, the inter-day precision, expressed as % RSD, for the QC samples of chlorin e6 ranged from 0.1119 to 0.9444. The intra-day and inter-day precision results are illustrated in **Table 2.2.** Moreover, the accuracy (% Bias) of chlorin e6 in the QC samples was observed to range from -0.5813 to 1.9686. These findings confirm that the variation associated with the QC samples falls within the acceptable limits, as per the guidelines. The results of the accuracy (% Bias) of this method are represented in **Table 2.3.**

Table 2.2. Intra-day precision and inter-day precision results of the chlorin e6 at quality control samples of the calibration range (n=9)

Analyte	Level	Nominal concentration (ng/ml)	Precision (% RSD)	
			Intra-day	Inter-day
Chlorin e6	LQC	75	1.8862	0.9444
	MQC	500	0.1632	0.2674
	HQC	900	0.1977	0.1119

Table 2.3. Accuracy (% bias) results of the chlorin e6 at the quality control samples of the calibration range

Concentration taken (ng/ml)	Concentration found (ng/ml)	% Recovery ± SD	Accuracy (% Bias)
75 (LQC)	75.43597	100.58 ± 0.71	-0.5813
500 (MQC)	490.1567	98.03 ± 1.31	1.9686
900 (HQC)	907.6909	100.85 ± 1.01	-0.8545

2.2. Analytical method development of Itraconazole by using High performance of liquid chromatography

2.2.1. Chromatographic Conditions

Using the Shimadzu HPLC system equipped with a photodiode array (PDA) detector (SPD-M20A), binary pump (LC-20AD), and autosampler (SIL-HTC, Shimadzu, Japan), a method with high sensitivity, accuracy, and reliability was developed for Itraconazole (ITZ). Method development was performed with an isocratic elution mode. The mobile phase used in the analysis comprised a blend of HPLC-grade acetonitrile and milli-Q water (pH 2.6, adjusted with trifluoroacetic acid). Prior to analysis, the mobile phase underwent filtration using a 0.22 µm membrane filter with a vacuum filtering assembly and was subsequently subjected to 30 minutes of bath sonication. During the analysis, the mobile phase was maintained at a flow rate of 1 ml/min, the column oven temperature was carefully controlled at 30 ± 0.2 °C, and a sample injection volume of 20 µl was used. The chromatographic separation was conducted using the Supeleco Discovery® C18 column (5 µm, 4.6 × 250 mm). **Table 2.4** provides the chromatographic conditions for all the methods used in the analytical determination of drug quantities permeated in deeper skin layers. The analysis was carried out utilizing LC Solution software. The HPLC system was primarily equilibrated for 30 min followed by an analysis of the samples.

2.2.2. Preparation of stock solutions, calibration curve standards, and quality control samples

The stock solutions was prepared for ITZ (1000 µg/ml), weighed an accurate amount of ITZ, and transferred into the Eppendorf tube containing methanol. To prepare a secondary stock solution with a concentration of 100 µg/ml, the stock solution was diluted using the mobile phase as the solvent. Subsequently, additional calibration curve samples were generated from the aforementioned stock solution within the range of 100-10000 ng/ml. Furthermore, using the aforementioned stock solution, low-quality control (LQC) samples were prepared at a concentration of 250 ng/ml, medium-quality control (MQC) samples at 5000 ng/ml, and high-quality control (HQC) samples at 9000 ng/ml, representing three distinct concentration levels.

2.2.3. Assay validation procedures

The validation of the HPLC method developed for the detection and quantification of ITZ was conducted in accordance with the guidelines provided by the International Council for Harmonisation (ICH).The following parameter was included such as specificity, linearity range, accuracy, precision, robustness, etc [9].

2.2.3.1. System Suitability

A system suitability test is preferred to assess the performance of the system for the intended application. In order to evaluate repeatability, retention time, resolution, column efficiency, tailing factor, and peak area, six injections of the same concentration were made. These parameters were employed to validate the overall performance of the chromatography system. To evaluate system suitability, the following criteria were considered: a relative standard deviation (RSD) of ≤ 2% for both peak area and retention time, a resolution greater than 2, a tailing factor below 2, and a theoretical plate count exceeding 3000 for both drugs [10].

2.2.3.2. Linearity and Range

ITZ weighed accurately and prepared in the primary stock solution (1 mg/ml). From the above stock solution working standard solutions were prepared. Linearity was evaluated by analyzing a concentration range of 100 to 10000 ng/ml, using seven calibration standards with three replicates of each concentration. The obtained data were plotted with the peak area of each standard versus the concentration of standard samples.

2.2.3.3. Limit of detection and limit of quantification

The estimation of the limit of detection (LOD) and limit of quantification (LOQ) was performed using the signal-to-noise ratio. The limit of detection (LOD) is defined as the minimum analyte concentration at which the signal-to-noise ratio should exceed 3. LOQ is the lowest concentration of analyte at which the signal-to-noise ratio should be more than 10. Furthermore, the analyte can be quantified with satisfactory accuracy and precision. The calculations for the limit of detection (LOD) and limit of quantification (LOQ) were performed using the formula specified in section 2.1.4.2.

2.2.3.4. Precision and Accuracy

Precision and accuracy were assessed by analyzing the quality control (QC) samples at three different concentrations: LQC (250 ng/ml), MQC (5000 ng/ml), and HQC (9000 ng/ml), for both intra-day and inter-day variations. The intraday precision and accuracy were performed by analyzing QC samples on the same day in six replicates for inter-day precision and accuracy by analyzing the QC samples for three successive days in six replicates. According to the guidelines, the precision and accuracy of the developed method of ITZ were calculated by the % RSD and % bias, respectively, with accepted criteria RSD ≤ 2 and $\leq 10\%$, respectively.

2.2.4. **Result and Discussion**

A systematic strategy was applied to develop analytical procedures using current knowledge in order to achieve optimal chromatographic conditions for the quantification of ITZ. Sample preparation and analysis special precautions were conducted. To prevent light exposure, the samples were processed in amber-colored tubes that were mainly enclosed with aluminum foil. During the development of the method, a systematic approach was employed to select the optimal chromatographic parameters, including the mobile phase (pH and polarity), stationary phase (column), flow rate, column oven temperature, and injection volume. These parameters were carefully chosen to ensure the attainment of desirable peak intensity.Initially, the organic phase (ACN and methanol) was used with other aqueous phases (buffer: sodium acetate, ammonium acetate) in an altered ratio. After a series of optimizations, the mobile phase consists of HPLC grade acetonitrile and milli-Q water (pH 2.6, adjusted with TFA (0.01 %) was chosen as the mobile phase because it produced symmetrical peak shapes and high peak intensities. C-18 column (5μm particle size, 150 mm × 4.6 mm) with mobile phase ACN: Milli Q water containing TFA (0.01 %) in the ratio of (45:55 v/v) at a 1 ml/min was finally chosen for the analysis of ITZ. HPLC-based analytical method for the quantification of ITZ was successfully developed (**Table 2.4**) wherein ITZ showed a retention time (Rt) of 8.2 min, as shown in **Figure. 2.4.** represents the HPLC chromatogram of Blank A) overlay of LQC, MQC, and HQC B).

Table 2.4 Chromatographic condition of ITZ in HPLC method

Stationary phase (Column)	C-18 column (5μm particle size, 250 mm × 4.6 mm)
Mobile phase	ACN: water (0.1% TFA) pH-2.6 (45:55% v/v)
Retention time (RT)	8.2 min

Flow rate	1 ml/min
Wavelength (λmax)	261 nm
Column temperature	30 ℃
Injection volume	20 μl
Run time	10 min
Linearity range	100-10000 ng/ml
LOD	56.35
LOQ	170.76
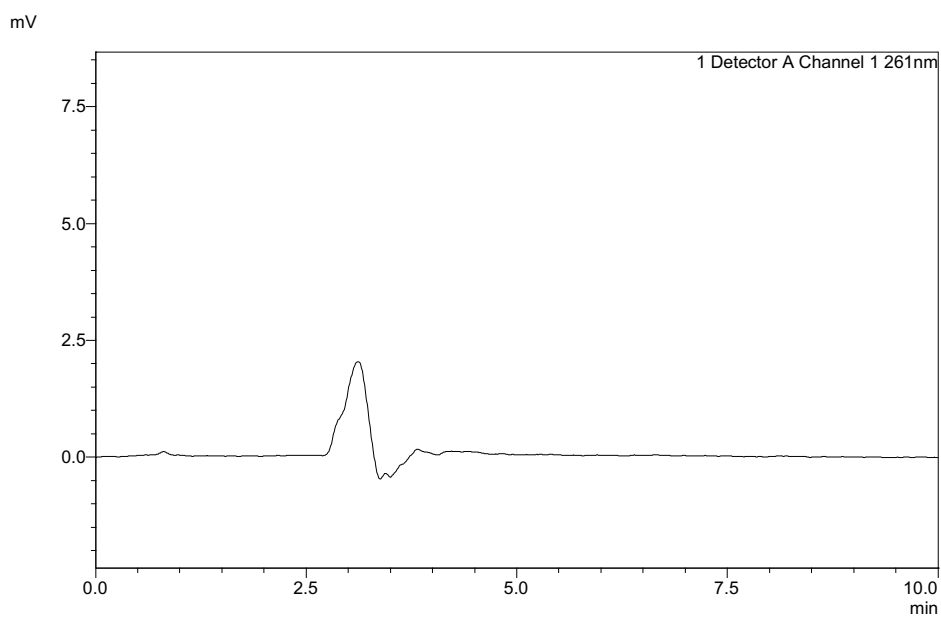
Figure 2.4 A Blank
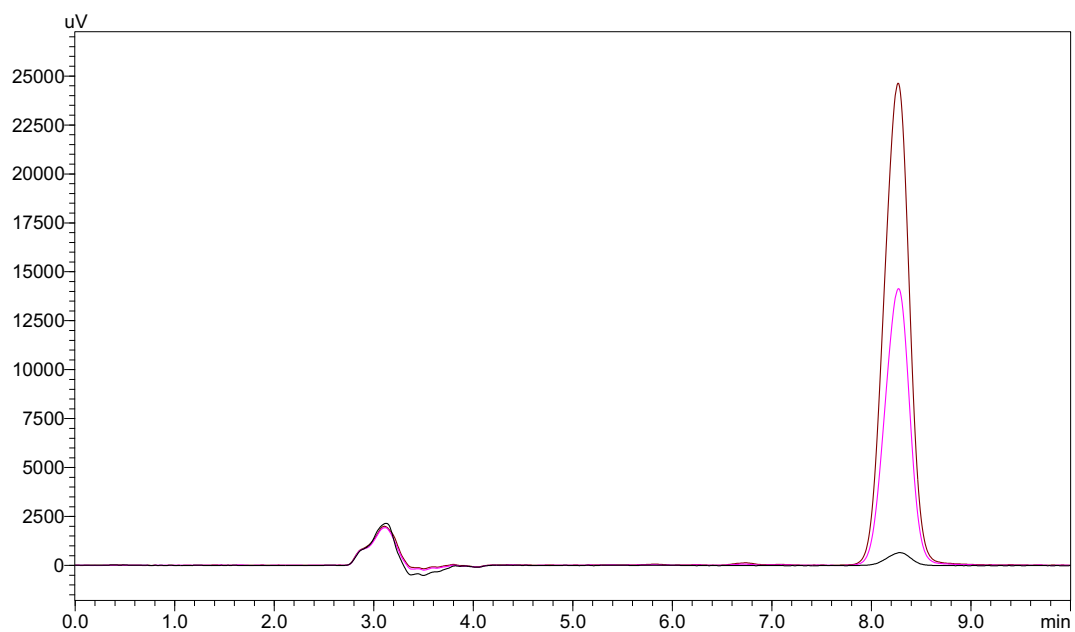
Figure 2.4 B Overlay of LQC (250 ng/ml), MQC (5000 ng/ml) and HQC (9000 ng/ml)

2.2.4.1. Assay Validation

In accordance with the ICH guidelines, the method validation encompassed multiple parameters such as accuracy, precision, specificity, and system suitability.

2.2.4.2. System suitability

The system suitability test confirmed the proper functioning of the system, demonstrating reproducibility and accurate resolution. The test was performed in the six replicates at the concentration of 1000 ng/ml. The percent RSD for the peak area and retention time were within acceptable limits (RSD ± 2%). Peak tailing was found to be for ITZ at 0.794 ±0.01. Theoretical plates were found to be for ITZ in 41021 ± 5.11 **(Table 2.5).**

Table 2.5. System suitable parameters of validated method of itraconazole.

Analytes	Conc (ng/ml)	Retention Time (tr-min)	Tailing factor (T)	HETP (mm)	Theoretical plate (N)
Itraconazole	1000	8.2 ± 0.01	0.794 ±0.01	40.18 ± 0.12	41021 ± 5.11

2.2.4.3. Linearity, Limit of detection, and limit of quantification

Six calibration curves were being used to assess linearity at seven different concentrations (100, 500, 2000, , 4000, 6000, 8000, 10000 ng/ml). The calibration standard curve for ITZ was observed to be reproducible and exhibited linearity across the concentration range of 100 ng/ml to 10000 ng/ml. The coefficient of determination (R^2) was found to be more than 0.999 for ITZ. The linear regression equation for ITZ was calculated as y = 42.37 x + 4682.60. Additionally, the limit of detection (LOD) and limit of quantification (LOQ) for chlorin e6 were found to be 20 ng/ml and 61.64 ng/ml, respectively. For curcumin, LOD and LOQ were found to be 56.35 ng/ml and 170.76 ng/ml respectively. **(Figure 2.5)** represents the linearity graph of ITZ.
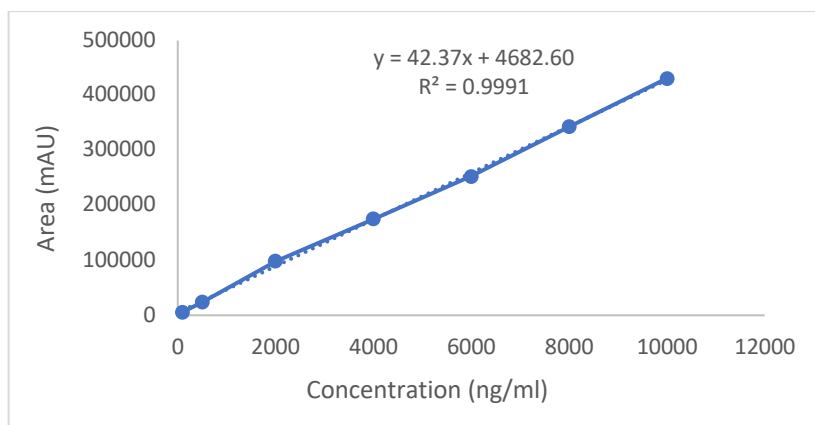
Figure 2.5. Represents the linearity graph of ITZ.

2.2.4.4. Accuracy and Precision

For interday and intra-day precision and accuracy studies, six different triplicates were examined for QC samples (LQC, MQC, and HQC). The percent recovery of ITZ in QC samples was used to evaluate accuracy. % RSD values of ITZ in QC samples were used to evaluate the precision. The deviation of inter-day and intra-day precision was found to be in the range of acceptable limits for ITZ ≤ 1.8221. However, accuracy (% bias) was found to be within the acceptable limits, for ITZ was found to be in the range of -1.0346 to 19459. Based on the obtained data, it was confirmed that all the values of accuracy and precision were in the acceptable ranges for ITZ as per standard guidelines. **Table 2.6.** indicates the accuracy and precision data.

Table 2.6. Accuracy and precision data of intraday and interday analysis of quality control samples (n=6).

Analytes	Levels (ng /ml)	Intraday			Interday		
		Measured concentration (mean ± SD, ng/ml)	Precision (% RSD)	Accuracy (%bias)	Measured concentration (mean ± SD, ng/ml)	Precision (% RSD)	Accuracy (% bias)
Itraconazole	LQC (250)	253.06 ± 1.29	0.5128	1.2245	254.35 ± 2.60	1.0251	1.7406
	MQC (5000)	5097.3 ± 3.60	0.0707	1.9459	5095.2 ± 7.04	0.1383	1.9050
	HQC (9000)	9051.8 ± 15.0	0.1665	0.5750	8906.8 ± 162.2	1.8221	-1.0346

2.3. Simultaneous analytical method development of Chlorin e6 and Curcumin by using High performance of liquid chromatography

The simultaneous method enables researchers in academia and industry to analyze multiple drugs in a single formulation efficiently, saving time and resources, thus facilitating cost-effective research. Based on the available literature data, there are no existing reports on a simultaneous HPLC method for the estimation of chlorin e6 and curcumin in nanocarrier-based topical formulations. For such novel dual-drug loaded formulations analysis, there is the current demand for a simultaneous high-performance liquid chromatography (HPLC) quantification technique which can be applied for the estimation of chlorin e6 and curcumin for the routine analysis of preformulation samples, drug loading, in-vitro studies, and ex-vivo studies.

There are challenges such as resolution, retention time, sensitivity and mobile phase selection, etc, in the quantification of both drugs in combination at various stages of method development [12]. However, for the analysis of chlorin e6 with other molecules, few HPLC techniques have been reported in conventional formulations. Isakau et al. have conducted a study using gradient-type HPLC to analyze chlorin e6 and its molecular complex with polyvinylpyrrolidone. The study showed sensitivity ranging from 1-100 µg/ml, but its applicability was limited. [13]. Kostryukova et.al. have reported the HPLC studies of chlorin e6 from plant phospholipids, which showed a linearity range from 5-50 µg/ml [14]. Li et. al. reported the HPLC method for the quantification of novel photosensitizer (Chlorin e6-C15-monomethyl ester) in beagle dog plasma. However, the reported methods have less sensitivity, high concentration of organic solvent in the mobile phase, and have poor resolution. Thus, specific methods pertaining to the quantification of chlorin e6 for the determination of entrapment efficiency and drug release study has not been reported to date [15].

Some HPLC techniques for determining curcumin with other molecules in bulk and other formulations have been published. Panigrahi et. al. reported the HPLC method for the determination of curcumin from nanoparticulate formulations. In the reported method, the analysis was completed within a run time of 20 minutes, using a flow rate of 1 ml/min [16]. A study conducted by Syed et al. involved the development of HPLC and UV methods for the quantitative determination of curcumin in both the extract of Curcuma longa and its formulation. The developed method exhibited linearity within the range of 2-200 µg/ml [17]. In a study conducted by Santos et al., an HPLC method was developed for the analysis of in-

situ gelling curcumin-loaded nanocrystals. The method demonstrated a linearity range of 0.5-75 μg/ml [18]. The most reported method of curcumin has shown certain limitations such as complex mobile phase, low sensitivity, purity of target peak, long run time, and restricted applicability. When there are a significant number of samples and extended run time it leads to time-consuming and non-economic for routine analysis in the laboratory. [17–21]. Moreover, it should be noted that the aforementioned methods have not been evaluated or validated in the presence of chlorin e6 and its combinational formulations. According to available literature data, there is a lack of an effective and significant simultaneous analytical method for accurately estimating chlorin e6 and curcumin in their co-loaded lipid formulations.

2.3.1. **Materials:**

The curcumin used in the study was obtained from Sigma-Aldrich chemicals, located in St. Louis, MO, United States. Chlorin e6 (purity ≥99%, HPLC) was procured from Cayman chemicals company, USA. Precirol ATO and Compritol ATO-888, which are solid lipids, were generously provided as gift samples by Gattefosse, a company based in France. Campul MCM C8 was obtained as a gift sample from Abitech corporation. Polysorbate 80 was purchased from Sigma Aldrich, India, while all solvents and excipients used in the experiment were of analytical grade. Thermo scientific (Eco pH meter) was utilized for measuring pH.

2.3.2. **Methods:**
2.3.3. Selection of wavelength (Isosbestic point)

Separate primary stock solutions were prepared for chlorin e6 and curcumin at a concentration of 1000 μg/ml. Using a combination of acetonitrile and methanol in a 1:1 ratio as diluting solvents, a secondary stock solution at a concentration of 100 μg/ml was prepared for both chlorin e6 and curcumin from the previously mentioned stock solution. To obtain the ultraviolet-visible spectrum, 10 μg/ml solutions of both chlorin e6 and curcumin were prepared using the previously mentioned stock solution. Aliquots of both samples were analyzed through UV spectrophotometer. Each sample (10 μg/ml) was taken in quartz cuvettes and scanned from 200–800 nm to detect the higher absorption point (λmax). Furthermore, the isosbestic wavelength with maximal absorption of chlorin e6 and curcumin was determined using a merged overlay of UV absorption spectra of both drugs. **Figure 2.6** Schematic representation of the isosbestic point of chlorin e6 and curcumin. Lambda maximum (λmax chlorin e6 (400 nm), λmax curcumin (425 nm), and Isosbestic point of both drugs is 412 nm).
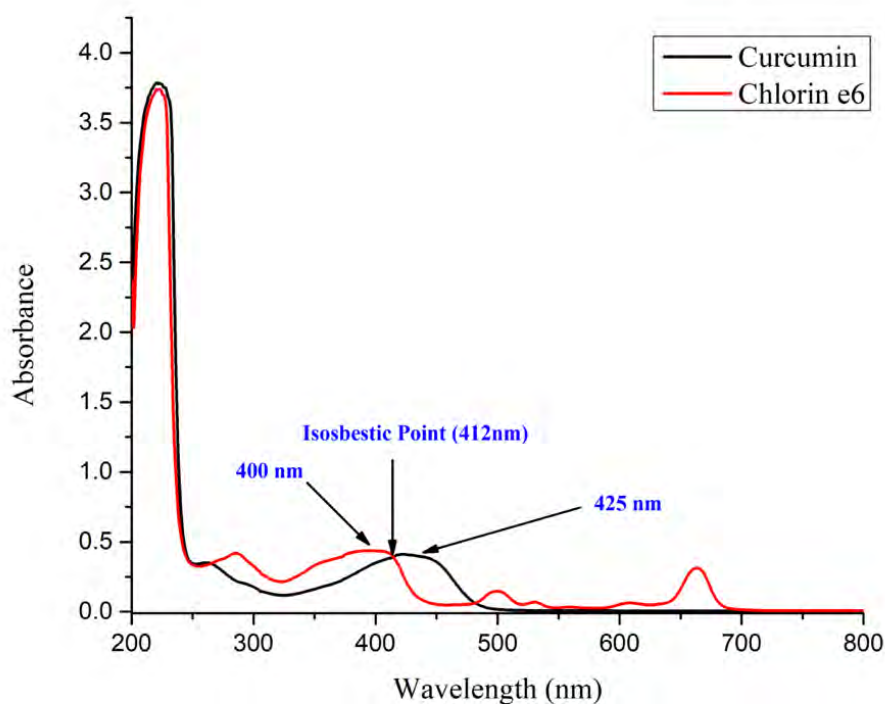
Figure 2.6. Schematic representation of the isosbestic point of chlorin e6 and curcumin. Lambda maximum (λmax chlorin e6 (400 nm), λmax curcumin (425 nm), and Isosbestic point of both drugs is 412 nm)

2.3.4. Instrumentations

Shimadzu HPLC with autosampler mode (UFLC LC-20AD liquid chromatograph- DGU-20A5R) with a two-channel UV detector was utilized for the development of the analytical method. LC solution software was used throughout the experiment. The column oven temperature was maintained throughout the study by using the oven (CTO-10AS VP). All the drug samples and standards were weighted on the sensitive calibrated weighing balance (Denver Instrument TB-215D).

2.3.5. Chromatographic conditions

C-18 column (5μm particle size, 150 mm × 4.6 mm) was used for the simultaneous separation of chlorin e6 and curcumin. Method development was performed with an isocratic elution mode. The mobile phase used in the analysis was prepared by combining HPLC grade acetonitrile and milli-Q water, adjusted to a pH of 2.6 with trifluoracetic acid. Prior to analysis, the mobile phase underwent filtration using a vacuum filtering assembly equipped with a 0.22

µm membrane filter. Subsequently, it was subjected to a 30-minute bath sonication. The mobile phase was delivered at a flow rate of 1 ml/min, while the column oven temperature was maintained at 30 ± 0.2 °C. For each injection, a sample volume of 20 µl was used. The HPLC system was equilibrated for around 30 minutes before the samples were analyzed. Prior to optimizing the chromatographic parameters of the method, multiple trials were conducted, involving adjustments to the mobile phase composition, flow rate, column selection, and column oven temperature conditions. These adjustments were made to achieve the desired levels of purity and sensitivity.

2.3.6. Preparation of stock solutions, calibration curve standards, and quality control samples

Accurate amounts of chlorin e6 and curcumin were weighed and then transferred into separate eppendorf tubes containing acetonitrile and methanol to prepare individual stock solutions with a concentration of 1000 µg/ml. Using the mobile phase as the diluting solvent, a secondary stock solution with a concentration of 100 µg/ml was prepared for both drugs from the original stock solution. Subsequently, calibration curve samples spanning the range of 100-10000 ng/ml were prepared from the aforementioned stock solution. Furthermore, utilizing the aforementioned stock solution, samples for low-quality control (LQC) at a concentration of 250 ng/ml, medium-quality control (MQC) at 5000 ng/ml, and high-quality control (HQC) at 9000 ng/ml were prepared at three distinct concentration levels.

2.3.7. Assay validation procedures

The validation of the developed HPLC method for the simultaneous detection and quantification of chlorin e6 and curcumin was conducted in accordance with the guidelines provided by the International Council for Harmonisation (ICH).The following parameters were included such as specificity, linearity range, accuracy, precision, robustness, etc [9].

2.3.7.1. System Suitability

For evaluating the suitability of the system for the desired application, it is preferable to conduct a system suitability test. To evaluate repeatability, retention time, resolution, column efficiency, tailing factor, and peak area, six injections of the same concentration were performed and analyzed. These parameters were employed to validate the overall performance of the chromatography system. In order to evaluate system suitability, the following criteria were applied: a relative standard deviation (RSD) of ≤ 2% for both peak area and retention time, a

resolution greater than 2, a tailing factor below 2, and a theoretical plate count exceeding 3000 for both drugs [10].

2.3.7.2. Linearity and Range

Accurate weighing was performed for chlorin e6 and curcumin, followed by their preparation in a primary stock solution with a concentration of 1 mg/ml.

Working standard solutions were prepared from the above stock solution. To assess linearity, seven calibration standards were prepared with a concentration range of 100 to 10000 ng/ml, with each concentration being analyzed in triplicate. The data obtained were graphically represented by plotting the peak area of each standard against its corresponding concentration.

2.3.7.3. Limit of detection and limit of quantification

The signal-to-noise ratio was employed to determine the limit of detection (LOD) and limit of quantification (LOQ). The limit of detection (LOD) refers to the minimum concentration of the analyte at which the signal-to-noise ratio must exceed 3. The limit of quantification (LOQ) represents the lowest analyte concentration at which the signal-to-noise ratio must exceed 10. Furthermore, the analyte can be quantified with a satisfactory level of accuracy and precision [11]. The calculations for the limit of detection (LOD) and limit of quantification (LOQ) were performed using the formula specified in section 2.1.4.2.

2.3.7.4. Precision and Accuracy

Precision and accuracy were evaluated by analyzing quality control (QC) samples at three different concentrations: LQC (250 ng/ml), MQC (5000 ng/ml), and HQC (9000 ng/ml), for both intra-day and inter-day variations. The intraday precision and accuracy were assessed by analyzing the quality control (QC) samples, with six replicates performed on the same day. The inter-day precision and accuracy were evaluated by analyzing the quality control (QC) samples with six replicates conducted over three consecutive days. According to the guidelines, the precision and accuracy of the developed method of chlorin e6 and curcumin were calculated by the % RSD and % bias, respectively, with accepted criteria RSD ≤ 2 and $\leq 10\%$, respectively.

2.3.7.5. Specificity

During the specificity analysis, the interface between formulation excipients and degradants was assessed. Chlorin e6 and curcumin were detected and quantified in the lipidic nanoparticles, along with the interface between campul MCM C8 and precirol ATO chromatograph was identified. Additionally, a developed method of chlorin e6 and curcumin was also utilized to determine the force degradation study of chlorin e6 and curcumin. In the force degradation study, analytes were degraded by utilizing the acid, base, hydrogen peroxide (H2O2), and UV. After the treatment of the above procedure, samples were examined for the degradation peak and % recovery. In the acid treatment, 0.1 N HCL was used to expose the chlorin e6 and curcumin analyte. Moreover, solutions of chlorin e6 and curcumin at a concentration of 1 µg/ml were prepared by using a diluting solvent composed of a mixture of ACN (acetonitrile) and methanol. These solutions were subsequently added to a solution of 0.1 N HCl. The acidic mixtures of analyte were heated up to 2 h at 60^0 C. The analyte sample was cooled at room temperature and neutralized to pH 7 with 1 N sodium hydroxide. Finally, the sample volume was adjusted to the desired concentration and subsequently passed through a 0.22 µm syringe filter to ensure proper filtration prior to injection into the system. In the basic degradation, 0.1 N NaOH was used to expose the chlorin e6 and curcumin analyte. The sample processing was the same as performed in acid hydrolysis. In the oxidative degradation study, 3% H_2O_2 was used to expose the chlorin e6 and curcumin analyte. 1 µg/ ml solutions of chlorin e6 and curcumin were prepared from the primary stock solution by ACN: methanol as diluting solvent and further added into the 3% H_2O_2. The mixtures of analyte were heated up to 2h at 60^0 C. Furthermore, the analyte sample was cooled to room temperature and adjusted to the desired concentration. Prior to injection into the system, it was filtered through a 0.45 µm syringe filter to ensure proper filtration. For the photodegradation study, a UV lamp was used to expose the analyte. 10000 ng/ml solution of chlorin e6 and curcumin was prepared from the primary stock solution by ACN: methanol as diluting solvent. The mixture of analytes was kept in a UV chamber and exposed for 2 h. In the final step, the solution was passed through a 0.45 µm syringe filter to achieve proper filtration, after which it was subsequently injected into the HPLC system [22,23].

2.3.8. **Result and discussion**

A systematic strategy was applied to develop analytical procedures using current knowledge in order to achieve optimal chromatographic conditions for simultaneous quantification of chlorin

e6 and curcumin. Chlorin e6 and curcumin are photosensitive, while sample preparation and analysis special precautions were conducted. To prevent light exposure, the samples were processed in amber-coloured tubes that were mainly enclosed with aluminium foil.

During the development of the simultaneous method, a systematic approach was employed to carefully select the optimal chromatographic parameters, including the mobile phase (pH and polarity), stationary phase (column), flow rate, column oven temperature, and injection volume. The objective was to achieve desirable peak intensities, optimal resolution between both drugs, consistent retention time, and satisfactory recovery. Initially, the organic phase (ACN and methanol) was used with other aqueous phases (buffer: sodium acetate, ammonium acetate) in an altered ratio. Following a series of optimizations, the mobile phase comprising HPLC-grade acetonitrile and milli-Q water, with a pH of 2.6 adjusted using 0.01% TFA (trifluoroacetic acid), was selected. This mobile phase demonstrated symmetrical peak shapes and yielded high peak intensities. For the simultaneous analysis of chlorin e6 and curcumin, a C-18 column with a particle size of 5μm and dimensions of 150 mm × 4.6 mm was selected. The mobile phase consisting of ACN (acetonitrile) and Milli-Q water, containing 0.01% TFA (trifluoroacetic acid), was utilized at a flow rate of 1 ml/min. The mobile phase composition was set to a ratio of 45:55 v/v. The total run time for the estimation of both drugs was set at 15 minutes, with an injection volume of 20 μl. Additionally, the retention times of chlorin e6 and curcumin were 13.5, and 11.7 min, respectively. Both drugs were analyzed at a detection wavelength of 412 nm. **Table 2.7.** represents the liquid chromatographic condition. **Figure 2.7.** represents the HPLC chromatogram of chlorin e6 and curcumin A); Overlay with Blank LQC, MQC, and HQC B).
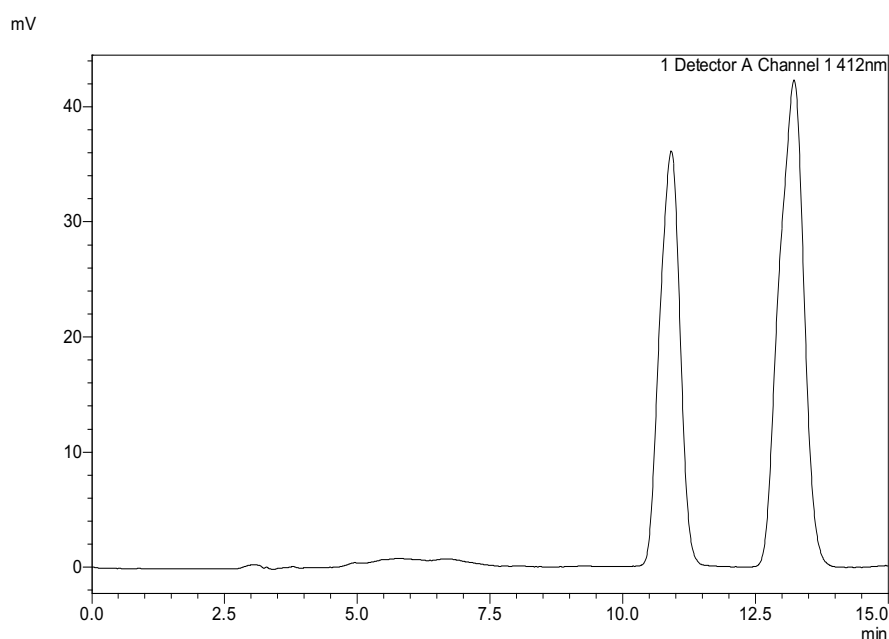
Figure 2.7. (A) represents the HPLC chromatogram of chlorin e6 and curcumin (Chlorin e6 RT- 13.52 and Curcumin RT- 11.3)
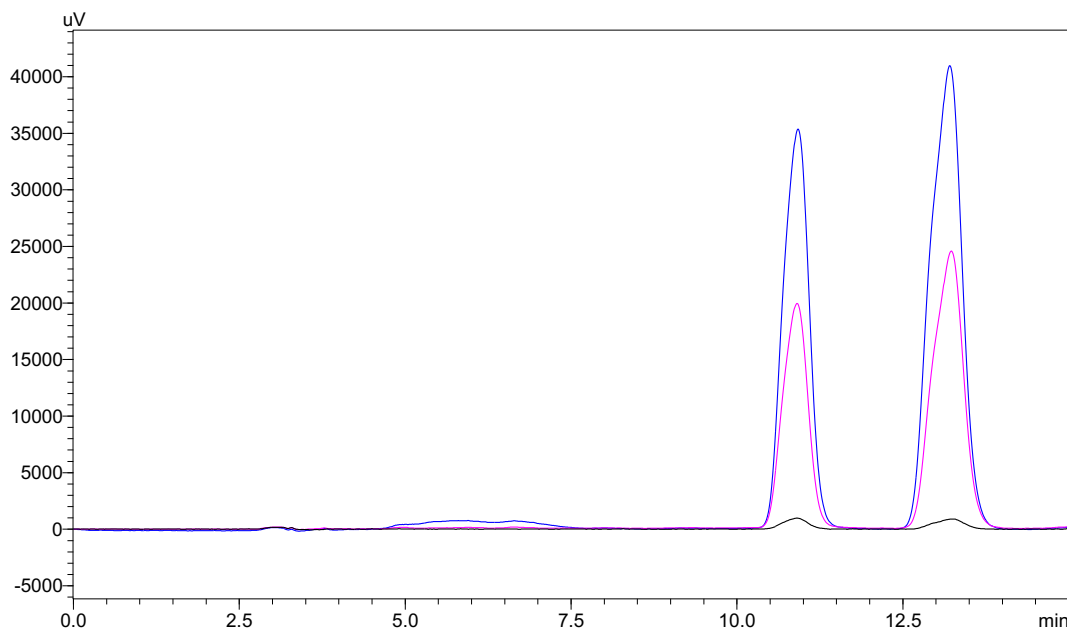
Figure 2.7. B) Overlay of LQC (250 ng/ml), MQC (5000 ng/ml) and HQC (9000 ng/ml).

Table 2.7. Chromatographic conditions for the curcumin and chlorin e6 analytical method

Stationary phase (Column)	C-18 column (5μm particle size ODS, 150 mm × 4.6 mm)
Mobile phase	ACN: water (0.1% TFA) pH-2.6 (45:55% v/v)
Retention time (RT)	13.52 for Chlorin e6, 11.3 for Curcumin
Flow rate	1 ml/ min
λmax	412 nm for both drugs
Column temperature	30 °C
Injection volume	20 μl

2.3.9. Validation of method

2.3.9.1. System suitability

Through the performance of the system suitability test, it was verified that the system operated effectively, displaying reproducibility and accurate resolution. The system suitability test was conducted by analyzing six replicates of samples at a concentration of 1000 ng/ml for both analytes. The percent relative standard deviation (RSD) for the peak area and retention time of both analytes remained within acceptable limits (RSD ± 2%). Peak tailing was found to be 0.98

and 0.89 for chlorin e6 and curcumin, respectively. Theoretical plates for chlorin e6 and curcumin were 4028 ± 21.37, and 4116 ± 4.04, respectively. **(Table 2.8)**

Table 2.8 System suitable parameters of validated method of chlorine e6 and curcumin.

Analytes	Conc (ng/ml)	Retention Time (tr-min)	Peak resolution (R)	Tailing factor (T)	HETP (mm)	Theoretical plate (N)
Chlorin e6	1000	13.52 ± 0.00	-	0.985 ±0.00	37.08 ± 0.10	4028 ± 21.37
Curcumin	1000	11.32 ± 0.01	3.012 ± 0.01	0.894 ±0.00	36.18 ± 0.19	4116 ± 4.04

2.3.10. Linearity, Limit of detection, and limit of quantification

Linearity assessment was performed using six calibration curves with seven different concentrations (100, 500, 2000, 4000, 6000, 8000, and 10000 ng/ml).

The calibration standard curve demonstrated both reproducibility and linearity over the concentration range of 100 ng/ml to 10000 ng/ml for both drugs. For both drugs, the coefficient of determination (R^2) was determined to exceed 0.999, indicating a high degree of correlation in the calibration curves. The linear regression equation for chlorin e6 was determined as y = 172.9 x – 3930, while for curcumin, it was y = 105.06 x + 279.86. The limit of detection (LOD) for chlorin e6 was established at 20 ng/ml, with a limit of quantification (LOQ) of 61.64 ng/ml. In the case of curcumin, the LOD was found to be 29.4 ng/ml, with an LOQ of 89.20 ng/ml.

2.3.11. Precision and Accuracy

For interday and intra-day precision and accuracy studies, six different triplicates were examined for QC samples (LQC, MQC, and HQC). The percent recovery of chlorin e6 and curcumin in QC samples were used to evaluate accuracy. % RSD values of chlorin e6 and curcumin in QC samples were used to evaluate the precision. The deviation of inter-day and intra-day precision was found to be in the range of acceptable limit for chlorin e6 ≤ 0.8442 and ≤ 0.8140. The deviation of inter-day and intra-day precision was found to be for curcumin ≤ 1.2867 and ≤ 1.6050. Accuracy (% bias) was found to be within the acceptable limits, for chlorin e6 found to be in the range of -1.2842 to 1.6552. Curcumin accuracy (% bias) was found to be in the range of 0.1075 to -2.2525. Based on the obtained data, it was confirmed that all the values of accuracy and precision were in the acceptable ranges (write range) for both

drugs as per standard guidelines. In HPLC method validation, it is generally accepted that precision should meet a criterion of %RSD ≤2%, while accuracy criteria should be less than 10%. **Table 2.9** indicates the accuracy and precision of data.

Table 2.9. Intra-day and interday analysis of accuracy and precision (n=6) of quality control samples

Analytes	Levels (ng /ml)	Interday			Intraday		
		Measured concentration (mean ± SD, ng/ml)	Precision (% RSD)	Accuracy (% bias)	Measured concentration (mean ± SD, ng/ml)	Precision (% RSD)	Accuracy (%bias)
Chlorin e6	LQC (250)	245.95 ± 2.07	0.8442	-1.6178	246.01 ± 2.00	0.8140	-1.5921
	MQC (5000)	4935.78 ± 3.92	0.0795	-1.2842	4930.24 ± 11.65	0.2368	-1.3951
	HQC (9000)	9148.97 ± 31.64	0.3477	1.6552	9148.97 ± 31.64	0.3477	1.6552
Curcumin	LQC (250)	243.83 ±3.13	1.2867	-2.4640	244 ± 3.92	1.6050	-2.2525
	MQC (5000)	4925.65 ± 17.16	0.3487	-1.4869	4931 ± 19.34	0.3926	-1.3600
	HQC (9000)	9008 ± 12.42	0.1373	0.0982	9009 ± 56.73	0.6298	0.1075

2.3.12. Specificity

To evaluate the specificity of the method, both drugs were exposed to different conditions. Specificity was also performed with formulations excipients. There was no extra peak observed, and no changes in the retention time were observed by comparing the blank mobile phase chromatogram. This demonstrates the specificity achieved through the development of the simultaneous method. The force degradation studies involved subjecting the analytes to various conditions such as acid, base, UV, and H_2O_2. The results obtained from the stress study are presented in **Table 2.10**. In the acid hydrolysis, chlorin e6 and curcumin were degraded by 15.3 % and 4.3 %, respectively. Additionally, in the chromatogram of acid hydrolysis, the degradant peak was observed at 7.6 and 16.8 min. In basic condition (0.1 N NaOH) at 60 ℃ for 30 min., chlorin e6 and curcumin showed degradations by 65.13 % and 74.5 %, respectively. In the chromatogram of basic condition, the degradant peak was observed at 3.4, 4.2, 5.2, and

16.2 min. In the oxidation stress condition, chlorin e6 and curcumin showed degradation by 19.2 % and 3.8 %. In the photodegradation study by the UV, both drugs showed degradation by more than 50 % within 2 h. Thus, it also indicates that both drugs are photosensitive. The developed method was confirmed to be selective and specific in forced degradation conditions, illustrating that it can identify and discriminate impurity peaks in the sample matrix. **(Figure 2.8)**

Table 2.10. % Degradation and impurities retention time of chlorin e6 and curcumin

Force degradation studies	Degradant peak observed at retention time (min)	% Degradation of Chlorin e6	% Degradation of Curcumin
Acid hydrolysis (0.1 N HCl)	7.6, 16.8	15.9	4.3
Base hydrolysis (0.1 N NaOH)	3.4, 4.2, 5.2, 16.2	74.5	65.13
Oxidation (H$_2$O$_2$)	-	19.2	3.8
Ultra-violet light	-	59	52
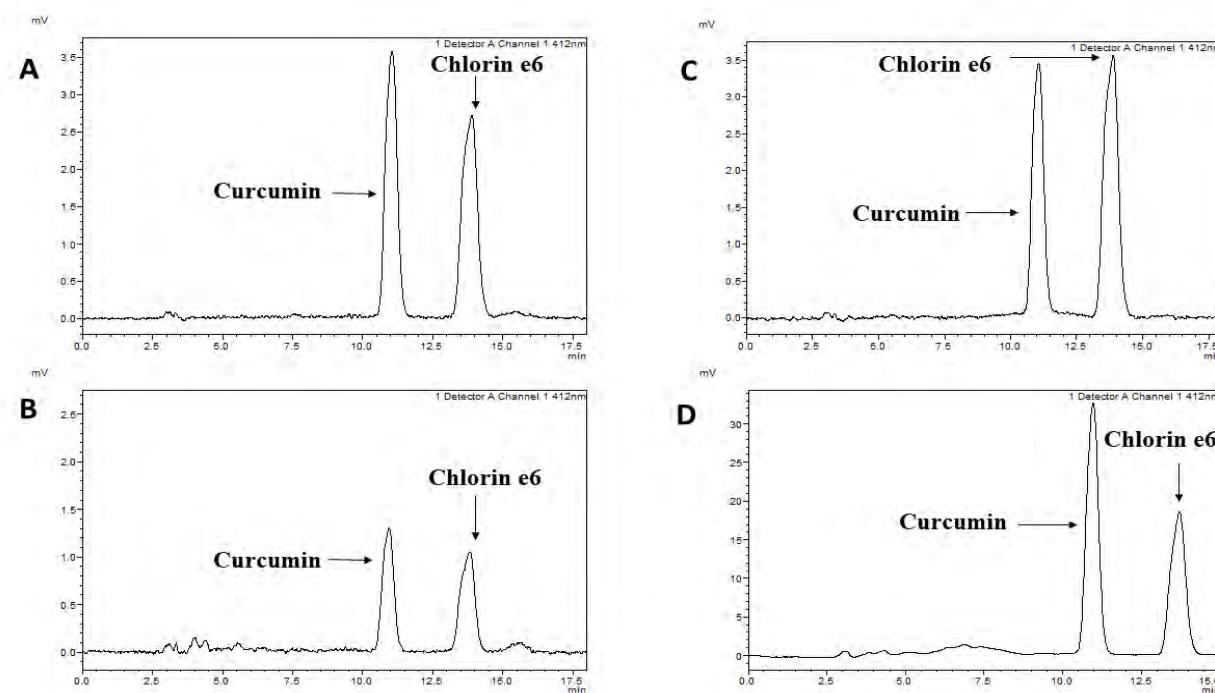
Figure 2.8. Chromatogram of chlorin e6 and curcumin A) 0.1 N HCL for 2h B) 0.1 N NaOH for 2h C) H$_2$O$_2$ exposure D) Light exposer (UV)

2.1.10. Conclusion

The objective of the present study was to develop an analytical method for the analysis of chlorin e6 within its formulation. The spectrofluorimetric method proposed for chlorin e6 in acetonitrile was determined to possess qualities of sensitivity, simplicity, rapidity, and environmental friendliness. Furthermore, a validated reverse-phase HPLC-based analytical method was developed for the analysis of ITZ. The calibration curve depicted the better correlation coefficient and linearity in the concentration range (100-1000 ng/ml) for ITZ in analytical samples. The developed methods could be employed for the determination of ITZ in the samples of drug loading, entrapment efficiency and drug release studies. In addition, a validated HPLC method that is simple, accurate, precise, and cost-effective was developed for the simultaneous detection and quantification of chlorin e6 and curcumin. Upon comparison with previously reported HPLC methods for chlorin e6 and curcumin, the developed and optimized chromatographic conditions were validated in accordance with the ICH Q2 (R1) standards. The results suggest that the optimized chromatographic conditions are economically feasible for regular analysis in laboratory environments. Different retention times were observed for distinct peaks of degradants under various conditions of acid, base, oxidation, and light exposure. The developed and validated method demonstrated successful detection and quantification of chlorin e6, itraconazole, and curcumin within the lipidic nanoparticles. To the best of our knowledge, the developed and validated spectrofluorimetric method and HPLC techniques are deemed suitable for both industry and academia in efficiently and economically estimating the levels of chlorin e6, itraconazole, and curcumin in nanoformulations.

References:

[1]   O. Coskun, Separation techniques: Chromatography, North Clin Istanb. 3 (2016) 156. https://doi.org/10.14744/NCI.2016.32757.

[2]   R. Rina, M. Baile, A. Jain, A multifaceted review journal in the field of pharmacy A Review: Analytical Method Development and Validation, Sys Rev Pharm. 12 (2021) 450–454.

[3]   K.V. Krishna, N. Saha, hydrochloride by a validated HPLC method †, (2018) 24740–24749. https://doi.org/10.1039/c8ra03379j.

[4]   S.K. Dubey, S. Duddelly, H. Jangala, R. Saha, Rapid and sensitive reverse-phase high-performance liquid chromatography method for estimation of ketorolac in pharmaceuticals using weighted regression, Indian J Pharm Sci. 75 (2013) 89–93. https://doi.org/10.4103/0250-474X.113535.

[5]   V. Vihar, Spectrophotometric Determination of Nor-Epinephrine Serotonin Reuptake Inhibitor (SNRI) Drug Milnacipran in Pure and in Dosage Forms, 25 (2013) 3682–3686.

[6]   F. Belal, M.K. Sharaf El-Din, M.M. Tolba, H. Elmansi, Highly sensitive spectrofluorimetric method for the determination of two antimigraine drugs in their tablets and in biological fluids. Application to content uniformity testing, Analytical Methods. 6 (2014) 2621–2627. https://doi.org/10.1039/c3ay41842a.

[7]   G. Balwani, E. Joseph, S. Reddi, V. Nagpal, R.N. Saha, Rapid, simple, and sensitive spectrofluorimetric method for the estimation of ganciclovir in bulk and pharmaceutical formulations, Journal of Spectroscopy. 1 (2013). https://doi.org/10.1155/2013/972806.

[8]   F.A. Aly, N. EL-Enany, H. Elmansi, A. Nabil, A fast spectrofluorimetric method for determination of carbinoxamine maleate in the nano-molar range. Application to pharmaceutical preparations, biological fluids and stability studies, Analytical Methods. 10 (2018) 3851–3858. https://doi.org/10.1039/c8ay01202d.

[9]   ICH harmonised tripartite guideline validation of analytical procedures: text and methodology q2(r1) Retrieved from the International Conference on Harmonisation of Technical Requirements for Registration of Pharmaceuticals for Human Use, (2014). www.somatek.com (accessed May 27, 2022).

[10]   K.V. Krishna, N. Saha, A. Puri, Pre-clinical compartmental pharmacokinetic modeling of 2-[1-hexyloxyethyl]-2-devinyl pyropheophorbide-a (HPPH) as a photosensitizer in rat plasma by validated HPLC method, (2019). https://doi.org/10.1039/c8pp00339d.

[11]   H. Naseef, R. Moqadi, M. Qurt, Development and validation of an HPLC method for determination of antidiabetic drug alogliptin benzoate in bulk and tablets, J Anal Methods Chem. 2018 (2018). https://doi.org/10.1155/2018/1902510.

[12]   A. Nezhadali, M.R. Shapouri, M. Amoli-Diva, A.H. Hooshangi, F. Khodayari, Method development for simultaneous determination of active ingredients in cough and cold pharmaceuticals by high performance liquid chromatography, Heliyon. 5 (2019) e02871. https://doi.org/10.1016/J.HELIYON.2019.E02871.

[13]   H.A. Isakau, T. V. Trukhacheva, A.I. Zhebentyaev, P.T. Petrov, HPLC study of chlorin e6 and its molecular complex with polyvinylpyrrolidone, Biomedical Chromatography. 21 (2007) 318–325. https://doi.org/10.1002/BMC.762.

[14]   L. V. Kostryukova, V.N. Prozorovskiy, N. V. Medvedeva, O.M. Ipatova, Comparison of a new nanoform of the photosensitizer chlorin e6, based on plant phospholipids, with its free form, FEBS Open Bio. 8 (2018) 201. https://doi.org/10.1002/2211-5463.12359.

[15]   X. Li, J. Wen, J. Jiang, X. Zhao, T. Zhou, G. Fan, Quantification of a Novel Photosensitizer of Chlorin e6-C15-Monomethyl Ester in Beagle Dog Plasma Using HPLC: Application to Pharmacokinetic Studies, Molecules : A Journal of Synthetic

Chemistry and Natural Product Chemistry. 22 (2017). https://doi.org/10.3390/MOLECULES22050693.

[16] S. Panigrahi, R. Hirlekar, A NEW STABILITY-INDICATING RP-HPLC METHOD FOR DETERMINATION OF CURCUMIN: AN APPLICATION TO NANOPARTICULATE FORMULATION, Int J Pharm Pharm Sci. 8 (2016) 149–155. https://doi.org/10.22159/IJPPS.2016V8I12.14473.

[17] H.K. Syed, K. Bin Liew, G.O.K. Loh, K.K. Peh, Stability indicating HPLC–UV method for detection of curcumin in Curcuma longa extract and emulsion formulation, Food Chem. 170 (2015) 321–326. https://doi.org/10.1016/J.FOODCHEM.2014.08.066.

[18] B. Fonseca-Santos, M.P.D. Gremião, M. Chorilli, A simple reversed phase high-performance liquid chromatography (HPLC) method for determination of in situ gelling curcumin-loaded liquid crystals in in vitro performance tests, Arabian Journal of Chemistry. 10 (2017) 1029–1037. https://doi.org/10.1016/J.ARABJC.2016.01.014.

[19] R.D. Jangle, B.N. Thorat, Reversed-phase High-performance Liquid Chromatography Method for Analysis of Curcuminoids and Curcuminoid-loaded Liposome Formulation, Indian J Pharm Sci. 75 (2013) 60. https://doi.org/10.4103/0250-474X.113555.

[20] W. Wichitnithad, N. Jongaroonngamsang, S. Pummangura, P. Rojsitthisak, A simple isocratic HPLC method for the simultaneous determination of curcuminoids in commercial turmeric extracts, Phytochemical Analysis. 20 (2009) 314–319. https://doi.org/10.1002/PCA.1129.

[21] G.K. Jayaprakasha, L.J.M. Rao, K.K. Sakariah, Improved HPLC method for the determination of curcumin, demethoxycurcumin, and bisdemethoxycurcumin, J Agric Food Chem. 50 (2002) 3668–3672. https://doi.org/10.1021/JF025506A.

[22] M. Blessy, R.D. Patel, P.N. Prajapati, Y.K. Agrawal, Development of forced degradation and stability indicating studies of drugs—A review, J Pharm Anal. 4 (2014) 159–165. https://doi.org/10.1016/J.JPHA.2013.09.003.

[23] M.R. Peram, S.S. Jalalpure, M.B. Palkar, P. V. Diwan, Stability studies of pure and mixture form of curcuminoids by reverse phase-HPLC method under various experimental stress conditions, Food Sci Biotechnol. 26 (2017) 591. https://doi.org/10.1007/S10068-017-0087-1.

CHAPTER 3

DESIGN AND CHARACTERIZATION OF ITRACONAZOLE AND CHLORIN E6 DUAL-DRUG LOADED LIPIDIC NANOCARRIERS FOR SKIN CANCER TREATMENT

3.1. Introduction

There are various treatment options available for both multiple myeloma (MM) and non-melanoma skin cancer (NMSC), including both surgical and non-surgical procedures. These treatment modalities encompass a range of approaches to address these conditions. [1]. Photodynamic therapy (PDT) is a non-surgical treatment that demonstrates excellent efficacy in targeting a broad region, leading to favourable clinical results. Among these treatment approaches, topical chemotherapy is also a widely used treatment approach due to its cost-effectiveness and convenience. However, problems associated with the above treatment modalities have been the most common choice of treatment, but it has its own disadvantages. However, due to prolonged chemotherapy, and poor penetration of tumours, limited light penetration ability, cells develop drug resistance and, thus, result in unsuccessful therapy. PDT has demonstrated efficacy in the treatment of pre-malignant and malignant NMSC, according to several clinical research studies. However, challenges arise when tumors develop resistance, recurrence, or metastasis, sometimes becoming more aggressive. As a result, there has been a growing emphasis in MM and NMSC research on investigating the synergistic potential of combining photodynamic therapy (PDT) with other treatment modalities to augment its therapeutic efficacy.

Depending on the characteristics and type of the tumor, photodynamic therapy (PDT) can be employed in conjunction with immunomodulatory agents like Imiquimod, as well as chemotherapeutic agents such as 5-fluorouracil, methotrexate, or ingenol mebutate. This combination approach allows for a tailored treatment strategy based on the specific needs of the patient. Additionally, inhibitors targeting molecules involved in the carcinogenic process or pathways, such as COX2 or MAPK inhibitors and Sonic Hedgehog pathway inhibitors, along with surgical techniques and radiotherapy, have been explored as combinational approaches. These innovative approaches present optimistic paths towards improving the prevention and elimination of skin cancer [2]. Research has shown that the hedgehog pathway plays a role in the development of basal cell carcinoma (BCC) and melanoma. [3,4]. One specific mutation in the Hh pathway is responsible for 85% of BCC cases. The initial-stage drug prototype, Cyclopamine, exhibited encouraging results as a hedgehog pathway inhibitor in the treatment of skin cancer, particularly basal cell carcinoma (BCC). However, clinical application of cyclopamine was hindered by its limited solubility and associated toxicity, leading to ineffective results [5].

In recent times, the USFDA has granted approval for vismodegib and sonidegib, which are derived from cyclopamine, for oral administration in the treatment of skin cancer. These approvals signify a significant development in the therapeutic options available for managing skin cancer. However, studies have indicated that oral vismodegib and sonidegib may cause adverse effects such as muscle spasms, alopecia, and weight loss.[6]. Resistance to vismodegib is a significant challenge, primarily due to specific Smo mutations occurring at positions 473 and 477. These mutations result in the loss of vismodegib's binding capacity. The administration of oral formulations poses challenges for unconscious patients due to difficulties in ingestion, the inability to mask the taste, and the cumbersome nature of bulky formulations. As a result, topical administration of anti-cancer drugs has emerged as a preferable and effective option for treating skin cancer. Topical treatments offer better patient compliance, a crucial factor, especially for cancer patients. Currently, only 5-fluorouracil and imiquimod drugs are available in the market for topical skin cancer treatment. However, these drugs are associated with adverse effects such as skin irritation, hair loss, pain, and changes in skin colour. Additionally, the limited ability of these medications to deeply penetrate tissues or lesions, coupled with the restricted permeability of light, poses significant challenges in terms of drug absorption through the outermost layer of the skin (stratum corneum). Consequently, their efficacy in managing disseminated tumors is notably diminished. In addition, the lack of specific targeting to the desired site significantly diminishes the effectiveness of single-drug therapy in treating cancer. The new generation of photosensitizers, such as chlorin e6, HPPH, etc. can irradiate at deeper lesions or tissues because these agents get activated at near-infrared (NIR) region and show a high singlet oxygen quantum yield.

Itraconazole (ITZ), a potent antifungal agent, was recently shown to be efficient for the treatment of BCC in a clinical trial. It exerts its effects through multiple mechanisms to impede tumor growth. These mechanisms encompass the inhibition of the Hedgehog pathway, reduction in endothelial cell proliferation, induction of cell cycle arrest, and stimulation of autophagocytosis. [7]. Its primary action involves preventing the localization of SMO to the cilia, making it an effective inhibitor of the Hedgehog pathway and earning the designation of a cilial translocation inhibitor. With an IC_{50} value of approximately 800 nM, it demonstrates potent inhibition of the Hh pathway. Furthermore, when administered orally, the systemic treatment provides sustained effects lasting for months.[6]. Itraconazole, when administered orally, exhibits a relatively weaker inhibition of the hedgehog (HH) pathway and has demonstrated evidence of reduced basal cell carcinomas (BCCs) in Ptch1+/− mice as well as

in a phase 2 trial. In mice, itraconazole has shown its ability to inhibit the growth of human melanoma and improve survival. This effect is attributed to its capacity to suppress Hedgehog signaling. Nevertheless, long-term treatment with oral itraconazole carries potential risks, including the development of liver dysfunction and congestive heart failure. [8,9]. It effectively inhibited the Hh pathway and growth of BCC by directly binding with SMO. Studies indicate that ITZ has the capacity to inhibit tumors that have developed resistance to other hedgehog inhibitors, such as vismodegib. This is due to ITZ ability to bind to a distinct position on SMO (Smoothened protein), offering an alternative mechanism of action [10,11]. Furthermore, ITZ is highly effective against BCC when it is combined with PDT therapy.

To overcome these drawbacks, a novel lipid nanoparticle platform has been created, which utilizes charged-based squalene, enabling the co-delivery of chlorin e6 photosensitizer and Itraconazole. lipid nanocarriers have been explored as an alternative approach for topical drug delivery. It has many advantages for better permeation due to the interaction of carrier lipids molecules with stratum corneum. Modification of the charge in the lipidic nanocarriers is hypothesized to permeate the drug through the skin.

To the best our knowledge, there is no effective topical formulation available for skin delivery of combining of chlorin e6 and ITZ in skin cancer treatment, and therefore, it is required to develop combinational drug delivery for the inhibit the tumors that has shown the resistance to other hedgehog inhibitors like vismodegib. Co-delivery of Chlorin e6 photosensitizing agent and ITZ antifungal (repurposing molecules) has the potential to improve anti-tumor efficacy and reduce cancer resistance.

3.2. Materials and methods:

Curcumin was obtained from Himedia in Mumbai, India, while Chlorin e6 was purchased from Cayman Chemical Company in the United States. The following items were purchased from Himedia in Mumbai, India: Phosphate Buffered Saline (PBS) with a pH of 7.4, 3-(4,5-dimethylthiazol-2-yl)-2,5-diphenyltetrazolium bromide (MTT), heat-inactivated fetal bovine serum (FBS), trypsin-EDTA, Fluoromount-G, Penicillin-streptomycin antibiotic, Trypan blue solution, and Dulbecco's Modified Eagle Medium (DMEM). Precirol® ATO 5, Glyceryl monostearate (GMS), Compritol® 888 ATO, and stearic acid were generously provided by Gattefosse in Lyon, France. BASF India Ltd in Mumbai, India kindly provided Solutol HS 15, Tween 80, and Span 80 as gifts. Abitec Corporation, located in Ohio, USA, generously supplied

Captex 355 and Capmul MCM C8 as gifts. Lipoid GmbH graciously provided DOTAP. Sigma-Aldrich in Bangalore, India supplied Dimethyl sulfoxide (DMSO), HPLC grade Methanol, paraformaldehyde, dichloro-dihydro-fluorescein diacetate (DCHF-DA), 4,6-diamidino-2-phenylindole (DAPI), 9,10-dimethyl anthracene (DMA), ethidium bromide, acridine orange (AO), N, N-Dimethyl-4-nitrosoaniline (RNO), and propidium iodide (Pi) for the research. Thermo Fisher Scientific in the USA provided the Singlet Oxygen Sensor Green (SOSG), while the GSure DNA genomic isolation kit was purchased from GCC Biotech Pvt Ltd in India. The Annexin-V-FITC apoptosis detection kit was obtained from R&D Systems, located in Minneapolis, USA.

3.2.1. Formulation of drug-loaded lipidic nanoparticles (LNPs)

To formulate lipidic nanoparticles loaded with the drug, the hot homogenization method was utilized, followed by probe sonication. Itraconazole (ITZ) was mixed with the liquid and solid lipid in a sterile vial and dissolved in methanol, which acted as the organic phase. Tween 20 and DOTAP were taken in another vial and vortexed for 10 minutes (aqueous phase). Both the vials were kept at constant heating at the same temperature (60°C) on a stirrer. Once the organic phase was fully evaporated from the lipid mixture, the aqueous phase was introduced to the oily phase. Subsequently, the resulting mixture was subjected to stirring for a duration of 5 minutes. Following that, the obtained pre-emulsion was subjected to sonication using a probe sonicator, and subsequently maintained at a low temperature to achieve the formation of lipidic nanoparticles (LNPs).

To eliminate the unentrapped ITZ, the LNPs underwent centrifugation at 5000 rate per minute for 5 min. Afterward, the collected liquid portion above the sediment, known as the supernatant, was obtained. The Malvern Nano ZS instrument utilizing dynamic light scattering (DLS) was employed to measure the average particle size, polydispersity index (PDI), and zeta potential of the samples. The drug loading percentage and entrapment efficiency were computed using the provided formula and mathematical calculations. [12].

$$\text{Encapsulation efficiency (\%)} = \frac{\text{Amount of drug in the LPNs}}{\text{Initial amount of drug taken}} \times 100$$

$$\text{Drug loading (\%)} = \frac{\text{Amount of drug in the LPNs}}{\text{weight of LPNs}} \times 100$$

3.2.2. Optimization of drug loaded lipidic nanoparticle by using Box Behnken Design

To optimize the lipidic nanoparticles (LNPs), a Box-Behnken Design (BBD) was utilized with the assistance of Design-Expert software (Version V 13, Stat-Ease Inc., Minneapolis, MN, U.S.A.). This design approach aimed to determine the optimal formulation with the minimum number of experiments needed. BBD allows for the evaluation of interaction effects between critical process parameters and materials attributes. The solid and liquid lipids, surfactant concentration, and probe sonication time were determined at three levels based on preliminary batches of LPNs. The independent variables were varied within ranges of solid lipid: liquid lipid ratio (X1) from 100 to 200 mg, surfactant concentration (X2) from 2 to 6 %, and probe sonication time (X3) from 2 to 6 min. To assess the reproducibility of the design, five centre points were used. The software generated 17 runs with high, medium, and low levels. The suggested experiments were carried out and the experimental data were included in the Design of the experiment software. A statistical analysis was carried out to determine the regression model that provides the best fit for each response variable. The model selection was based on the inclusion of significant additional terms, non-aliased models, and the highest-order polynomial. To determine the most appropriate model, an analysis of variance (ANOVA) was conducted for all the response variables. During the evaluation process, multiple criteria were utilized, including the multiple correlation coefficient (R^2), adjusted and predicted correlation coefficients, standard deviation, and coefficient of variance. Design-Expert software was utilized to generate numerical and graphical data, including 3D response surface plots and 2D counterplots, to visualize the experimental results. The generated visualizations were employed to examine the interaction effects between the independent and dependent variables. The main focus of model optimization was to attain the smallest particle size and the highest percentage of entrapment efficiency. The final optimized batch was validated by comparing predicted values to experimental batch results in terms of percent variation or error. The BBD model was validated quantitatively in this manner

3.2.3. Preparation and characterization of dual drug-loaded lipidic nanoparticles of ITZ and Ce6 (ITZ/Ce6@LNPs)

After optimizing the validated batch, we formulated a final formulation batch (ITZ/Ce6@LNPs) by combining precirol ATO (145 mg), Squalene (50 mg), chlorin e6 (5 mg), and ITZ (5 mg) and Span 80 (200 mg) in a vial (Organic phase). We added 200 µl of methanol ACN mixture and 10 µl of DMSO to the vial as an organic solvent to dissolve the ingredients.

In a separate vial, we mixed and continuously vortexed tween 20 (200 mg) and DOTAP phospholipid for 10 minutes before adding the solubilized component to the water phase. We then followed the same methodology protocol as discussed earlier to further treat the formulation. To determine the % EE and drug loading of the ITZ from the ITZ/Ce6@LNPs. The samples were analyzed using high-performance liquid chromatography (HPLC) at a wavelength of 271 nm to estimate their properties. In order to assess the entrapment efficiency of chlorin e6 in ITZ/Ce6@LNP, we developed and validated a fluorescence spectroscopy method specifically for chlorin e6 using spectrofluorolog.

3.2.4. Physiochemical Characterization of ITZ/Ce6@LNPs

To determine the morphology of the developed ITZ/Ce6@LNPs, we utilized Field Emission-Scanning Electron Microscopy (FE-SEM) and scanning transmission electron microscopy. The FE-SEM equipment used was the FEI Quanta FEG 250 SEM.

3.2.4.1. Morphological analysis

To determine the surface morphology of the ITZ/Ce6@LNPs, Scanning Electron Microscopy (SEM) was used with a NOVA NANOSEM 450 with the inclusion of a cryoprotectant (mannitol). During the sample preparation, a consistent layer of ITZ/Ce6@LNPs was applied onto adhesive carbon tape, which was securely attached to aluminum stubs followed by the gold coating under 20 kV for further examination.

3.2.4.2. Spectroscopic analysis

UV spectroscopy on free ITZ, free Ce6, and ITZ/Ce6@LNPs was performed using the Jasco UV-670 Spectrophotometer from the United States. [13]. In order to verify the encapsulation of both drugs, the ITZ/Ce6@LNPs were dissolved in ethanol, and their UV spectrum was obtained and compared.

3.2.4.3. Kinetic stability

The stability of the dual drug-loaded ITZ/Ce6@LNPs was assessed by storing it at 4°C for 24 days, during which the drug absorbance was monitored for the first six days using a UV instrument.

3.2.4.4. Evaluation of singlet oxygen generation (SOG)

This study aimed to evaluate the production of singlet oxygen ($^1O_2$) by ITZ, Ce6, and ITZ/Ce6@LNPs. To measure $_1O^2$ generation, a fluorescent dye called 9,10-dimethyl

anthracene (DMA) was utilized. Ce6-containing formulations (1.5 µg) were dissolved in 1 ml of DMSO and Phosphate buffer Saline pH 7.4. Subsequently, DMA (20 mM) was added to the mixture. After a 10-minute equilibration period, the mixture was exposed to a laser source (660 nm) at an intensity of 0.5 W/cm^2 for various durations. [14]. Fluorescence intensity measurements of DMA were conducted using a microplate reader at excitation and emission wavelengths of 360 nm and 380-550 nm, respectively. These measurements aimed to quantify the reduction in fluorescence intensity. [15].

To assess the production of singlet oxygen ($_1O^2$) by ITZ/Ce6@LNPs, free ITZ, and free Ce6, a singlet oxygen indicator called N,N-dimethyl-4-nitrosoaniline (RNO) was utilized in combination with histidine, which serves as a $_1O^2$ trap. The free drugs and ITZ/Ce6@LNPs were mixed with an aqueous solution containing 100 µl of RNO (250 mM) and 300 µl of histidine (30 mM). Subsequently, the resulting mixture (200 µl) was added to a 96-well plate and exposed to a laser source with a wavelength of 660 nm and an intensity of 0.5 W/cm^2. The absorbance of RNO at 440 nm (λmax) was measured using a UV-vis microplate reader at specific time intervals during the irradiation process. [16].

The singlet oxygen sensor green (SOSG) was utilized to determine the presence of singlet oxygen ($_1O^2$) in the ITZ, Ce6, and ITZ/Ce6@LNPs in their free forms. This involved dissolving the ITZ/Ce6@LNPs at a specific concentration with 0.25 µM of Ce6 in PBS pH 7.4. The mixture was then combined with 2.5 µM of SOSG. Subsequently, all samples were exposed to a laser source with a wavelength of 660 nm (lambda max). The singlet oxygen sensor green (SOSG) fluorescence intensity was measured at excitation and emission wavelengths of 494 nm and 534 nm, respectively, following the irradiation process. [17].

3.2.4.5. In-vitro drug release analysis

To evaluate the in-vitro release of ITZ/Ce6@LNPs, free ITZ, and free Ce6, the dialysis bag method was employed using a buffer system that mimicked skin conditions. The buffer consisted of 15% ethanol, 2% Tween 80, and pH 6.4 phosphate buffer saline, which provided stability and a sink condition for ITZ+Ce6. For the experiment, a dialysis bag with a molecular weight cutoff of 12 KDa (Himedia) was filled with the ITZ/Ce6@LNPs formulation (equivalent to 0.1 mg of ITZ and Ce6 in 1 ml, n = 3) as well as the pure drug formulation (ITZ+Ce6). The bag was then placed in 30 ml of the aforementioned release medium. The samples were incubated at 32 ℃ in a shaking incubator at 200 rpm. At specific time intervals (0.5, 1, 2, 4, 6, 8, 12, and 24 h), 1 ml aliquots were collected, and an equal volume of fresh

release medium was added back to the dialysis bag. The collected samples were filtered and analyzed using an HPLC method to quantify ITZ levels. Simultaneously, the samples were analyzed by fluorescence spectroscopy method to determine the concentration of Ce6.

Various kinetic models, such as zero order, first order, Higuchi, and Korsmeyer-Peppas, were assessed using the DD solver program (Excel add-in), and the most appropriate model was chosen based on the highest correlation coefficients (R^2).

3.2.5. Preparation and characterization of an ITZ/Ce6@LNPs Gel

To formulate the gel containing ITZ/Ce6@LNPs, SEPINEOTM P 600 was used as the gel-forming agent at a concentration equivalent to 0.05% w/w of ITZ and Ce6 (10 g). SEPINEOTM P 600 consists of acrylamide/sodium Acryloyl dimethyl/Taurate copolymer/isohexadecane & polysorbate 80. The gel preparation involved adding 2% w/w of SEPINEOTM P 600 to a beaker, followed by the addition of freshly prepared ITZ/Ce6@LNPs. Gentle stirring was applied to ensure a homogeneous gel consistency. The final ITZ/Ce6@LNPs gel was characterized by examining its pH, spreadability, and morphology using a scanning electron microscope (SEM).

3.2.5.1. Rheological behaviour and stability of ITZ/Ce6@LNPs Gel

3.2.5.1.1. Simple Viscosity

The Rheological and flow properties of the ITZ/Ce6@LNPs gel were analyzed using a Rheometer (MCR 92, P-PTD 200, Anton Paar, Germany). To determine the viscosity of the gel, a parallel plate (PP-25 mm diameter) with a 0.2 mm gap between the plate and probe was utilized. The shear rate was maintained at 10 s-1 for a duration of 5 minutes, and a total of 30 data points were recorded to calculate the viscosity in cP (centipoise). [18].

3.2.5.1.2. Temperature-dependent viscosity

To investigate the thermal properties of the gel, temperature-dependent viscosity analysis was conducted. This test aimed to observe the gel's behavior when subjected to different temperatures. The experiment involved using a parallel plate (PP-25 mm diameter) with a 0.2 mm gap between the container and probe. The optimized sample of ITZ/Ce6@LNPs Gel (500 mg) was loaded onto the plate, and the temperature was gradually increased from 25°C to 40°C. The heating rate was set at 1°C per minute, and a total of 30 data points were recorded during the experiment.

3.2.5.1.3. Amplitude sweeps test and Frequency sweeps test

The amplitude sweep test is a commonly used method to evaluate the characteristics of gels, dispersions, and pastes. It helps determine the linear viscoelastic region (LVE), which represents the range where the sample structure remains unchanged. The yield point estimation measures the critical stress at which gels or dispersed materials start to flow, indicating the force required to initiate gel flow.

In this study, the optimized sample of ITZ/Ce6@LNPs (500 mg) was loaded onto the plate at a temperature of 25°C. To determine the storage modulus (G') and loss modulus (G"), the shear strain γ was systematically varied from 0.01% to 1% at a frequency rate of 10 rad/sec. The frequency sweep test was conducted to examine the internal structure and long-term stability of the gel dispersion. It provides information on the time-dependent behavior of the gel within the range of non-destructive deformation. The ITZ/Ce6@LNPs gel was subjected to an angular frequency range of 0.1 to 100 rad/s, and parameters such as G', G", and complex viscosity were evaluated. [19].

3.2.5.2. Stability study of ITZ/Ce6@LNPs and ITZ/Ce6@LNPs Gel

The stability of the developed ITZ/Ce6@LNPs formulations and ITZ/Ce6@LNPs gel was investigated for a period of 90 days at temperatures of 2-8 °C and 32 °C. The average particle size of ITZ/Ce6@LNPs was determined using the Malvern Nano ZS instrument, while the entrapment efficiency was calculated using a similar formula as mentioned before. To assess the stability of the ITZ/Ce6@LNPs gel, the drug content (assay) was analyzed. A 100 mg sample of the gel was mixed with a solvent combination of ACN and methanol (1:1 ratio) in microcentrifuge tubes. The mixture was sonicated in a bath for 5 minutes to extract the drugs. Subsequently, the samples were centrifuged at 12000 RPM for 15 minutes, and the resulting supernatant was analyzed using both RP-HPLC method and fluorescence spectroscopy to determine the drug content. This stability evaluation aimed to determine the performance of the formulations over the designated timeframe and under different storage conditions.

3.2.5.3. Texture analysis

The textural properties of the ITZ/Ce6@LNPs gel formulation, including firmness and adherence, were evaluated using the TA-XT2 Texture Analyzer^{TM}. This analysis aimed to study the gel's textural profile. To perform the analysis, the prepared ITZ/Ce6@LNPs gel was transferred to a glass beaker with a capacity of 100 ml. The gel was filled up to the 70 ml mark

to prevent the formation of air bubbles and ensure a flat surface. The analytical probe was then used to compress the gel at a rate of 2 mm/s to a depth of 30 mm. The regulated texture analyzer software was employed to obtain various texture parameters such as firmness, cohesiveness, and consistency. Through this analysis, the texture analyzer provided insights into the physical properties of the ITZ/Ce6@LNPs gel, helping to characterize its firmness, adherence, and other relevant textural attributes.

3.2.6. In-vitro cell culture studies

3.2.6.1. Cellular uptake studies

The cell uptake of Ce6 and ITZ/Ce6@LNPs by B16F10 and A431 cells was evaluated through quantitative and qualitative methods. In brief B16F10 and A431 cells (50,000 cells each) were seeded in 12-well plates followed by incubation overnight at 37°C. The media was then replaced with fresh media containing Ce6 and ITZ/Ce6@LNPs at a concentration of 6 µg/ml of Ce6, followed by further incubation at 37°C for varying durations (1to 4 h). For quantitative analysis using flow cytometry, the cells were treated similarly, washed with PBS 7.4, trypsinized, and centrifuged to collect the cell pellet. The cells were then washed and resuspended in PBS 7.4. The fluorescence intensity of 10,000 viable cells was measured using a flow cytometer. The acquired data was processed using FACS DIVA Software. Qualitative observations of cellular internalization were also conducted using a fluorescence microscope. After removing the media, the cells were washed with cold PBS, followed by fixed with 4% paraformaldehyde and stained with DAPI. Subsequently, the cells were rinsed with PBS and examined under a fluorescence microscope (Leica, Germany) to visualize the internalization at 1 and 4 h. This combined approach allowed for both quantitative and qualitative assessment of the uptake of Ce6 and ITZ/Ce6@LNPs by B16F10 and A431 cells, providing valuable insights into the cellular interactions of these compounds.

3.2.6.2. Cell viability assay

In this study, in vitro cell experiments were performed using two cell lines: B16F10, representing adherent murine melanoma cells, and A431, representing epidermoid carcinoma cells. To evaluate cytotoxicity, B16F10 and A431 cells were seeded in 96-well plates at a density of 10,000 cells per well and allowed to adhere for 24 h. Subsequently, various doses of ITZ, Ce6, ITZ + Ce6, and ITZ/Ce6@LNPs were added to the cells, ranging from 3.125 to 100 µg/ml, and incubated for 24 and 48 h. After a 12 h treatment period, the cells in the 96-well plates were subjected to NIR laser radiation at 666 nm (± L with light and without light, 0.5

W/cm2) for 5 minutes, followed by an additional 12 h incubation. Following incubation, the culture media was removed, and 50 µl of MTT solution i n DMEM was added to each well. The cells were further incubated in the dark for 4 h. Subsequently, the MTT solution was replaced with 150 µl of DMSO to dissolve the formazan crystals in each well. The absorbance of the samples was measured at wavelengths of 570 nm and 620 nm using a Spectramax™ multiplate reader (Molecular Devices, US).The following formula was used for quantification:

$$Cell\ viability\ \% = \frac{Absorbance\ of\ sample}{Absorbance\ of\ control} \times 100$$

The software GraphPad Prism 9.0.2 was utilized to calculate the IC_{50} value. After conducting the experiments in triplicate, the results obtained from each test were averaged.

3.2.6.3. Combination index analysis

The synergy of the drug combinations was quantified using the Chou-Talalay method. The IC_{10} to IC_{90} values of the free drugs, combinations, and prepared formulations were calculated using GraphPad Prism. To assess the combination index (CI) and develop a graph correlating the CI with the fraction affected (Fa), CompuSyn Software was utilized. The CI value indicates the nature of the drug interaction: a value less than one indicates synergistic effects, a value equal to one indicates additive effects, and a value greater than one indicates antagonistic effects. [20].

$$CI_x = \frac{D_1}{A_1} + \frac{D_2}{A_2}$$

Where A_1: a dose of drug 1 to produce x% cell kill alone;

D_1: a dose of drug 1 to produce x % cell kill in combination with $(D)_2$;

A_2: a dose of drug 2 to produce x % cell kill alone;

D_2: a dose of drug 2 to produce x % cell kill in combination with $(D)_1$

3.2.6.4. Annexin V assay

To determine apoptosis induced by ITZ, Ce6, ITZ + Ce6, and ITZ/Ce6@LNPs in B16F10 and A431 cells, the TACS® Annexin V-FITC Kit was utilized. The cells were cultured in 12-well plates and treated with the respective compounds for 12 h at a constant Ce6 concentration of

10 µg/ml. Subsequently, the cells were exposed to a 666 nm NIR laser for 5 minutes at a power density of 0.5 W/cm^2. After thorough washing with PBS buffer, the cells were trypsinized and suspended in 1X binding buffer. Annexin V-FITC conjugate was added to each cell suspension and incubated at room temperature for 10 minutes, protected from light. Following this, the cells were treated with propidium iodide (PI) solution at a concentration of 1 µg/ml for 5 minutes. The samples were then analyzed using a flow cytometer. Apoptotic cells were identified by their exclusive staining with Annexin V-FITC conjugate within a gated cell population, enabling the determination of the percentage of apoptotic cells.

3.2.6.5. Cell cycle analysis

Cell-cycle analysis and the distribution of cells in the various phases such as S, G0/G1, and G2/M were performed using flow cytometry. The cells (B16F10 and A431) were cultured and maintained in 12-well plates as mentioned earlier. They were then treated with ITZ, Ce6, ITZ + Ce6, or ITZ/Ce6@LNPs, with or without 666 nm NIR laser radiation, and incubated for 12 h at a fixed Ce6 concentration of 10 µg/ml. After treatment, the cells were trypsinized, centrifuged, washed with 1X PBS, and centrifuged again. The cell samples were fixed with chilled ethanol and stored at -20 °C for 3 h. They were then centrifuged and rinsed with 1X PBS. Each sample was treated with RNase and incubated for 15 minutes. Subsequently, PI solution was added from the 1mM stock solution, and the samples were kept for incubation in the dark condition for 20 minutes. Flow cytometry analysis was performed using a flow cytometer system (BD Biosciences, USA).

3.2.6.6. Mitochondrial membrane potential (MMP) Study

The disruption of mitochondrial membrane potential ($\Delta\Psi$m) can serve as an indicator of cellular stress and early apoptosis. To assess $\Delta\Psi$m, the JC-1 dye was employed, which can reversibly form clusters in the mitochondrial membrane based on its potential. At low $\Delta\Psi$m, JC-1 exists as j-monomers, emitting green fluorescence in the cytosol at 530 nm. At higher $\Delta\Psi$m, it forms j-aggregate complexes, resulting in red fluorescence in the mitochondrial membrane. The ratio of green-to-red fluorescence emission indicates the extent of mitochondrial membrane depolarization, making JC-1 a valuable marker for early apoptosis. To investigate this phenomenon, B16F10 and A431 cells were separately treated with ITZ, Ce6, ITZ + Ce6, or ITZ/Ce6@LNPs at their respective IC$_{50}$ concentrations. Subsequently, the cells were exposed to NIR laser radiation at 666 nm (1 W/cm^2) for 5 minutes. After 24 h, the

cells were trypsinized, centrifuged, washed with PBS, and stained with JC-1 dye (2 µM) for 15 minutes. Quantitative analysis was performed using a flow cytometer (BD FACS Area III) with excitation at 485 nm and emission at 590 nm, applying appropriate compensation and threshold settings. Qualitative analysis was conducted using a fluorescence microscope to capture images for further examination. [21].

3.2.6.7. Reactive oxygen species (ROS) assay

To assess the production of reactive oxygen species (ROS) in B16F10 and A431 cells, the redox-sensitive fluorogenic probe 2',7'-dichlorodihydrofluorescein diacetate (DCF-DA) was employed. After treatment with ITZ, Ce6, ITZ + Ce6, or ITZ/Ce6@LNPs, the cells were exposed to light source (NIR laser radiation at 666 nm ($\pm$ L) for 5 minutes). DCF-DA, which is initially non-fluorescent, undergoes intracellular transformation and oxidation mediated by esterases to generate the highly fluorescent compound as 2',7'-dichlorofluorescein (DCF). For the experimental procedure, B16F10 and A431 cells were cultured in 12-well plates and treated separately with ITZ, Ce6, ITZ + Ce6, or ITZ/Ce6@LNPs at a constant Ce6 concentration of 10 µg/ml for 24 h. After treatment, the cells were rinsed with PBS and subjected to incubation with DCF-DA dye at 37°C for a duration of 30 minutes. Subsequently, the cells were labeled with DAPI and images were captured using a fluorescence microscope (green channel). The fluorescence excitation was set at 492-495 nm, and emission was recorded at 517-527 nm.

3.2.6.8. Nuclear staining assay

To examine nuclear morphological changes, DAPI staining was conducted on B16F10 and A431 cells treated with ITZ, Ce6, ITZ + Ce6, or ITZ/Ce6@LNPs, with or without exposure to NIR laser radiation at 666 nm. DAPI is a fluorescent dye that specifically binds to DNA regions rich in adenine-thymine base pairs, enabling visualization of both live and fixed cells. For the experimental procedure, approximately 1x105 A431 and B16F10 cells were cultured in a 12-well plate. The cells were treated with ITZ, Ce6, ITZ + Ce6, or ITZ/Ce6@LNPs for a duration of 24 h. Following the incubation period, the cells were washed with PBS, fixed with 4% paraformaldehyde for 20 minutes at 37 °C, and stained with DAPI (10 µl, 0.5 µg/ml) for 5 minutes. Additionally, acridine orange (AO) staining (0.1 mg/ml) was performed for 20 minutes. After another PBS wash to remove excess stain, the cells were visualized using a fluorescence microscope (Leica, Germany) with emission in the green channel (AO, 480-490 nm) and the blue channel (DAPI, 358 nm).

3.2.6.9. DNA fragmentation

A431 and B16F10 cell lines were seeded in a 6-well tissue culture plate at a density of 5x104 cells per well and allowed to grow overnight. The cells were then treated with free ITZ, free Ce6, ITZ + Ce6, and ITZ/Ce6@LNPs at a Ce6 concentration of 10 µg/ml, followed by a 12 h incubation period at 37 °C. After the incubation, the cells were exposed to a 660 nm laser at a power density of 0.5 W/cm^2 for 5 minutes. Subsequently, they were incubated for an additional 12 h at 37 °C. Upon completion of the treatment period, the cells were collected, and DNA extraction was carried out using GSure DNA genomic isolation kits. The purity of the isolated DNA was assessed by measuring the absorbance at 260 nm and 280 nm. The extracted DNA samples were then loaded onto a 1.5% agarose gel containing ethidium bromide dye at a concentration of 0.5 µg/ml. Visualization of the gel was performed using a Fusion Pulse GelDoc system (Vilber, Germany), and the degree of DNA fragmentation was observed under a microscope.

3.2.7. Ex-vivo and in vivo assement of ITZ/Ce6@LNPs Gel
3.2.7.1. Ex-vivo skin permeation studies

Using a vertical Franz diffusion cell, ex vivo of ITZ/Ce6@LNPs gel (0.05 % w/w) penetration through the whole thickness of goat skin was assessed. The fresh goat ear skin was taken from the butcher shop. The subcutaneous fat and hair were removed, and the skin was properly cleaned three times with PBS. A vertical Franz diffusion cell was used to mount the processed skin, and 15 % ethanol, 2 % Tween 80, and 6.4 pH phosphate buffer solvent system were used in the receptor compartment. The volume of the receptor compartment was 18 ml with a surface area of 1.17 cm^2. Prior to the experiment, the processed skin was kept for 2 h for hydration. Then 100 mg of the plane gel (ITZ+Ce6) and 100 mg of the ITZ/Ce6@LNPs gel formulation were applied to the donor compartment. The entire system was maintained at 200 rpm on a magnetic stirrer at 32 ± 0.5 °C. 1 ml of aliquot was collected, followed by replacement of the same volume with fresh release media at time intervals *viz.* 0.5 h, 1h, 2h, 4h, 6h, 8h, 12h, 24h. The collected sample was filtered through the 0.44 µm syringe filter and analyzed by using the in-house developed and validated RP-HPLC and Fluorescence spectroscopy. After analysing the results, a graph was constructed with time on the x-axis and

the % cumulative ITZ/Ce6@LNPs permeate on the y-axis. Further, steady-state flow and lag time was calculated, and the slope of the graph gives the permeation flux ($\mu g/cm^2$) [22].

3.2.7.2. Establishment of B16F10 cells induced skin cancer model in C57 BL/6 mice.

In vivo studies using B16F10 cells have demonstrated their ability to form tumors in mice that closely resemble human melanoma tumors. These tumors exhibit key characteristics of cancer, including uncontrolled proliferation, angiogenesis, and invasion into surrounding tissues. The animal experiments conducted under protocols BITS-Hyd/IAEC/2022/57 were approved by the Institutional Animal Ethics Committee (IAEC) and followed the guidelines set forth by the CPCSEA. The animals were housed in standard plastic cages under laboratory conditions and allowed to acclimate for one week prior to the start of the experiments. A 12 h light and 12 h dark cycle was maintained for the animals. Tumors were induced by injecting 100 µl of B16F10 cells, at a concentration of 1.5 million cells, into the right flank of female C57 mice under anaesthesia. Subsequently, the mice were divided into five groups, with each group consisting of five mice: control (PBS/Free gel), free Ce6, free ITZ, ITZ+Ce6, and ITZ/Ce6@LNPs gel.

3.2.7.3. Ex vivo bioimaging in tumor skin of the C57BL/6 mice

The distribution of ITZ/Ce6@LNPs in the tumor skin of C57BL/6 mice was examined using an ex-vivo approach. Here Ce6 acts as a fluorescence marker. The superficial tumor skin of C57BL/6 mice was obtained and placed between the donor and receptor compartments of Franz diffusion cells, securely held in place by clamps. The receptor compartment was filled with 18 ml of PBS (pH 6.4) containing 15% ethanol and 2% Tween 80, while the donor compartment contained either the free drug formulation gel (ITZ+Ce6) or the ITZ/Ce6@LNPs gel, equivalent to 100 µg of Ce6. The skin samples were incubated for specific time intervals of 6, 12, and 24 h at a temperature of $37 \pm 1°C$ with stirring at 800 rpm. At each designated time point, the skin samples were carefully washed, air-dried, and subjected to tape-stripping using 19 mm Scotch cellophane tape in order to remove the outermost layer of the skin, known as the stratum corneum. The remaining skin was then analyzed using ex-vivo bioimaging techniques. The imaging process involved using an In Vivo Imaging System (IVIS) with excitation and emission wavelengths set at 405 nm and 665 nm, respectively. This allowed for the visualization and quantification of the distribution of ITZ/Ce6@LNPs within the tumor skin samples.

3.2.7.4. Topical biodistribution study in C57BL/6 mice skin cancer model

In order to evaluate the in vivo topical biodistribution using imaging (, mice with B16F10 tumors (approximately 50 mm3) were treated topically with either 200 mg of free drug formulation gel (ITZ+Ce6) or ITZ/Ce6@LNPs gel (equivalent to 100 μg of Ce6). The mice were anesthetized and monitored using an IVIS in vivo imaging system at different intervals (1, 3, 6, 12, 24, and 48 h) after topical application. Furthermore, at 48 h post-treatment, mice were euthanized to examine nanoparticle distribution in the main organs, including the heart, liver, spleen, lung, kidney, and tumor, using IVIS imaging.

3.2.7.5. In Vivo antitumor efficacy

Once the tumors reached a size of approximately 50 mm^3, the mice carrying the tumors were separated into five groups: PBS, free ITZ, free Ce6, ITZ+Ce6, and ITZ/Ce6@LNPs gel. The treatment doses for ITZ and Ce6 were 2.5 mg/kg each. A total of 200 mg of gel was topically applied to the tumor area on a regular basis for 8 days. After a post-application period of 12 h, the mice bearing B16F10 tumors were subjected to light irradiation (NIR laser radiation at 666 nm, with a power of 0.5 W/cm^2) for 5 minutes. Throughout the treatment period, body weight and tumor growth rate were observed by measuring the perpendicular diameter using calipers. The volume of each tumor was calculated using the equation: tumor volume = (length × width^2)/2. At the conclusion of the treatment period, the mice were sacrificed, and major organs, such as the heart, liver, spleen, lung, and kidney, along with the tumors, were excised for histological examination. Hematoxylin and eosin (H&E) staining, imaging, and immunohistochemistry were performed to assess the tissue samples.

3.2.7.6. Immunohistochemistry
3.2.7.6.1. Apoptosis assay by TUNEL assay

To evaluate the apoptotic effect, the TUNEL assay was applied on frozen tumor sections following the manufacturer's instructions. The tumor cryo-sections, with a thickness of 5 μm, were obtained using a cryotome (Leica), These sections were then fixed in a solution containing 4% paraformaldehyde for 10 minutes at room temperature. The FragELTM DNA Fragmentation Detection Kit was employed for the TUNEL test, which detects DNA fragmentation in apoptotic cells. The tumor sections were subjected to the TUNEL assay according to the manufacturer's instructions. The presence of apoptotic cells, exhibiting green fluorescence, was observed, while the cell nuclei were stained with blue fluorescence. Images

of the tumor slices were captured using a fluorescent microscope and enabling visualization and examination of the apoptotic cells.

3.2.7.6.2. Immuno-histochemical analysis for hematoxylin & eosin staining and Ki-67

Hematoxylin and eosin (H&E) staining is a commonly used method to examine the morphology of tissues that have undergone preservation, processing, embedding, and sectioning. Following eight days of treatment with different substances, including control (PBS), free Ce6, ITZ, ITZ+Ce6, and ITZ/Ce6/LNPs gel, the mice were euthanized. The heart, kidney, spleen, lung, liver, and tumor were isolated and fixed in a solution containing 4% paraformaldehyde. These tissue samples were then embedded in paraffin and subjected to H&E staining to assess potential organ toxicity and evaluate apoptosis of cancer cells. To assess cell proliferation within the tumor, immunohistochemistry analysis was performed using Ki67 staining. Ki67 is a nuclear antigen expressed during active phases of the cell cycle (M, G2, S, and G1), except during the resting phase (G0), making it a valuable marker for measuring cell proliferation. For the Ki67 analysis, slices of the tumor cryo-sections were incubated with a diluted solution of Ki67 antibody at a temperature of 4 °C. Subsequently, the slices were washed with PBS and treated with a secondary antibody labeled with Alexa Fluor® 488 for a duration of 2 h. Following that, the tissue slices were washed again with PBS and observed under a fluorescence microscope. This allowed for the visualization and analysis of the Ki67-stained cells within the tumor tissue.

3.2.7.7. ROS Production in tumor tissues

To assess the activity of reactive oxygen species (ROS) in tumor tissue, an experiment was conducted in mice. Initially, ITZ+Ce6 and ITZ/Ce6@LNPs were topically applied to the tumor area. After 24 h, a 50 µl intratumoral injection of DCFH-DA (25 µM) was administered. Following a 30-minute incubation period, the mice were anesthetized and observed using an in-vivo imaging system (IVIS® Lumina III, PerkinElmer, USA). Subsequently, the tumors were dissected and sectioned into 5 µm thick slices using a cryostat (Leica Biosystems, Germany). These tissue sections were stained with DAPI, mounted on glass slides, and examined under a fluorescence microscope (Leica, Germany) to visualize the fluorescence signals.

3.2.7.8. Statistics analysis

The findings of each test were performed in triplicate and are presented as mean and standard deviation (mean SD). The t-test and one-way ANOVA were performed to evaluate the significance of differences between all groups using GraphPad Prism software. When P values less than 0.05, the analysis was statistically significant. P values of 0.05, 0.01, and 0.001 are denoted by the *, **, and ***, respectively.

3.3. Results and discussion

The development of optimized lipidic nanoparticles (LNPs) using the QbD methodology and design of experiments involved statistically adjusting process parameters and material attributes to obtain the optimal batch with the fewest possible trials. We utilized BBD to optimize formulation with a 17-trial batch (3 factors and 3 levels) using Design-Expert 13.0 software from State-Ease Inc., Minneapolis, USA. The lipidic nanocarrier system was prepared using low-temperature homogenization followed by the probe sonication method, with the concentration of lipid (oil phase) and surfactant (aqueous phase) being the main factors affecting particle size and percentage entrapment efficiency. Three levels (low, medium, and high) of independent variables were selected **(Table 3.1)**, and the results are presented in **Table 3.2**. The interactions between the independent variables and their responses were described using polynomial equations generated by the software. ANOVA was used to assess the validation of these equations **(Table 3.3)**, and response surface plots were generated to study the interaction effect between responses such as percentage entrapment efficiency and particle size. The polynomial equations and surface plots helped to understand the effect of each variable individually and in combination with other variables on each response. Using response surface regression, full quadratic model equations for particle size and entrapment efficiency were obtained using Design-Expert software and are presented in **Table 3.4**.

Table 3.1. Levels of independent factors used in the design.

Variables		Selected CMAs and CPPs	Goal	Lower level (-1)	Middle level (0)	Upper level (+1)
Independent variables	X1	Amount of lipid (mg)	In range	100	150	200
	X2	Surfactant concentration (%)	In range	2	4	6
	X3	Probe sonication time (min)	In range	2	4	6
Dependent variables	Y1	Particle size (nm)	Minimum (80-100)			
	Y2	Entrapment efficiency (%)	Maximum (> 50 %)			

The regression equation includes the input variables A (lipid amount in mg), B (surfactant concentration in %), and C (probe sonication time in min), where a (+) positive sign indicates a positive quantifiable relationship between the input variable and the response value, while a (-) negative sign indicates an adversarial effect, resulting in a decrease in response value with the respective input variable. The analysis of the coefficient of equations and response surface plots **(Figure 3.1)** indicates that the particle size and entrapment efficiency are significantly dependent on the independent factors of lipid amount, surfactant concentration, and probe sonication time.

Table 3.2. The design of experiments executed for optimization of lipidic nanoparticles.

Batch No.	Independent variables			Response variables	
	Lipid (mg)	Surfactant (%)	Sonication (min)	Size (nm)	Entrapment Efficiency (%)
1	100	4	2	92.957 ± 1.65	56.458 ± 2.45
2	150	2	6	136.589 ± 5.18	72.943 ± 1.73
3	150	4	4	120.687 ± 0.63	73.121 ± 1.00
4	150	2	2	147.985 ± 2.06	57.477 ± 1.21
5	150	6	2	168.173 ± 2.69	63.245 ± 2.52
6	200	4	2	193.167 ± 2.21	75.280 ± 0.99
7	150	4	4	121.610 ± 1.53	75.248 ± 1.15
8	100	4	6	88.686 ± 1.21	65.418 ± 2.15
9	150	4	4	116.806 ± 1.33	76.055 ± 2.03
10	150	6	6	142.273 ± 1.96	75.477 ± 1.83
11	100	6	4	81.068 ± 1.27	65.688 ± 2.58
12	200	6	4	188.933 ± 0.49	87.216 ± 0.96
13	150	4	4	114.913 ± 1.49	74.379 ± 1.03
14	100	2	4	102.367 ± 1.88	57.955 ± 1.65
15	150	4	4	120.125 ± 1.18	77.047 ± 2.52
16	200	2	4	152.533 ± 2.45	78.063 ± 0.58
17	200	4	6	162.248 ± 1.01	86.707 ± 0.57

Table 3.3. ANOVA for regression coefficients for Box Behnken designed effects (linear, quadratic, and interaction) against the CQAs i.e., dependent variables (particle size and entrapment efficiency) to establish the best fitted quadratic equation

Effect	Variable	Particle size		Entrapment efficiency	
		F- value	P- value	F- value	P- value
Linear effect	A	1529	< 0.0001	317.43	< 0.0001
	B	28.27	0.0011	32.80	< 0.0001
	C	76.49	< 0.0001	83.18	< 0.0007
Interaction effect	AB	106.24	< 0.0001	0.0000	-
	AC	19.95	0.0029	0.3599	-
	BC	2.95	-	0.8098	0.0300
Quadratic term	A^2	0.6573	-	0.0464	-
	B^2	95.34	< 0.0001	17.78	0.0040
	C^2	132.87	< 0.0001	23.35	< 0.0019

Table 3.4. Full quadratic model equations for particle size and entrapment efficiency generated by the design of expert software

CQA s	Coded equations	Predicted R^2	Adjusted R^2
Particle size	+ 118.80 + 40.25A + 5.50 B – 9.00 C + 15.00 AB – 6.50 AC – 2.50 BC - 1.15 A^2 +13.85 B^2 + 16.35 C^2	0.9569	0.9920
Entrapment efficiency (%)	+74.60 +10.50 A + 3.38 B +5.38 C + 0.0 AB + 0.5000 AC - 0.7500 BC - 0.1750 A^2-3.43 B^2 -3.92 C^2	0.9106	0.9670
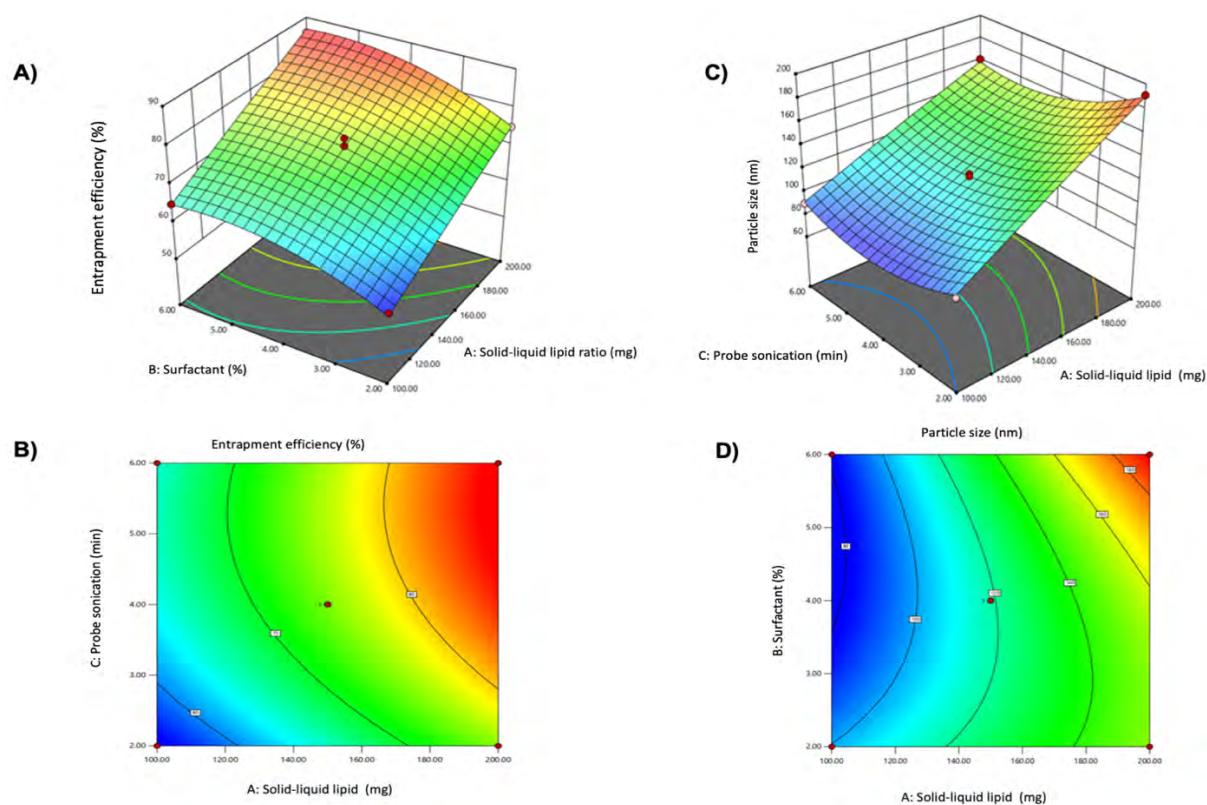
Figure 3.1. Box-Behnken optimization of surface response plots showing the effect of input variables particle size (nm) and entrapment efficiency (%) of ITZ/Ce6@LNPs. The 3D plot of input variables affecting response factor entrapment efficiency (%)A); The contour plot of input variables affecting response factor entrapment efficiency (%)B); The 3D plot of input variables affecting response factor particle size (nm) C); The contour plot of input variables affecting response factor particle size (nm) D).

The adjusted R^2 values (0.9920) and predicted R^2 values (0.9569) for particle size showed close agreement (with a difference of less than 0.2), while for entrapment efficiency, there was close agreement between the adjusted R^2 values (0.9670) and predicted R^2 values (0.9106) (with a difference of less than 0.2). The batch with a lipid amount of 180 mg, a surfactant concentration of 4 %, and a probe sonication time of 4 min was selected based on the experimental results. The predicted results for particle size and entrapment efficiency were validated by comparing them with the experimental results, and the % relative deviation was calculated and reported in **Table 3.5**. Increasing the amount of lipid while decreasing the concentration of surfactant and sonication time led to an increase in particle size. This is because as the lipid concentration increases, the viscosity of the melted lipid phase also increases, leading to a larger dispersion. On the other hand, a longer probe sonication time had a negative effect on particle size but a positive effect on entrapment efficiency. Similarly, surfactant concentration had a negative

effect on particle size but a positive effect on entrapment efficiency. The optimal batch was determined using a numerical method and desirability validation based on minimum particle size and maximum entrapment efficiency [23].

Table 3.5. Validation batch by the numerical method

Responses	Predicted results	Actual results	% Relative
Particle size (nm)	91.54 ± 3.14	93.6860 ± 4.7221	-6.32
Entrapment efficiency (%)	78.99 ± 3.5	75.563 ± 5.538	-26.44

In this formulation, we have used Precirol ATO and Squalene, which have been studied extensively for their potential as a component of lipidic nanoparticles in topical therapy. It has been shown to improve the stability and release of active ingredients from LNPs, as well as enhance their skin penetration ability. Herein the DOTAP (1,2-di-O-octadecenyl-3-trimethylammonium-propane), was the main component to maintaining the positive charge and stability of LNPs. Positively charged lipids are often used in LNPs because they can help to stabilize the lipid bilayer. The positively charged head group of DOTAP interacts with the negatively charged phosphate groups of other lipids in the bilayer, forming electrostatic interactions that can help to prevent the lipids from separating or aggregating. In addition to stabilizing the lipid bilayer, positively charged lipids like DOTAP can also improve the interaction of LNPs with target cells. The positively charged lipids can bind to negatively charged cell membranes, facilitating the uptake of the LNPs into the cell [24,25]. Additionally, We have used two surfactants such as Span 80 and Tween 20. The reason behind the selecting surfactants was the Hydrophilic lipophilic balance. In the formulation of lipidic nanoparticles, HLB values are used to select appropriate surfactants that can stabilize the nanoparticles and prevent them from aggregating or coalescing. This stabilizes the nanoparticles by creating a barrier between the hydrophobic core and the surrounding aqueous medium, preventing aggregation, coalescence, or precipitation [26] In addition to stabilizing the nanoparticles, surfactants with appropriate HLB values can also help to improve the drug loading and release properties of the formulation. By optimizing the HLB value of the surfactant or emulsifier, it is possible to achieve a better balance between hydrophilic and lipophilic interactions, which can enhance drug solubility and promote drug incorporation into the nanoparticle core. Overall, the HLB value plays a critical role in the stabilization of lipidic nanoparticle formulations by

influencing the adsorption and orientation of surfactant or emulsifier molecules at the particle interface. Therefore combining the two HLB value provides better stability and high drug loading [27,28].

3.3.1. Preparation of a combined Batch of ITZ and Ce6 (ITZ/Ce6@LNPs) and its characterization

After the finalization of the validated batch, the formulation batch was prepared for the dual drug-loaded lipid nanoparticle of ITZ and Ce6 by using low temperature followed by the probe sonication method. **Figure 3.2 A** represents the Formulation containing ITZ/Ce6@LNPs formulation (A-a); ITZ/Ce6@LNPs gel (SEPINEO^{TM} P 600) (A-b). The prepared ITZ/Ce6@LNPs formulation was characterized using particle size, zeta potential, scanning transmission electron microscopic (STEM), and scanning electron microscope (SEM). The particle size, PDI, and zeta potential of the ITZ/Ce6@LNPs were determined by DLS and were found to be 92.98 ± 5.21 nm. 0.201 ± 0.021, + 21 ± 5.2, respectively. The particle size and potential zeta graphs of ITZ/Ce6@LNPs are represented in **Figures 3.2 B & 3.2 C**. % drug loading and entrapment efficiency of ITZ was 4.11 % and 76.23 % and for Ce6 4.23 % and 79.2%. The respective SEM image of drug ITZ/Ce6@LNPs represented that the ITZ/Ce6@LNPs were uniformly fabricated, spherical shapes with a uniform particle size distribution, as shown in **Figure 3.2 D**. The UV spectrum overlay graph **Figure 3.2 E** represents the ITZ, Ce6, and ITZ/Ce6@LNPs formulations. ITZ shows a peak at 271 nm, while Ce6 shows two peaks at 400 nm and 666 nm. Similar peaks were observed for ITZ/Ce6@LNPs formulations when dissolved in ethanol. Therefore, it confirmed that the drugs were encapsulated into the ITZ/Ce6@LNPs, and the addition of ethanol disintegrated the ITZ/Ce6@LNPs. Periodical evaluation of particle size and the tracking of Ce6 and ITZ absorbance intensity over time for the LNPs stability on storage **(Figure 3.2 F)**. The particle size was between 88.21 to 112 nm for ITZ/Ce6@LNPs on storage at 4ºC for 24 days. Thus, the kinetic stability data revealed that insignificant deviation in the Ce6 signal in ITZ/Ce6@LNPs at 4 ◦C from day 1 to day 24.
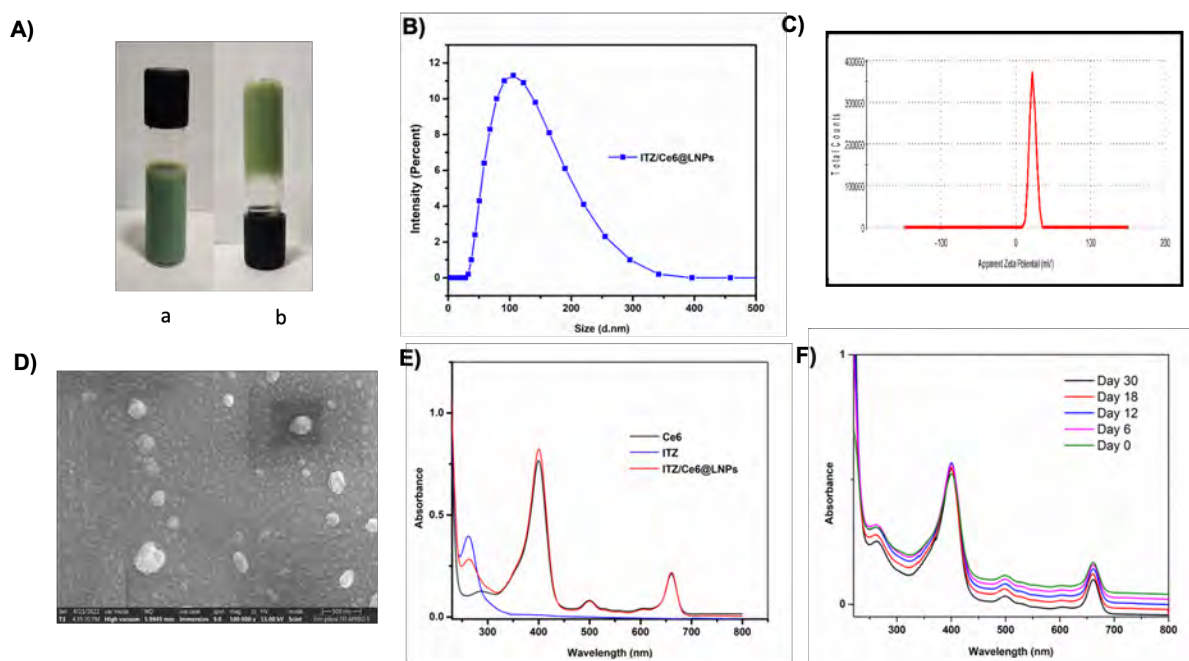
Figure 3.2. Physiochemical characterization of ITZ/Ce6@LNPs. Formulation containing ITZ/Ce6@LNPs formulation (A-a); ITZ/Ce6@LNPs gel (SEPINEO^{TM} P 600) (A-b); Particles size distribution of ITZ/Ce6@LNPs (B); zeta potential of ITZ/Ce6@LNPs (C); Scanning electron micrograph of ITZ/Ce6@LNPs (D); UV absorbance spectra of free ITZ, free Ce6, and ITZ/Ce6@LNPs in methanol, (E); and Kinetic stability of ITZ/Ce6@LNPs (F).

3.3.2. Evaluation of the photoactivity and singlet oxygen generation

Fluorescence spectrophotometry was used to identify the photoactivity of ITZ/Ce6@LNPs and the generation of singlet oxygen ($^1O_2$) from ITZ/Ce6@LNPs following irradiation, as shown in **(Figure 3.3).** Ce6 has maximum absorption at 405 and 640 nm. The free Ce6 or ITZ/Ce6@LNPs produced single oxygen with varied fluorescence intensity of DMA with 255000 and 89500, respectively. The reduction in fluorescence intensity of DMA has shown an increase in singlet oxygen generation. The ITZ/Ce6@LNPs generated higher than the free Ce6, as shown in **Figure 3.3 A**. Since free Ce6 was aggregated in the water, there was a decline in singlet oxygen generation **(Figure 3.3 B).** However, there was a noticeable difference between the $^1O_2$ generation dissolved in ITZ/Ce6@LNPs and free Ce6 in DMSO.
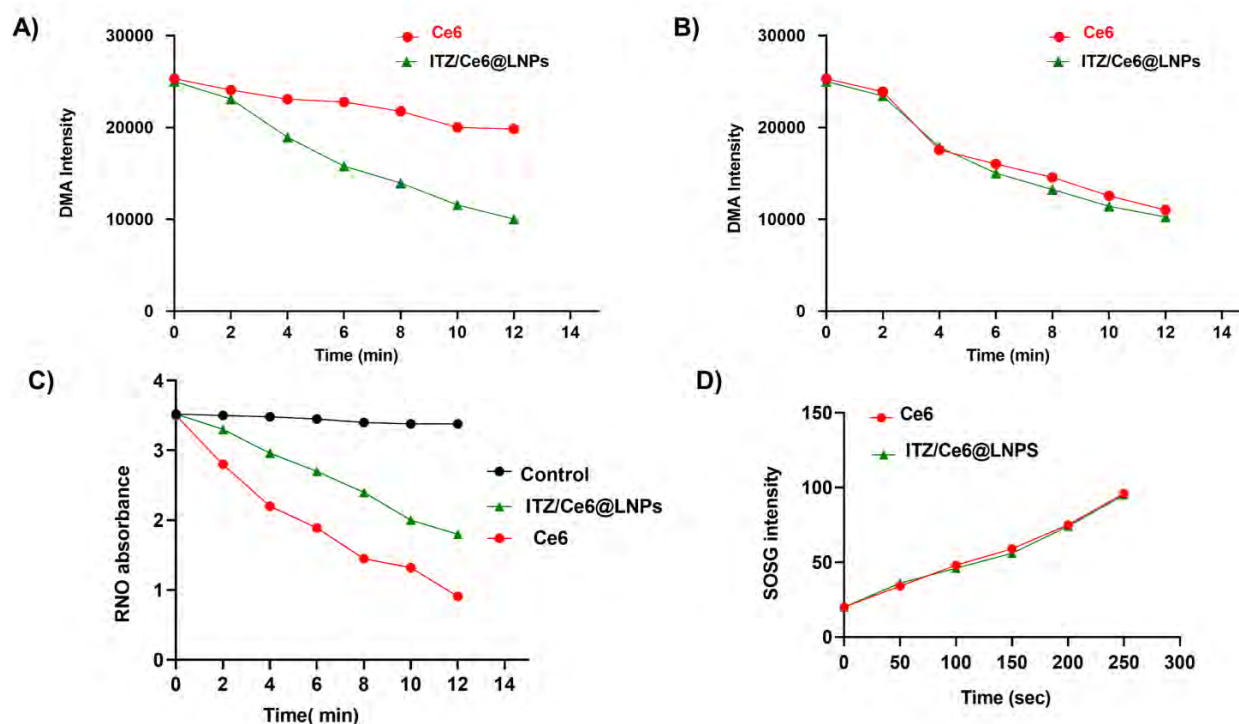
Figure 3.3 Biochemical analysis of Ce6-mediated ROS generation. Change in the fluorescence intensity of DMA (Ex. 360 nm; Em. 436 nm) w.r.t. time in the presence of free Ce6, ITZ/Ce6@LNPs in PBS (A), and in DMSO (B); time-dependent photo-bleaching of RNO by free Ce6, ITZ/Ce6@LNPs in PBS (C); Changes in fluorescence intensity of SOSG in the presence of free Ce6, ITZ/Ce6@LNPs in water (D).

Next, $^1O_2$ generation was investigated using RNO when histidine was present. The reaction was with histidine and RNO, the $^1O_2$ that was generated proceeds through a bleaching process. A transannular peroxide intermediate is formed when $^1O_2$ is taken in by the imidazole ring of the histidine molecule. The photobleaching occurs as a result of further interaction with RNO. The rate of formation of singlet oxygen was found to be determined by the variance in the photobleaching. Using a laser source with a wavelength of 660 nm, the ITZ/Ce6@LNPs, free ITZ, and free Ce6 were subjected to irradiation at a laser intensity of 0.5 W/cm^2 over different time durations. The absorbance of RNO was determined at 440 nm **(Figure 3.3 C).** When the irradiation time increased, the free Ce6 generated singlet oxygen at a faster rate than ITZ/Ce6@LNPs. This was proven by the substantial reduction in RNO absorbance. Due to the presence of a hydrophobic core in the nanocarrier, the entrance of histidine was limited, which led to the barrier in the formation of a singlet oxygen−histidine−RNO chain. Therefore leading to an unsuccessful detection of $^1O_2$.

The $^1O_2$ production capacity of DDLN in an aqueous solution was assessed using SOSG by evaluating the fluorescence and laser irradiation. The $^1O_2$ yield ITZ/Ce6@LNPs was significantly higher than free Ce6 **(Figure 3.3 D).**

3.3.3. In-vitro drug release

The drug release graph of developed ITZ/Ce6@LNPs and free drug of ITZ and Ce6 was represented in **(Figure 3.4).** Both free drugs showed 100% cumulative drug release within 6 h, while ITZ/Ce6@LNPs containing ITZ and Ce6 showed less than 50% cumulative release in 6 h and then 50 to 95% by the end of 24 h. The kinetic release model was investigated using a DD solver (add on Xcel sheet). The model of the release kinetics is shown in **(Table 3.6),** and it contains the correlation coefficient data, along with the AIC value and the MSC value. Throughout the process of evaluating the several models, the "best-fit" model was chosen to be the one that had the highest R^2 value, the lowest AIC, and MSC values which were higher than 2. It was confirmed by the tabulated data that the ITZ/Ce6@LNPs followed the 1st order kinetic model for both drugs **(Table 3.6)**.
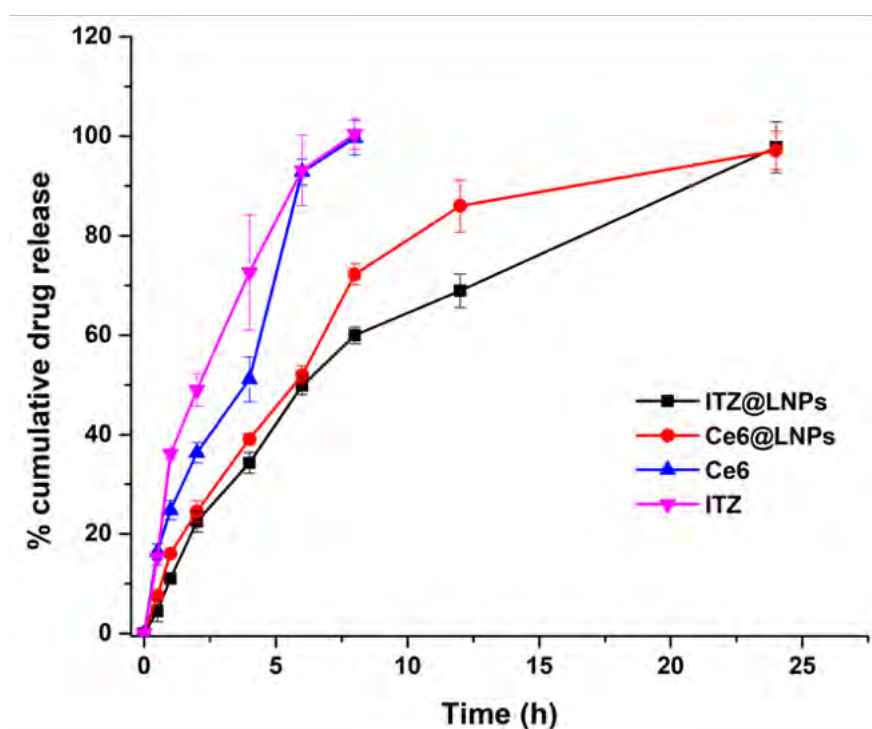
Figure 3.4 Represent the cumulative drug release graph of developed ITZ/Ce6@LNPs and free drug of ITZ and Ce6

Table 3.6. The release mechanism of ITZ/Ce6@LNPs formulation and free drugs by curve fitting method.

Kinetic models	Ce6 LNP				Free drug Ce6			
	R^2	k	AIC	MSC	R^2	k	AIC	MSC
Zero order	0.6611	5.3227	75.0595	0.6438	0.9399	13.7304	45.7677	2.2456
First order	0.9908	0.1419	42.6470	4.2452	0.9362	0.2719	46.1786	2.1869
Higuchi	0.9527	21.5567	57.3292	2.6138	0.9281	32.5342	47.0158	2.0673
Hixson Crowell	0.9901	0.0403	40.2222	4.5146	0.9548	0.0748	43.7621	2.5321
Koresmeyer peppas	0.9532 n =0.516	20.7454	59.2345	2.4021	0.9734 n=0.735	22.2110	42.0666	2.7743
Kinetic models	ITZ LNP				Free drug ITZ			
	R^2	k	AIC	MSC	R^2	k	AIC	MSC
Zero order	0.7971	4.9312	69.2784	1.1831	0.8393	14.8037	52.7657	1.1680
First order	0.9934	0.1112	38.5094	4.6019	0.9875	0.3717	34.8704	3.7244
Higuchi	0.9724	19.5520	51.3129	3.1792	0.9848	35.9905	36.2728	3.5241
Hixson Crowell	0.9895	0.0315	42.6155	4.1456	0.9867	0.0998	35.3436	3.6568
Koresmeyer peppas	0.9835 n =0.580	16.0485	48.6762	3.4722	0.9891 n= 0.557	32.8692	35.9417	3.5714

3.3.4. Characteristic of ITZ/Ce6@LNPs gel

The prepared ITZ/Ce6@LNPs formulation **(Figure 3.2 A a,)** was incorporated into a topical gel (SEPINEO™ P 600) **(Figure 3.2 A-b).** When nanoparticles are incorporated into a gel, they may form separation into gel or aggregates quickly. Thus, to ensure the microstructure of DDLN gel, SEM analysis was performed **(Figure 3.5 A).** The ITZ/Ce6@LNPs gel was a topical hydrogel preparation that was intended to be applied directly to the skin, and a pH analysis was required to confirm that the formulation remained unchanged. It was observed that the pH of the ITZ/Ce6@LNPs gel was 6.2 ± 0.7, and this result was confirmed to be within the acceptable range for human skin pH (4.5–6.4). As a result, the optimized composition was identified as suitable for usage in order to reduce the risk of causing skin irritation during the application.

3.3.4.1.Rheological behaviour

The viscosity (η) of ITZ/Ce6@LNPs gel was found to be 70231 cP at 25 °C under the constant shear rate of 10 s−1 **(Figure 3.5 B).** According to **Figure 3.5 B**, the rheograms exhibited non-Newtonian flow behaviour with shear-thinning characteristics and variable thixotropic behaviour.   The thermal behaviour of the gel was determined by using temperature-dependent viscosity. In the temperature-dependent viscosity, by applying the constant share rate with varying temperatures from 25 to 40 ℃ viscosity was measured. As a result, it was confirmed that there were no changes in viscosity **(Figure 3.5 C).** To analyze the deformation behaviour and time-dependent behaviour of the sample, an amplitude sweep test and frequency sweep test were carried out. LVE demonstrates the extent to which analysis could be carried out without affecting the gel structure. In the amplitude sweep test, LVE region was found to be for ITZ/Ce6@LNPs 0.02 (% in terms of strain). **Figure 3.5 D** result demonstrates that G' is greater than G", which indicates a solid viscoelastic structure or a gel-like structure. After identifying the LVE region, the frequency sweep test was performed to evaluate the gel stability during long-term storage as well as the flow behavior and internal structure of the ITZ/Ce6@LNPs gel. The obtained G' and G" for ITZ/Ce6@LNPs gel were confirmed to be in the LVE region, and as a result **(Figure 3.5 E),** the sample has not changed over the course of the test.

3.3.4.2. Texture analyzer

To find out the texture of the gel, various parameters, including firmness, consistency, and cohesiveness, were recorded to obtain an interpretation of a gel texture. The firmness, consistency, and cohesiveness of ITZ/Ce6@LNPs gel were found to be 81.12 ± 5.12 g, 986 ± 23.12 g s^{-1}, and -452.65 ± 42 g, respectively **(Figure 3.5 F).** The above values indicated that the physical appearance of the gel was uniform and smooth, free from grittiness and or particulate matter. The results demonstrate that the DDLN gel could provide superior exclusiveness and also high effectiveness of loaded drugs in terms of the high permeability and retention of drugs in the application site.
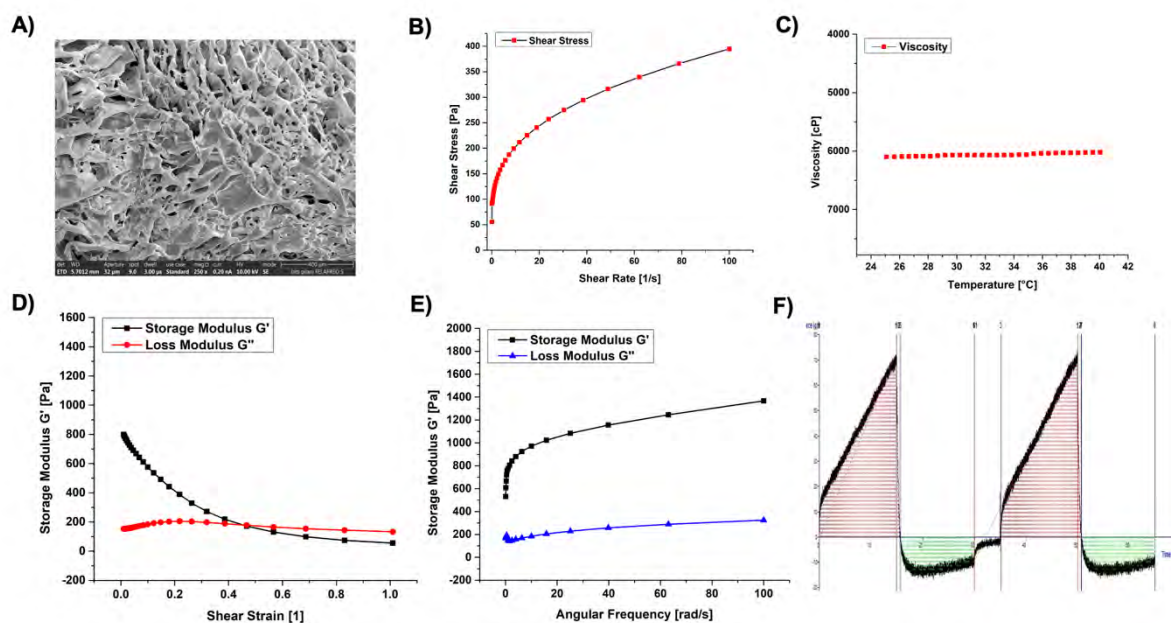
Figure 3.5 Characterization of ITZ/Ce6@LNPs gel; Scanning electron microscopic images of ITZ/Ce6@LNPs gel (A); Rheological behavior share stress vs share rate (B); temperature-dependent viscosity (25°C to 40 °C) (C); Amplitude sweeps test (D); Frequency sweep test (E); Texture analysis of ITZ/Ce6@LNPs gel (F).

3.3.4.3. Assessment of stability of ITZ/Ce6@LNPs and ITZ/Ce6@LNPs gel

 The developed ITZ/Ce6@LNPs and ITZ/Ce6@LNPs gel were tested for storage stability for up to 90 days at two different temperatures such as 4 °C and 25 °C (**Table 3.7**). After being stored for a period of 90 days, the level of ITZ and Ce6 and did not significantly alter. Also, the results from the assay of the gel, particle size, and entrapment efficiency have not shown a substantial difference between 4 °C and 25 °C. It reveals that the ITZ/Ce6@LNPs and ITZ/Ce6@LNPs gel were stable with consideration of both the rheological and physiological characteristics.

Table 3.7 Stability data of ITZ/Ce6@LNPs and ITZ/Ce6@LNPs gel at different storage conditions

Stability condition	Days	ITZ/Ce6@LNPs	Particle size (nm)	% Entrapment efficiency (mean ± SD)	Assay of nanocarrier loaded gel/ ITZ/Ce6@LNPs gel (mean ± SD)
2-8 °C	**0 day**	**Ce6**	94.65 ± 3.5	78.96 ± 7.70	98.11 ± 2.1
	0 day	**ITZ**		76.09.11 ± .08	99.33 ± 1.22
	30 days	**Ce6**	99.14 ± 8.5	75.12 ± 4.5	101.03 ± 1.2
	30 days	**ITZ**		72.53 ± 9.04	98.05 ± 2.3
	90 days	**Ce6**	100.87 ± 2.4	76.94 ± 6.50	97.98 ± 2.3

	90 days	ITZ		70.23 ± 5.43	99.09 ± 2.3
	0 day	Ce6	90.4 ± 4.9	80.11 ± 6.32	98.22 ± 1.33
	0 day	ITZ		77.33 ± 4.33	99.12 ± 2.76
25 ± 0.5 °C	30 days	Ce6	101.15 ± 10.2	76.12 ± 13.4	97.22 ± 4.10
	30 days	ITZ		75.12 ± 6.08	98.11 ± 1.3
	90 days	Ce6	112.56 ± 4.9	72.23 ± 12.3	97.11 ± 2.1
	90 days	ITZ		70.09 ± 17.12	99.11 ± 1.9

3.3.5. In-vitro assays

3.3.5.1. Cellular uptake

The cellular internalization of Ce6 and ITZ/Ce6@LNPs was evaluated using fluorescence microscope and flow cytometry techniques. This allowed for both qualitative and quantitative analysis of the internalization process in B16F10 and A431 cells. In both cell lines, a distinct and intense red fluorescence was observed in the cytoplasm and nuclei of cells treated with ITZ/Ce6@LNPs, indicating rapid internalization of the ITZ/Ce6@LNPs. The red fluorescence intensity of Ce6 and ITZ/Ce6@LNPs increased from 1 to 4 h, indicating a time-dependent cellular uptake in both B16F10 and A431 cell lines (**Figure 3.6A** for B16F10 cells and **Figure 3.6 B** for A431 cells).

Furthermore, flow cytometry studies were conducted to validate the enhanced internalization and intracellular release of ITZ/Ce6@LNPs. The histogram analysis of mean fluorescence intensity demonstrated an increase in values for ITZ/Ce6@LNPs and Ce6 from 1 to 4 h. These results were visually represented as bar graphs (**Figure 3.7A** for B16F10 cell lines and **Figure 3.7B** for A431 cell lines) to illustrate the observed changes in fluorescence intensity over time. The geometric mean fluorescence of ITZ/Ce6@LNPs (+ L) treated cells from 1522.2 ± 12.22 to 3343.54 ± 16.27 from 1 to 4 h for B16F10 cells, whereas the geometric mean fluorescence of free Ce6-treated cells was increased from 746.4±33.7 to 1603.7±23.67. Similarly, the geometric mean fluorescence of ITZ/Ce6@LNPs (+ L) treated cells from 1712.32 ± 10.32 to 3890.54 ± 22.27 from 1 to 4 h for A431 cell lines. (**Figure. 3.7 C** for B16F10 and **Figure 3.7 D** for A431cell lines). The time-dependent increase in fluorescence could be easily observed in both cell lines by the shift in the peak.
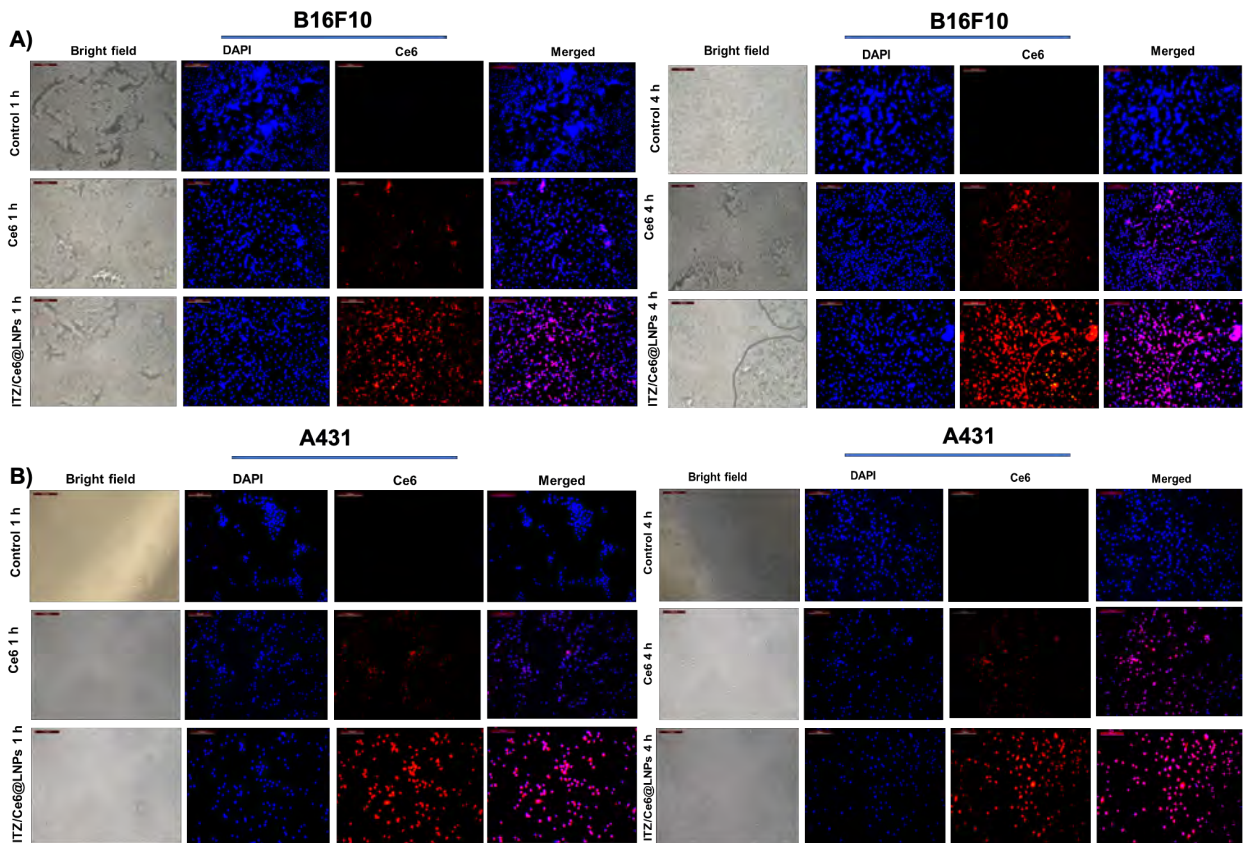
Figure 3.6. Cellular uptake study of free ce6, ITZ/Ce6@LNPs in B16F10 (A) and A431 cell lines (B) cells after 1 and 4 h of incubation (Ce6 concentrations. 6 µg/ml). Red and blue, and signals represent cells stained by Ce6 and DAPI, respectively.
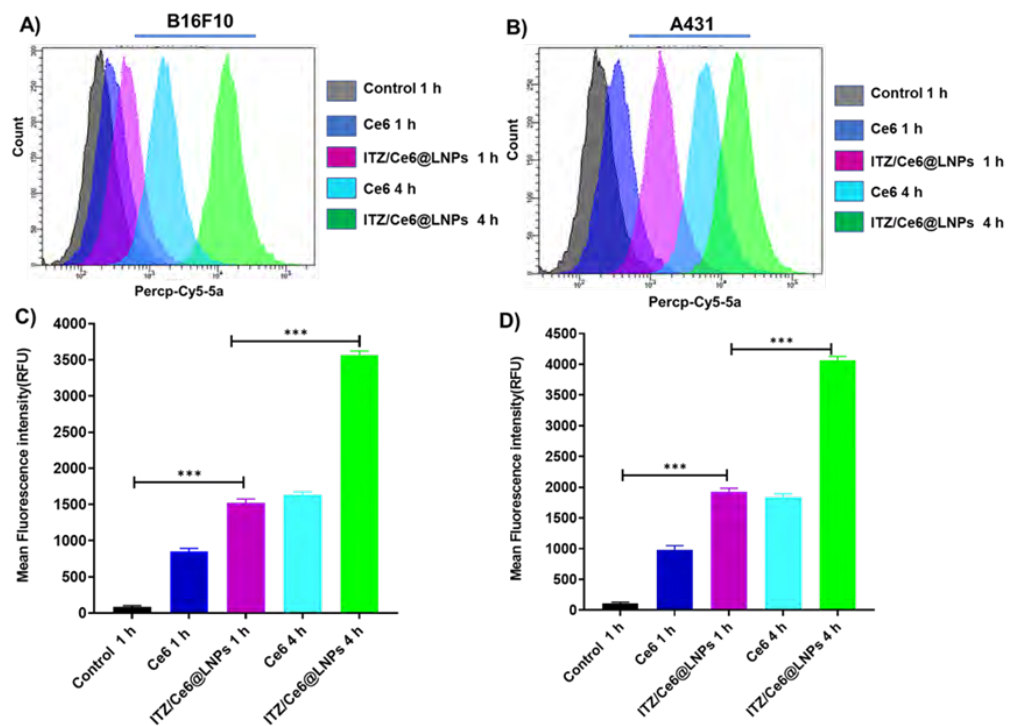
Figure 3.7. The histogram and bar graph represent the quantitative uptake of NPs using flow cytometry for B16F10 (A) and (C), respectively; Assessment of the geometric mean of fluorescence of the A431 at 1 and 4 h incubation by histogram plots and bar graphs (B) and (D). The data in bar graphs represent mean ± standard deviation, calculated from three sets of experiments (**p < 0.01).

3.3.5.2. Cell viability assay

The MTT assay indicated a time and concentration-dependent decrease in the cell viability in both B16F10 and A431 cell lines for the various formulations treated, as represented in **Figures 3.8 and 3.9.** The figure illustrates that the positive control group (+L alone) exhibited similar cell survival rates compared to the negative control group (PBS, -L), indicating that laser irradiation alone did not cause significant harm to the cells. In general, the cells subjected to laser irradiation (+L) displayed higher levels of cell death compared to the non-irradiated cells (-L) at both 24 and 48 h. As the intensity, dose, and duration of ITZ/Ce6@LNPs increased along with laser treatment, the number of surviving cells decreased, indicating a dosage, time, and laser-dependent relationship. The strong inhibitory effect of ITZ/Ce6@LNPs without laser could be attributed to the release of Ce6 and ITZ.

It was observed that the cytotoxic effect was highest for ITZ/Ce6@LNPs, followed by ITZ+Ce6 as compared to free Ce6 and ITZ. The ITZ/Ce6@LNPs showed an IC_{50} of 11.12 µg/ml for 24 h on B16F10 cell lines, which was lower than the IC_{50} of free Ce6 (+ L), ITZ (+L), and ITZ+Ce6 (+L), which were 20.14 µg/ml, 26.12 µg/ml, and 14.12 µg/ml, respectively. Similarly, ITZ/Ce6@LNPs (+ L) treatment for 24 h on A431 cell lines showed an IC_{50} of 9.81 µg/ml, while free Ce6 (+ L), free ITZ (+ L), and ITZ+Ce6 (+ L) exhibits IC50s of 19.14 µg/ml, 23.45 µg/ml, and 12.41 µg/ml, respectively. Interestingly, the ITZ/Ce6@LNPs treatment showed the lowest IC_{50} values of any of the conditions that were assessed. The ~3.1 fold decrease in IC_{50} values of ITZ/Ce6@LNPs than free Ce6 and free ITZ at 24 h (+L). Therefore, it indicates that the longer retention of ITZ/Ce6@LNPs intracellularly reaches optimum concentration to exert cytotoxic action.

3.3.5.3. Combination index analysis

Combination indexes (CI) at all tested fractions affected, including IC_{10}, IC_{20}, IC_{30}, IC_{40}, IC_{50}, IC_{60}, IC_{70}, IC_{80}, and IC_{90} for both the cell lines and at all the tested treatment regimens (24 h + L, - L) and (48 h + L, -L) were represented in **Figure 3.8 E, F, G, and H and 3.9 E, F, G, and**

H. The lowest CI was observed at 24 h (+L), and 48 h (+ L) time point at 50 % fraction affected as mentioned in **Table 3.8** for in B16F10 and A431 cell lines. It was observed that ITZ/Ce6@LNPs formulation with a drug loading ratio of 1:1 showed a synergistic effect for both cell lines, with combination indices values below 1.
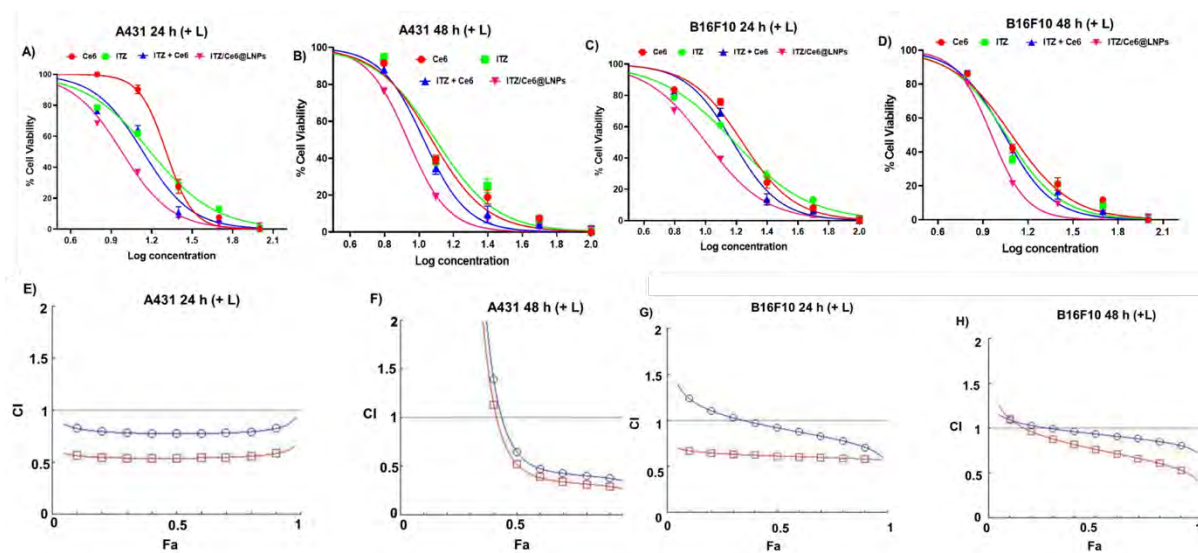
Figure 3.8. The dose-response curve for the determination of IC_{50} values of free ITZ, free Ce6, ITZ+Ce6, and ITZ/Ce6@LNPs (24 and 48 h) in cultured A431 (A and B) and B16F10 cell lines (C and D) with (+L) laser; graphs representing combination index (CI) in A431 (E and F) and B16F10 cells (G and H) with (+L) laser.
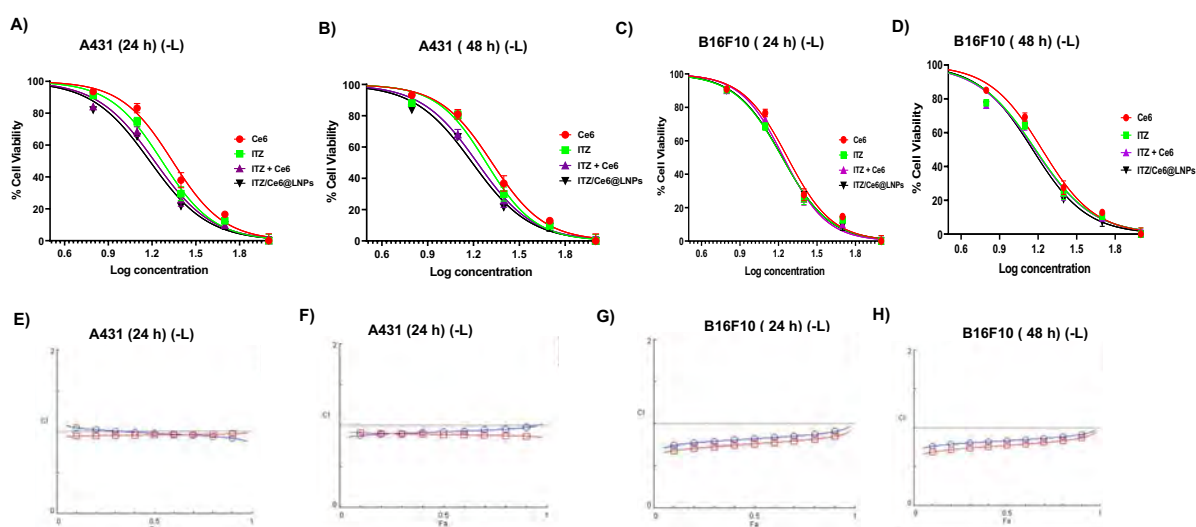
Figure 3.9. The dose-response curve for the determination of IC$_{50}$ values of free ITZ, free Ce6, ITZ+Ce6, and ITZ/Ce6@LNPs (24 and 48 h) in cultured A431 (A and B) and B16F10 cell lines (C and D) with (-L) laser; graphs representing combination index (CI) in A431 (E and F) and B16F10 cells (G and H) with (-L) laser.

Table 3.8. The combination index value of ITZ/Ce6@LNPS

Group	CI value (B16F10 cell lines)	CI value (A431 cell lines)
IC$_{10}$	0.980	0.862
IC$_{20}$	0.934	0.832
IC$_{30}$	0.919	0.817
IC$_{40}$	0.900	0.801
IC$_{50}$	0.880	0.790
IC$_{60}$	0.864	0.760
IC$_{70}$	0.836	0.754
IC$_{80}$	0.828	0.738
IC$_{90}$	0.781	0.726

3.3.5.4. Annexin V assay

In order to explore the relationship between cell growth suppression and cell cycle progression, flow cytometry was utilized to analyse the cell cycle distribution of B16F10 and A431 cells. The extent of apoptosis for free ITZ, free Ce6, ITZ+Ce6, and ITZ/Ce6@LNPs formulations is shown in **Figures 3.10 A and B.** It can be observed that for B16F10 cell lines, while free Ce6 (- L, +L)   showed an apoptosis % of 10.23 %, and 13.40 %, free ITZ (- L, + L) showed apoptosis of 9.58 %, 9.72 %, ITZ+Ce6 (- L, + L) showed apoptosis of 18.32 %, 20.58 %, and ITZ/Ce6@LNPs (- L, + L) showed apoptosis of 35.58 %, 45.14 %. Similarly, in A431 cell lines, free Ce6 (- L, +L)   showed an apoptosis % of 14.25 %, 17.25 %, free ITZ (- L, + L) showed apoptosis of 12.24 %, 16.04 %, ITZ+Ce6 (- L, + L) showed apoptosis of 24.2 %, 33.07 %, and ITZ/Ce6@LNPs (- L, + L) showed apoptosis of 40.41 %, 63.24 %.

The ITZ/Ce6@LNPs (+L) formulation exhibited the highest apoptotic response in both cell lines, suggesting that multiple factors contribute to this effect. These factors may include the high cellular uptake and retention of ITZ/Ce6@LNPs within cellular compartments, as well as

the combined chemo-photodynamic therapy mediated by Ce6 and ITZ. The results further supported the previous findings on cytotoxicity, demonstrating that ITZ/Ce6@LNPs treatment (+L) was more effective in terms of therapeutic impact compared to free ITZ, Ce6, and ITZ+Ce6 treatments
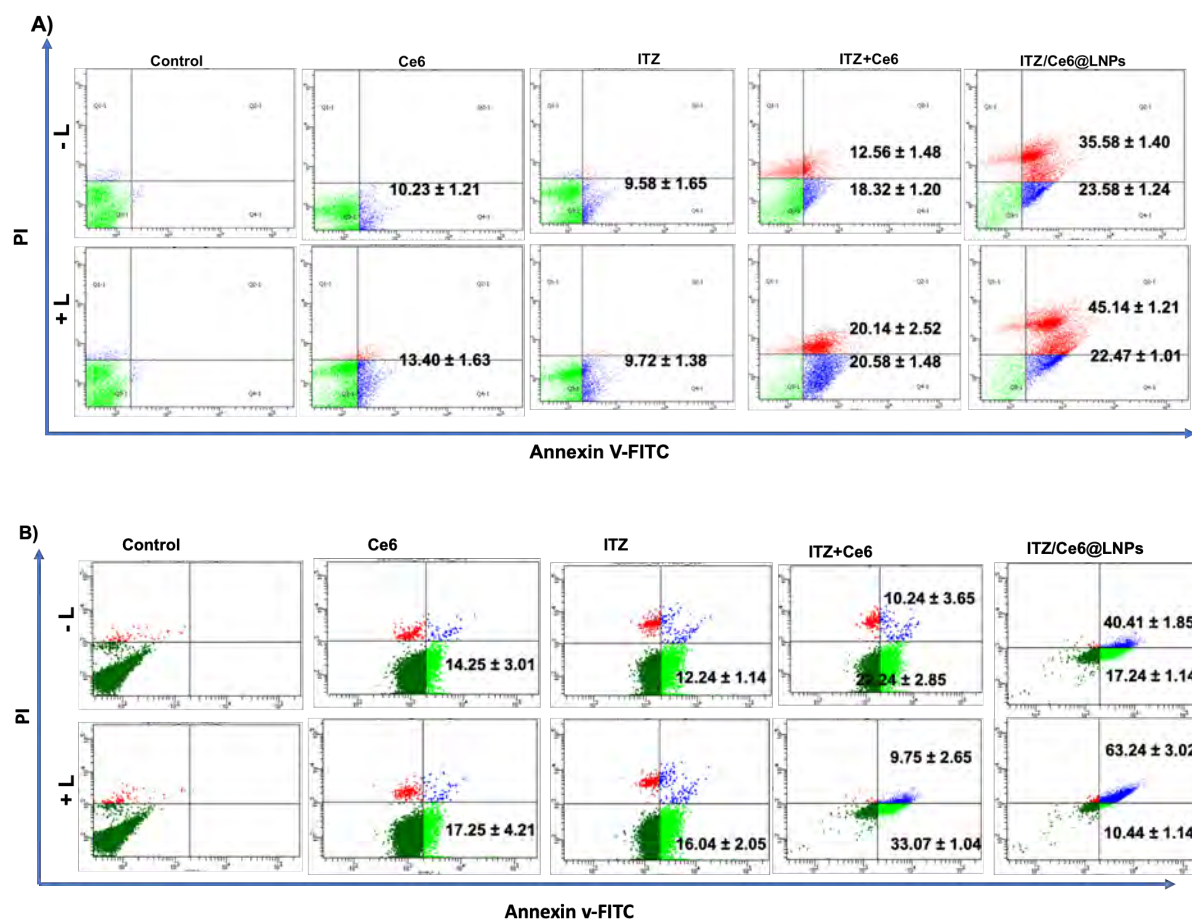
Figure 3.10. Annexin V assay performed by flow cytometry. The extent of apoptosis was evaluated by analyzing B16F10 cells (A) and A431 cells (B) treated with free ITZ, free Ce6, ITZ+Ce6, and ITZ/Ce6@LNPs (with and without laser, +L, -L) at a Ce6 and ITZ concentrations of 10 µg/ml (incubation time. 24 h) by using flow cytometry. Untreated cells are designated as control. The Q3 and Q4 quadrants represent early and late apoptosis, respectively (gated cell number. 10,000); the numerals represent the quantified percent cell populations in Q2 quadrants.

3.3.5.5. Cell Cycle Analysis

Treatment with free ITZ, free Ce6, ITZ+Ce6, and ITZ/Ce6@LNPs induced cell cycle arrest in the G2/M phase in both the tested cell population. The arrest was significantly higher in ITZ/Ce6@LNPs (+ L) -treated cells than in free Ce6, free ITZ, and ITZ+Ce6 treatment. The different phases of the cell population are represented in **Figures 3.11 A and B.** The cell population of ITZ and Ce6 in the G2 phase of B16F10 cells was found to be approximately

7.32-fold and 3.52-fold higher, respectively, compared to untreated cells. Ce6 was observed to induce cell arrest in the early anaphase stage (M-phase), and a similar pattern was observed with all the formulations, with the maximum cell arrest occurring in the G2-M phase as depicted in the graph.
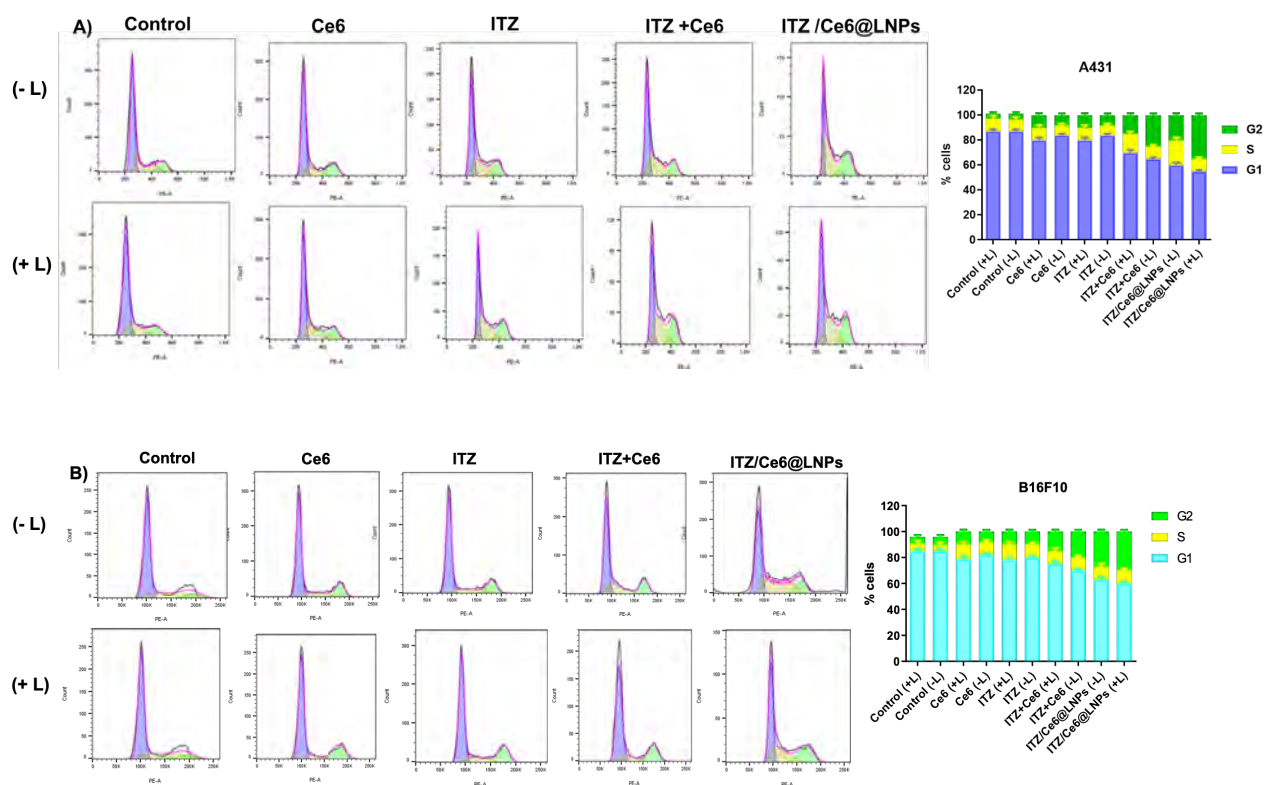
Figure 3.11. Cell cycle arrest by free ITZ, free Ce6, ITZ+Ce6, and ITZ/Ce6@LNPs with and without laser, +L, -L) as analyzed by flow cytometry. Untreated cells are mentioned as a control. The histogram plots (left) and the representative bar graphs (right) show cell populations in various stages of cell cycles.

3.3.5.6. Mitochondrial membrane potential (MMP)

Mitochondrial membrane potential (MMP) refers to the difference in electrical potential across the inner mitochondrial membrane, which is maintained by the proton gradient generated during oxidative phosphorylation. It is a crucial parameter that reflects the functional state of mitochondria and has implications in cellular metabolism, signaling, and apoptosis. JC-1, a cationic dye, is utilized to assess MMP. In healthy mitochondria, JC-1 forms aggregates emitting red fluorescence, while in depolarized or dysfunctional mitochondria, it remains in a monomeric form, emitting green fluorescence. Mitochondrial damage can be exacerbated by the production of reactive oxygen species (ROS), leading to cellular apoptosis. To investigate

the effect of free ITZ, Ce6, ITZ+Ce6, and ITZ/Ce6@LNPs treatment on MMP, we examined A431 and B16F10 cells. Flow cytometry analysis revealed that treatment with ITZ/Ce6@LNPs resulted in a greater disruption of MMP in both cell lines, as depicted in **Figures 3.12A** and **B** (B16F10) and **3.13A and B** (A431).
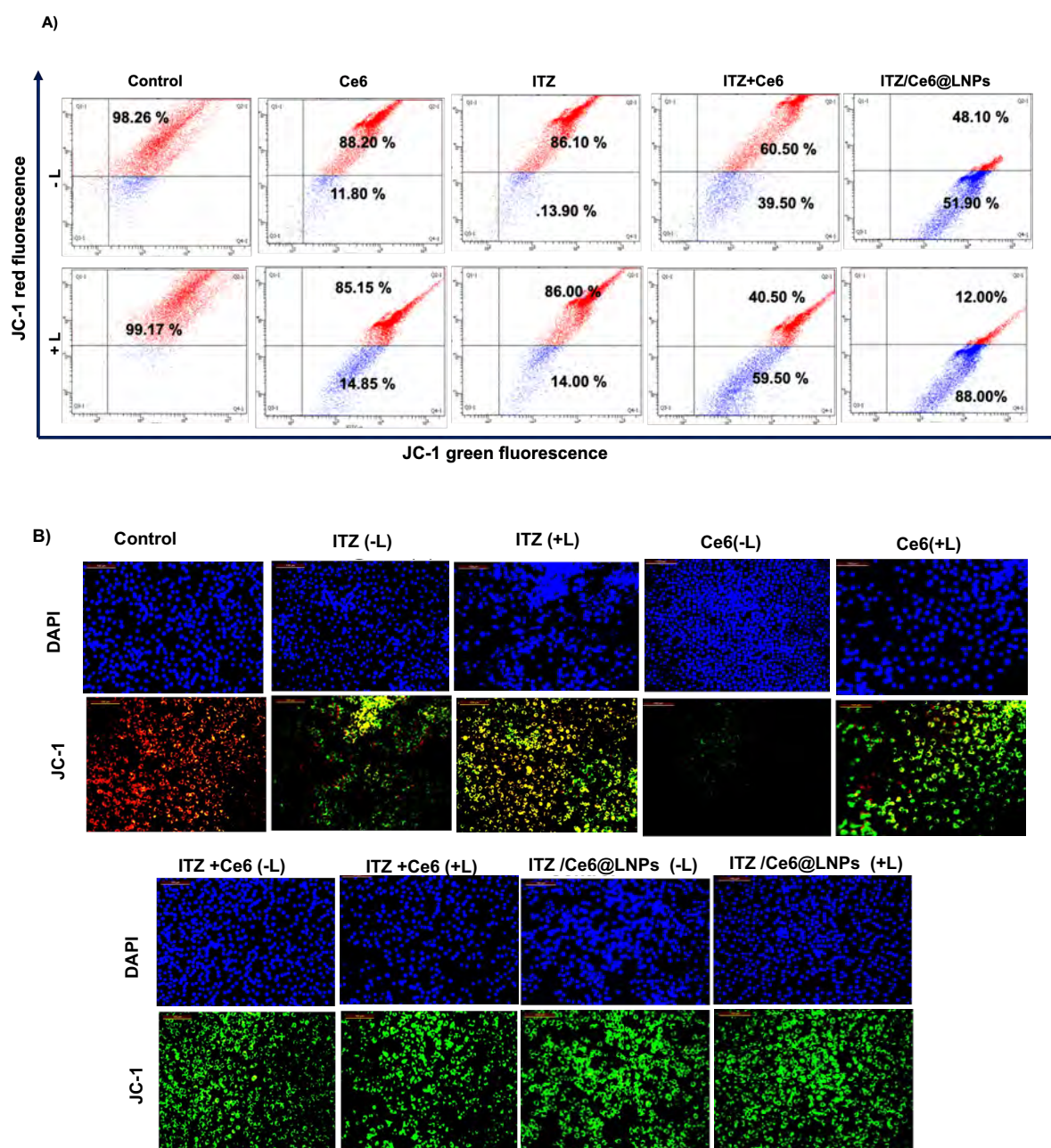
Figure 3.12. Qualitative and quantitative assessment of mitochondrial membrane potential in B16F10 cells treated with free Ce6, ITZ, ITZ+Ce6, ITZ/Ce6@LNPs followed by incubation of cells with mitochondria depolarization indictor JC-1 dye by flow cytometry (A) and fluorescence microscopy (B), and The JC-1 fluorescence was visualized under a laser, ex/em. 488/530 nm in both fluorescence microscopy and flow cytometry. Gated cell population. 10,000 for the flow cytometry analysis.
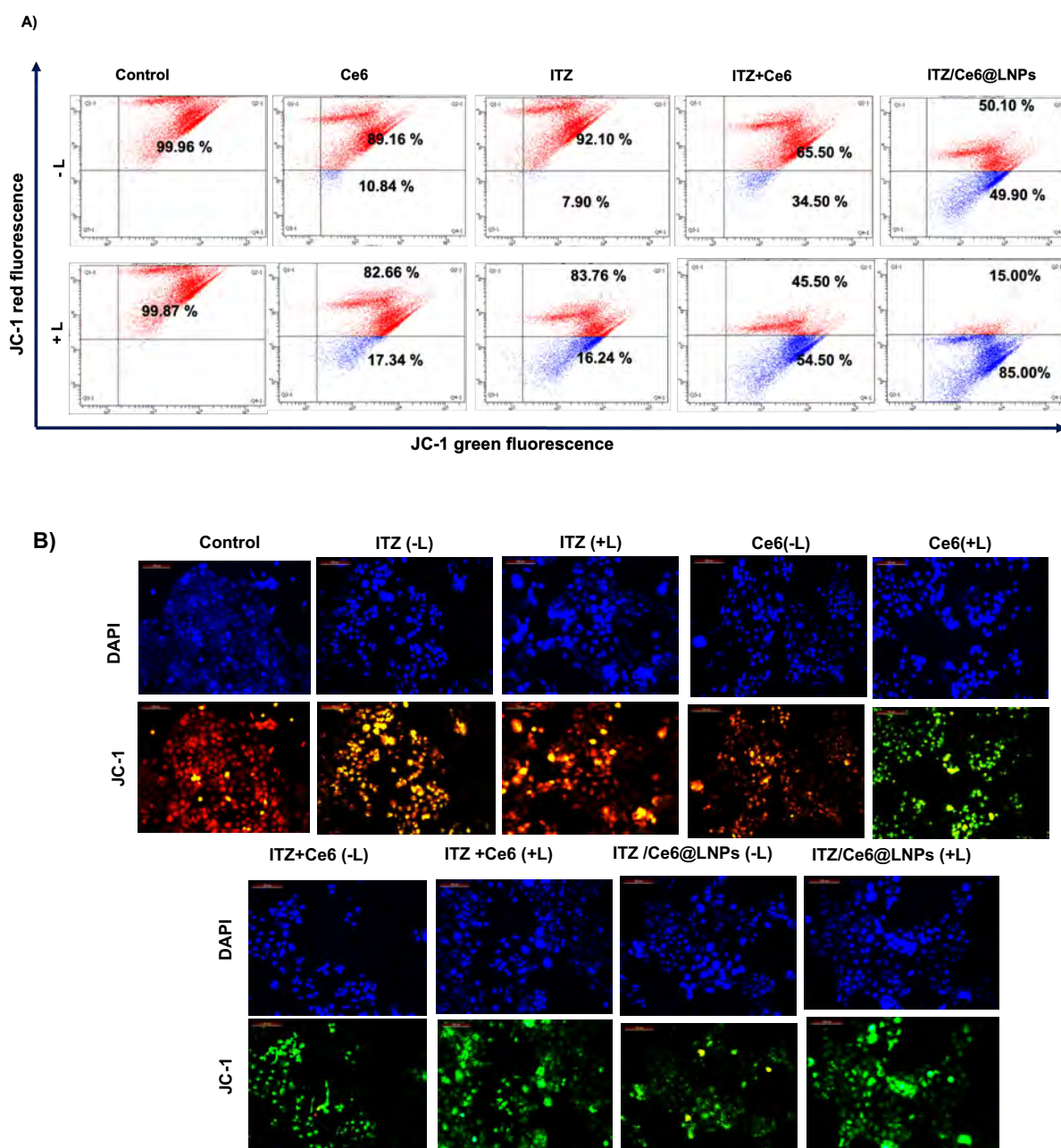
Figure. 3.13 Qualitative and quantitative assessment of mitochondrial membrane potential in A431 cells treated with free Ce6, ITZ, ITZ+Ce6, ITZ/Ce6@LNPs followed by incubation of cells with mitochondria depolarization indictor JC-1 dye by flow cytometry (A) and fluorescence microscopy (B), and the JC-1 fluorescence was visualized under a laser, ex/em. 488/530 nm in both fluorescence microscopy and flow cytometry. Gated cell population. 10,000 for the flow cytometry analysis.

3.3.5.7. DNA Fragmentation Assay

To assess the condition of the DNA, an agarose gel electrophoresis was carried out. The DNA damage caused due to free ITZ, free Ce6, ITZ+Ce6, and ITZ/Ce6@LNPs formulations with (L and +L) on A431 and B16F10 cell lines are represented in **Figures 3.14 A and B and 3.14 C and D.** It was observed that ITZ/Ce6@LNPs with laser irradiation caused the maximum DNA fragmentation (ladder-like pattern) as compared to only ITZ/Ce6 and free Ce6, emphasizing the synergistic effect of ITZ in the formulation.
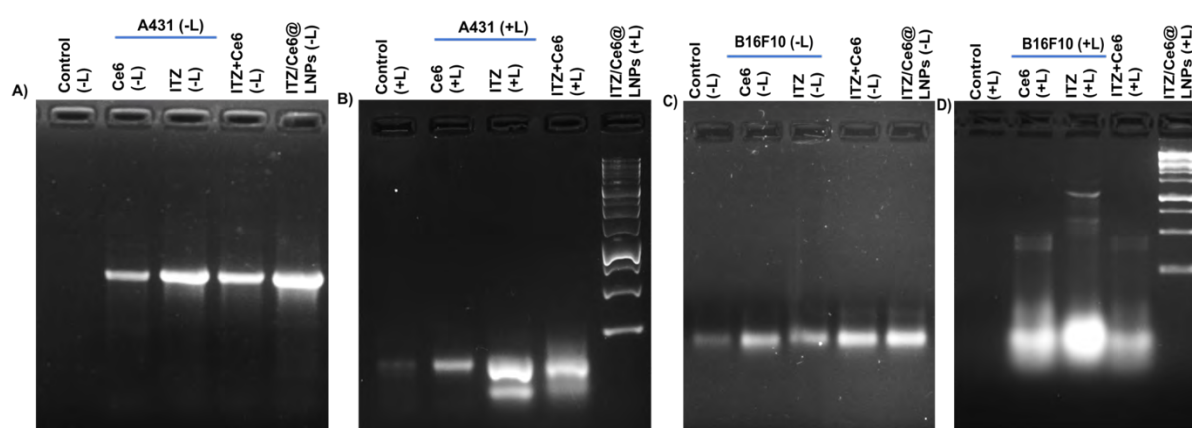
Figure 3.14. DNA fragmentation analysis following treatment with DNA from untreated free Ce6, ITZ, ITZ+Ce6, ITZ/Ce6@LNPs (with and without laser, +L, -L). DNA extracted from B16F10 and A431 cells was viewed on ethidium bromide-stained agarose gel.

3.3.5.8. Reactive oxygen generation assay

To observe the formation of reactive oxygen species (ROS) induced by ITZ/Ce6@LNPs, the intracellular sensor DCFH-DA dye was utilized in both B16F10 and A431 cell lines. Remarkable green fluorescence was observed in B16F10 and A431 cells treated with ITZ, Ce6, ITZ+Ce6, and ITZ/Ce6@LNPs in the presence of laser irradiation. However, no significant green fluorescence was observed in the absence of laser irradiation. These observations suggest that the NPs induced higher intracellular ROS production when combined with laser irradiation. This phenomenon indicates the potential benefits of ITZ/Ce6@LNPs in enhancing the outcomes of chemo-photodynamic combination therapy and effectively killing cancer cells, as depicted in **Figure 3.15A** (B16F10) and **3.15 B** (A431).
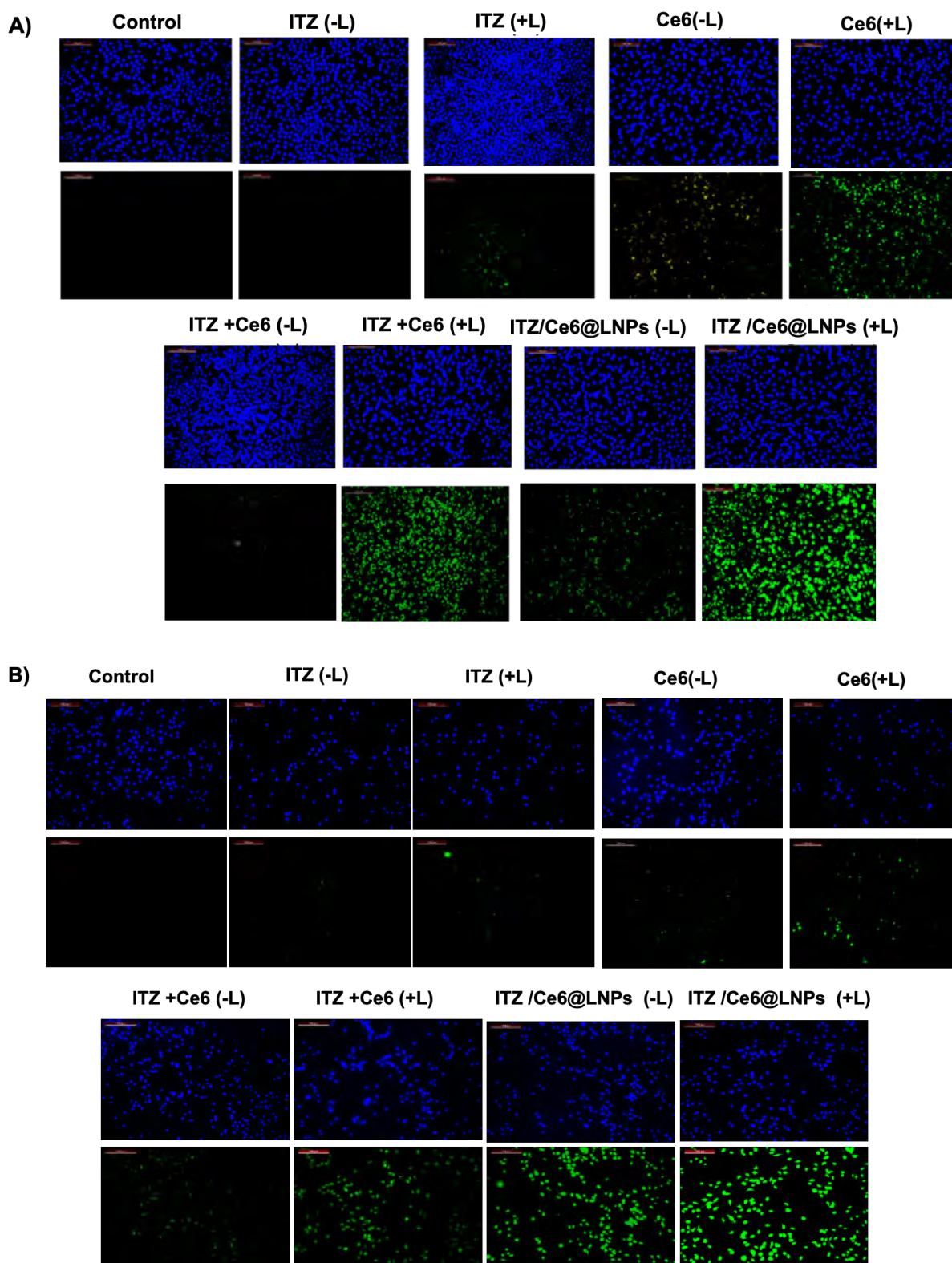
Figure 3.15: Intracellular ROS generation in B16F10 and A431 cells treated with free ITZ, free Ce6, ITZ+Ce6, and ITZ/Ce6@LNPs (with and without laser,+L,-L) by fluorescence microscopy (A) and (B) Untreated cells are designated as control. The ROS level was detected by tracking the fluorescence of DCFHDA dye (ex/em. 488/525 nm).

3.3.5.9. Nuclear staining assay

DAPI is a fluorescent stain that has a strong affinity for A-T-rich regions of DNA, making it useful for visualizing chromatin condensation or nuclear damage. It can differentiate between living cells and apoptotic cells by staining the condensed nuclei of apoptotic cells with a bright blue color. Therefore, we employed DAPI staining to detect apoptosis induction in A431 cells and B16F10 cells treated with ITZ, Ce6, ITZ+Ce6, and ITZ/Ce6@LNPs. **Figures 3.16 A and B** exhibit the nuclear fragmentation (NF) and cytoplasmic shrinkage (CS) observed in the cells with the various treatments. Blebbing was observed, which is considered a marker for apoptosis. It was observed that the cells treated with ITZ/Ce6@LNPs formulation showed the highest cellular damage highlighting the synergistic effect of Ce6 and ITZ. The AO-EtBr techniques were used in order to provide an understanding of the mechanism in which cells died, namely in terms of apoptosis and necrosis. The vital dye AO can stain every cell, whether they are alive or dead, while cells whose membrane integrity has been disrupted can take up the stain EtBr. And hence, normal cells which remain intact appear to be green, whereas cells that are in the early or late stages of apoptosis and have compressed or damaged nuclei appear to be yellowish-orange or reddish, respectively. AO penetrated normal or early apoptotic cells, producing green fluorescence after binding with DNA. However, EB could only enter through damaged membranes and emitted orange-red fluorescence after binding to condensed apoptotic nuclei. In contrast, necrotic cells stain orange but possess normal nuclear morphology with no condensed chromatin. The assay could detect normal cells, cells at different stages of apoptosis, and necrotic cells by changing cellular fluorescence and morphology. Both B16F10 and A431 cell lines were undergoing apoptosis after ITZ/Ce6@LNPs treatment, as indicated by an orange fluorescence.
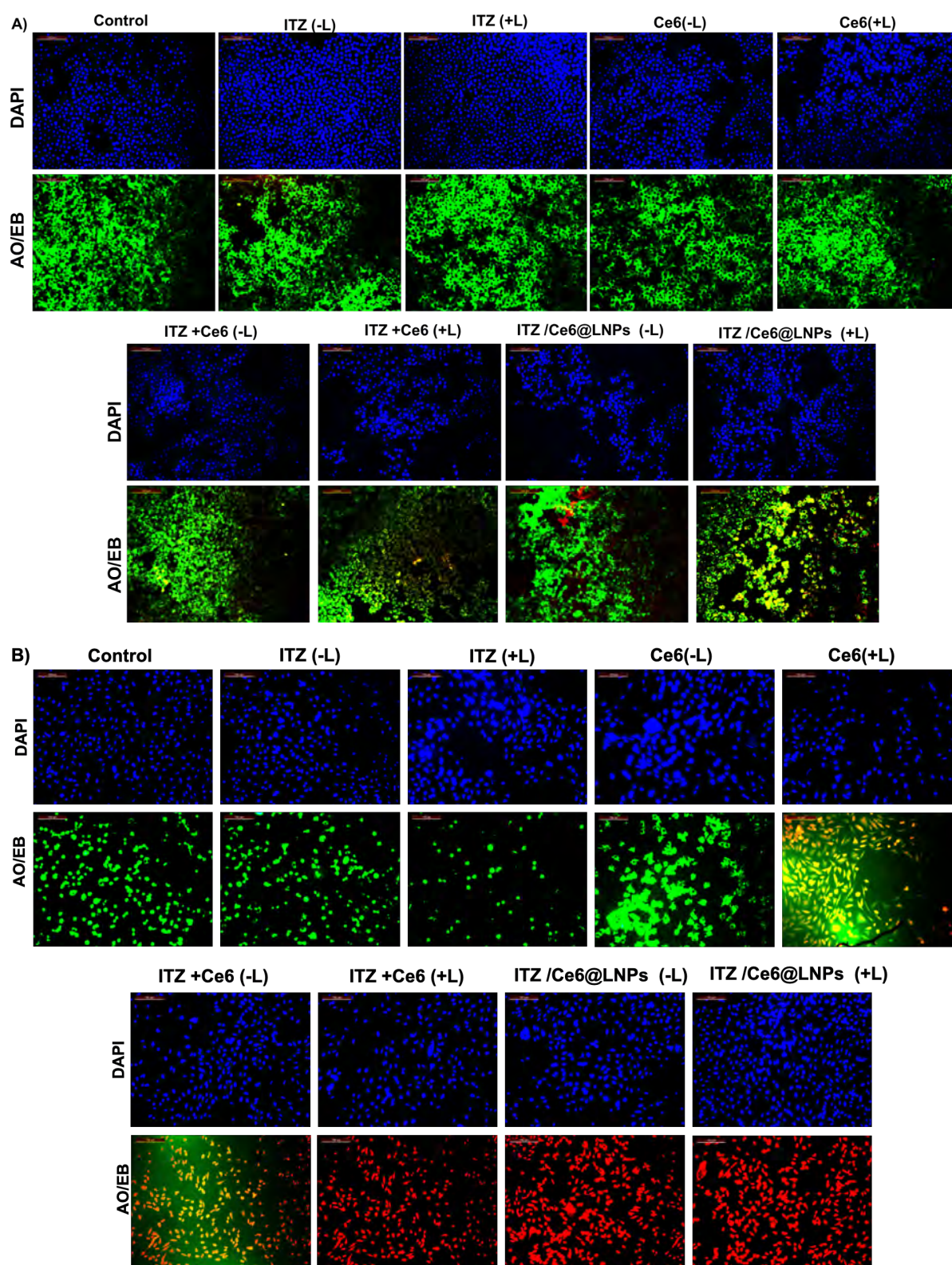
Figure 3.16. Analysis of nuclear morphology. Examples of B16F10 (A) and A431 cells (B) stained with DAPI, acridine Orange, and ethidium bromide following the treatment by free ITZ, free Ce6, ITZ+Ce6, and ITZ/Ce6@LNPs (ITZ and Ce6 concentration 10 µg/ml) (control cells received no treatment) (with and without laser, +L, -L), visualized under a fluorescence microscope on 40x Magnification. Scale bar. 100 µm.

3.3.6. Ex-vivo Studies

3.3.6.1. Ex-vivo Skin Permeation Study

The Franz diffusion cell, was utilized in the skin permeation study. **Figure 3.17 A** shows the *ex-vivo* permeation of ITZ/Ce6@LNPs and plain gel (ITZ+Ce6) formulation permeated through goat skin. The amount of ITZ and Ce6 permeated (% permeation) through ITZ/Ce6@LNPs gel and plain gel (ITZ+Ce6) after 24 h was found to be up to 78 % and 30 %, respectively **(Figure 3.17 A).** The permeation ($\mu g/cm^2$) of ITZ and Ce6 drugs from ITZ/Ce6@LNPs gel and plain gel (ITZ+Ce6) through the goat skin was about upto 68 $\mu g/cm^2/24$ h and up to 30 $\mu g/cm^2/24$ h respectively **(Figure 3.17 B),** which indicates ITZ/Ce6@LNPs gel has significantly higher skin permeation than the plain (ITZ+Ce6) The flux value of ITZ/Ce6@LNPs gel containing ITZ and Ce6 was found to be 7.1303 ± 0.97 $\mu g/cm^2/h$, 6.296 ± 0.24 $\mu g/cm^2/h$ respectively. Additionally, the flux values of plain gel (ITZ+Ce6) containing ITZ and Ce6 were found to be 1.4166 ± 0.32 $\mu g/cm^2/h$, 1.1803 ± 0.21 $\mu g/cm^2/h$, respectively. The ITZ/Ce6@LNPs gel demonstrated more ability to penetrate the goat skin than the plane gel, which was attributable to the enhancement of penetration by the DOTAP lipid (cationic charge-based lipid), solid lipid, and liquid lipid. The positively charged head group of the cationic lipid can interact with the negatively charged head groups of the lipids in the stratum corneum. This interaction can disrupt the organized structure of the stratum corneum and create temporary pathways for the drug to penetrate the skin. Additionally, the positively charged head group of the cationic lipid can interact with the negatively charged cell membranes of the skin cells, which can facilitate the penetration of the drug into the skin. Furthermore, positive charge lipids can also form complexes with drugs, called cationic lipid-drug complexes. These complexes can improve the solubility and stability of drugs, allowing them to penetrate the skin more effectively. Additionally, Positive charge-based lipids (DOTAP) can form an interaction between extracellular lipid matrices of the skin resulting in the disruption of lipid orientation, which creates the diffusion or pathway to cross nanoparticles through the skin.
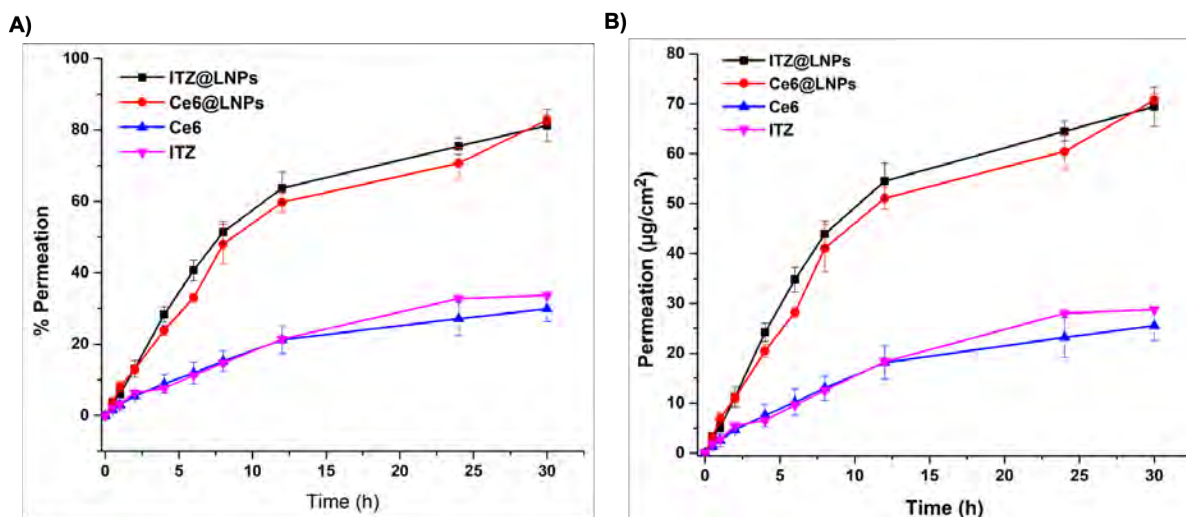
Figure 3.17. Ex vivo skin permeation profile of ITZ/Ce6@LNPs and free ITZ and free Ce6 permeated through the skin (% Permeation) (Data represented as mean ± SD, n = 3) (A); Ex vivo skin permeation profile of ITZ/Ce6@LNPs and free ITZ and Ce6 permeated through the skin ($\mu g/cm^2$) (Data represented as mean ± SD, n = 3) (B).

3.3.6.2. Ex vivo bioimaging in tumor skin of the C57/BL6 mice

In **Figure 3.18A** of the study, the bioimaging results of tape-stripped ex vivo skin cancer tissue are presented. The tissue was treated with either free ITZ+Ce6 gel or ITZ/Ce6@LPNs gel for 6, 12, and 24 h using Franz diffusion cells. Images were captured using the In Vivo Imaging System (IVIS PerkinElmer, Inc., USA) to excite Ce6 at 405 nm and record the corresponding emission at 665 nm. The results demonstrate that the ITZ/Ce6@LPNs gel exhibited significantly higher fluorescence compared to the free ITZ+Ce6 gel at all time points. This indicates that the incorporation of ITZ/Ce6 into LPNs enhanced the penetration of the drug into deeper layers of the skin.

A)
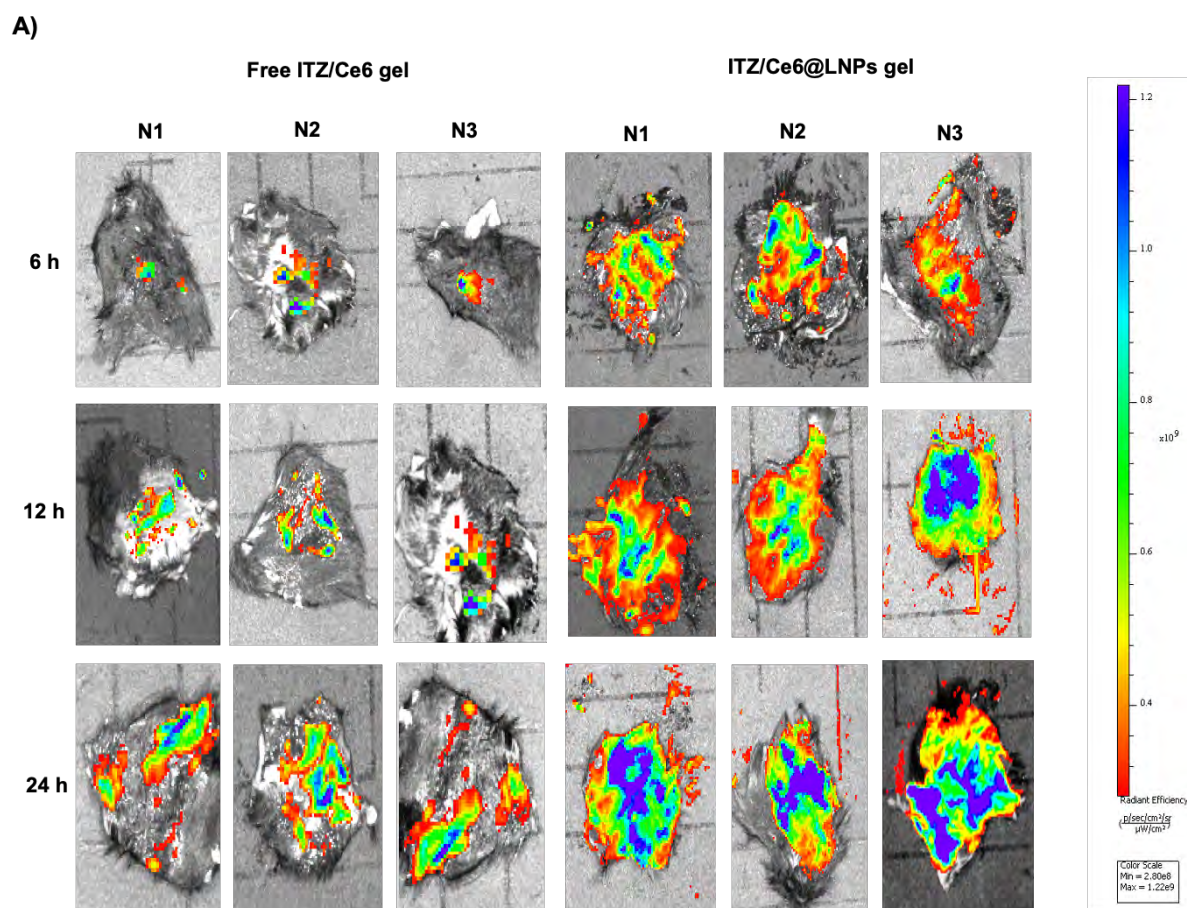
Figure 3.18. A Bio-imaging using IVIS spectrum of tape-stripped ex vivo skin cancer tissue treated with either free ITZ+Ce6 gel or ITZ/Ce6@LPNs gel at 6, 12, and 24 h (Data represented as mean ± SD, n = 3).

3.3.6.3. Topical In Vivo Biodistribution Study in C57/BL6 Mice Skin Cancer Model

The biodistribution of free Ce6 and ITZ/Ce6@LNPs gel was investigated topically in B16F10 tumor-bearing mice to study there in vivo distribution. The fluorescence distribution of Ce6 was observed at various time points (0.5, 1, 3, 6, 12, 24, and 48 h) after topical application. The results showed that the fluorescence intensity at the tumor site of the ITZ/Ce6@LNPs gel-treated group gradually increased up to 12 h post-application. In contrast, the free Ce6-treated group exhibited a significantly lower signal, indicating that the ITZ/Ce6@LNPs gel may accumulate more effectively at the tumor site (**Figure 3.19A**). **Figure 3.19B** demonstrates the total body fluorescence intensity over time. It can be observed that even 48 h after topical application, the tumor in the ITZ/Ce6@LNPs gel-treated group still exhibited a strong fluorescence signal, indicating the high targeting and retention capacity of the ITZ/Ce6@LNPs gel. The mice were topically treated with ITZ/Ce6@LNPs gel, and after 48 h, they were

sacrificed, and their major organs and tumor tissues were collected for fluorescence imaging, as depicted in **Figure 3.19 C**. However, there was still some measurable ITZ/Ce6@LNPs fluorescence present in the tumor, resulting in a significantly higher accumulation of ITZ/Ce6@LNPs observed in the tumor tissue. it suggests that they are selectively accumulating in the target tissue (superficial skin cancer), which is a desirable outcome for ITZ/Ce6@LNPs gel.
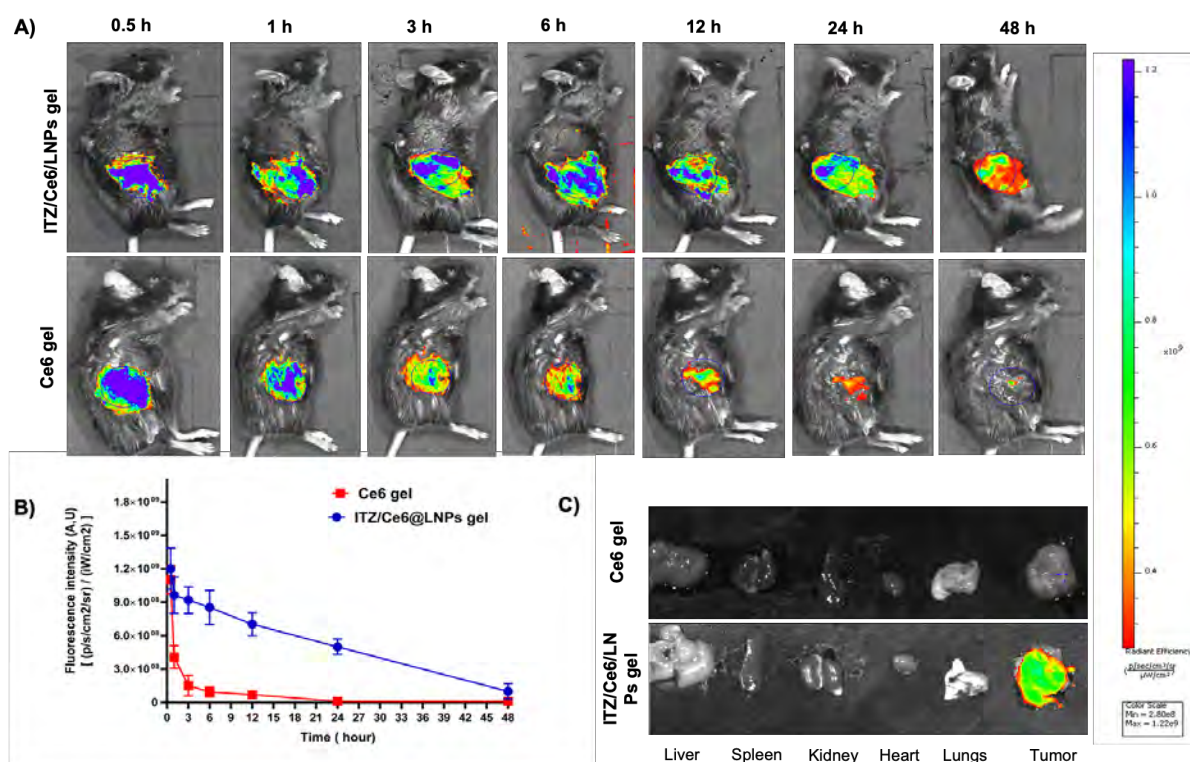
Figure 3.19: In vivo Biodistribution evaluation by IVIS live tumor-bearing mice after topical application of Ce6+ITZ gel, ITZ/Ce6@LNPs gel at various predetermined time points (0.5 h to 48 h) (A); The fluorescence intensity for the region of interest (tumor-bearing mice) was recorded as total photon counts per tumor (B); Ex vivo NIR fluorescence images of major organs and tumor excised at 48 h post-treatment of topical gel (with Ce6+ITZ gel, ITZ/Ce6@LNPs gel) (C).

3.3.6.4. In vivo antitumor activity of ITZ/Ce6/LNPs gel

To assess the in vivo anticancer potential of the ITZ/Ce6/LNPs gel, we conducted experiments following the promising results obtained from the combined chemo-photodynamic therapy in vitro. The tumor volume growth rate was observed to be faster in the PBS-treated control (Blank Gel) group compared to the other treated groups. Notably, the ITZ/Ce6/LNPs gel

exhibited the slowest rate of increase in tumor volume. The average tumor volumes at the end of the eight-day period were measured as 708 ± 31 mm3, 502 ± 10 mm3, 545 ± 17 mm3, 402 ± 10 mm3, and 170 ± 18 mm3 for the control, free Ce6, ITZ, ITZ+Ce6, and ITZ/Ce6/LNPs gel, respectively (**Figure 3.20A and 3.20 B**). Furthermore, we monitored the body weights of the mice throughout the experiment. **Figure 3.20 C** demonstrates that the body weight of the mice in all experimental groups did not show significant changes, indicating good biocompatibility and biosafety of the ITZ/Ce6/LNPs gel when applied in vivo.

Additionally, the tumor weight in the ITZ/Ce6/LNPs gel-treated group was significantly reduced compared to the control, free Ce6, ITZ, and ITZ+Ce6 groups (**Figure 3.20 D**). These findings further support the potential of the ITZ/Ce6/LNPs gel as an effective therapeutic approach for tumor growth inhibition.
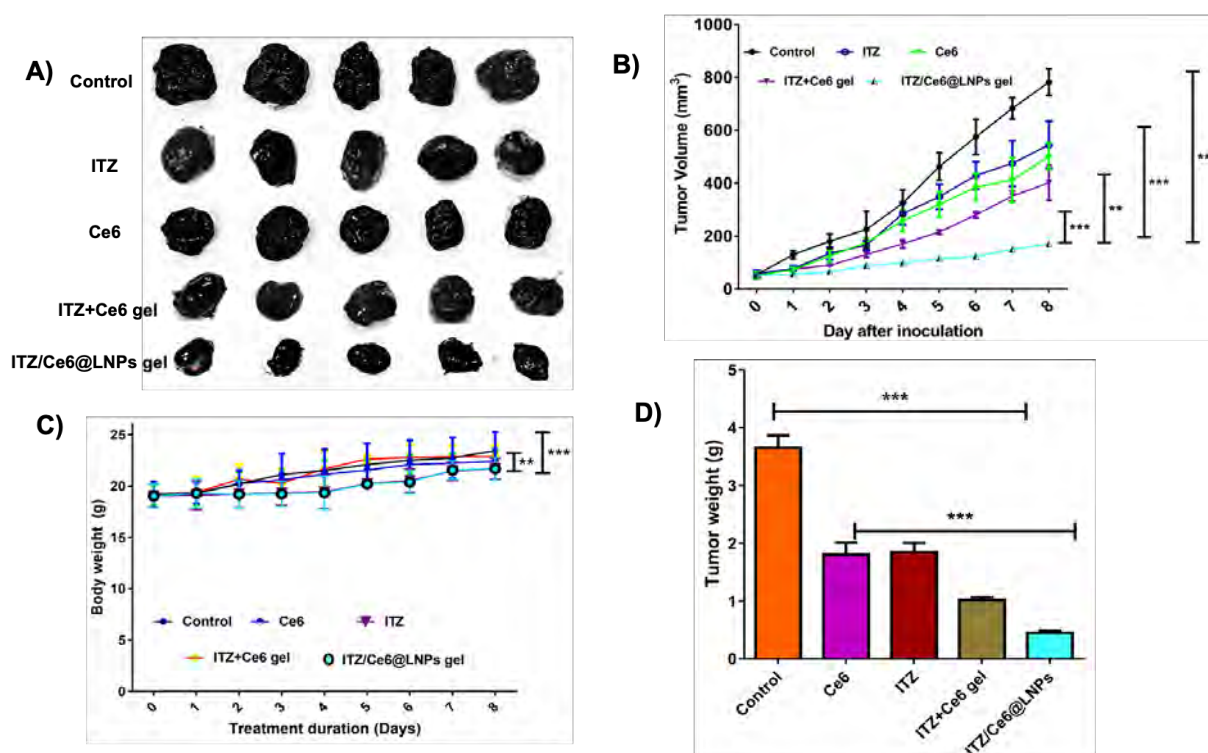
Figure 3.20. Evaluation of in vivo therapeutic efficacy of Ce6, ITZ, ITZ+Ce6 gel, and ITZ/Ce6@LNPs at ITZ equivalent dose of 2.5 mg/kg or a Ce6 dose of 2.5 mg/kg with laser light (666 nm 0.5 W/cm^2 for 5 min) in B16F10 tumor-bearing mice. images of tumors collected randomly from mice that received treatment as mentioned (A); Graph representing the tumor volume reduction over time. (B); Graphical representation of the body weight over time (C); a Bar graph representing tumor weight of individual groups after study (D) ***p < 0.005.

3.3.6.5. Immunohistochemical Analysis

To further evaluate the therapeutic effect of the treatments, we performed additional analyses on the tumor tissues. The tumor tissues were stained with DCFDA dye to assess the levels of reactive oxygen species (ROS). The terminal deoxynucleotidyl transferase-mediated dUTP nick end labeling (TUNEL) assay was used to detect apoptotic cells, while Ki-67 immunohistochemistry was employed to identify proliferating cells. These analyses provided valuable insights into the cellular response and therapeutic efficacy of the treatments. Our in-vitro efficacy studies have shown that the combination of ITZ+Ce6 and ITZ/Ce6@LNPs can effectively induce cancer cell death through the generation of ROS. To further investigate the therapeutic effect in an in vivo setting, we conducted a study where tumor tissues were treated with ITZ/Ce6@LNPs and the generation of reactive oxygen species (ROS) was measured using DCFH-DA fluorescence and the IVIS-Lumina in-vivo imaging system. The results of this study are presented in **Figure 3.21 A** and **B**. Additionally, the ROS and TUNEL assays showed increased green fluorescence in tumor samples treated with ITZ/Ce6@LNPs gel compared to other treatment groups, indicating a higher number of apoptotic cells and significant ROS production. In the Ki-67 assay, higher cell proliferation was observed in the control group (displaying the greenest fluorescence), while the ITZ/Ce6@LNPs gel treatment group showed the least proliferation, indicating reduced tumor growth. These results are presented in **Figure 3.22 A** and **B**. Furthermore, organ damage in the treatment groups was assessed through hematoxylin and eosin (H&E) staining. No histological damage was observed in other organs, such as the kidney, lungs, spleen, and liver, indicating low toxicity of the formulation (**Figure 3.23**).
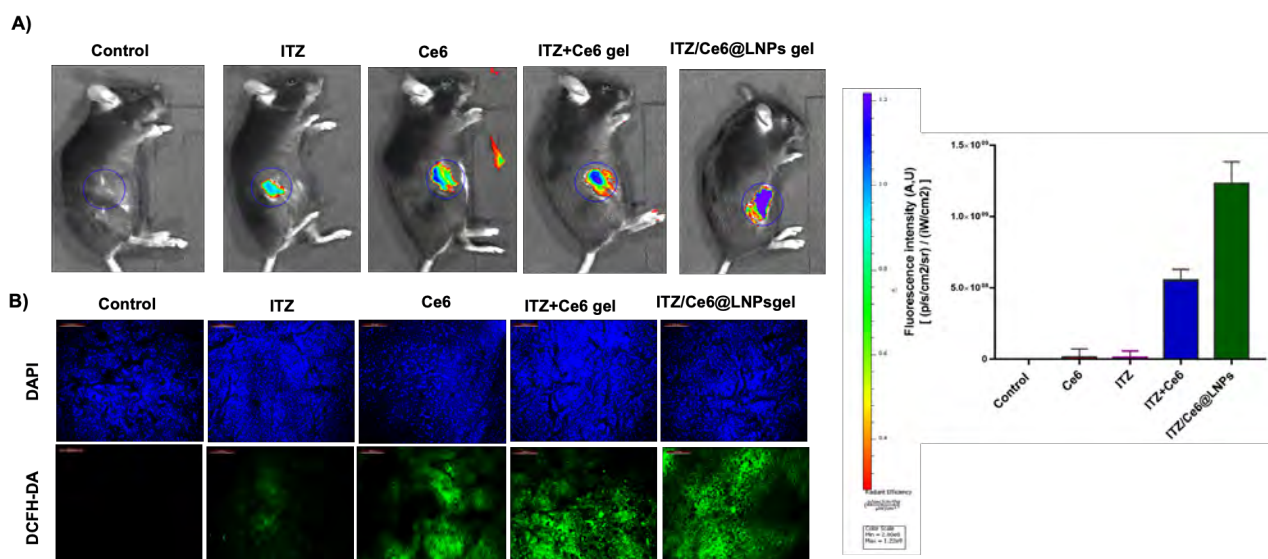
Figure 3.21. In-vivo ROS analysis: DCFH-DA fluorescent images of the whole body of the mice with different treatments (A); Total body fluorescent intensity analysis. DAPI (blue) and DCFH-DA (green) fluorescence images of the sectioned tumor tissues (B).
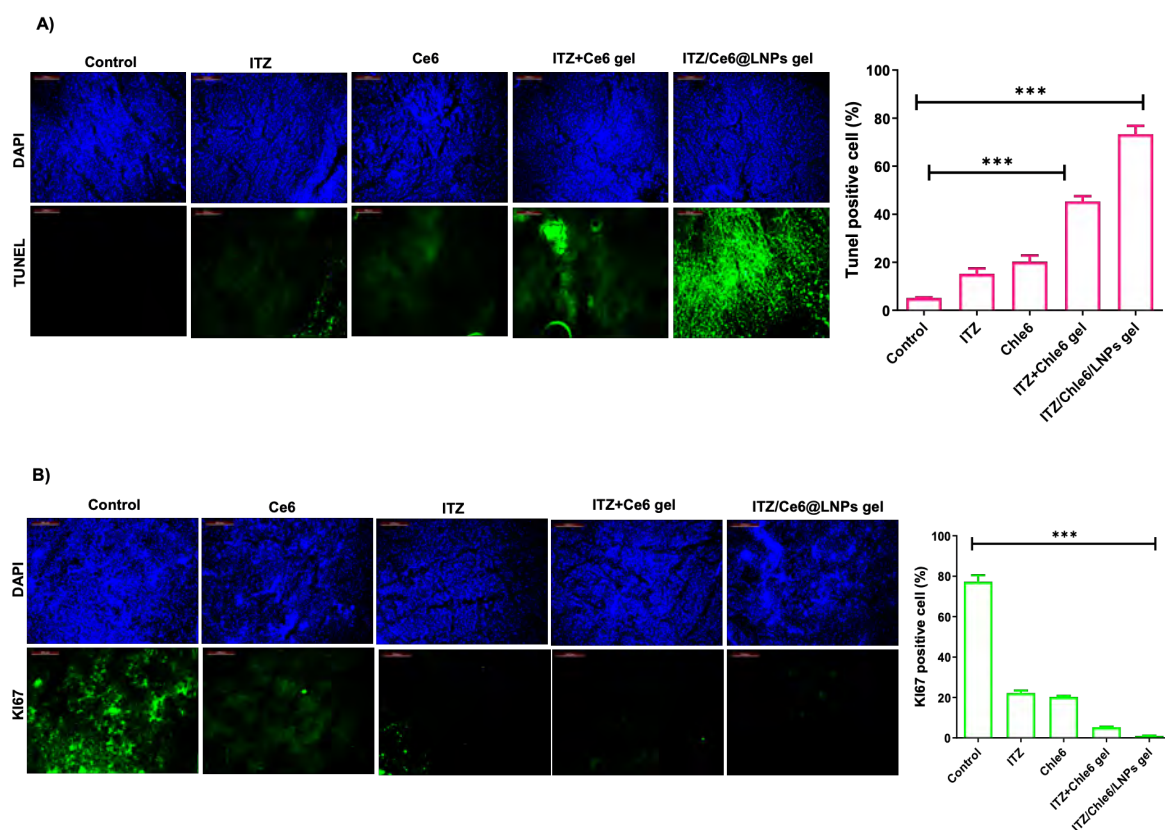
Figure 3.22. Effect of Ce6, ITZ, ITZ+Ce6 gel, and ITZ/Ce6@LNPs treatment on tumor Evaluation of apoptosis in tumor tissues by TUNEL assay (A); Quantification of fluorescence (TUNEL Positive cells %) from TUNEL assay (B); Evaluation of cell proliferation in tumor

tissues by Ki67 immunohistofluorescence assay (C); Quantification of fluorescence (Ki67 Positive cells %) from Ki67 immunohistofluorescence assay. ***$p < 0.005$.
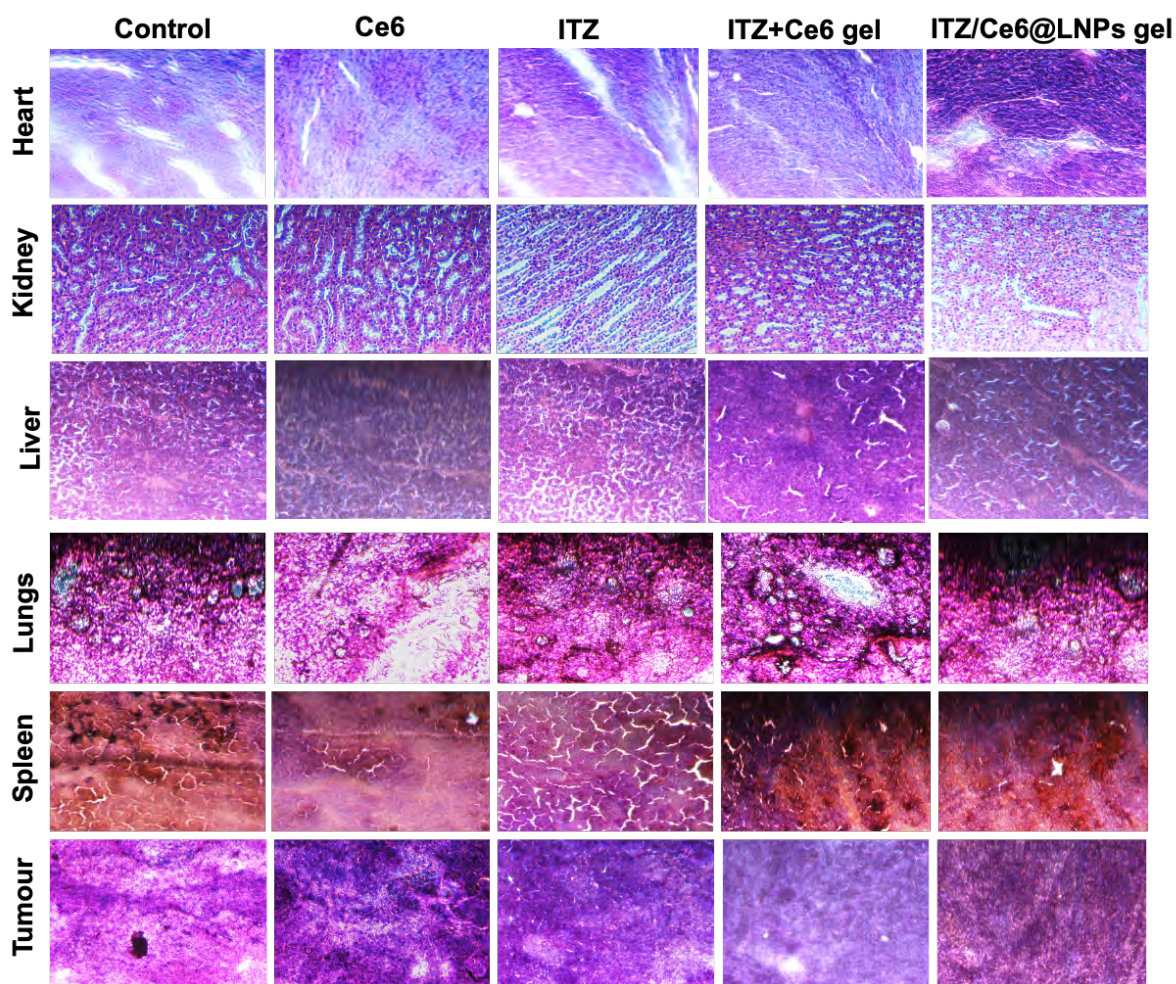
Figure 3.23. Histopathological analysis of frozen organ sections from mice was conducted using 5µm-thick slices stained with hematoxylin and eosin. The staining allowed for the differentiation of the nucleus (appearing purple) and cytoplasm (appearing pink).

Conclusion: In summary, photo-triggered ROS-generating dual drug-based lipidic nanostructured particles were designed for synergistic effects against basal cell and melanoma cancer. In this work, chlorine e6 as a photosensitizer and ITZ as an anticancer agent (Repurposing agent) encapsulated in lipid nanocarriers and embedded in the SEPINEO gel to enhance the skin and tumor penetration. The optimized formulation showed a uniform nano-size range with high entrapment efficiency for both drugs. This developed dual-drug formulation gel provided high skin penetration and exhibited higher singlet oxygen generation and stability. The skin retention study showed that ITZ/Ce6@LNPs gel has high skin retention compared to the free drugs (ITZ+Ce6), which was confirmed by the IVIS. On a cellular level, the combined formulation showed an excellent synergetic effect compared to free drugs on the B16F10 and A431 cell lines. Moreover, a cellular uptake study with B16F10 and A431 revealed that ITZ/Ce6@LNPs show higher cellular uptake than free drugs. The in vivo antitumor efficacy study demonstrated a significant reduction in tumor weight in the group treated with ITZ/Ce6/LNPs gel compared to the control, free Ce6, ITZ, and ITZ+Ce6 groups. The combination of ITZ and Ce6 delivery by a lipidic system exhibits more therapeutic efficiency than the individual treatment. This lipidic system may provide a unique platform for delivering potent hydrophobic moiety for different ill conditions such as cancer, psoriasis, skin infections, etc. It may also be adequate for clinical testing and commercial application.

References :

[1]   P. Koelblinger, R. Lang, New developments in the treatment of basal cell carcinoma: Update on current and emerging treatment options with a focus on vismodegib, Onco Targets Ther. 11 (2018) 8327–8340. https://doi.org/10.2147/OTT.S135650.

[2]   S. Lucena, N. Salazar, T. Gracia-Cazaña, A. Zamarrón, S. González, Á. Juarranz, Y. Gilaberte, Combined Treatments with Photodynamic Therapy for Non-Melanoma Skin Cancer, Int J Mol Sci. 16 (2015) 25912–25933. https://doi.org/10.3390/ijms161025912.

[3]   Basal cell carcinoma pathogenesis and therapy involving hedgehog signaling and beyond, (n.d.). https://www.ncbi.nlm.nih.gov/pmc/articles/PMC5962346/ (accessed January 28, 2021).

[4]   A. Bakshi, S.C. Chaudhary, M. Rana, C.A. Elmets, M. Athar, Basal cell carcinoma pathogenesis and therapy involving hedgehog signaling and beyond, Mol Carcinog. 56 (2017) 2543–2557. https://doi.org/10.1002/mc.22690.

[5]   N. Mahindroo, C. Punchihewa, N. Fujii, Hedgehog-Gli signaling pathway inhibitors as anticancer agents, J Med Chem. 52 (2009) 3829–3845. https://doi.org/10.1021/jm801420y.

[6]   M. Wahid, A. Jawed, R.K. Mandal, S.A. Dar, S. Khan, N. Akhter, S. Haque, Vismodegib, itraconazole and sonidegib as hedgehog pathway inhibitors and their relative competencies in the treatment of basal cell carcinomas, Crit Rev Oncol Hematol. 98 (2016) 235–241. https://doi.org/10.1016/j.critrevonc.2015.11.006.

[7]   R. Pounds, S. Leonard, C. Dawson, S. Kehoe, Repurposing itraconazole for the treatment of cancer (review), Oncol Lett. 14 (2017) 2587–2597. https://doi.org/10.3892/ol.2017.6569.

[8]   G.K. Sohn, G.P. Kwon, I. Bailey-Healy, A. Mirza, K. Sarin, A. Oro, J.Y. Tang, Topical Itraconazole for the Treatment of Basal Cell Carcinoma in Patients with Basal Cell Nevus Syndrome or High-Frequency Basal Cell Carcinomas: A Phase 2, Open-Label, Placebo-Controlled Trial, JAMA Dermatol. 155 (2019) 1078–1080. https://doi.org/10.1001/jamadermatol.2019.1541.

[9]   G. Liang, M. Liu, Q. Wang, Y. Shen, H. Mei, D. Li, W. Liu, Itraconazole exerts its anti-melanoma effect by suppressing Hedgehog, Wnt, and PI3K/mTOR signaling pathways, Oncotarget. 8 (2017) 28510–28525. https://doi.org/10.18632/oncotarget.15324.

[10]   J. Kim, B.T. Aftab, J.Y. Tang, D. Kim, A.H. Lee, M. Rezaee, J. Kim, B. Chen, E.M. King, A. Borodovsky, G.J. Riggins, E.H. Epstein, P.A. Beachy, C.M. Rudin, Itraconazole and Arsenic Trioxide Inhibit Hedgehog Pathway Activation and Tumor Growth Associated with Acquired Resistance to Smoothened Antagonists, Cancer Cell. 23 (2013) 23–34. https://doi.org/10.1016/j.ccr.2012.11.017.

[11]   J. Kim, J.Y. Tang, R. Gong, J. Kim, J.J. Lee, K. V. Clemons, C.R. Chong, K.S. Chang, M. Fereshteh, D. Gardner, T. Reya, J.O. Liu, E.H. Epstein, D.A. Stevens, P.A. Beachy, Itraconazole, a Commonly Used Antifungal that Inhibits Hedgehog Pathway Activity

and Cancer Growth, Cancer Cell. 17 (2010) 388–399. https://doi.org/10.1016/j.ccr.2010.02.027.

[12] R. Jain, R. Pradhan, S. Hejmady, G. Singhvi, S.K. Dubey, Fluorescence-based method for sensitive and rapid estimation of chlorin e6 in stealth liposomes for photodynamic therapy against cancer, Spectrochim Acta A Mol Biomol Spectrosc. 244 (2021) 118823. https://doi.org/10.1016/J.SAA.2020.118823.

[13] L. Li, B.C. Bae, T.H. Tran, K.H. Yoon, K. Na, K.M. Huh, Self-quenchable biofunctional nanoparticles of heparin–folate-photosensitizer conjugates for photodynamic therapy, Carbohydr Polym. 2 (2011) 708–715. https://doi.org/10.1016/J.CARBPOL.2011.05.011.

[14] P. Huang, Z. Li, J. Lin, D. Yang, G. Gao, C. Xu, L. Bao, C. Zhang, K. Wang, H. Song, H. Hu, D. Cui, Photosensitizer-conjugated magnetic nanoparticles for in vivo simultaneous magnetofluorescent imaging and targeting therapy, Biomaterials. 32 (2011) 3447–3458. https://doi.org/10.1016/J.BIOMATERIALS.2011.01.032.

[15] C. Yang, H. Chen, J. Zhao, X. Pang, Y. Xi, G. Zhai, Development of a folate-modified curcumin loaded micelle delivery system for cancer targeting, Colloids Surf B Biointerfaces. 121 (2014) 206–213. https://doi.org/10.1016/J.COLSURFB.2014.05.005.

[16] S.J. Lee, H. Koo, H. Jeong, M.S. Huh, Y. Choi, S.Y. Jeong, Y. Byun, K. Choi, K. Kim, I.C. Kwon, Comparative study of photosensitizer loaded and conjugated glycol chitosan nanoparticles for cancer therapy, J Control Release. 152 (2011) 21–29. https://doi.org/10.1016/J.JCONREL.2011.03.027.

[17] M. Hoebeke, X. Damoiseau, Determination of the singlet oxygen quantum yield of bacteriochlorin a: a comparative study in phosphate buffer and aqueous dispersion of dimiristoyl-L-α-phosphatidylcholine liposomes, Photochemical & Photobiological Sciences. 1 (2002) 283–287. https://doi.org/10.1039/B201081J.

[18] V.K. Rapalli, S. Sharma, A. Roy, G. Singhvi, Design and dermatokinetic evaluation of Apremilast loaded nanostructured lipid carriers embedded gel for topical delivery: A potential approach for improved permeation and prolong skin deposition, Colloids Surf B Biointerfaces. 206 (2021) 111945. https://doi.org/10.1016/J.COLSURFB.2021.111945.

[19] S.M. Gandhi, A.K. Khan, S. Rathod, R. Jain, S.K. Dubey, D. Ray, V.K. Aswal, A. Joshi, P. Bahadur, S. Tiwari, Water driven transformation of a nonionic microemulsion into liquid crystalline phase: Structural characterizations and drug release behavior, J Mol Liq. 326 (2021) 115239. https://doi.org/10.1016/J.MOLLIQ.2020.115239.

[20] S. Kumbham, M. Paul, A. Itoo, B. Ghosh, S. Biswas, Oleanolic acid-conjugated human serum albumin nanoparticles encapsulating doxorubicin as synergistic combination chemotherapy in oropharyngeal carcinoma and melanoma, Int J Pharm. 614 (2022). https://doi.org/10.1016/J.IJPHARM.2022.121479.

[21] S. Kumbham, M. Paul, H. Bhatt, B. Ghosh, S. Biswas, Oleanolic acid-conjugated poly (D, L-lactide)-based micelles for effective delivery of doxorubicin and combination

chemotherapy in oral cancer, J Mol Liq. 320 (2020). https://doi.org/10.1016/J.MOLLIQ.2020.114389.

[22] S. Gorantla, E.R. Puppala, V.G.M. Naidu, R.N. Saha, G. Singhvi, Hyaluronic acid-coated proglycosomes for topical delivery of tofacitinib in rheumatoid arthritis condition: Formulation design, in vitro, ex vivo characterization, and in vivo efficacy studies, Int J Biol Macromol. (2022). https://doi.org/10.1016/J.IJBIOMAC.2022.10.117.

[23] M. Shah, K. Pathak, Development and Statistical Optimization of Solid Lipid Nanoparticles of Simvastatin by Using 23 Full-Factorial Design, AAPS PharmSciTech. 11 (2010) 489. https://doi.org/10.1208/S12249-010-9414-Z.

[24] A. Mancuso, M.C. Cristiano, M. Fresta, D. Torella, D. Paolino, Positively charged lipid as potential tool to influence the fate of ethosomes, Applied Sciences (Switzerland). 11 (2021) 7060. https://doi.org/10.3390/APP11157060/S1.

[25] C. Hald Albertsen, J.A. Kulkarni, D. Witzigmann, M. Lind, K. Petersson, J.B. Simonsen, The role of lipid components in lipid nanoparticles for vaccines and gene therapy, Adv Drug Deliv Rev. 188 (2022) 114416. https://doi.org/10.1016/J.ADDR.2022.114416.

[26] D.J. McClements, S.M. Jafari, Improving emulsion formation, stability and performance using mixed emulsifiers: A review, Adv Colloid Interface Sci. 251 (2018) 55–79. https://doi.org/10.1016/J.CIS.2017.12.001.

[27] S. Uddin, Md.R. Islam, R.Md. Moshikur, R. Wakabayashi, M. Moniruzzaman, M. Goto, Modification with Conventional Surfactants to Improve a Lipid-Based Ionic-Liquid-Associated Transcutaneous Anticancer Vaccine, Molecules. 28 (2023) 2969. https://doi.org/10.3390/MOLECULES28072969.

[28] J. Basso, M. Mendes, T. Cova, J. Sousa, A. Pais, A. Fortuna, R. Vitorino, C. Vitorino, A Stepwise Framework for the Systematic Development of Lipid Nanoparticles, Biomolecules 2022, Vol. 12, Page 223. 12 (2022) 223. https://doi.org/10.3390/BIOM12020223.

CHAPTER 4

DESIGN AND CHARACTERIZATION OF CHLORIN E6 AND CURCUMIN DUAL DRUG-LOADED LIPIDIC NANOCARRIERS FOR SKIN CANCER TREATMENT

4.1 Introduction

Melanoma is one of the deadliest forms of skin cancer due to its rapid metastasis. The most common causes of skin cancer are genetic factors and long-term exposure to direct sunlight. Treatment options include surgical intervention and recent therapeutic approaches such as chemotherapy, radiation, and immunotherapy. However, these modalities may have undesirable effects, such as drug resistance. Combining different treatment modalities has shown promise in improving anti-tumoral efficacy [1].

PDT is a newly established treatment approach acknowledged as a non-invasive and indispensable tool in cancer therapeutics [2]. PDT has shown significant efficacy against skin carcinoma [3]. However, the problem associated with the delivery of PS molecules via the topical route includes limited light penetration ability and permeation through cancerous tissue or stratum corneum, rendering it ineffective [4]. An FDA-approved second-generation PS [5], Chlorin e6 (Ce6) has several advantages, such as it can irradiate at deeper lesions or tissues, has a high clearance rate, and has high singlet oxygen and quantum yield [6]. Despite these properties, Ce6 possesses significant drawbacks such as hydrophobicity, limited penetration through the stratum corneum, and self-aggregation upon contact with water, resulting in lower quantum yield and singlet oxygen generation ($^1O_2$), consequently limiting its clinical efficacy [7].

Another naturally occurring polyphenol molecule is Curcumin (CUR), extracted from turmeric (curcuma longa). CUR was found in multiple research as a novel molecule with the potential for melanoma treatment [8]. It can inhibit wide range of targets involved in the development and metastasis of melanoma, such as MST1, JNK, FoxO3, Bim1, MCL1, BCL2, Bax and JAK-2/STAT-3. According to a report, melanoma cells and basal cell carcinoma with the mutant p53 gene have a high resistance rate to conventional chemotherapeutic drugs [9]. CUR has been shown in studies to overcome multi-drug resistance (MDR) by inhibiting the PI3K/Akt/NF-kB signalling pathway and decreasing P-gp expression (15). As a result, CUR may be able to overcome drug resistance. Despite these properties, CUR has various drawbacks, such as being highly hydrophobic and having poor water solubility, poor permeation through stratum corneum, low stability, etc[8,10]

To address the above drawbacks of Ce6 and CUR, various strategies such as encapsulation with polymeric-based nanoparticles, polymeric-drug conjugates, and polymeric micelle have been developed. For instance, conjugation of Ce6 with CUR has been demonstrated to improve PDT efficacy on pancreatic cell lines [11]. Conjugation of Ce6 with 4-arylaminoquinazoline

(targeted moiety) improved drug accumulation in the A431 cells [12]. However, synthesizing inorganic nanoparticles, conjugating the two drugs, and grafting functional groups often required laborious synthesis and challenging material engineering. Synthetic nanocarriers and other materials present various challenges, such as toxicity arising from the degradation products of polymers, biocompatibility concerns, restricted drug loading capacity, difficulties in scaling up the manufacturing process, and time-consuming procedures. Therefore, to overcome these undesirable properties of existing nanocarriers, lipidic nanocarriers came into the limelight for their numerous advantages, such as high drug loading capacity of hydrophobic drugs, low toxicity, high biocompatibility, etc. Additionally, lipidic nanocarriers can improve the permeation and drug delivery to the tumor site.

When PDT is combined with chemotherapy, it helps to overcome the MDR of chemotherapeutic drugs [13]. Topical therapeutic delivery can successfully remove primary melanoma lesions and improve patient compliance. The main advantages of topical drug delivery for treating cutaneous skin cancer are easy to administrate in long-term treatment and eliminate systemic toxicity etc. It would be excellent to select a combinational approach with topical drug administration to achieve a better and more efficient therapeutic approach to treat melanoma. Therefore, the current work centered on the specific aspect of interest in dual drug-loaded lipidic nanoparticles and their combination chemo-photodynamic therapeutic effect against cutaneous melanoma cancer. The graphical representation of the study is shown in Scheme 1.

To accomplish the foretold, we have fabricated the dual drug-loaded lipidic nanoparticles (DDLN) embedded hydrogel. Our novel DDLN gel has been developed to deliver the Ce6 and CUR via topical delivery, which can provide high entrapment, controlled release, and improved cellular uptake, avoiding high loco-regional concentration at the affected site. A series of batches using different solid-liquid lipids and surfactants were selected to achieve a stable formulation with smaller particle size and high entrapment efficiency that could penetrate the viable part of the skin, i.e., deeper skin tissues and to deliver the targeted drug site. In this DDLN, we have used a DOTAP cationic lipid that capable of interacting with the extracellular lipid matrices of the skin, leading to the disturbance of the skin's lipid orientation., which in turn creates the diffusion pathway for nanoparticles to cross through the skin. Additionally, it also shows a dominant effect on cellular uptake mechanisms as well as intracellular fate. Both CUR and Ce6 are highly hydrophobic and potent molecules that were encapsulated in DDLN and subsequently formulated into hydrogel using SEPINEO™ P 600.

Scheme 1. Schematic Illustration of Dual-Drug-Loaded Lipidic Nanoparticles and Its Combination Chemo-Photodynamic Therapeutic Effect against Cutaneous Melanoma Cancer
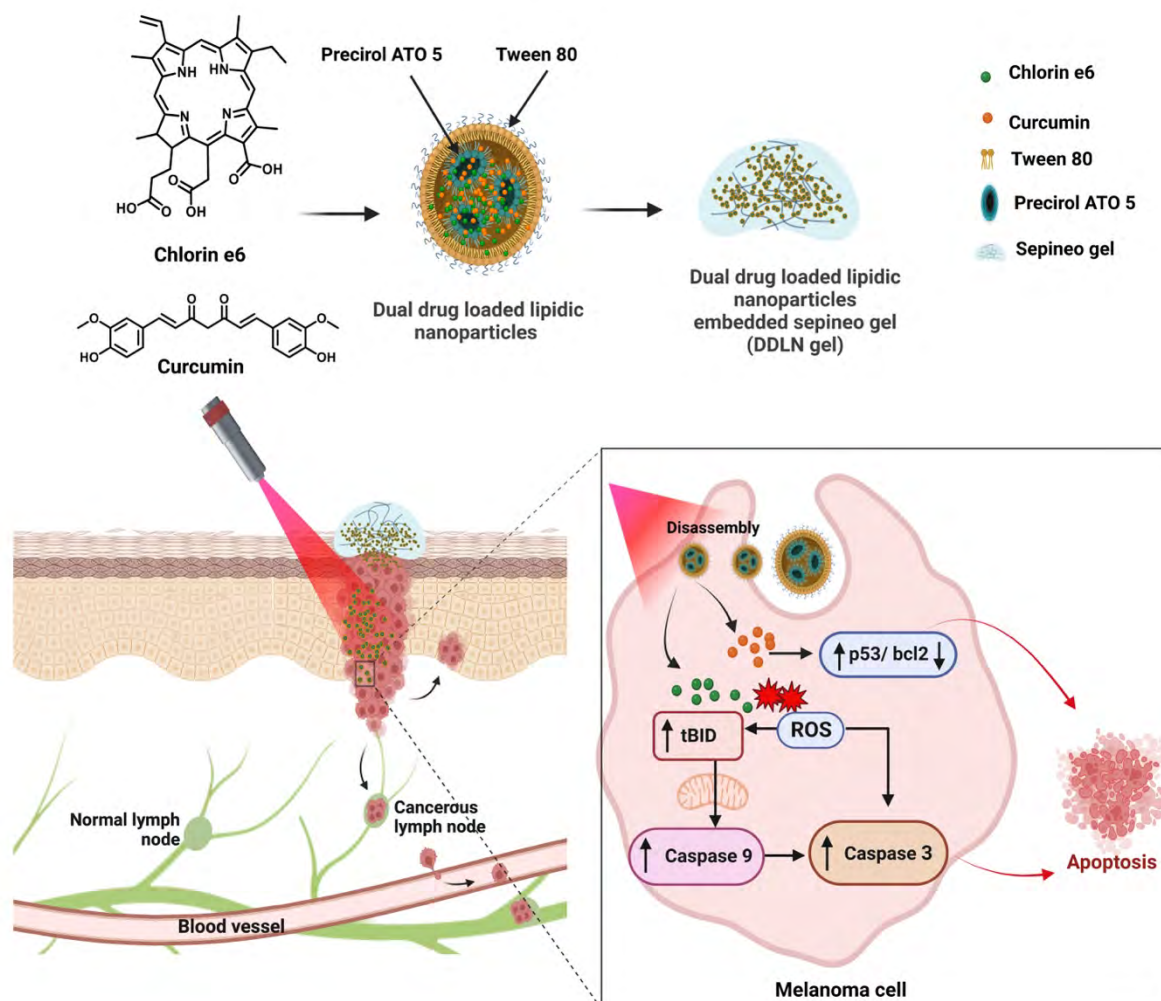
4.2 Materials and Methods

CUR was procured from Himedia, Mumbai, India. Ce6 was purchased from Cayman Chemical Company, USA. Different lipids such as Precirol® ATO 5, Glyceryl monostearate (GMS), stearic acid, and compritol® 888 ATO were provided from Gattefosse (Lyon, France). Capmul MCM C8 and Captex 355 were received as a gift from Abitec Corporation (OH, USA). DOTAP was received as a kind gift from lipoid GMBH. Acridine orange (AO), and ethidium bromide, propidium iodide (Pi), N, N-Dimethyl-4-nitrosoaniline (RNO), and dichloro-dihydro-fluorescein diacetate (DCHF-DA) were purchased from Sigma-Aldrich, Bangalore, India.

4.2.1. Formulation of drug-loaded lipid carriers

Dual drug-loaded lipid nanocarriers (DDLN) were fabricated by hot homogenization followed by the probe sonication method [14]. In brief, solid lipid, liquid lipid, and CUR were taken in a sterile vial and dissolved using acetone (organic phase). In another vial, tween-80 and DOTAP phospholipid) were mixed and vortexed for 5min. Further, the above surfactant solution was added into the aqueous phase. Both the vials containing aqueous and organic phases were kept at the same temperature (60 °C) on a hot stirrer. Once the organic solvent was completely evaporated, the aqueous phase was mixed with the organic phase and kept in stirring for 5 min. The lipid nanoparticles were obtained by subjecting pre-emulsion to probe sonication followed by cooling at 4 °C.

Additionally, The unentrapped drug was isolated by subjecting the mixture to centrifugation at 5000 rpm for a duration of 5 min. Selection and screening of lipids (solid lipid and liquid lipid) and surfactant ratios are based on the solubility criteria. The supernatant of DDLN was taken and analyzed for further characterization, including mean particle size and zeta potential. The calculation of Entrapment efficiency (EE %) and drug loading were calculated by using the following formula [15].

$$\text{Encapsulation efficiency (\%)} = \frac{\text{Amount of drug in the DDLN}}{\text{Initial amount of drug taken}} \times 100$$

$$\text{Drug loading (\%)} = \frac{\text{Amount of drug in the DDLN}}{\text{weight of DDLN}} \times 100$$

4.2.2. Optimization of dual drug-loaded lipidic nanoparticles (DDLN) by using box-Behnken Design

A Box–Behnken Design (BBD) was applied to obtain the number of experiments required to optimize the DDLN using Design-Expert software. BBD provides information about the interaction effect of critical process parameters and the attributes of the critical materials. Three levels of solid and liquid lipids, surfactant concentration, and probe sonication time were determined based on the preliminary batches of DDLN. The independent variables, including the solid lipid to liquid lipid ratio (X1) ranging from 100 to 200 mg, surfactant concentration (X2) ranging from 0.5 to 2.5%, and probe sonication time (X3) ranging from 1 to 5 minutes, were subjected to variation. To assess the reproducibility of the Design, five center points were used. 17 runs were obtained from the software with high, medium, and low levels. Suggested

experiments were carried out, and experimental data was incorporated into the Design of the experiment software. A statistical model was selected for individual response based on the highest-order polynomial and a non-aliased models

Furthermore, regression models can be linear, quadratic, or two-factor interaction for each response. Following that, an analysis of variance (ANOVA) was performed, and the best-fit model was selected based on several statistical criteria, such as multiple correlation coefficients (R^2), adjusted R^2, predicted R^2, etc. Design-Expert software was utilized for optimizing the DDLN formulation along with 3D response surface graphs, and 2D counterplots were employed to evaluate the interaction effects between independent and dependent variables. The output variables such as the lower particle size and highest % entrapment efficiency were considered for the model optimization. The validation of the final optimized batch was performed. The BBD model was validated quantitatively by comparing the predicted batch values to the experimental batch results in terms of percent variation or error [16].

4.2.3. Preparation and characterization of combined batch of CUR and Ce6 (DDLN)

After optimizing the final validated batch, the combined formulation batch was developed, herein final formulation batch (DDLN) was prepared by using precirol ATO 135 mg (solid lipid), 45 mg campul MCM C8 (liquid lipid), and Ce6 (5 mg) and CUR (5 mg) in a vial. To the vial, 200 µl acetone and 50 µl DMSO were added as an organic solvent to dissolve the ingredients. In a separated eppendorf tube., tween-80 and DOTAP phospholipid were mixed and vortexed continuously for 10 min, and the solubilized component was added into the water phase. The formulation was further treated by following the same protocol discussed earlier in the methodology section.

EE % and drug loading of DDLN were calculated by the mentioned formula in the section (4.2.1) . A simultaneous analytical method was developed for the analysis of CUR and Ce6 from DDLN using high-performance liquid chromatography (HPLC) [17].

4.2.3.1. Physiochemical characterization of DDLN

4.2.3.2. Morphological analysis

Surface morphology analysis of the fabricated DDLN formulation was facilitated through the utilization of FE-SEM and scanning transmission electron microscopy. To prepare the samples, a carbon adhesive tape mounted on aluminum stubs was utilized as a substrate for applying a uniform layer of lipidic nanoparticles. Followed by the gold coating and subjected to 20 kV analysis.

4.2.3.3. Spectroscopic analysis

UV Spectroscopy was performed using UV Spectrophotometer for free CUR, free Ce6, and dual drug-loaded lipidic nanoparticles [18]. To confirm the encapsulation of both drugs, the DDLN was dissolved in an organic solvent, and the UV spectrum was obtained and compared.

4.2.3.4. Kinetic stability

The DDLN was stored at 4 °C for 24 days, and the drug absorbance was checked for continuous/first six days using a UV instrument to analyze the stability of the DDLN.

4.2.3.5. Evaluation of singlet oxygen generation (SOG)

The assessment of singlet oxygen ($^1O_2$) generation was conducted using fluorescent dyes, specifically 9,10-dimethylanthracene (DMA), N,N-dimethyl-4-nitrosoaniline (RNO), and singlet oxygen sensor green (SOSG) [19]. The formulations containing Ce6 (1.5 µg/ml in DMSO/PBS solution, pH 7.4), were followed by the addition of DMA (20 mM) and kept for equilibration for 10 minutes. A laser source of 660 nm at an intensity of 0.5 W/cm^2 was irradiated at the reaction mixture at predetermined time intervals. After the irradiation at ex/em. 360/380-550 nm wavelengths, the decrease in the fluorescence intensity of DMA was measured. The alteration in the intensity at various time intervals was measured using a spectrofluorophotometer [20].

In order to evaluate the generation of $_1O^2$ by DDLN, free CUR, and RNO, a singlet oxygen indicator was utilized in the presence of histidine, which assists in the capture of $^1O_2$. This was performed so that the $^1O_2$ could be determined. Free CUR, free Ce6, and DDLN were mixed uniformly with an aqueous solution of 100 µl RNO containing 250 mM concentration and 300 µl histidine-containing 30 mM concentration. The 200 µl above mixture was added to well

plate and irradiated by utilizing a laser light source (660 nm@ 0.5 W/cm^2). RNO The absorbance RNO was determined at 440 nm λmax by UV after light irradiation for a specific time interval [21].

The determination of singlet oxygen generation for the free CUR, free Ce6, and DDLN at Ce6 (0.25 μM in PBS pH 7.4). The concentration of 2.5 μM SOSG was mixed with the NPs solution, and the samples were irradiated with a laser source of 660 nm @ 0.5 W/cm^2. The measurements for the samples were taken using a spectrofluorophotometer at ex/em wavelengths of light of 494/534 nm. Following the irradiation, the changes in the sample's fluorescence were quantified for SOG at an excitation/emission wavelength 494/534 nm [22].

4.2.3.6. In-vitro Drug Release Analysis

The percent cumulative drug release (% CDR) of DDLN, a mixture of free CUR and free Ce6 (FCC+FCE), was determined by the dialysis method. The media comprised of PBS pH 6.4 containing 15% ethanol and 2% Tween 80. The above-release medium was selected based on the sink condition of FCC+ FCE. Briefly, DDLN formulation (equivalent to 0.25 mg of CUR and Ce6 in 1 ml, n = 3) and pure drug formulation (FCC +FCE) were placed in a dialysis bag (Himedia, MW 12 KDa) in a 30 ml of above release medium. The samples' temperature was maintained at 32 °C in a shaking incubator at 200 rpm. After taking an aliquot of 1 ml in volume, which was then followed by the replacement with a new release medium with the same volume at predetermined time intervals from 0.5-24 h, respectively. The collected samples were filtered and analyzed by using the previously developed RP-HPLC method for CUR and Ce6. Further, drug release kinetics models were evaluated using DD solver add-in.

4.2.4. Preparation and characterization of DDLN Gel

DDLN gel batch equivalent 0.05% w/w of Ce6 and 0.05% w/w for CUR was prepared by using SEPINEO^{TM} P 600. Briefly, SEPINEO^{TM} P 600 (2 % w/w) was added to the beaker, followed by the addition of freshly prepared DDLN, and mixed gently to obtain the uniform gel.

4.2.4.1. Rheological behaviour of DDLN Gel
4.2.4.1.1. Simple Viscosity

The rheological and flow behavior of DDLN gel was evaluated by a Rheometer (MCR 92, P-PTD 200, Anton Paar, Germany). For the measurement of the viscosity of DDLN gel, Briefly, a parallel plate (PP-25 mm diameter) was used, and a 0.2 mm gap was set between the plate

and probe. The share rate was set at 10 s-1 for 5 min, and 30 points were measured for the estimation of viscosity (cP) [14].

4.2.4.1.2. Temperature-dependent viscosity

The temperature-dependent viscosity was utilized in order to examine the thermal behavior of the gel. Typically, these tests are aimed at investigating the behavior of gel when the sample is heated at a specific temperature. Briefly, a parallel plate (PP-25 mm diameter) was used, and a 0.2 mm gap was set between the container and probe. The optimized DDLN gel (500 mg) sample was carefully loaded at the plate, and the temperature range was selected from 25 °C to 40 °C. 30 points were selected, and the heating rate was 1°C/min.

4.2.4.1.3. Amplitude sweeps test and frequency sweeps test

An amplitude sweep test is typically used to describe the behavior of the gel, dispersion, paste, etc. It also helps to identify the linear viscoelastic region (LVE). LVE region denotes the range in which the test can be performed without affecting the sample structure. Yield point estimation is the critical stress at which gel or dispersed materials initially start the flow or the force required for applying the gel formulation can be determined. The Optimized DDLN gel (500 mg) sample was carefully loaded on a plate at 25 °C. Shear strain (γ) range was selected from 0.01 to 1 % at a frequency rate (10 rad/sec) to analysed the storage (G') and loss modulus (G''). In frequency sweeps test is typically used to describe the behavior of the inner structure of the gel and the stability of the dispersion. Additionally, it also helps to find out the time-dependent behavior of gel samples in the non-destructive deformation form. The DDLN gel was measured with an angular frequency range from 0.1 to 100 rad/s. G', G'' and complex viscosity are the parameters evaluated by the frequency sweep test [23].

4.2.4.2. Texture analysis

The TA-XT2 Texture Analyzer[TM] was used to evaluate the DDLN gel formulation's textural profile in order to find the formulation firmness and adherence. This was carried out to study the formulation of a textural profile. The prepared DDLN gel was transferred to the glass beaker with a capacity of 100 ml and filled to the upto the mark of 70 ml to avoid the formation of air bubbles and to ensure that a flat surface was produced. At the rate of 2mm.s^{-1}, the analytical

probe was utilized to compress the gel to a depth of 30 mm. The various texture parameters were obtained with the help of regulated texture analyzer software.

4.2.5. In-vitro cell culture studies

4.2.5.1. Cell viability assay

In-vitro cell studies were carried out on the adherent murine melanoma *cell* line (B16F10) and epidermoid carcinoma cell line as they mimic the condition of skin cancer. An MTT study was carried out on both cell lines in order to determine the level of cytotoxicity caused by free CUR, free Ce6, and DDLN [24]. In a nutshell, B16F10 and A431 were both seeded into 96 well plates at a density of 10,000 cells per well, and the plates were incubated overnight [25]. The following day cells were treated with free Ce6, free CUR, and DDLN in triplicates at different concentrations (i.e, 1.56 to 100 µg/ml equivalent drug concentrations) and incubated for 12 h. After the incubation period, cells were irradiated using laser (0.5 W/cm^2) for 5 min. Then kept for another 12 h; After the end of the treatment period, 50 µl MTT reagent (5 mg/ml) was mixed with the contents of each well and kept in incubation for 4 h. Then the formed purple formazan crystals were dissolved by adding DMSO (150 µl/well) followed by incubation.

Following a 1h of incubation period, the absorbance of the samples was measured at 570 nm and 620 nm using a Multiplate reader. Cell viability was calculated using the equation provided below.

$$Cell\ viability\ \% = \frac{Absorbance\ of\ sample}{Absorbance\ of\ control} \times 100$$

4.2.5.2. Combination index analysis.

The Chau-Talalay method was used to find out the synergy quantification. GraphPad Prism software was used to calculate the IC$_{10}$ - IC$_{90}$ values of the free drugs, combinations, and prepared formulations. The combination index (CI) was calculated using the below formula, and CompuSyn Software was used to develop the graph between the combination index and fraction affected (Fa). CI value is less than one, the effects are said to be synergistic; when it is equal to one, the effects are said to be additive; and when it is greater than one, the effects are said to be antagonistic [26].

$$CI_x = \frac{D_1}{A_1} + \frac{D_2}{A_2}$$

Where A_1: a dose of drug 1 to produce x% cell kill alone;

D_1: a dose of drug 1 to produce x % cell kill in combination with $(D)_2$;

A_2: a dose of drug 2 to produce x % cell kill alone;

D_2: a dose of drug 2 to produce x % cell kill in combination with $(D)_1$;

4.2.5.3. Cellular uptake analysis

The cellular internalization of the DDLN formulations, a cellular uptake study was performed on both B16F10 and A431 cells. Initially, both cell lines were seeded in a 12-well tissue culture plate at a density of 50000 cells/well and kept for incubation [27]. After 24 h, the cells were treated with the developed formulation containing free Ce6 and free CUR (6 µg/ml) to observe absorption after 1 h and 4 h. At the end of the set period, the cells were rinsed with PBS 7.4, followed by fixation (4% paraformaldehyde) and staining with DAPI (100 µg/ml, 60 µl/well). The fluorescent microscope was utilized to capture the images. For analysis using flow cytometry, the cells were treated similarly for the same time period, followed by PBS 7.4 wash, trypsinizing the cells and centrifuging the cell suspension, collecting the cell pellet, washing and resuspending it in PBS 7.4. The cellular uptake was then analyzed by quantifying the fluorescence.

4.2.5.4. Nuclear staining

50000 cells/well of B16F10 cells and A431 were seeded in 12- the well plate. After 24 h, the cells were treated with free CUR, free Ce6, FCE+FCC, and DDLN (Ce6 concentration at 10 µg/ml) and incubated for 12 h. Following incubation, the cells were irradiated using a 660 nm laser (0.5 W/cm^2) for 5 min and further incubated for 12 h incubation at 37 °C. Next, the cells were rinsed with PBS 7.4 and subjected to fixation using 4% paraformaldehyde (500 µl/well) for 20 minutes under low light conditions. Followed by staining using DAPI (10 µg/ml, 90 µl/well) and acridine orange (100 µg/ml, 90 µl/well), visualized under a fluorescence microscope at 358 nm and 480-490 nm [28].

4.2.5.5. DNA fragmentation

A431 and B16F10 cell lines (5x10 4 cells/well) were seeded in a 6-well tissue culture plate, grown overnight and free CUR, free Ce6, FCE+FCC, and DDLN (Ce6 concentration at 10 µg/ml) and incubated for 12 h at 37 °C. After the incubation period, cells were irradiated using

a 660 nm laser (0.5 W/cm^2) for 5 min and then kept for another 12 h for incubation at 37 °C. Following treatment, the cells were collected, and DNA was extracted using GSure DNA genomic isolation kits. Absorbance was checked at 260 nm and 280 nm for the purity of the isolated DNA. Subsequently, the DNA was run using ethidium bromide dye (0.5 μg/ml) on agarose gel (1.5 %). The fragmentation was then observed under the microscope using Fusion Pulse GelDoc system (Vilber, Germany).

4.2.5.6. Reactive oxygen species generation

To find out the reactive oxygen species generation in the cells (B16F10 and A431 cells) DCFH-DA was used as a fluorescent probe to evaluate the ROS. B16F10 cells and A431 cells were seeded in a 12-well tissue culture plate (50000 cells/well). After 24 h, the cells were treated with free CUR, free Ce6, FCE+FCC, and DDLN (Ce6 concentration of 10 μg/ml) and incubated for 12 h. After the incubation period, cells were irradiated using a 660 nm laser (0.5 W/cm^2) for 5 min (14). Then kept for another 12 h at 37°C. After incubation, the cells were washed using PBS 7.4, fixed using 4% paraformaldehyde (500 µl/well), stained using DCHFDA (5 µM, having excitation and emission wavelength of 504 nm and 529 nm, respectively) for 20 mins, after staining wash with PBS, and observe fluorescence under green channel of fluorescence microscope.. In the presence of ROS species and cellular esterase, the acetate group cleaves, and the molecule gets oxidized to form DCF, which produces fluorescence [29].

4.2.5.7. Annexin-V assay

To evaluate the induction of apoptosis by free CUR, free Ce6, FCE+FCC, and DDLN (with a Ce6 concentration of 10 µg/ml) in B16F10 and A431 cells, the TACS® Annexin V-FITC Apoptosis Detection Kit was utilized. Initially, the cells were cultured in a 12-well plate and treated with the respective compounds for a 12 h duration. Following the incubation period, the cells were exposed to a specific laser for 5 minutes and subsequently maintained at 37°C for an additional 12 h. After washing with PBS buffer was performed, followed by trypsinization and reconstitution of the cells in 1X binding buffer. Annexin V-FITC conjugate was then added to each cell suspension, and the samples were incubated at room temperature for 10 minutes, shielded from light. A 5-minute treatment with PI solution (1 µg/ml) was conducted. Finally, the samples were analyzed using a BD FACS Area III flow cytometer.

4.2.5.8.   Cell cycle analysis

To determine the distribution of cells in the different phases cell cycle such as S, G0/G1, and G2/M. The cell-cycle analysis was conducted using flow cytometry with DNA-specific labeling. B16F10 and A431 cells were cultured and treated with free CUR, free Ce6, FCE+FCC, and DDLN formulations (Ce6 concentration: 10 µg/ml), and incubated for 12 h. After the incubation, the cells were exposed to a specific laser light (0.5 W/cm^2) for 5 minutes and then maintained at 37 °C for an additional 12 h. Subsequently, the cells were trypsinized, centrifuged (at 1200 rpm for 5 minutes), washed with 1X PBS, and centrifuged again following appropriate incubation. To induce cellular fixation, chilled ethanol was applied and kept at -20 °C for 3 h, followed by centrifugation and washing with 1X PBS. After that, For each sample, a 50 µl volume of RNase was added, followed incubation period (15 minutes). Subsequently, 50 µl of PI from the stock solution 1 mM was added to the samples, which were then kept in a dark area for 20 minutes. The flow cytometry analysis was performed using a flow cytometer.

4.2.6. Ex-vivo studies

4.2.6.1.   Ex-vivo Skin Permeation Studies

Using a vertical Franz diffusion cell, ex vivo of DDLN gel (0.05 % w/w) penetration through the whole thickness of goat skin was assessed. The fresh goat ear skin was taken from the butcher shop. The subcutaneous fat and hair were removed, and the skin was properly cleaned three times with PBS. A vertical Franz diffusion cell was used to mount the processed skin, and 15 % ethanol, 2 % Tween 80, and 6.4 pH phosphate buffer solvent system were used in the receptor compartment. The volume of the receptor compartment was 18 ml with a surface area of 1.17 cm^2. Prior to the experiment, the processed skin was kept for 2 h for hydration. Then 200 mg of the plane gel (free drug gel/FCE+FCC) and 200 mg of the DDLN gel formulation were applied to the donor compartment. The entire system was maintained at 200 rpm on a magnetic stirrer at 32 ± 0.5 °C. 1 ml of aliquot was collected, followed by replacement of the same volume with fresh release media at time intervals *viz.* 0.5 h, 1h, 2h, 4h, 6h, 8h, 12h, 24h. The collected samples were filtered through the 0.44 µm syringe filter and analyzed by using the in-house developed and validated simultaneous estimation CUR and Ce6 RP-HPLC method. After analyzing the results, a graph was constructed with time on the x-axis and the % cumulative DDLN permeation on the y-axis. Further, steady-state flow and lag time was calculated, and the slope of the graph gives the permeation flux (µg/cm^2) [30].

4.2.6.2. Skin retention study

After the completion of a skin permeation experiment which lasted for 24 h, the donor compartment was detached from the skin. To discard the applied gel, a cotton swab was used to clean the stratum corneum of the skin. The obtained skin sample was kept dry for 6 h. Further, the tape stripping method was applied to analyze the Ce6 and CUR from the stratum corneum and viable part of the skin. For tape stripping, a 19 mm Scotch tape (3M, USA) cellophane was utilized. In the first step, two tapes were removed to eliminate the unabsorbed Ce6 and CUR. For the separation of stratum corneum from the skin, 13 tapes were applied, and the remaining skin tissue was homogenized. The homogenized skin tissue was added to an eppendorf tube containing the ACN and methanol. To extract the Ce6 and CUR, the eppendorf tube was subjected to sonication for up to 1 h. All the processed samples were examined with a simultaneously developed and validated method of HPLC [31].

4.2.6.3. Visualization of skin penetration study with confocal microscopy

To evaluate skin penetrability and dermal distribution study on the skin by utilizing confocal microscopy. 200 mg of plain gel (FCE+FCC gel 0.05 % w/w) and 200 mg of DDLN gel (0.05 % w/w) were applied on the surface of the donor chamber. The entire Franz diffusion assembly was maintained at 200 rpm on a magnetic stirrer at 32 ± 0.5 °C. During the experiment, after 8 h and 16 h, the whole skin was detached and washed with PBS (pH 7.4). After that, the obtained skin was placed under the cryotome and cut into pieces of 5 μm in thickness. The sectioned tissues were observed under confocal microscopy [32].

4.2.6.4. Dermatokinetic of DDLN gel and Free drug gel

For the estimation dermatokinetic study, a tape stripping technique has been used. The excised fresh goat ear skin was utilized for dermatokinetic studies. The skin tissue was prepared as per the above-discussed paragraph (4.2.6.2). A known weighed amount (200 mg) of DDLN formulation and plain free drug gel (FCE+FCC-gel) was applied on the skin. At specific time intervals (1, 2, 4, 6, 8, 12, 18, 24, 30 h), the whole skin was separated from the Franz diffusion cell and washed three times with phosphate buffer saline (PBS, pH 7.4) to eliminate any residual formulation. Adhesive tape strips (19 mm Scotch -3M, US) with a surface area of (2.5 $\times$ 2.5 cm^2) were placed on the skin, pressed down tightly, and then peeled off in an alternative way for up to 30 strips. When the epidermis was completely removed, the surface of the skin

showed a glistering appearance. The CUR and Ce6 were successfully extracted from the tape strips technique by sonicating 5 ml of an ACN to methanol (1:1) mixture at 40 °C for 1 h. After that remaining dermis layer was chopped into small pieces and dissolved in 5 ml of ACN: methanol (1:1) mixture for complete drug extraction. After passing the samples through a membrane filter with a pore size of 0.44 μm, the filtrates were recovered and evaluated using a simultaneously developed HPLC method for CUR and Ce6. After that, the data for dermal pharmacokinetics were determined, including C_{Skin} (drug concentration in the skin at time t,) C_{max} (Maximum concentration of drug obtained in the skin layer), AUC_{0-t} and $AUC_{0-\infty}$. From the obtained experimental data, the non-compartmental pharmacokinetic model was applied to determine T_{max}, $C_{max.}$ AUC_{0-t} and $AUC_{0-\infty}$ values were calculated using the linear trapezoidal method by utilizing the Phoenix WinNolin 8.3 (Certera™, USA) software [33].

4.2.7. Assessment of stability study of DDLN and DDLN Gel

The developed formulation of DDLN and DDLN gel was examined for 90 days at 2 - 8 °C and 25 ± 0.5 °C. The stability study of the developed formulations was evaluated by their average particle size and entrapment efficiency. The stability of the DDLN gel was performed by drug content (assay). The particle size of the DDLN was analyzed through the Malvern Nano ZS. The entrapment efficiency (%) of the DDLN was performed in a similar way as given above and calculated by using the above-mentioned formula in the section (4.2.1). Analysis of gel (assay) was performed; briefly, 100 mg of gel was mixed with the ACN and methanol solvent in combination (1:1) in microcentrifuge tubes and bath sonicated for 5 min to extract the drugs. The further samples were kept for centrifugation at 12000 RPM for 15 min, and then the supernatant was analyzed through the RP-HPLC method.

4.2.8. Statistical analysis

The findings of each test were performed in triplicate and are presented as mean and standard deviation (mean SD). The t-test and one-way ANOVA were performed to evaluate the significance of differences between all groups using GraphPad Prism software. When P values less than 0.05, the analysis was statistically significant. P-values of 0.05, 0.01, and 0.001 are denoted by the *, **, and ***, respectively.

4.3. Result and Discussion

4.3.1. Formulation development and optimization using QbD

Applying the quality by design (QbD) methodology and design of experiments, dual drug-loaded lipidic nanoparticle optimization was developed. The optimal batch was prepared with the fewest possible trials by statistically adjusting the process parameters and material attributes. We have used BBD to optimize DDLN formulation with 17 trials batch (3 factors and 3 levels) using design-expert software (Design-Expert 13.0, State-Ease Inc., Minneapolis, USA). DDLN were prepared by low-temperature homogenization followed by the probe sonication method, and it mainly relies on the concentration of lipid (oil phase- 5) and surfactant (aqueous phase). Based on the preliminary batches, the concentration of surfactant (Tween 80) and amount of lipid (solid - Precirol ATO and liquid lipid- Capmul MCM C8), and time of probe sonication significantly impacted the response, such as particle size and percentage entrapment efficiency. Three levels (low, medium, and high) of independent variables were selected **(Table 4.1.)**, and the results obtained are mentioned in **(Table 4.2.)**. The polynomial equations involved in the interactions between the independent variables and their responses are described by this design. Using analysis of variance (ANOVA), a statistical analysis was performed to assess the validation of these polynomial equations generated by software **(Table 4.3.)** Response surface plots were generated from software and were utilized to study the interaction effect between responses such as percentage entrapment efficiency and particle size. Understanding the effect of each variable individually and in combination with other variables on each response is achieved using polynomial equations and surface plots. Using response surface regression, the full quadratic model equations for particle size and entrapment efficiency were obtained by design expert software and as shown in **Table 4.4.**

Table 4.1. Levels of independent factors used in the design.

Variables		Selected CMAs and CPPs	Goal	Lower level (-1)	Middle level (0)	Upper level (+1)
Independent variables	X1	Amount of lipid (mg)	In range	100	150	200
	X2	Surfactant concentration (%)	In range	0.5	1.5	2.5
	X3	Probe sonication time (min)	In range	1	3	5
Dependent variables	Y1	Particle size (nm)	Minimum (80-150 nm)			
	Y2	Entrapment efficiency (%)	Maximum (> 50 %)			

Where, A-lipid amount (mg), B-surfactant concentration (%), and C-probe sonication time

The (+) positive sign in the regression equation denotes the positive quantifiable relationship between the relevant input variable and the response value. The (-) negative sign in the regression equation denotes the adversarial effect showing a decrease in response value with the respective input variable. The particle size and entrapment efficiency are significantly dependent on independent factors (Amount of lipid in mg, surfactant concentration in %, and probe sonication time in min), as shown by the clear analysis of the coefficient of equations and response surface plots. Close agreement was found between both the Adjusted R^2 values (0.9740) and Predicted R^2 (0.9496) values (difference was less than 0.2) of particle size. For entrapment efficiency, a close agreement was found between both the adjusted R^2 values (0.9508) and predicted R^2 (0.7838) values (the difference was less than 0.2).

Table 4.2. Design and characterizations of dual drug-loaded lipidic nanocarriers (DDLN)

Batch No.	Independent variables			Response variables	
	Lipid (mg)	Surfactant (%)	Sonication (min)	Size (nm)	Entrapment Efficiency (%)
1	100	1.50	5	65.33 ± 1.53	45.41 ± 1.52
2	200	1.50	1	214.67 ± 5.03	65.97 ± 1.97
3	100	2.50	3	57.83 ± 1.61	67.47 ± 0.64
4	150	0.50	5	174.33 ± 4.51	45.43 ± 1.19
5	150	1.50	3	84.17 ± 2.02	75.63 ± 2.16
6	150	1.50	3	80.87 ± 2.01	75.60 ± 0.88
7	150	1.50	3	92.90 ± 2.89	71.00 ± 1.74
8	150	2.50	1	193.90 ± 4.55	59.53 ± 0.60
9	150	1.50	3	88.67 ± 3.51	72.78 ± 0.66
10	150	0.50	1	220.00 ± 5.57	43.83 ± 0.35
11	200	2.50	3	89.23 ± 3.61	80.20 ± 2.30
12	150	1.50	3	94.10 ± 4.48	73.80 ± 0.61
13	100	1.50	1	158.67 ± 6.51	45.77 ± 0.67
14	150	2.50	5	54.07 ± 3.66	62.07 ± 0.75
15	100	0.50	3	102.13 ± 3.07	43.73 ± 0.40
16	200	0.50	3	198.23 ± 3.25	67.83 ± 0.58
17	200	1.50	5	90.27 ± 1.59	80.73 ± 3.19

* Lipid (Solid- Precirol ATO 5, Liquid- Capmul MCM C8) and Surfactant (Tween 80)

Table 4.3. ANOVA for regression coefficients for Box Behnken designed effects (linear, quadratic, and interaction) against the CQAs i.e., dependent variables (particle size and entrapment efficiency) to establish the best fitted quadratic equation.

Effect	Variable	Particle size		Entrapment efficiency	
		F- value	P- value	F- value	P- value
Linear effect	**A**	58.37	< 0.0001	118.86	< 0.0001
	B	142.77	< 0.0001	65.71	< 0.0001
	C	236.42	< 0.0001	5.54	< 0.0001
Interaction effect	**AB**	11.64	0.0077	5.21	0.0484
	BC	20.70	0.0014	-	-
	AC	-	-	6.29	0.0334
Quadratic term	**A2**	-	-	-	-
	B2	33.81	0.0003	28.10	0.0005
	C2	97.00	< 0.0001	81.11	< 0.0001

Table 4.4. Full quadratic model equations for particle size and entrapment efficiency generated by the design of expert software.

CQA s	Coded equations	Predicted R^2	Adjusted R^2
Particle size	$+86.50 + 24.94\ A - 39.00\ B - 50.19\ A\ B -21.00\ B\ C + 26.29\ B^2 +44.25\ C^2$	0.9496	0.9740
Entrapment efficiency	$+72.22 +11.06\ A +8.23\ B +2.39\ C -3.28\ A\ B +3.60\ A\ C -7.40\ B^2 -12.58\ C^2$	0.7838	0.9508

The decrease in sonication time and concentration of surfactant led to an increase in particle size, which was caused by an increase in the amount of lipid that was present. As lipid concentration increases, the viscosity of the melted lipid phase, or the dispersed phase, also

rises, thus further increasing the size of the dispersion. A probe sonication time exhibited a negative effect on the particle size and a positive effect on the entrapment efficiency.

The impact of surfactant concentration on two response variables in a formulation process, such as particle size and entrapment efficiency.

The surfactant concentration exhibited a negative effect on a response of particle size but a positive effect on the entrapment efficiency. When the surfactant concentration increases, it can reduce the particle size of the resulting particles in a formulation. This is because the surfactant molecules can help to stabilize the particles and prevent them from aggregating or clumping together, leading to smaller particle sizes. However, if the surfactant concentration becomes too high, it can also cause excessive adsorption onto the particle surfaces, which can lead to a reduction in particle size. On the other hand, when the surfactant concentration increases, it can also improve the entrapment efficiency of the formulation. This is because the surfactant molecules can help to stabilize the drug or active ingredient within the particle, preventing it from escaping or being lost during the formulation process [34,35]. Therefore, the overall impact of surfactant concentration on a formulation will depend on the specific formulation system and the desired response variables **(Figure 4.1 A, B, C and D).**

By applying numerical method and desirability validation batch was optimized. For the optimized batch selection, the criterion chosen was to minimize particle size and maximize entrapment efficiency. The experimental values for the formulation parameters, including lipid amount (181 mg), surfactant concentration (1.5%), and probe sonication time (3.9 min), were utilized. The predicted results for each response, such as particle size and entrapment efficiency, were then validated by comparing them with the actual results obtained from the executed experimental batch. Based on the predicted batch values versus experimental batch values, % relative deviation was calculated and mentioned in **(Table 4.5.)**.

Table 4.5. Validation batch by numerical method

Responses	Predicted results	Actual results	% Relative
Particle size (nm)	92.12 ± 4.25	94.50 ± 4.58	-0.761
Entrapment efficiency (%)	77.66 ± 1.57	78.73 ± 1.31	-1.382
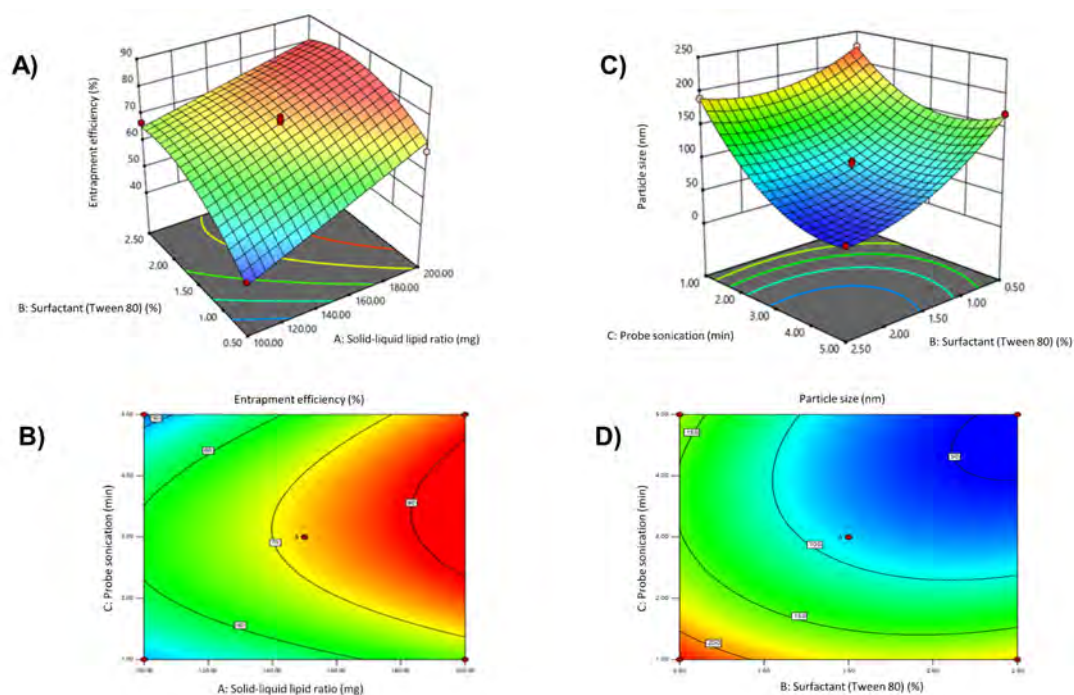
Figure 4.1. Box-Behnken optimization of surface response plots showing the effect of input variables particle size (nm) and entrapment efficiency (%) of DDLN. (A) The 3D plot of input variables affecting response factor entrapment efficiency (%); (B) The contour plot of input variables affecting response factor entrapment efficiency (%).; (C) The 3D plot of input variables affecting response factor particle size (nm); (D) The contour plot of input variables affecting response factor particle size (nm).

4.3.2.   Preparation of a combined batch of CUR and Ce6 and its characterization

After the finalization of the validated batch, the formulation batch was prepared for the dual drug-loaded lipid nanoparticle (DDLN) of CUR and Ce6 by using low temperature followed by the probe sonication method. The prepared DDLN formulation was characterized using particle size, zeta potential, scanning transmission electron microscopic (STEM), and scanning electron microscope (SEM). The particle size, PDI, and zeta potential of the DDLN were determined by DLS and were found to be 88 nm. 0.201, + 21, respectively. The particle size and potential zeta graphs of DDLN are represented in **Figures 4.2 A** and **B**. % drug loading and entrapment efficiency of CUR was 4.31 % and 79.82 %, and for Ce6, 4.57 % and 82.2%. The respective SEM and STEM images of drug DDLN represented that the DDLN were uniformly fabricated, spherical shapes with a uniform particle size distribution, as shown in **Figures 4.2 C & D.** The UV spectrum overlay graph **Figure 4.2 E** represents the CUR, Ce6, and DDLN formulations. CUR shows a peak at 425 nm, while Ce6 shows two peaks at 405 nm and 666 nm. Similar peaks were observed for DDLN formulations when dissolved in ethanol.

Therefore, it confirmed that the drugs were encapsulated into the DDLN, and the addition of ethanol disintegrated the DDLN. Periodical evaluation of particle size and the tracking of Ce6 and CUR fluorescence intensity over time for the lipidic nanoparticle's stability on storage **(Figure 4.2 F).** The particle size was between 88.21 to 95 nm for DDLN on storage at 4ºC for 24 days. Thus, the kinetic stability data revealed that insignificant deviation/decrease in the Ce6 signal in DDLN at 4 ◦C from day 1 to day 24.
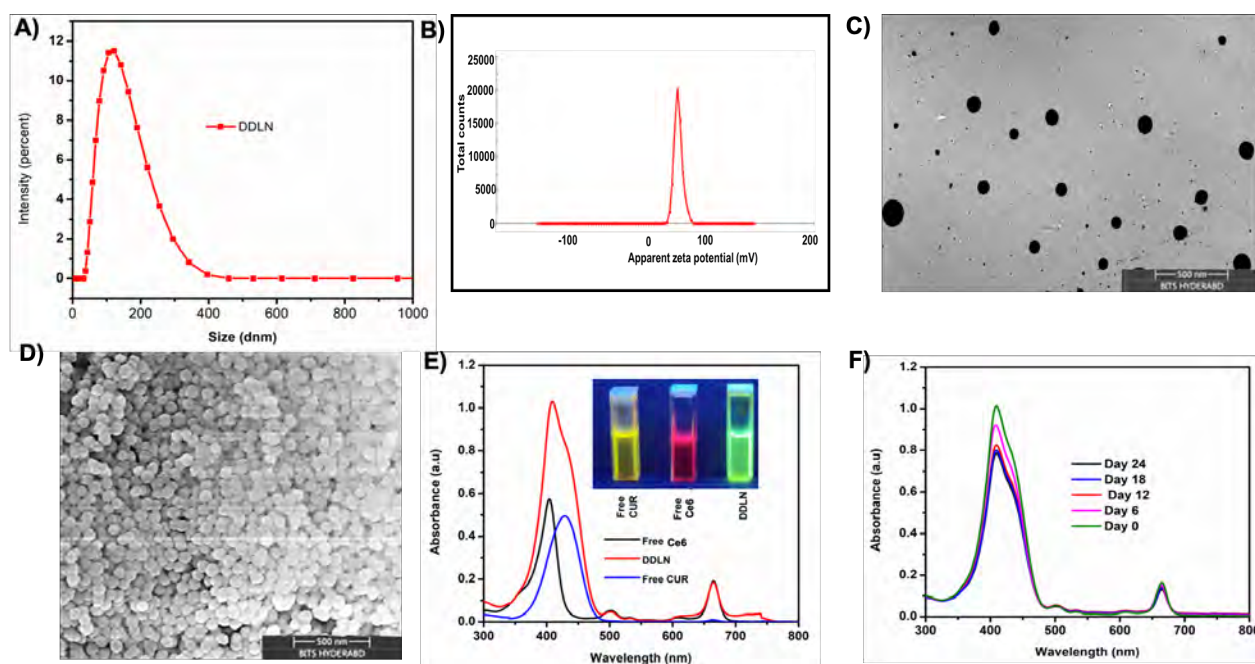
Figure 4.2. Physiochemical characterization of DDLN. Particles size distribution of DDLN (A); zeta potential of DDLN (B); scanning transmission electron microscopic image of DDLN (C); Scanning electron micrograph of DDLN (D); UV absorbance spectra of free CUR, free Ce6, and DDLN in methanol (E); and Kinetic stability of DDLN (F).

4.3.3. Evaluation of the photoactivity and singlet oxygen generation

Fluorescence spectrophotometry was used to identify the photoactivity of DDLN and the generation of singlet oxygen ($^1O_2$) from DDLN following irradiation, as shown in **(Figure 4.3A).** Ce6 showed maximum absorption at 405 and 640 nm. The free Ce6 or DDLN produced single oxygen with varied fluorescence intensity of DMA with 255000 and 89500, respectively. The reduction in fluorescence intensity of DMA has shown an increase in singlet oxygen generation. The DDLN generated higher than the free Ce6, as shown in **Figure 4.3B**. Since free Ce6 was aggregated in the water, there was a decline in singlet oxygen generation **(Figure**

4.3B). However, there was a noticeable difference between the $^1O_2$ generation dissolved in DDLN and free Ce6 in DMSO.

Next, singlet oxygen generation was investigated using RNO when histidine was present. The reaction with histidine and RNO, the $^1O_2$ that was generated proceeds through a bleaching process. A transannular peroxide intermediate is formed when $^1O_2$ is taken in by the imidazole ring of the histidine molecule. The photobleaching occurs as a result of further interaction with RNO. The rate of formation of singlet oxygen was found to be determined by the variance in the photobleaching. Using a laser source with a wavelength of 660 nm, the DDLN, free CUR, and free Ce6 were subjected to irradiation at a laser intensity of 0.5 W/cm^2 over different time durations. The absorbance of RNO was determined at 440 nm **(Figure 4.3 C)**. When the irradiation time increased, the free Ce6 generated singlet oxygen at a faster rate than DDLN. This was proven by the substantial reduction in RNO absorbance. Due to the presence of a hydrophobic core in the nanocarrier, the entrance of histidine was limited, which led to the barrier in the formation of a singlet oxygen−histidine−RNO chain. Therefore leading to an unsuccessful detection of $^1O_2$.

The $^1O_2$ production capacity of DDLN in an aqueous solution was assessed using SOSG by evaluating the fluorescence and laser irradiation. The $^1O_2$ yield DDLN was significantly higher than free Ce6 **(Figure 4.3D).**
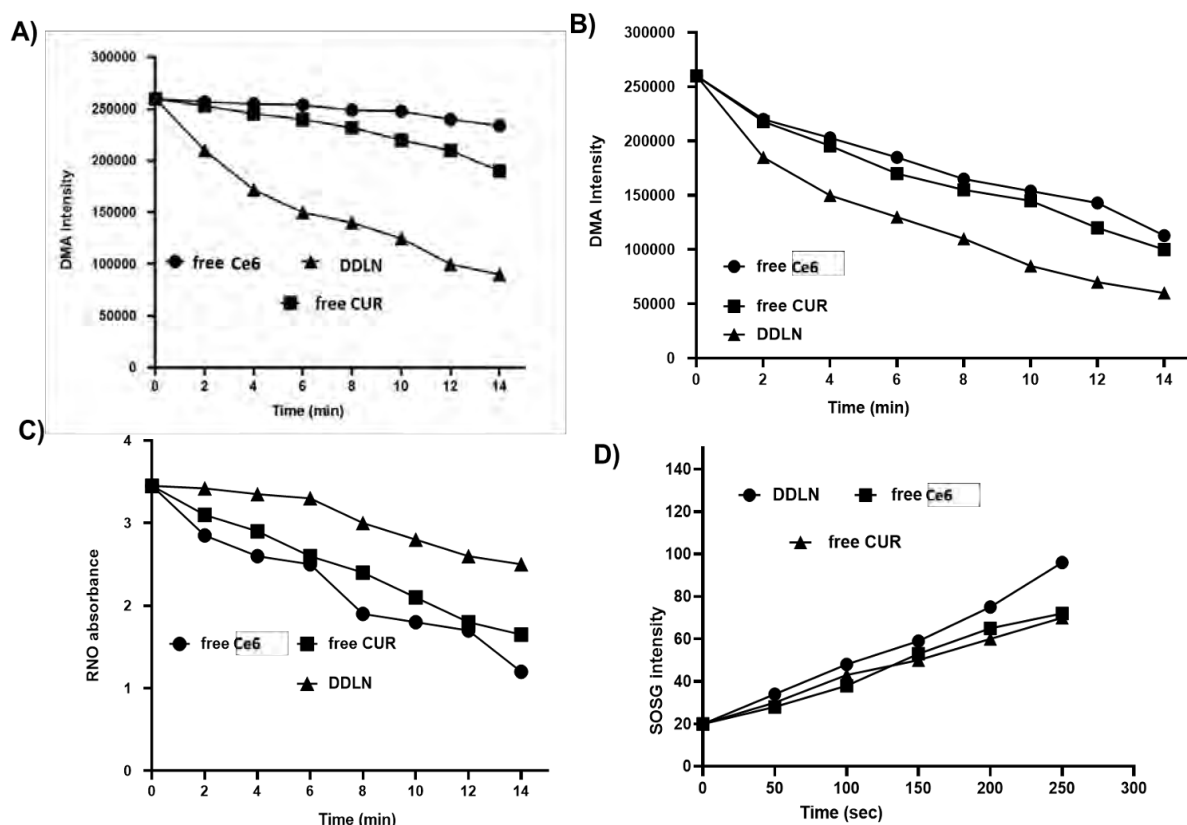
Figure 4.3. Biochemical analysis of Ce6-mediated ROS generation. Change in the fluorescence intensity of DMA (Ex. 360 nm; Em. 436 nm) w.r.t. time in the presence of free CUR, free Ce6, DDLN in PBS (A), and in DMSO (B); time-dependent photo-bleaching of RNO by free CUR, free Ce6, DDLN in PBS (C); Changes in fluorescence intensity of SOSG in the presence of free CUR, free Ce6, DDLN in water (D).

4.3.4. In-vitro drug release

The drug release graph of developed DDLN and free drug of CUR and Ce6 was represented in **(Figure 4.4).** Both free drugs showed 100% cumulative drug release within 6 h, while DDLN containing CUR and Ce6 showed less than 50% cumulative release in 6 h and then 50 to 95% by the end of 24 h. The kinetic release model was investigated using a DD solver (add on Xcel sheet). The model of the release kinetics is shown in **(Table 4.6),** and it contains the correlation coefficient data, along with the AIC value and the MSC value. Throughout the process of evaluating the several models, the "best-fit" model was chosen to be the one that had the highest R^2 value, the lowest AIC, and MSC values which were higher than 2. It was confirmed by the tabulated data that the DDLN followed the 1st order kinetic model for both drugs
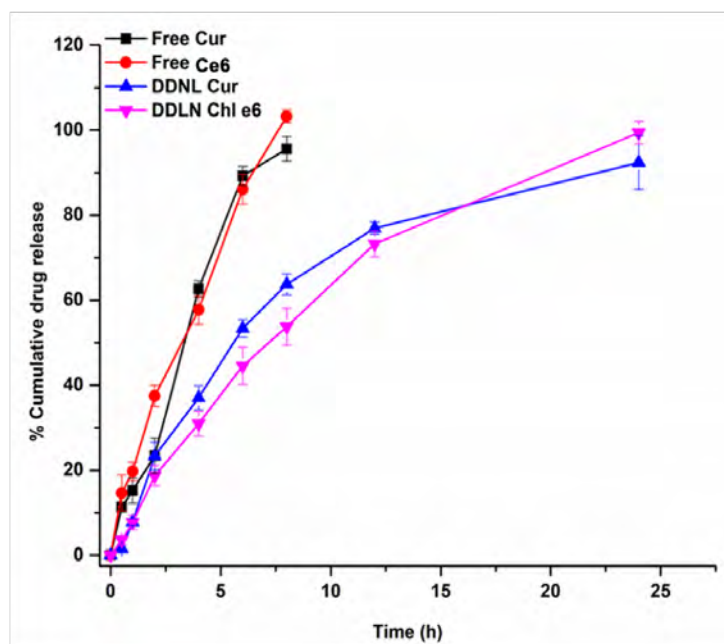
Figure 4.4 Cumulative drug release graph of developed DDLN and free drug of CUR and Ce6

Table 4.6. The release mechanism of DDLN formulation and free drugs by curve fitting method.

Kinetic model	DDLN curcumin				Free drug curcumin			
	R^2	k	AIC	MSC	R^2	k	AIC	MSC
Zero order	0.6480	4.962	65.0120	0.7940	0.8167	9.599	53.3398	1.0529
First order	0.9937	0.122	32.7659	4.8248	0.9790	0.213	38.1573	3.2219
Higuchi	0.9333	19.934	51.6998	2.4580	0.9269	27.710	46.9003	1.9729
Koresmeyer peppas	0.9386 n = 0.548	17.727	53.0350	2.2911	0.9408 n= 0.608	22.443	47.4264	1.8977
Kinetic model	DDLN chlorin e6				Free drug chlorin e6			
	R^2	k	AIC	MSC	R^2	k	AIC	MSC
Zero order	0.8448	4.914	58.7186	1.6129	0.9740	13.781	33.8377	2.9149
First order	0.9885	0.103	37.9272	4.2118	0.9545	0.272	37.2053	2.3536
Higuchi	0.9434	19.144	50.6484	2.6217	0.9416	32.899	38.6994	2.1046
Koresmeyer peppas	0.9817 n = 0.647	13.284	43.6279	3.4992	0.9971 n= 0.778	20.663	22.7725	4.7591

4.3.5. Characteristic of DDLN gel

The prepared DDLN formulation **(Figure 4.5 A-a, b, c)** was incorporated into a topical gel (SEPINEO™ P 600) **(Figure 4.5 A-d).** When nanoparticles are incorporated into a gel, they may form separation into gel or aggregates quickly. Thus, to ensure the microstructure of DDLN gel, SEM analysis was performed **(Figure 4.5 B).** The DDLN gel was a topical hydrogel preparation that was intended to be applied directly to the skin, and a pH analysis was required to confirm that the formulation remained unchanged. It was observed that the pH of the DDLN gel was 6.01 ± 0.4, and this result was confirmed to be within the acceptable range for human skin pH (4.5–6.4). As a result, the optimized composition was identified as suitable for usage in order to reduce the risk of causing skin irritation during the application.

4.3.5.1. Rheological behaviour

At a temperature of 25 °C and under a constant shear rate of 10 s−1, the viscosity (η) of the DDLN gel was measured to be 12235 cP **(Figure 4.4 C)**. Analysis from **Figure 4.5 D** indicates that the rheograms displayed non-Newtonian flow properties characterized by shear-thinning behavior and varying degrees of thixotropic behaviour. The thermal behavior of the gel was determined by using temperature-dependent viscosity. In the temperature-dependent viscosity, by applying the constant share rate with varying temperatures from 25 to 40 °C viscosity was measured. As a result, it was confirmed that there were no changes in viscosity **(Figure 4.5 D).** To analyze the deformation behavior and time-dependent behavior of the sample, an amplitude sweep test and frequency sweep test were carried out. LVE demonstrates the extent to which analysis could be carried out without affecting the gel structure. In the amplitude sweep test, LVE region was found to be for DDLN gel 0.02 (% in terms of strain). **Figure 4.5 E** result demonstrates that G' is greater than G", which indicates a solid viscoelastic structure or a gel-like structure. After finding the LVE region, the frequency sweep test was conducted to evaluate the gel stability during long-term storage as well as the flow behaviour and internal structure of the DDLN gel. The obtained G' and G" for DDLN gel were confirmed to be in the LVE region, and as a result **(Figure 4.5 F),** the sample has not changed over the course of the test.

4.3.5.2. Texture analysis

To find out the texture of the gel, various parameters, including firmness, consistency, and cohesiveness, were recorded to obtain an interpretation of a gel texture. The firmness,

consistency, cohesiveness, and viscosity index of DDLN gel were found to be 123.98 ± 9.87 g, 1043 ± 56.76 g s^{-1}, and -702.65 ± 87 g, respectively **(Figure 4.5 G).** The above values indicated that the physical appearance of the gel was uniform and smooth, free from grittiness and or particulate matter. The findings indicate that the DDLN gel exhibits excellent drug retention and permeability at the application site, highlighting its ability to effectively deliver loaded drugs with superior exclusivity.
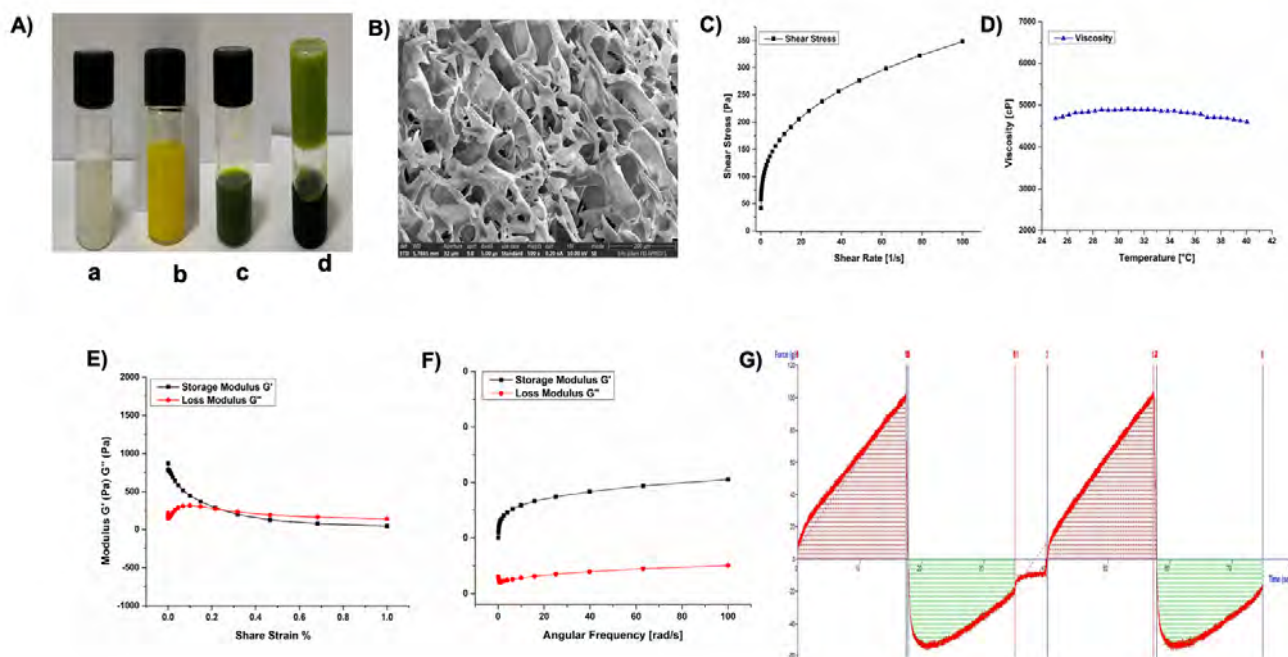
Figure 4.5. Characterization of CUR and Ce6 co-loaded gel; Blank formulation (A-a); formulation containing CUR (A-b); DDLN formulation (A-c); DDLN gel (SEPINEO^{TM} P 600) (A-d); Scanning electron microscopic images of DDLN gel (B); Rheological behavior share stress vs share rate (C); temperature-dependent viscosity (25℃ to 40 ℃); Amplitude sweeps test (E); Frequency sweep test (F); Texture analysis of DDLN gel (G).

4.3.6. In-vitro assays

4.3.6.1. Cell viability assay

The MTT assay indicated a time and concentration-dependent decrease in the cell viability in both B16F10 and A431 cell lines for the various formulations treated, as represented in **Figures 4.6 A and B**. It was observed that the cytotoxic effect was highest for DDLN, followed by FCE+FCC as compared to free Ce6. The DDLN (+ L) Showed an IC$_{50}$ of 4.712 µg/ml for 24 h on B16F10 cell lines, which was lower than the IC$_{50}$ of free CUR (+ L), FCE+FCC (+ L), and free Ce6 (+ L), which were 17.40 µg/ml, 13.56 µg/ml, and 17.241 µg/ml, respectively.

Similarly, DDLN (+ L) treatment for 24 h on A431 cell lines showed an IC_{50} of 5.826 µg/ml, while free CUR (+ L), FCE+FCC (+ L), and free Ce6 (+ L) exhibits IC50s of 17.038 µg/ml, 13.13 µg/ml, and 17.20 µg/ml, respectively. Moreover, the receptor-mediated endocytic internalization of lipidic nanoparticles allows longer intracellular retainment with less efflux than the free drugs undergoing diffusion for cell entry/exit. Interestingly, the DDLN treatment showed the lowest IC_{50} values of any of the conditions that were assessed. The ~4.2-fold decrease in IC_{50} values of DDLN than free Ce6 and free CUR at 24 h (+L). Therefore, it indicates that the longer retention of DDLN intracellularly reaches optimum concentration to exert cytotoxic action.

4.3.6.2. Combination index analysis

Combination indexes (CI) at all tested fractions affected, including IC_{10}, IC_{20}, IC_{30}, IC_{40}, IC_{50}, IC_{60}, IC_{70}, IC_{80}, and IC_{90} for both the cell lines and at all the tested treatment regimens (24 h + L, - L) and (48 h + L, -L) were represented in **Figure 4.6 C and D**. The lowest CI was observed at 24 h (+L), 48 h (+ L) time point at 50 % fraction affected as mentioned in **Table 4.7** for in B16F10 and A431 cell lines. It was observed that DDLN formulation with a drug loading ratio of 1:3 showed a synergistic effect for both cell lines, with combination indices values below 1 (represented in **Figure 4.6**).

Table 4.7. The combination index value of DDLN

Group	CI value (B16F10 cell lines)	CI value (A431 cell lines)
IC_{10}	0.932	0.892
IC_{20}	0.921	0.882
IC_{30}	0.900	0.847
IC_{40}	0.895	0.831
IC_{50}	0.881	0.830
IC_{60}	0.872	0.820
IC_{70}	0.861	0.814
IC_{80}	0.852	0.808
IC_{90}	0.842	0.800
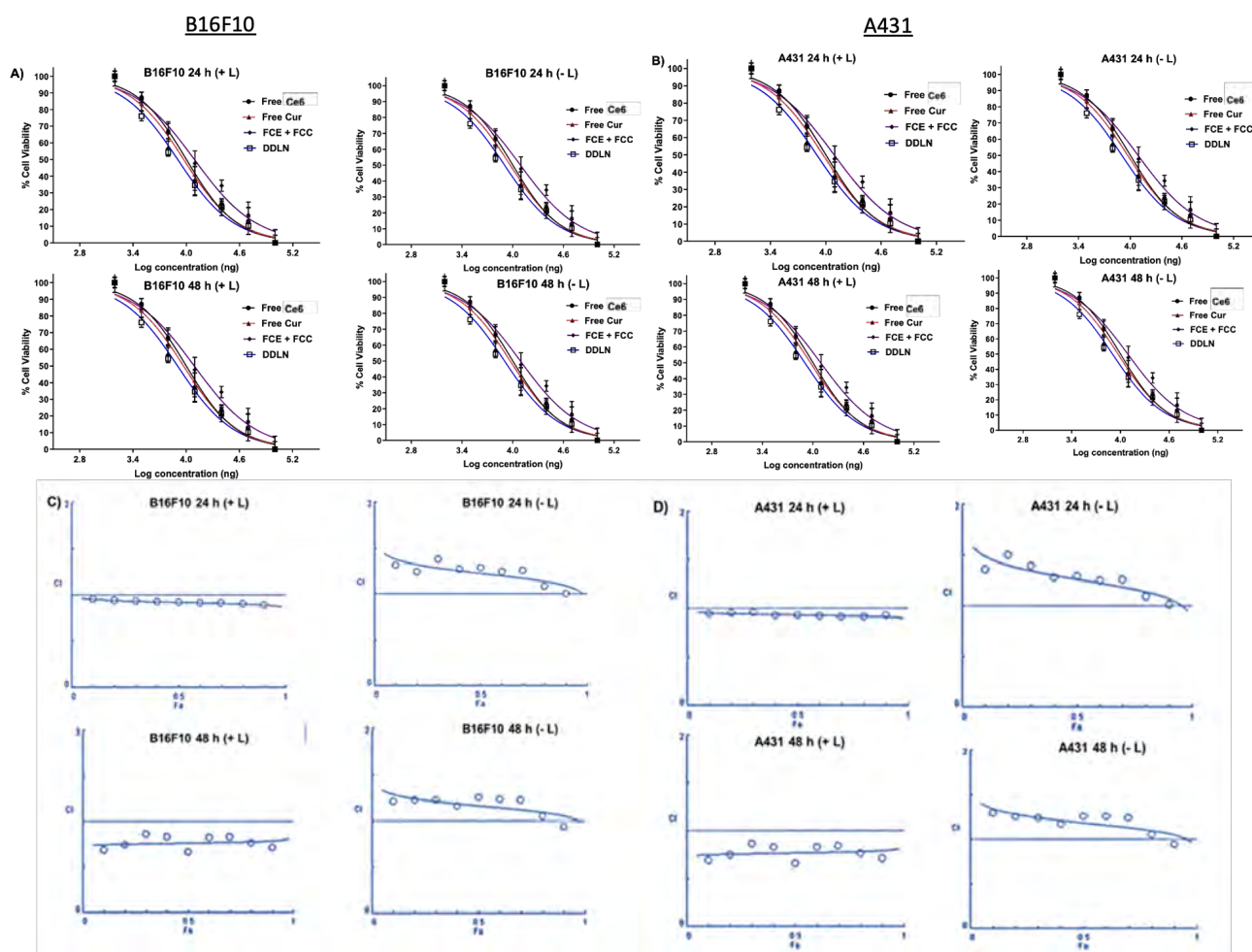
Figure 4.6 In vitro evaluation of the anticancer activity of free CUR, free Ce6, FCE+FCC, and DDLN by MTT assay. The dose-response curve for the determination of IC_{50} values of free CUR, free Ce6, FCE+FCC, and DDLN (24 and 48 h) in cultured B16F10 and A431 cell lines with (+L) or without laser (-L) (A and B); graphs representing combination index (CI) in B16F10 (C) and A431 cells (D), with (+L) and without laser (-L).

4.3.6.3. Cellular Uptake Analysis

The fluorescence micrographs of free CUR, free Ce6, FCE+FCC, and DDLN at 1h and 4h for B16F10 and A431 cells were represented in **Figures 4.7 A and 4.8 A**. In both cell lines, clear, brighter fluorescence in the cytoplasm and nuclei was observed in DDLN-treated cells, suggesting quick internalization of DDLN. From 1 to 4 h, the red fluorescence and green fluorescence intensity of free Ce6, free CUR, FCE+FCC, and DDLN groups were increased, demonstrating time-dependent cellular uptake for both cell lines. This was affirmed by the flow cytometry graphs as shown in **Figures 4.6 B and 4.7 B**. In the flow cytometer histogram, the bar graph revealed an increase in the mean fluorescence intensity values for DDLN and Free Ce6 from 1 to 4 h. (**Figure 4.6 B**, **4.7 B right**). The geometric mean fluorescence of DDLN

(+L)-treated cells from 1672.2±34.22 to 3445.54±16.27 from 1 to 4 h for B16F10 cell, whereas the geometric mean fluorescence of free Ce6-treated cells was increased from 850.4±20.7 to 1620.7±23.67. Similarly, the geometric mean fluorescence of DDLN (+ L) treated cells from 1752.32 ± 20.32 to 3945.54 ± 26.27 from 1 to 4 h for A431 cell lines. The time-dependent increase in fluorescence could be easily observed in both cell lines by the shift in the peak.
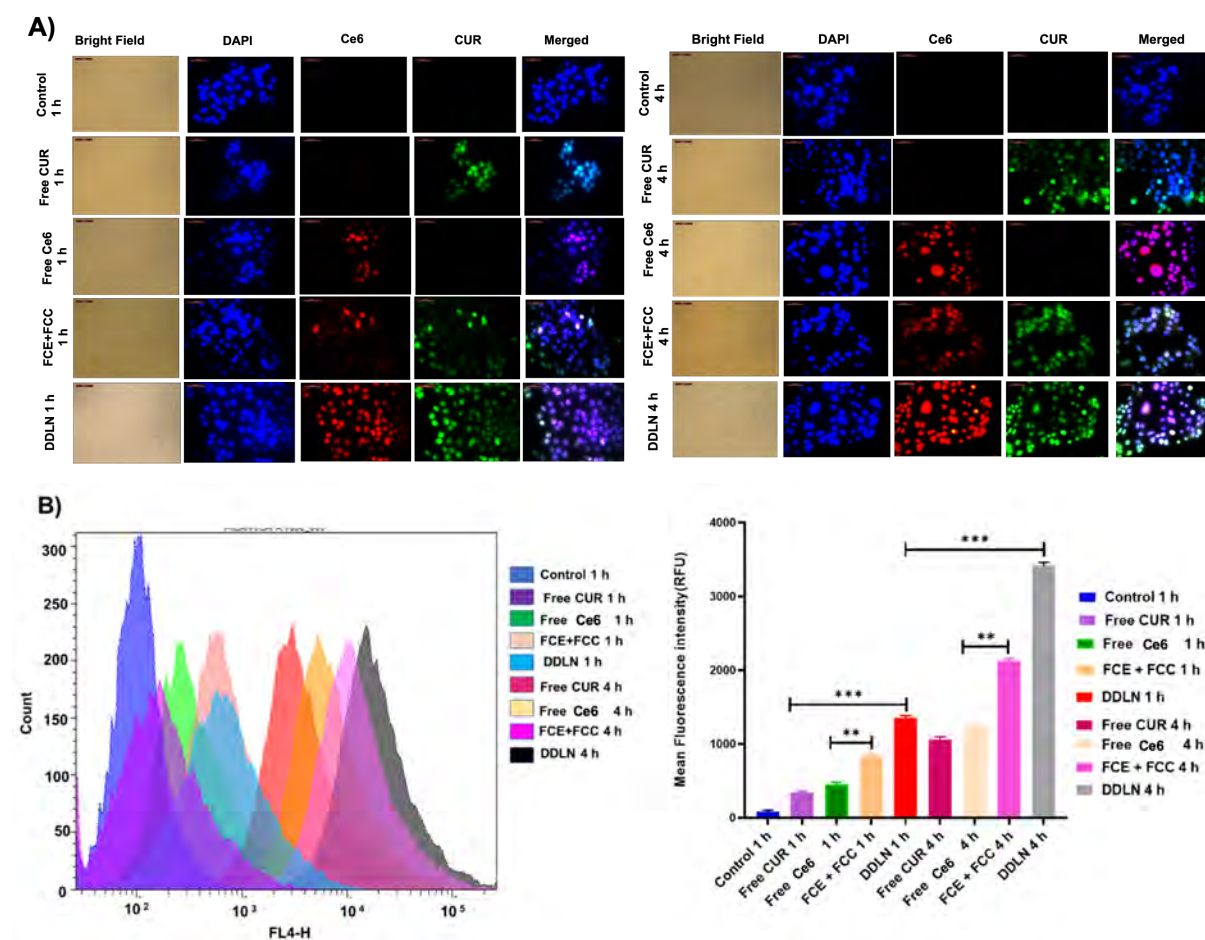
Figure 4.7. Cellular uptake of free CUR, free Ce6, FCE+FCC, and DDLN in B16F10 cell lines (Ce6 and CUR concentrations. 6 µg/ml) (A); Red, blue, and green signals represent cells stained by Ce6, DAPI, and CUR, respectively; assessment of the geometric mean of fluorescence of the B6F10 (B) at 1 and 4 h incubation by histogram plots and bar graphs. The data in bar graphs represent mean ± standard deviation, calculated from three sets of experiments.
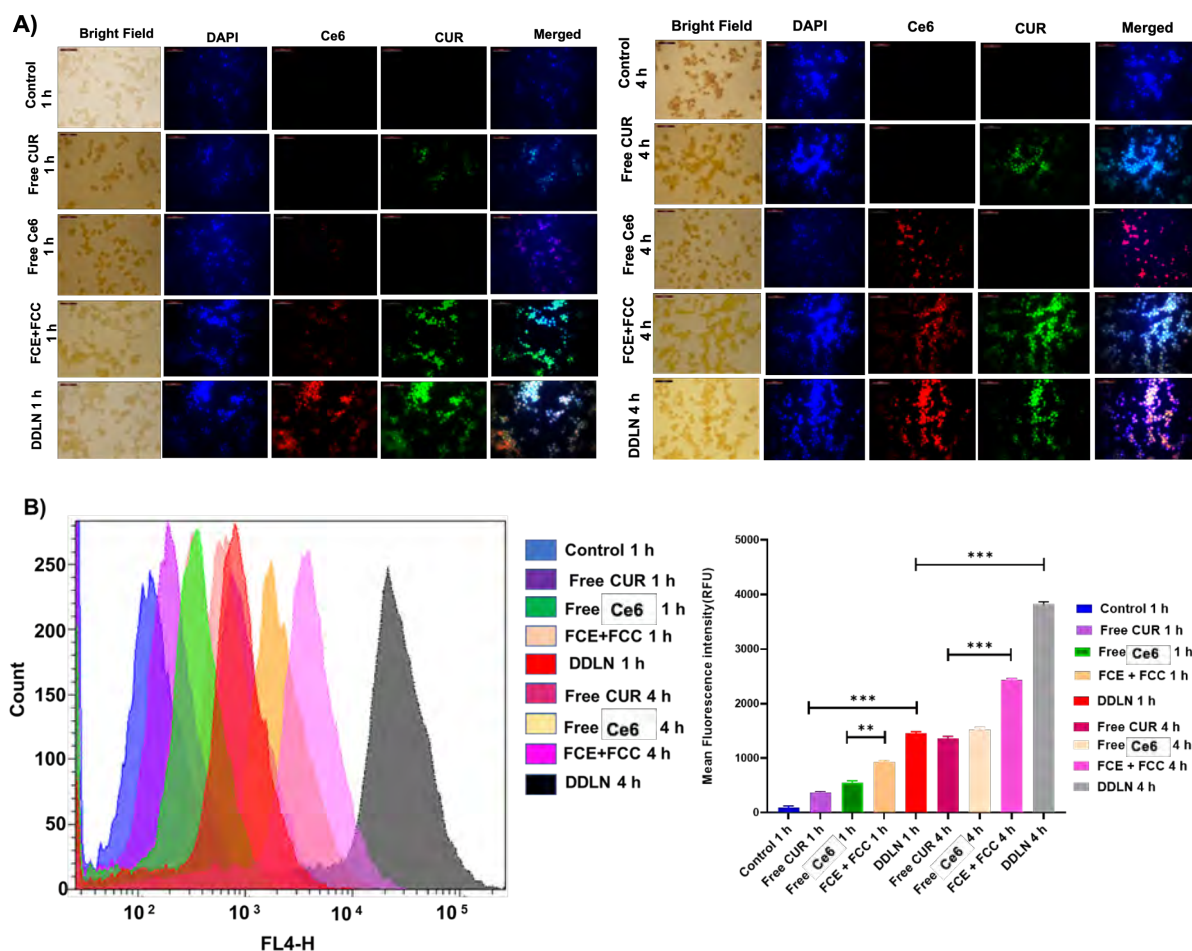
Figure 4.8. Cellular uptake of free CUR, free Ce6, FCE+FCC, and DDLN in A431 cell lines (Ce6 and CUR concentrations. 6 µg/ml) (A); Red, blue, and green signals represent cells stained by Ce6, DAPI, and CUR, respectively; assessment of the geometric mean of fluorescence of the A431 (B) at 1 and 4 h incubation by histogram plots and bar graphs. The data in the bar graphs represent mean ± standard deviation, calculated from three sets of experiments.

4.3.6.4.   Nuclear Staining Assay

Figures 4.9 A and **B** exhibit the nuclear fragmentation (NF) and cytoplasmic shrinkage (CS) observed in the cells with the various treatments. Blebbing was observed, which is considered a marker for apoptosis. It was observed that the cells treated with DDLN formulation showed the highest cellular damage highlighting the synergistic effect of Ce6 and CUR. The AO-EtBr techniques were used in order to provide an understanding of the mechanism in which cells died, namely in terms of apoptosis and necrosis. The vital dye AO can stain every cell, whether they are alive or dead, while cells whose membrane integrity has been disrupted can take up the stain EtBr. And hence, normal cells which remain intact appear to be green, whereas cells that are in the early or late stages of apoptosis and have compressed or damaged nuclei appear to be yellowish-orange or reddish, respectively. AO penetrated normal or early apoptotic cells,

producing green fluorescence after binding with DNA. However, EB could only enter through damaged membranes and emitted orange-red fluorescence after binding to condensed apoptotic nuclei. In contrast, necrotic cells stain orange but possess normal nuclear morphology with no condensed chromatin. The assay could detect normal cells, cells at different stages of apoptosis, and necrotic cells by changing cellular fluorescence and morphology. Both B16F10 and A431 cell lines were undergoing apoptosis after DDLN treatment, as indicated by an orange fluorescence [36].
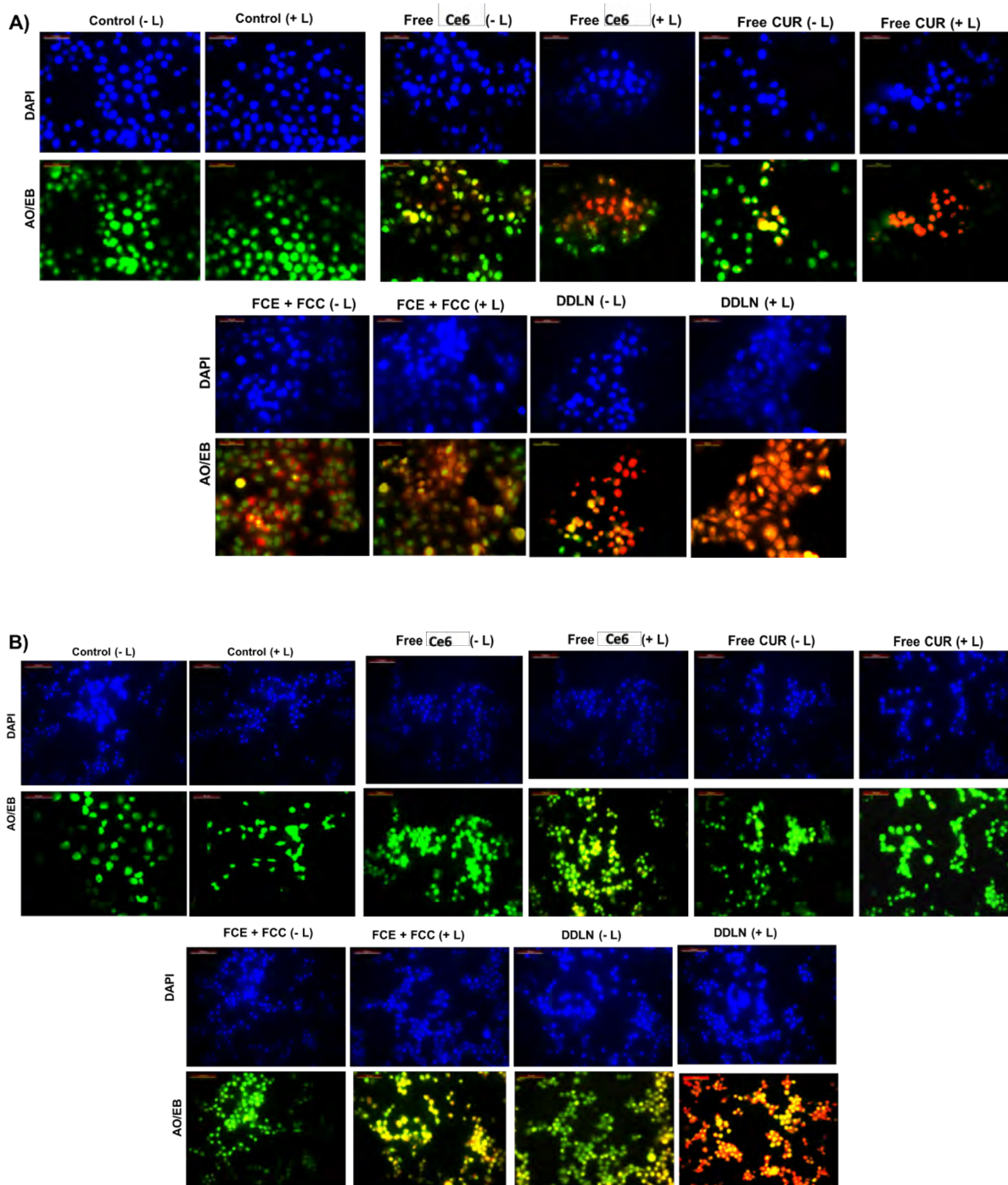
Figure 4.9. Analysis of nuclear morphology. Examples of B16F10 (A) and A431 cells (B) stained with DAPI, acridine Orange, and ethidium bromide following the treatment by free CUR, free Ce6, FCE+FCC, and DDLN (Ce6 and CUR concentration 10 µg/ml) (control cells received no treatment) (with and without laser, +L, -L), visualized under a fluorescence microscope on 40x Magnification. Scale bar. 100 µm.

4.3.6.5. DNA Fragmentation Assay

In order to assess the condition of the DNA, an agarose gel electrophoresis was carried out. The DNA damage caused due to free CUR, free Ce6, FCE+FCC, and DDLN formulations on B16F10 and A431 cell lines are represented in **Figures 4.10 A and 4.10 B**. It was observed that DDLN with laser irradiation caused the maximum DNA fragmentation (ladder-like pattern) as compared to only FCE+FCC and free Ce6, emphasizing the synergistic effect of CUR in the formulation.
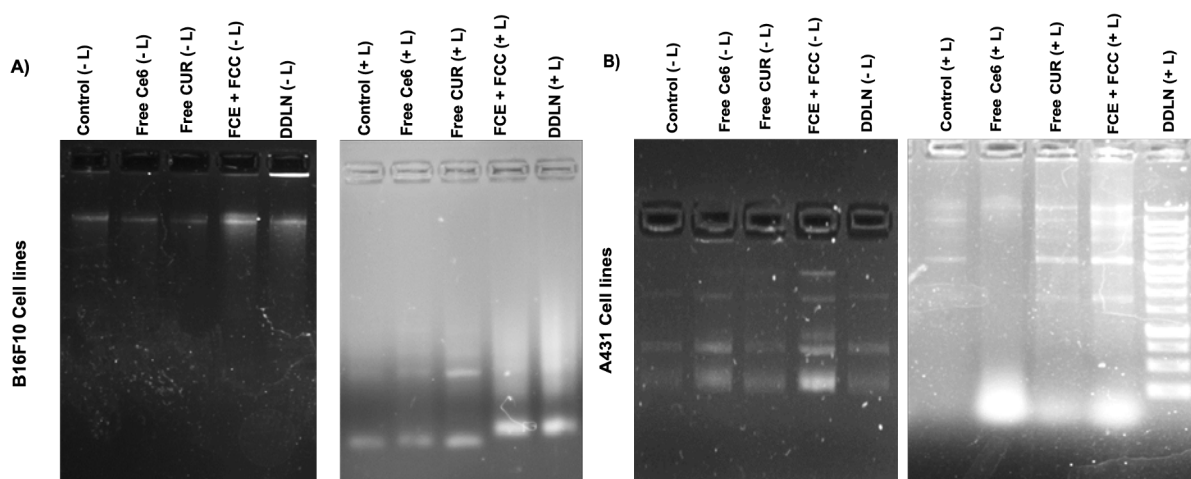
Figure 4.10. DNA fragmentation analysis following treatment with DNA from untreated cells (control), free CUR, free Ce6, FCE+FCC, and DDLN (with and without laser, +L, -L). DNA extracted from B16F10 (A) and A431 cells (B) viewed on ethidium bromide-stained agarose gel.

4.3.6.6. Intracellular ROS Assay

The presence of the esterase cleaves the acetate group from DCHFDA, while ROS species lead to the oxidation of DCHFDA, which activates the fluorescein molecule to exhibit fluorescence. The fluorescence obtained by treating the cells using different formulations by fluorescence microscope imaging is shown in **Figure 4.11 A** for **B16F10** and **Figure 4.11 B** for **A431**. It was observed that DDLN showed the highest fluorescence indicating the maximum generation

of ROS species occurs in the cells treated with DDLN leading to maximum cellular damage due to ROS generation.
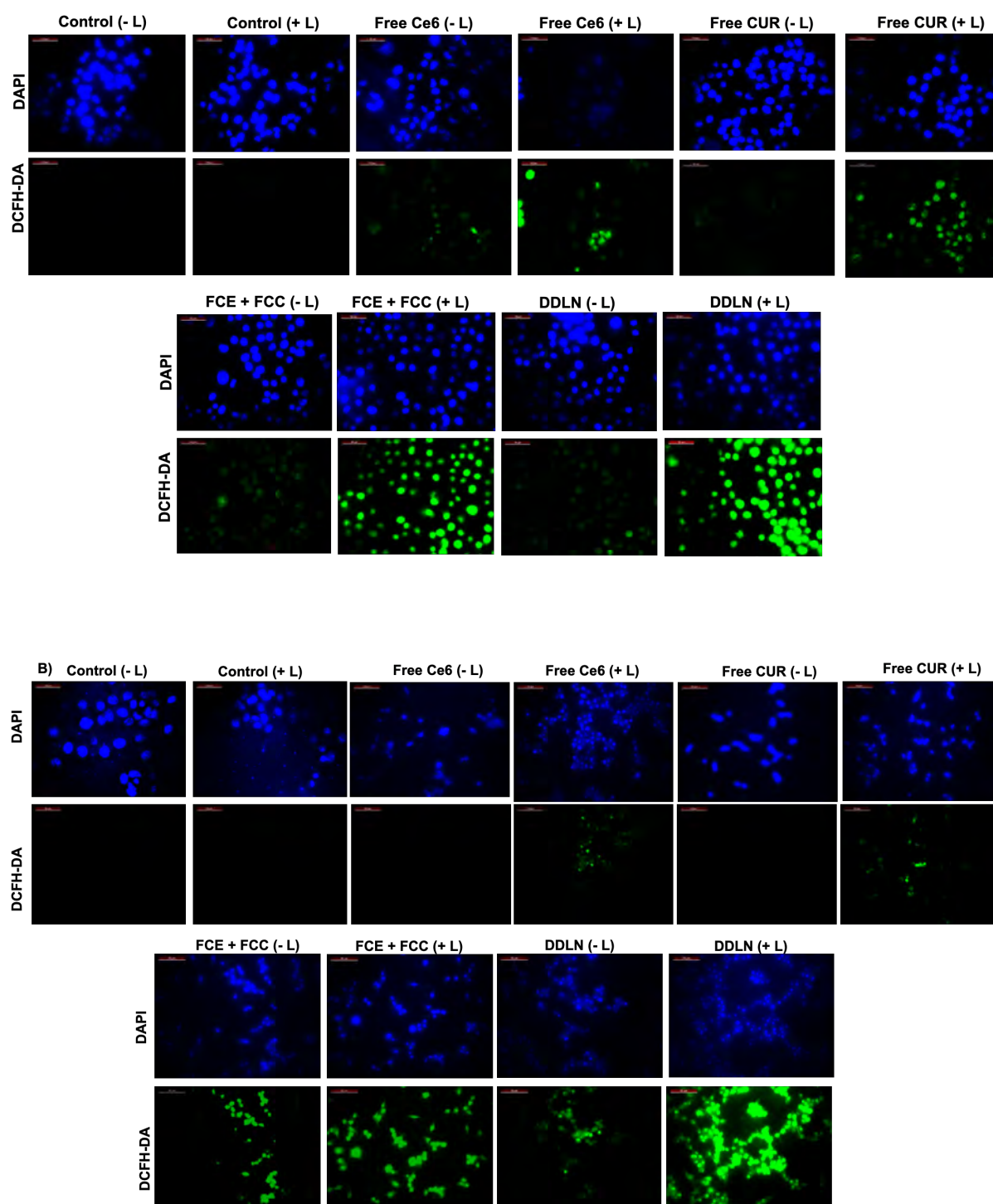
Figure 4.11. Intracellular ROS generation in B16F10 and A431 cells treated with free CUR, free Ce6, FCE+FCC, and DDLN (with and without laser,+L,-L) by fluorescence microscopy

(A) and (B). Untreated cells are designated as control. The ROS level was detected by tracking the fluorescence of DCFHDA dye (ex/em. 488/525 nm).

4.3.6.7. Cell Cycle Analysis

Treatment with free CUR, free Ce6, FCE+FCC, and DDLN induced the cell cycle arrest in the G2/M phase in both the tested cell population. The arrest was significantly higher in DDLN (+ L) -treated cells than in free Ce6, free CUR, and FCE+FCC treatment. The different phases of the cell population were represented in **Figures 4.12 A** and **B**. The cell population of CUR and Ce6 was found to be ~ 7.32 and ~ 3.52 fold in the G2 phase of B16F10 cells compared to untreated cells, respectively. The mechanism of action of Ce6 in which cells are arrested in the early anaphase stage (M-phase), and a similar result was observed with all the formulations as the maximum arrest of the cells were observed in the G2-M phase as shown in the graph.

Figure 4.12 Cell cycle arrest by free CUR, free Ce6, FCE+FCC, and DDLN (with and without laser, +L, -L) as analyzed by flow cytometry on B16F10 (A) and A431 (B). Untreated cells are mentioned as a control. The histogram plots (left) and the representative bar graphs (right) show cell populations in various stages of cell cycles.
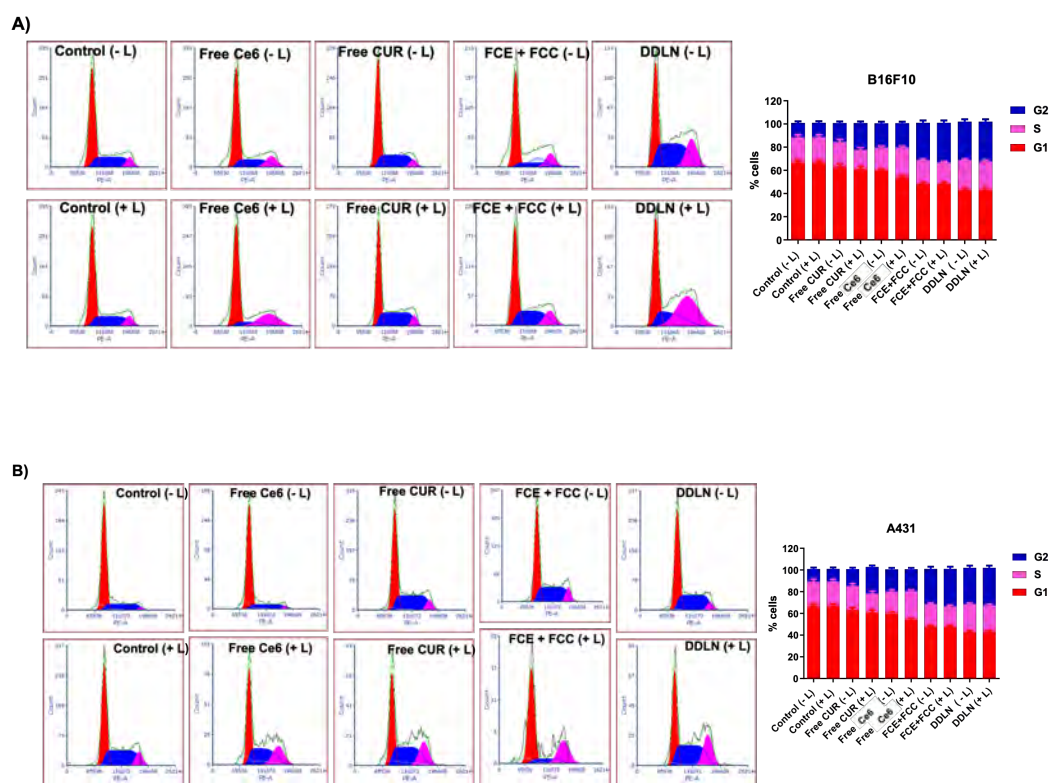
4.3.6.8. Annexin-V Assay

The extent of apoptosis for free CUR, free Ce6, FCE+FCC, and DDLN formulations is shown in **Figures 4.13 A** and **B**. It can be observed that for B16F10 cell lines, while free Ce6 (- L, +L) showed an apoptosis % of 5.38%, 8.91 %, free CUR (- L, + L) showed apoptosis of 4.21% , 10.2 %, FCE+FCC (- L, + L) showed apoptosis of 19.02 %, 29.02 %, and DDLN (- L, + L) showed apoptosis of 32.02 %, 48.02 %. Similarly, in A431 cell lines, free Ce6 (- L, + L) showed apoptosis % of 4.95 %, 7.31%, free CUR (- L, + L) showed apoptosis of 6.02 % , 12.2 %, FCE+FCC (- L, + L) showed apoptosis of 23.02 %, 32.02 %, DDLN (- L, + L) showed apoptosis of 38.02 %, 50.02 %. The DDLN (+L) formulation demonstrated the highest apoptotic response in both cell lines, which can be attributed to several factors, including enhanced cellular uptake and retention of DDLN within cellular compartments, as well as the combined chemo-photodynamic therapy effect mediated by Ce6 and CUR.

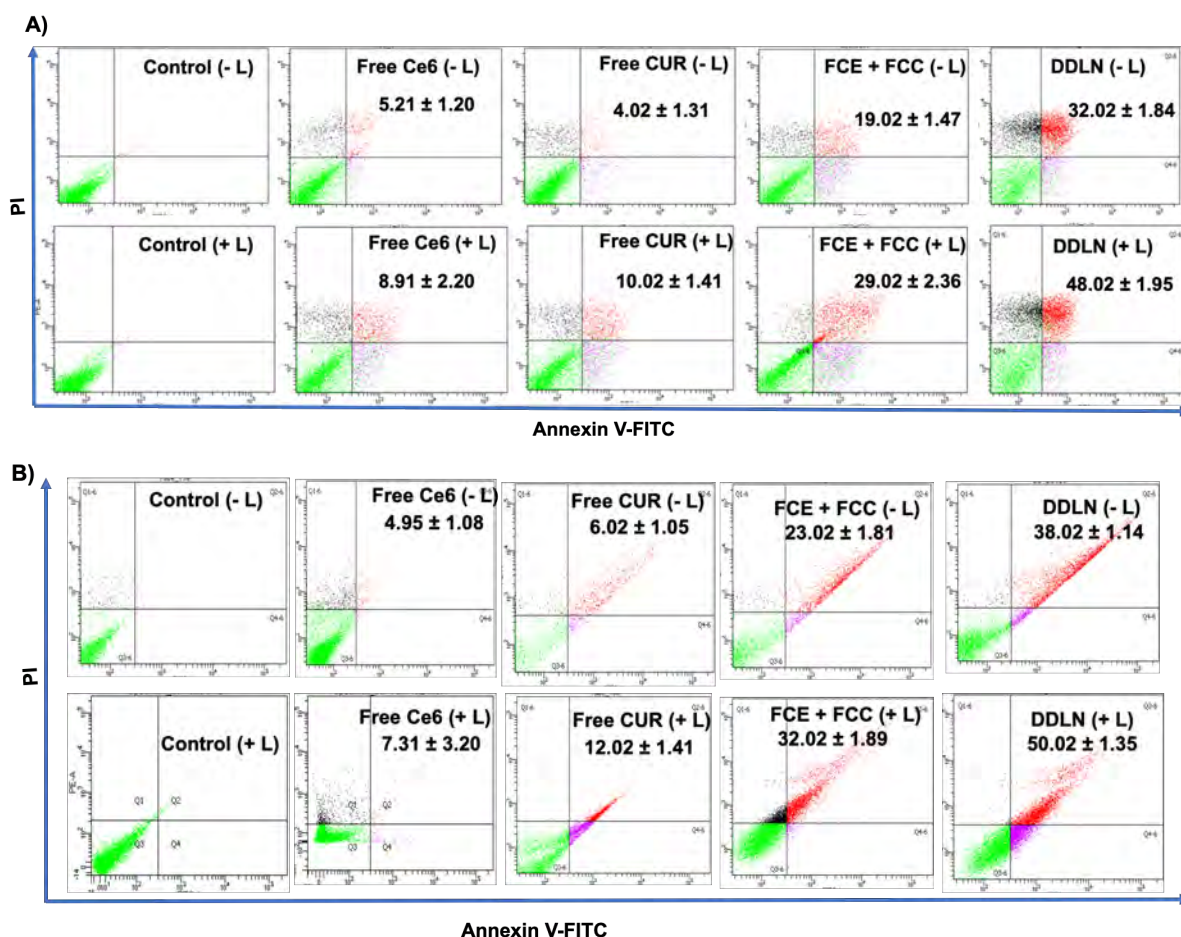**Figure 4.13** Annexin V assay performed by flow cytometry. The extent of apoptosis was evaluated by analyzing B16F10 cells (A) and A431 cells (B) treated with free CUR, free Ce6, FCE+FCC, and DDLN (with and without laser, +L, -L) at a Ce6 and CUR concentrations of 10 µg/ml (incubation time. 24 h) by using flow cytometry. Untreated cells are designated as control. The Q3 and Q4

quadrants represent early and late apoptosis, respectively (gated cell number. 10,000); the numerals represent the quantified percent cell populations in Q2 quadrants.

4.3.7. Ex-vivo Studies

4.3.7.1. Ex-vivo Skin Permeation Study

The Franz diffusion cell, which was utilized in the skin permeation study, is depicted in a schematic form here. (**Figure 4.14 A**). **Figure 4.14 B** shows the ex-vivo permeation of DDLN and plain gel (free drug gel/FCE+FCC) formulation permeated through goat skin. The amount of CUR and Ce6 permeated (% permeation) through DDLN gel and plain gel (free drug gel/FCE+FCC) after 24 h was found to be up to 80 and 35 %, respectively (**figure 4.14 B**). The permeation ($\mu g/cm^2$) of CUR and Ce6 drugs from DDLN gel and plain gel (free drug gel/FCE+FCC) through the goat skin was about upto 70 $\mu g/cm^2/24$ h and upto 30 $\mu g/cm^2/24$ h respectively (**Figure 4.14 C**), which indicates DDLN gel has significantly higher skin permeation than the plain (free drug gel/FCE+FCC). The flux value of DDLN gel containing CUR and Ce6 was found to be 4.52 ± 0.58 $\mu g/cm^2/h$, 4.61 ± 0.11 $\mu g/cm^2/h$ respectively. Additionally, the flux values of plain gel (free drug gel/FCE+FCC) containing CUR and Ce6 were found to be 1.30 ± 0.21 $\mu g/cm^2/h$, 1.28 ± 0.41 $\mu g/cm^2/h$, respectively. The DDLN gel demonstrated more ability to penetrate the goat skin than the plane gel (free drug gel/FCE+FCC), which was attributable to the enhancement of penetration by the DOTAP lipid (cationic charge-based lipid), solid lipid, and liquid lipid. The positive charge-based lipid containing DDLN gel can easily deposit and penetrate the keratinocyte tissues. The permeation alters the crystal arrangement of the skin, and it increases the lipid fluidity of the horny layers [37].

4.3.7.2. Skin retention study

The percentage of CUR and Ce6 recovered from skin tissue was observed as 98.45 ± 1.29 % and 99.14 ± 0.89 %, respectively. After 24 h of treatment, the skin was collected from the Franz diffusion cell, and the amount of CUR and Ce6 in the intradermal (viable part of skin and stratum corneum) was quantified. In comparison to free drug gel (FCE+FCC), DDLN gel containing CUR and Ce6 demonstrated 6.7 and 3.81 times greater retention in the stratum corneum, respectively. Furthermore, when compared to free drug gel (FCE+FCC), DDLN gel containing CUR and Ce6 demonstrated 4 and 4.26 times greater retention in viable skin, respectively. (**Figure 4.14 D**) DDLN gel shows higher retention times in viable skin and stratum corneum compared to plain gel (free drug gel/FCE+FCC), suggesting that DDLN gel

can effectively penetrate the deeper layers of skin. This was due to the smaller size of DDLN (less than 100 nm). Additionally, the small particle size favours DDLN accumulation at the inflamed site due to the EPR. Positive charge-based lipids (DOTAP) can form an interaction between extracellular lipid matrices of the skin resulting in the disruption of lipid orientation, which creates the diffusion or pathway to cross nanoparticles through the skin.
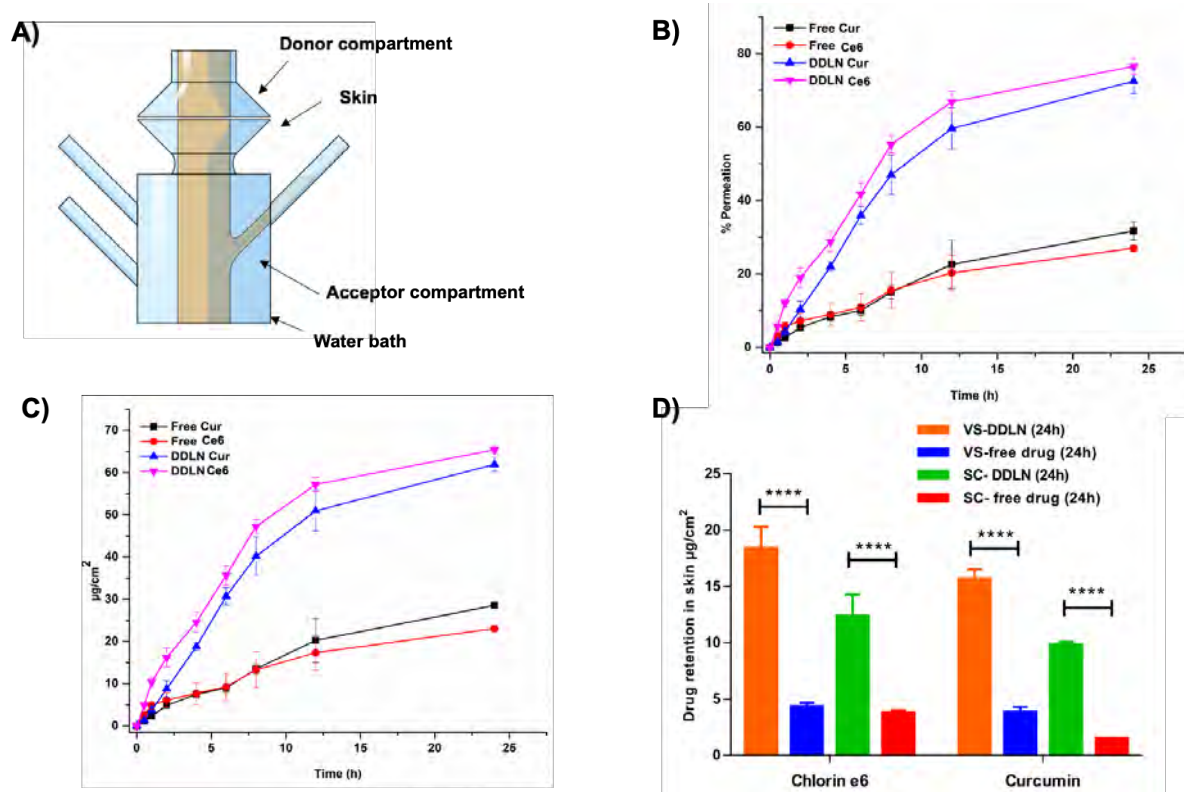
Figure 4.14. Schematic illustration of the Franz diffusion cell system used for the skin permeation study(A); Ex vivo skin permeation profile of DDLN and free drug CUR and Ce6 permeated through the skin (% Permeation) (Data represented as mean ± SD, n = 3) (B): Ex vivo skin permeation profile of DDLN and free drug CUR and Ce6 permeated through the skin ($\mu g/cm^2$) (Data represented as mean ± SD, n = 3) (C); The amount of CUR and Ce6 from DDLN gel and plain gel (free drug gel/FCE+FCC) in stratum corneum and viable skin (epidermis and dermis) (Data represented as mean ± SD, n = 3) (****P < 0.0001) (D).

4.3.7.3. Visualization of skin penetration study with confocal microscopy

For the analysis of the drug distribution or depth into different layers of the skin, DDLN gel and plain gel (free drug gel/FCE+FCC) formulation were applied on the skin, and qualitative/microscopical/visual results were observed with confocal microscopy. Figure 4.14 A represents the confocal microscopy images of the skin after permeation with formulation for 8 and 16 h. Both drugs have the fluorescence property CUR (green) and Ce6 (red**). Figure**

4.15. **A** demonstrates a higher fluorescent signal in skin cells treated with DDLN gel after 8 h and 16 h in comparison with plain gel (free drug gel/FCE+FCC). This suggests that DDLN gel can effectively penetrate the skin layers.

4.3.7.4. Dermatokinetic of DDLN gel and Free Drug Gel

The assessment of dermal bioavailability involves the estimation of the drug at the target site, which includes the different layers of skin. Skin cancers majorly originate from the viable epidermis of the skin. The dermis is invaded by compact masses or sheets of tumor cells in the epidermis due to the uncontrolled or irregular development of cells in the viable epidermis, which leads to metastasis. Therefore, for desired treatment efficacy, the drug should be deposited between the skin's epidermis and dermis. Hence, we have evaluated a dermal kinetic to determine the concentration of CUR and Ce6 in the target site with respect to time.

Figure 4.15 B and **C** present the distribution of CUR and Ce6 concentration in different layers of skin (epidermal and dermal) after a single dose application of DDLN gel and plain gel (free drug gel/ FCE+FCC-gel). The results showed that compared to plain gel DDLN gel was a significantly high distribution of CUR and Ce6 into the epidermis and dermis layer. **Table 4.8** indicates the numerical values of dermatokinetic parameters such as AUC_{0-30} h, maximum CUR and Ce6 concentration in the skin (C_{max} skin), time to achieve maximum level in the skin (T_{max}), and clearance. The total concentration of CUR and Ce6 (DDLN gel) retained AUC_{0-32} skin in the epidermis and dermis layers was significantly high compared to the FCE+FCC-gel. The total amount of concentration of CUR and Ce6 in the epidermis layer was increased with DDLN gel (CUR) (711.32 ± 39.02 µg/cm^2∗h) and for DDLN gel (Ce6) (833.89 ± 20.90 µg/cm^2∗h) in comparison to FCE+FCC-gel-CUR (294.91 ± 5.338 µg/cm^2∗h) and for FCE+FCC-gel-Ce6 (277.50 ± 4.202 µg/cm^2∗h). C_{max} skin was found to be significantly ($p < 0.05$) more in the epidermis and dermis of skin treated with DDLN gel of CUR and Ce6 in comparison to FCE+FCC-gel. According to the literature, it was reported that lipidic-containing nanocarriers are efficient in intermingling with lipid bilayer membranes which results in lipid rearrangement that could exhibit higher permeation and higher residence time in the skin layers. The formulation contains phospholipid as well as surfactant-based colloidal nanoparticles, which improve the drug transport over the skin by altering the lipid-tight packing junctions [38].

Cancer cells can have a slight negative charge due to an overexpression of anionic phospholipids, which contain negatively charged groups such as phosphate. This can be due to

the abnormal metabolism of cancer cells. The slight negative charge on the surface of cancer cells can make them more attractive to positively charged nanocarriers like cationic lipids, which can interact with the negatively charged surface of cancer cells and facilitate the uptake of drugs [39,40]. This is known as electrostatic interaction. Positively charged-based nanocarriers could result in more electrostatic interactions with the negatively charged bioactive components of the skin and electrostatic deposition in the skin layers. Therefore, positive charge nanocarriers are potential nanocarriers to enhance the permeation through the skin or tumor tissues. The dermal kinetics study that was conducted revealed that the developed DDLN gel could not only improve the penetration of CUR and Ce6 but also increase the residence time in the different layers of skin. Furthermore, the DDLN and SEPINEO™ P 600 gel could have contributed to developing a depot for CUR and Ce6 gel.
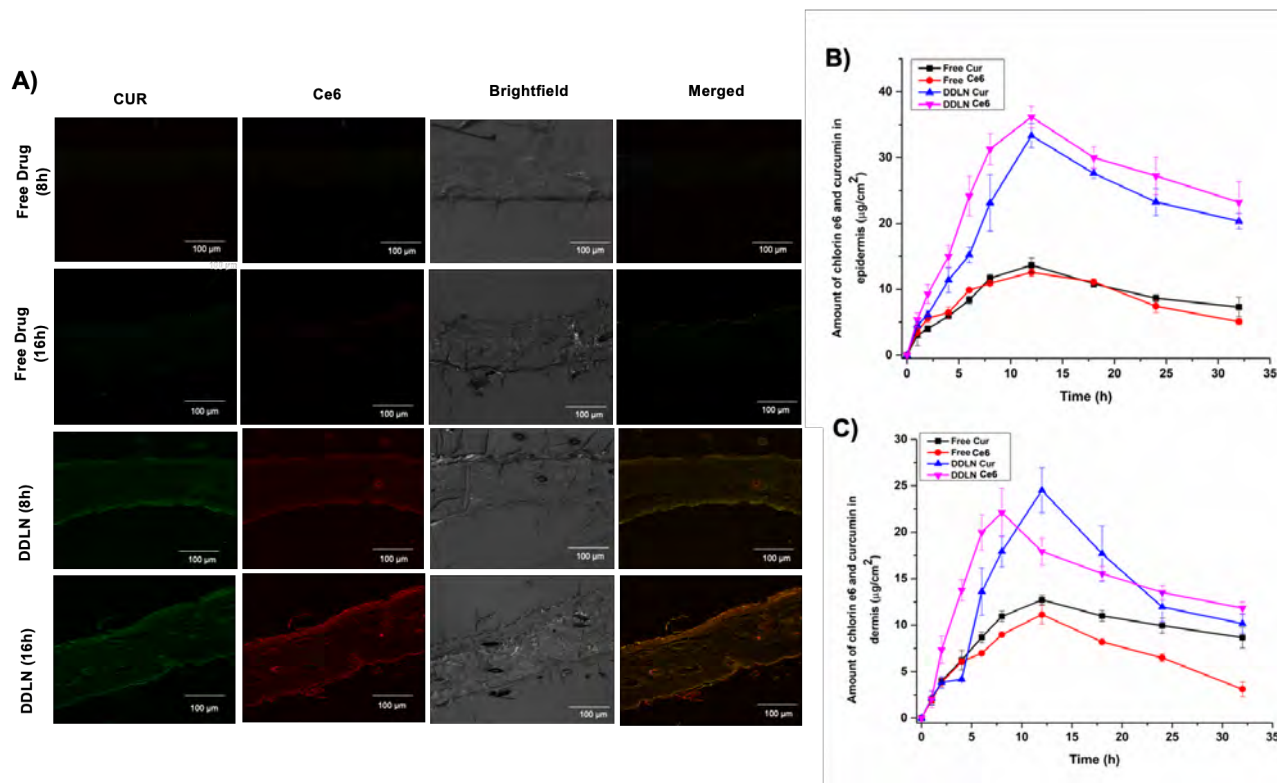
Figure 4.15. Fluorescent images of the skin after incubation with different formulations of DDLN gel and plain gel for 8 h and 16 h. Scale bar: 100 μm (A); Dermal pharmacokinetics of DDLN gel and plain gel (B,C), i.e., amount of CUR and Ce6 in epidermis and dermis at various time points (Data represented as mean ± SD, n = 5).

Table 4.8. Dermatokinetics parameters (mean ± SD) of topical application of curcumin and chlorin e6 formulations (DDLN-gel and plain gel) in epidermis and dermis (n = 5).

Parameters	Units	Plain gel (Curcumin)		DDLN gel (curcumin)		Plain gel (Chlorin e6)		DDLN gel (Chlorin e6)	
		Epidermis	Dermis	Epidermis	Dermis	Epidermis	Dermis	Epidermis	Dermis
$AUC_{total\ (0-32h)}$ (Mean ± SD, n = 5)	$\mu g/cm^2*h$	294.91 ± 5.33	304.00 ± 13.73	711.32 ± 39.02	447.87 ± 43.39	277.50 ± 4.2	220.76 ± 6.424	833.89 ± 20.90	471.11 ± 24.22
AUC_{0-inf} (Mean ± SD, n = 5)	$\mu g/cm^2*h$	727.59 ± 455.36	915.51 ± 403.52	1660.95 ± 174.15	717.83 ± 46.6	369.88 ± 22.65	268.4 ± 23.2	7076.00 ± 67.3	1097.35 ± 211
C_{max} Skin (Mean ± SD, n = 5)	$\mu g/cm^2$	13.65 ± 1.10	12.71 ± 0.51	33.33 ± 1.86	24.52 ± 2.41	12.55 ± 0.57	11.14 ± 1.01	36.17 ± 1.65	22.11 ± 2.63
T_{max} Skin (Mean ± SD, n = 5)	h	12	12	12	12	12	12	12	8
Cl (Mean ± SD, n = 5)	$\mu g/h$	0.1701 ± 0.07	0.1223 ± 0.04	0.0609 ± 0.00	0.1396 ± 0.00	0.2710 ± 0.01	0.3744 ± 0.03	0.0460 ± 0.02	0.0932 ± 0.01

4.3.8. Assessment of stability of DDLN and DDLN gel

The developed DDLN and DDLN gel were tested for storage stability for up to 90 days at two different temperatures such as 4 °C and 25 °C (**Table 4.9**). After being stored for a period of 90 days, the level of Ce6 and CUR did not significantly alter. Also, the results from the assay of the gel, particle size, and entrapment efficiency have not shown a substantial difference between 4 °C and 25 °C. It reveals that the DDLN and DDLN gel were stable with consideration of both the rheological and physiological characteristics.

Table 4.9. Stability data of DDLN Gel at different storage conditions

Stability condition	Days	DDLN	Particle size (nm)	% Entrapment efficiency (mean ± SD)	Assay of nanocarrier loaded gel/ DDLN Gel (mean ± SD)
2-8 ℃	0 day	Chlorin e6	94.65 ± 3.5	89.47 ± 1.70	101.29 ± 1.1
	0 day	Curcumin		79.11 ± 4.08	98.23 ± 0.87
	30 days	Chlorin e6	99.14 ± 8.5	86.12 ± 2.80	97.03 ± 2.5
	30 days	Curcumin		76.53 ± 3.01	99.32 ± 0.12
	90 days	Chlorin e6	100.87 ± 2.4	89.47 ± 4.20	96.47 ± 3.55
	90 days	Curcumin		78.93 ± 6.05	100.9 ± 0.29
25 ± 0.5 ℃	0 day	Chlorin e6	90.4 ± 4.9	86.47 ± 3.20	98.12 ± 0.65
	0 day	Curcumin		78.93 ± 2.08	99.05 ± 0.46
	30 days	Chlorin e6	101.15 ± 10.25	89.10 ± 3.4	97.42 ± 0.10
	30 days	Curcumin		75.12 ± 2.08	99.45 ± 0.12
	90 days	Chlorin e6	112.56 ± 4.9	87.23 ± 1.0	97.25 ± 0.12
	90 days	Curcumin		74.19 ± 6.58	98.05 ± 3.5

4.4. Conclusion

In summary, photo-triggered ROS-generating dual drug-based lipidic nanoparticles were designed for synergistic effects against cutaneous melanoma cancer. In this work, chlorine e6 as a photosensitizer and CUR as an anticancer agent encapsulated in lipid nanocarriers and embedded in the SEPINEO gel to enhance the skin and tumor penetration. The optimized formulation showed a uniform nano-size range with high entrapment efficiency for both drugs. This developed dual-drug formulation gel provided high skin penetration and exhibited higher singlet oxygen generation and stability. The skin retention study showed that DDLN gel had high skin retention compared to the free drugs (FCC+FCE). On a cellular level, the combined formulation showed an excellent synergetic effect compared to free drugs on the B16F10 and A431 cell lines. Moreover, a cellular uptake study with B16F10 and A431 revealed that DDLN shows higher cellular uptake than free drugs. The combination of Ce6 and CUR delivery by a lipidic system exhibits more therapeutic efficiency than the individual treatment. This lipidic system may provide a unique platform for delivering potent hydrophobic moiety for different ill conditions such as cancer, psoriasis, skin infections, etc. It may also be adequate for clinical testing and commercial application.

References:

[1] S. Rawal, M.M. Patel, Threatening cancer with nanoparticle aided combination oncotherapy, Journal of Controlled Release. 301 (2019) 76–109. https://doi.org/10.1016/J.JCONREL.2019.03.015.

[2] S. Yano, S. Hirohara, M. Obata, Y. Hagiya, S. ichiro Ogura, A. Ikeda, H. Kataoka, M. Tanaka, T. Joh, Current states and future views in photodynamic therapy, Journal of Photochemistry and Photobiology C: Photochemistry Reviews. 12 (2011) 46–67. https://doi.org/10.1016/J.JPHOTOCHEMREV.2011.06.001.

[3] M. Champeau, S. Vignoud, L. Mortier, S. Mordon, Photodynamic therapy for skin cancer: How to enhance drug penetration?, J Photochem Photobiol B. 197 (2019) 111544. https://doi.org/10.1016/J.JPHOTOBIOL.2019.111544.

[4] M.T. Jarvi, M.J. Niedre, M.S. Patterson, B.C. Wilson, The Influence of Oxygen Depletion and Photosensitizer Triplet-state Dynamics During Photodynamic Therapy on Accurate Singlet Oxygen Luminescence Monitoring and Analysis of Treatment Dose Response, Photochem Photobiol. 87 (2011) 223–234. https://doi.org/10.1111/J.1751-1097.2010.00851.X.

[5] H.A. Isakau, M. V. Parkhats, V.N. Knyukshto, B.M. Dzhagarov, E.P. Petrov, P.T. Petrov, Toward understanding the high PDT efficacy of chlorin e6–polyvinylpyrrolidone formulations: Photophysical and molecular aspects of photosensitizer–polymer interaction in vitro, J Photochem Photobiol B. 92 (2008) 165–174. https://doi.org/10.1016/J.JPHOTOBIOL.2008.06.004.

[6] A. P, B. K, C. KA, F. TH, G. AW, G. SO, H. SM, H. MR, J. A, K. D, K. M, M. J, M. P, N. D, P. J, W. BC, G. J, Photodynamic therapy of cancer: an update, CA Cancer J Clin. 61 (2011) 250–281. https://doi.org/10.3322/CAAC.20114.

[7] A.I. Gavrina, M. V. Shirmanova, N.A. Aksenova, D. V. Yuzhakova, L.B. Snopova, A.B. Solovieva, P.S. Timashev, V. V. Dudenkova, E. V. Zagaynova, Photodynamic therapy of mouse tumor model using chlorin e6- polyvinyl alcohol complex, J Photochem Photobiol B. 178 (2018) 614–622. https://doi.org/10.1016/J.JPHOTOBIOL.2017.12.016.

[8] H. Mirzaei, G. Naseri, R. Rezaee, M. Mohammadi, Z. Banikazemi, H.R. Mirzaei, H. Salehi, M. Peyvandi, J.M. Pawelek, A. Sahebkar, Curcumin: A new candidate for melanoma therapy?, Int J Cancer. 139 (2016) 1683–1695. https://doi.org/10.1002/IJC.30224.

[9] J.A. Bush, K.J.J. Cheung, G. Li, Curcumin Induces Apoptosis in Human Melanoma Cells through a Fas Receptor/Caspase-8 Pathway Independent of p53, Exp Cell Res. 271 (2001) 305–314. https://doi.org/10.1006/EXCR.2001.5381.

[10] K. Nagahama, T. Utsumi, T. Kumano, S. Maekawa, N. Oyama, J. Kawakami, Discovery of a new function of curcumin which enhances its anticancer therapeutic potency OPEN, Nature Publishing Group. (2016). https://doi.org/10.1038/srep30962.

[11] S.S. Jalde, A.K. Chauhan, J.H. Lee, P.K. Chaturvedi, J.S. Park, Y.W. Kim, Synthesis of novel Chlorin e6-curcumin conjugates as photosensitizers for photodynamic therapy against pancreatic carcinoma, Eur J Med Chem. 147 (2018) 66–76. https://doi.org/10.1016/J.EJMECH.2018.01.099.

[12] V.F. Otvagin, A. V. Nyuchev, N.S. Kuzmina, I.D. Grishin, A.E. Gavryushin, Y. V. Romanenko, O.I. Koifman, D. V. Belykh, N.N. Peskova, N.Y. Shilyagina, I. V. Balalaeva, A.Y. Fedorov, Synthesis and biological evaluation of new water-soluble photoactive chlorin conjugate for targeted delivery, Eur J Med Chem. 144 (2018) 740–750. https://doi.org/10.1016/J.EJMECH.2017.12.062.

[13] W. Zhang, J. Shen, H. Su, G. Mu, J.H. Sun, C.P. Tan, X.J. Liang, L.N. Ji, Z.W. Mao, Co-Delivery of Cisplatin Prodrug and Chlorin e6 by Mesoporous Silica Nanoparticles for Chemo-Photodynamic Combination Therapy to Combat Drug Resistance, ACS Appl Mater Interfaces. 8 (2016) 13332–13340. https://doi.org/10.1021/ACSAMI.6B03881/ASSET/IMAGES/LARGE/AM-2016-03881F_0009.JPEG.

[14] V.K. Rapalli, S. Sharma, A. Roy, G. Singhvi, Design and dermatokinetic evaluation of Apremilast loaded nanostructured lipid carriers embedded gel for topical delivery: A potential approach for improved permeation and prolong skin deposition, Colloids Surf B Biointerfaces. 206 (2021) 111945. https://doi.org/10.1016/J.COLSURFB.2021.111945.

[15] R. Jain, R. Pradhan, S. Hejmady, G. Singhvi, S.K. Dubey, Fluorescence-based method for sensitive and rapid estimation of chlorin e6 in stealth liposomes for photodynamic therapy against cancer, Spectrochim Acta A Mol Biomol Spectrosc. 244 (2021) 118823. https://doi.org/10.1016/J.SAA.2020.118823.

[16] V.K. Rapalli, S. Banerjee, S. Khan, P.N. Jha, G. Gupta, K. Dua, M.S. Hasnain, A.K. Nayak, S.K. Dubey, G. Singhvi, QbD-driven formulation development and evaluation of topical hydrogel containing ketoconazole loaded cubosomes, Materials Science and Engineering C. 119 (2021). https://doi.org/10.1016/J.MSEC.2020.111548.

[17] R. Jain, S.K. Dubey, G. Singhvi, Stability indicating validated high-performance liquid chromatography method for simultaneous estimation of chlorin e6 and curcumin in bulk and drug-loaded lipidic nanoformulation, Sep Sci Plus. (2022). https://doi.org/10.1002/SSCP.202200107.

[18] L. Li, B.C. Bae, T.H. Tran, K.H. Yoon, K. Na, K.M. Huh, Self-quenchable biofunctional nanoparticles of heparin–folate-photosensitizer conjugates for photodynamic therapy, Carbohydr Polym. 2 (2011) 708–715. https://doi.org/10.1016/J.CARBPOL.2011.05.011.

[19] P. Huang, Z. Li, J. Lin, D. Yang, G. Gao, C. Xu, L. Bao, C. Zhang, K. Wang, H. Song, H. Hu, D. Cui, Photosensitizer-conjugated magnetic nanoparticles for in vivo simultaneous magnetofluorescent imaging and targeting therapy, Biomaterials. 32 (2011) 3447–3458. https://doi.org/10.1016/J.BIOMATERIALS.2011.01.032.

[20] C. Yang, H. Chen, J. Zhao, X. Pang, Y. Xi, G. Zhai, Development of a folate-modified curcumin loaded micelle delivery system for cancer targeting, Colloids Surf B Biointerfaces. 121 (2014) 206–213. https://doi.org/10.1016/J.COLSURFB.2014.05.005.

[21] S.J. Lee, H. Koo, H. Jeong, M.S. Huh, Y. Choi, S.Y. Jeong, Y. Byun, K. Choi, K. Kim, I.C. Kwon, Comparative study of photosensitizer loaded and conjugated glycol chitosan nanoparticles for cancer therapy, J Control Release. 152 (2011) 21–29. https://doi.org/10.1016/J.JCONREL.2011.03.027.

[22] M. Hoebeke, X. Damoiseau, Determination of the singlet oxygen quantum yield of bacteriochlorin a: a comparative study in phosphate buffer and aqueous dispersion of dimiristoyl-L-α-phosphatidylcholine liposomes, Photochemical & Photobiological Sciences. 1 (2002) 283–287. https://doi.org/10.1039/B201081J.

[23] S.M. Gandhi, A.K. Khan, S. Rathod, R. Jain, S.K. Dubey, D. Ray, V.K. Aswal, A. Joshi, P. Bahadur, S. Tiwari, Water driven transformation of a nonionic microemulsion into liquid crystalline phase: Structural characterizations and drug release behavior, J Mol Liq. 326 (2021) 115239. https://doi.org/10.1016/J.MOLLIQ.2020.115239.

[24] M. Paul, A.M. Itoo, B. Ghosh, S. Biswas, Hypoxia alleviating platinum(IV)/chlorin e6-based combination chemotherapeutic-photodynamic nanomedicine for oropharyngeal

carcinoma, J Photochem Photobiol B. 238 (2023) 112627. https://doi.org/10.1016/J.JPHOTOBIOL.2022.112627.

[25] P. Kumari, M. Paul, H. Bhatt, S.V.K. Rompicharla, D. Sarkar, B. Ghosh, S. Biswas, Chlorin e6 Conjugated Methoxy-Poly(Ethylene Glycol)-Poly(D,L-Lactide) Glutathione Sensitive Micelles for Photodynamic Therapy, Pharm Res. 37 (2020). https://doi.org/10.1007/S11095-019-2750-0.

[26] S. Kumbham, M. Paul, A. Itoo, B. Ghosh, S. Biswas, Oleanolic acid-conjugated human serum albumin nanoparticles encapsulating doxorubicin as synergistic combination chemotherapy in oropharyngeal carcinoma and melanoma, Int J Pharm. 614 (2022). https://doi.org/10.1016/J.IJPHARM.2022.121479.

[27] S. Kumbham, M. Paul, H. Bhatt, B. Ghosh, S. Biswas, Oleanolic acid-conjugated poly (D, L-lactide)-based micelles for effective delivery of doxorubicin and combination chemotherapy in oral cancer, J Mol Liq. 320 (2020). https://doi.org/10.1016/J.MOLLIQ.2020.114389.

[28] A.M. Itoo, M. Paul, B. Ghosh, S. Biswas, Oxaliplatin delivery via chitosan/vitamin E conjugate micelles for improved efficacy and MDR-reversal in breast cancer, Carbohydr Polym. 282 (2022). https://doi.org/10.1016/J.CARBPOL.2022.119108.

[29] N.R. Vysyaraju, M. Paul, S. Ch, B. Ghosh, S. Biswas, Olaparib@human serum albumin nanoparticles as sustained drug-releasing tumour-targeting nanomedicine to inhibit growth and metastasis in the mouse model of triple-negative breast cancer, Https://Doi.Org/10.1080/1061186X.2022.2092623. (2022). https://doi.org/10.1080/1061186X.2022.2092623.

[30] S. Gorantla, E.R. Puppala, V.G.M. Naidu, R.N. Saha, G. Singhvi, Hyaluronic acid-coated proglycosomes for topical delivery of tofacitinib in rheumatoid arthritis condition: Formulation design, in vitro, ex vivo characterization, and in vivo efficacy studies, Int J Biol Macromol. (2022). https://doi.org/10.1016/J.IJBIOMAC.2022.10.117.

[31] S. Gorantla, E.R. Puppala, V.G.M. Naidu, R.N. Saha, G. Singhvi, Hyaluronic acid-coated proglycosomes for topical delivery of tofacitinib in rheumatoid arthritis condition: Formulation design, in vitro, ex vivo characterization, and in vivo efficacy studies, Int J Biol Macromol. 224 (2023) 207–222. https://doi.org/10.1016/J.IJBIOMAC.2022.10.117.

[32] T. Jiang, T. Wang, T. Li, Y. Ma, S. Shen, B. He, R. Mo, Enhanced Transdermal Drug Delivery by Transfersome-Embedded Oligopeptide Hydrogel for Topical Chemotherapy of Melanoma, ACS Nano. 12 (2018) 9693–9701. https://doi.org/10.1021/ACSNANO.8B03800/ASSET/IMAGES/MEDIUM/NN-2018-038009_M001.GIF.

[33] V.K. Rapalli, S. Sharma, A. Roy, A. Alexander, G. Singhvi, Solid lipid nanocarriers embedded hydrogel for topical delivery of apremilast: In-vitro, ex-vivo, dermatopharmacokinetic and anti-psoriatic evaluation, J Drug Deliv Sci Technol. 63 (2021). https://doi.org/10.1016/J.JDDST.2021.102442.

[34] A.L. Onugwu, A.A. Attama, P.O. Nnamani, S.O. Onugwu, E.B. Onuigbo, V. V. Khutoryanskiy, Development and optimization of solid lipid nanoparticles coated with chitosan and poly(2-ethyl-2-oxazoline) for ocular drug delivery of ciprofloxacin, J Drug Deliv Sci Technol. 74 (2022) 103527. https://doi.org/10.1016/J.JDDST.2022.103527.

[35] J. Emami, H. Mohiti, H. Hamishehkar, J. Varshosaz, Formulation and optimization of solid lipid nanoparticle formulation for pulmonary delivery of budesonide using Taguchi and Box-Behnken design, Res Pharm Sci. 10 (2015) 17–33.

[36] R. Jain, M. Paul, S.G. Padaga, S.K. Dubey, S. Biswas, G. Singhvi, Dual-Drug-Loaded Topical Delivery of Photodynamically Active Lipid-Based Formulation for

Combination Therapy of Cutaneous Melanoma, Mol Pharm. (2023). https://doi.org/10.1021/ACS.MOLPHARMACEUT.3C00280.

[37] P. Desai, R.R. Patlolla, M. Singh, Interaction of nanoparticles and cell-penetrating peptides with skin for transdermal drug delivery, Mol Membr Biol. 27 (2010) 247. https://doi.org/10.3109/09687688.2010.522203.

[38] P. Ghasemiyeh, S. Mohammadi-Samani, Potential of Nanoparticles as Permeation Enhancers and Targeted Delivery Options for Skin: Advantages and Disadvantages, Drug Des Devel Ther. 14 (2020) 3271. https://doi.org/10.2147/DDDT.S264648.

[39] W. Szlasa, I. Zendran, A. Zalesińska, M. Tarek, J. Kulbacka, Lipid composition of the cancer cell membrane, J Bioenerg Biomembr. 52 (2020) 321. https://doi.org/10.1007/S10863-020-09846-4.

[40] A.C. Alves, D. Ribeiro, C. Nunes, S. Reis, Biophysics in cancer: The relevance of drug-membrane interaction studies, Biochimica et Biophysica Acta (BBA) - Biomembranes. 1858 (2016) 2231–2244. https://doi.org/10.1016/J.BBAMEM.2016.06.025.

CHAPTER 5

CONCLUSIONS AND FUTURE PROSPECTS

5.1. Conclusion

Skin cancer can manifest in various forms, such as melanoma, basal cell, and squamous cell carcinoma. Cutaneous melanoma develops from melanocyte tumor mutation and originates from the lower layers of the epidermis or deeper skin tissues. Pathogenesis of skin cancer is heterogeneous, depending on the location and stage of the malignancy. Surgical intervention may be used to treat primary cutaneous melanoma; however, this is not always practical. Recent therapeutic approaches, including chemotherapy, radiation, immunotherapy, and other treatments, have been reported to have undesirable effects, such as immune response, non-specificity, and drug resistance.

The main treatment option for skin cancer is surgery, although there are less invasive treatments available, including topical 5-FU, Imiquimod, and other drugs, such as Diclofenac sodium and Ingenol mebutate. However, the recurrence rate is higher after surgical therapy, requiring the development of more effective treatments. The cure rates associated with topical drugs are much lower compared to surgical therapy. Besides, current topical therapies do not penetrate well and require frequent, prolonged applications. Consequently, patient adherence is inconsistent, and the risk of developing severe inflammation. The conventional preparations (creams, ointments, etc.) exhibit lower efficacy and cause local toxicity (e.g., skin atrophy, skin infections, stretch marks, and redness) due to rapid loco-regional drug release, poor penetrability, and low bioavailability at the site action resulted in poor efficacy that leads to metastasis.

PDT is a novel as well as an efficient strategy for tumor treatment; however, the low solubility and low stability of the photosensitizers often limit its application in biological systems [80] The problem associated with the delivery of PDT-containing PS molecules via the topical route includes limited light penetration ability and permeation through cancerous tissue or stratum corneum, rendering it ineffective. Additionally, the excessive thickness of the tumor, more collagen content inside the tumor, ulceration, infiltrative growth tissue, and the presence of melanin can cause resistance to PDT. In order to address these challenges, the focus has been switched to nanotherapeutics. There are several reports claiming that nano-carriers are preferred for their promising delivery of therapeutic agents to localized skin surfaces due to their smaller size, greater permeation through biological barriers, better surface properties, high skin deposition, and sustained drug release properties; they were able to prove advantageous in treating skin cancer.

To address the drawbacks of traditional therapy, researchers are exploring innovative drug delivery methods such as nanocarriers and combination-topical based treatments. Topical delivery is preferred as it is safe and convenient for patients. Combination treatment involves the delivery of two therapeutic agents or a combination of different therapies, such as chemotherapy with immunotherapy, photothermal therapy (PTT) with PDT, or radiotherapy. A combinational therapy approach has various benefits, including enhanced therapeutic effects, reduced toxic effects, improved therapeutic outcomes, suppression of drug resistance, and release of the drug in a controlled and sustained manner. In skin cancer, combined therapy helps to avoid adverse effects, such as burning sensations, and also decreases the tumor recurrence rate. PDT is mainly used in association with other therapies for improved efficacy and lesser incidence of drug resistance.

The present research work disclosed the development of a scalable dual drug-loaded lipid nano-carrier-based platform technology for delivering hydrophobic small molecules, including chlorin e6, curcumin, and itraconazole for the treatment of melanoma and basal cell carcinoma by topical route. For the development of itraconazole and chlorin e6 dual drug lipidic nanoparticles, Precirol ATO 5 was selected as the solid lipid, and Squalene was chosen as the liquid lipid. In another combined formulation, Precirol ATO 5 was again chosen as the solid lipid, and Capmul MCM C8 was selected as the liquid lipid for the development of curcumin and chlorin e6 dual drug lipidic nanoparticles.

Our study demonstrates the potential of lipid nanocarrier systems for the topical delivery of dual drugs, (chlorin e6+ curcumin) and (itraconazole + chlorin e6) to treat skin cancer, including cutaneous melanoma and basal cell carcinoma using photodynamic therapy. The developed formulations were uniformly fabricated, spherical shapes with a uniform particle size distribution. The prepared formulation showed the highest singlet oxygen generation. The prepared photo-triggered ROS-generating dual drug-based lipidic nanoparticles showed synergistic effects against cancer cells upon NIR activation, resulting in higher cellular uptake, better cancer growth inhibition, and pronounced apoptotic events compared to free drugs in B16F10 and A431 cell lines. Interestingly we have found that a combination of itraconazole and chlorin e6 lipidic nanoformulation showed the highest apoptosis on the B16F10 and A431 cell lines compared to free drugs. Furthermore, incorporating nanoparticles in gel allowed for better skin permeation and retention at dermal layers. In the in-vivo studies, the developed dual drug lipid-based

formulation exhibited the slowest tumor growth compared to the treatment group. This improved tumor site targeted delivery of potent molecules resulted in a significantly enhanced *in-vivo* anti-tumor efficacy against a C57 skin cancer mouse model with increased intratumorally ROS generation and apoptosis. In the ROS and TUNEL assay, more bright green fluorescence was observed in tumor samples following treatment with inhouse developed gel compared to other treatment groups, confirming more apoptotic bodies and significant production of ROS. Additionally, In the Ki-67 assay, more cell proliferation was observed in the control group (greenest fluorescence). The least in the in-house developed gel treatment group indicated Ki-67 positive tumor cells, confirming the least tumor growth. Altogether, the current study demonstrated that the combination approach could effectively target drug resistance pathways in-vitro, and the in-vivo delivery of this drug combination using lipidic-based nanoparticles and charge-based lipidic nanoparticles could increase tumor accumulations, resulting in improved anti-tumor efficacy against skin cancer.

To tackle more superficial, less deadly, less complicated, and early-stage cancers like BCC, SCC, and early-stage melanoma, the Curcumin and Chlorin e6 combination is more efficacious as the combination includes a second-generation PS like Chlorin e6 with more penetrability and targetability and a first-generation PS like Curcumin with a wide range of activities. The synergistic effect acts direct and fast. However, once the cancer cells have started metastasizing, and gotten more complex, the Itraconazole and chlorin e6 combination is a better option as this combination utilizes a wide range of mechanistic pathways to eliminate the cancer cells from the body. Curcumin acts as a PS and the synergistic effect with a chemotherapeutic drug like Itraconazole offers a more holistic approach to tackling the tumor cells. So, for malignant melanoma, Itraconazole and chlorin e6 is a better choice.

This lipidic system may provide a unique platform for delivering dual potent hydrophobic moiety for different ill conditions such as cancer, psoriasis, skin infections, etc. It may also be adequate for clinical testing and commercial application.

5.2. Future prospects

In the present work, we have developed scalable dual-drug photo-triggered ROS-generating lipidic nanoparticles for delivering various hydrophobic molecules (Chlorin e6, Itraconazole, and Curcumin) for the treatment of cutaneous melanoma and basal cell carcinoma. There are several facets of the developed formulations and nano-platform that could be investigated in the future to facilitate their clinical translation.

♦ These developed nano-formulations could be further scale-up using a High-pressure homogenizer for clinical translation

♦ Apart from the above-mentioned drug molecules, other potent hydrophobic drugs and other cells penetrating peptides could be loaded into this platform and could be explored for their skin cancer model

♦ These dual-drug lipidic nano-systems could be explored for treating several dermal problems e.g. cancer, eczema, acne, and rare diseases.

♦ These nano-carriers could also be modified with targeting groups on the lipidic block, or modified targeted lipids could be used for active targeting of therapeutic agents.

♦ The surface chemistry of the lipidic nanoparticles could be modified for delivering proteins, peptides, and oligonucleotides.

APPENDICES

PUBLICATIONS FROM THESIS

Research

- R. Jain, M. Paul, S.G. Padaga, S.K. Dubey, S. Biswas, G. Singhvi, Dual-Drug-Loaded Topical Delivery of Photodynamically Active Lipid-Based Formulation for Combination Therapy of Cutaneous Melanoma, Mol Pharm. (2023). https://doi.org/10.1021/ACS.MOLPHARMACEUT.3C00280.

- R. Jain, R. Pradhan, S. Hejmady, G. Singhvi, S.K. Dubey, Fluorescence-based method for sensitive and rapid estimation of chlorin e6 in stealth liposomes for photodynamic therapy against cancer, Spectrochim Acta A Mol Biomol Spectrosc. 244 (2021) 118823. https://doi.org/10.1016/J.SAA.2020.118823.

- R. Jain, S.K. Dubey, G. Singhvi, Stability indicating validated high-performance liquid chromatography method for simultaneous estimation of chlorin e6 and curcumin in bulk and drug-loaded lipidic nanoformulation, Sep Sci Plus. (2022). https://doi.org/10.1002/SSCP.202200107.

Review articles

- R. Jain, S. Dubey, G.S.-D. discovery today, undefined 2021, The Hedgehog pathway and its inhibitors: emerging therapeutic approaches for basal cell carcinoma, Elsevier. (n.d.). https://www.sciencedirect.com/science/article/pii/S1359644621005390 (accessed March 14, 2022).

- R. Jain, S. I, S. G, D. SK, Nanocarrier Based Topical Drug Delivery- A Promising Strategy for Treatment of Skin Cancer, Curr Pharm Des. 26 (2020) 4615–4623. https://doi.org/10.2174/1381612826666200826140448.

- R. Jain, S. Mohanty, I. Sarode, S. Biswas, G. Singhvi, S.K. Dubey, Multifunctional Photoactive Nanomaterials for Photodynamic Therapy against Tumor: Recent Advancements and Perspectives, Pharmaceutics 2023, Vol. 15, Page 109. 15 (2022) 109. https://doi.org/10.3390/PHARMACEUTICS15010109.

Book Chapter

- V.K. Rapalli, A. Khosa, G. Singhvi, V. Girdhar, **R. Jain**, S.K. Dubey, Application of QbD Principles in Nanocarrier-Based Drug Delivery Systems, Pharmaceutical Quality by Design: Principles and Applications. (2019) 255–296. https://doi.org/10.1016/B978-0-12-815799-2.00014-9.

Patent Filed from Thesis

- Positive charge-based lipid formulations for drug delivery (202211054911 TEMP/E-1/61961/2022-DEL)

- A photodynamic chemotherapeutic lipidic nanoparticle, a nano-formulation thereof and a method of preparing the nanoformulation (202311003263 TEMP/E-1/1794/2023-DEL)

BIOGRAPHIES

Dr. Gautam Singhvi

About

He is working as an Associate Professor in the Department of Pharmacy, BITS, Pilani. He obtained his Ph.D. from BITS Pilani. He has been working as a faculty member in BITS-Pilani since the year 2015. He has industrial research experience on solid oral, pellets, and complex pharmaceutical product development. Currently, he is involved in industrially feasible nanocarrier-based formulation development and optimization for various therapeutic agents. He has many publications in reputed international and national peer-reviewed journals and filed 6 patents. He is actively involved in sponsored research projects in collaboration with the pharmaceutical industries. He is also passionate about practicing the newer teaching pedagogy in his classroom teaching and motivating students to face the challenges of the new era.

Dr. Sunil Kumar Dubey Biography

About

Dr. Sunil Kumar Dubey is presently working as the General Manager, Medical Research, R&D Healthcare Division at Emami Ltd, Kolkata. He is involved in planning and ensuring the timely execution of several preclinical and clinical studies. His expertise involves in validating the effectiveness of a vast range of healthcare products and providing business development-related insights. He is responsible for developing product concept notes, technical notes, monographs, and dossiers. His team is also involved in supporting medico-marketing, product licensing activities, and training personnel from marketing and sales teams. Collectively, his efforts are towards bridging the gap between the industry, consumers, and the scientific community.

Overall, he has more than 16 years of industrial, teaching, research, and administrative experience. Prior to this, he was Assistant Professor in the Department of Pharmacy, Birla Institute of Technology and Science (BITS), Pilani, India. He was also a visiting Assistant Research Professor in the Department of Chemical and Biomolecular Engineering at the University of Maryland, USA. Currently, he also serves as a guest faculty at various leading institutes including NIPER Guwahati, NIPER Raebareli, Jamia Hamdard, etc.

He has an extensive research experience in the area of pharmacokinetic pharmacodynamic modelling and simulations, development of phytopharmaceuticals and numerous nano-technology-based platforms. He has supervised Ph.D., postgraduate and undergraduate students. He has published more than 150 articles and book chapters in renowned high-impact journals and presented papers at conferences in India and abroad. He is included in the list of 'World's Top 2% Most-Cited Scientists' as per the Elsevier-Stanford University report.

He has successfully completed various government and industry funded projects related to new product development, pharmacokinetic and pharmacodynamic investigations. All these concerted efforts have led to the grant of patents to his name as well.

Mr. Rupesh Sanjaykumar Jain Biography

About

Rupesh Jain is a Research Scholar in the Department of Pharmacy, Birla Institute of Technology and Science (BITS), Pilani, India. He completed his post-graduation degree from the Manipal Academy of Higher Education (MAHE). His post-graduate work focused on the development of transdermal patches for selective drugs. Currently, his Ph.D. worked on the design and evaluation of photodynamically active lipid-based nanoformulations for combination therapy against skin cancer. He has research experience in the development and characterization of lipid-based nanoformulations for topical, and parenteral drug delivery. Additionally, He has research experience in In-vitro cell lines and In-vivo tumor-bearing mice models.